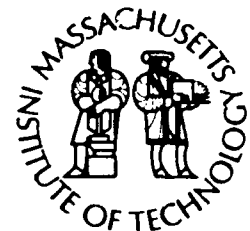




# Woods Hole Oceanographic Institution Massachusetts Institute of Technology



Joint Program  
in Oceanography/  
Applied Ocean Science  
and Engineering



---

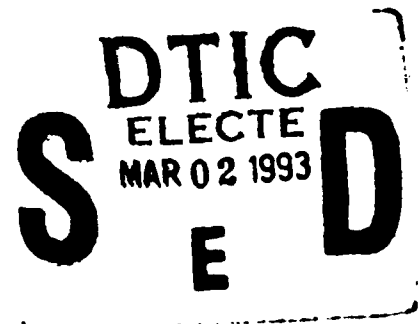
DOCTORAL DISSERTATION

Eddy Generation at a Convex Corner by a Coastal  
Current in a Rotating System

by

Barry A. Klinger

March 1992



**DISTRIBUTION STATEMENT**

Approved for public release;  
Distribution Unlimited

93 3 1 001

93-04235



**WHOI-92-22**

**Eddy Generation at a Convex Corner by a Coastal  
Current in a Rotating System**

by

**Barry A. Klinger**

**Woods Hole Oceanographic Institution  
Woods Hole, Massachusetts 02543**

and

**The Massachusetts Institute of Technology  
Cambridge, Massachusetts 02139**

**March 1992**

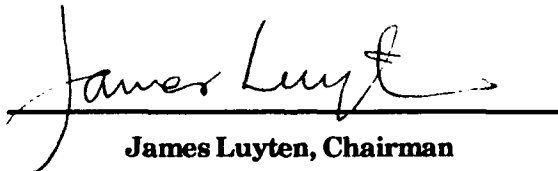
**DOCTORAL DISSERTATION**

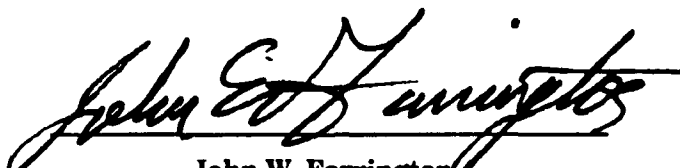
**Funding was provided by the National Science Foundation  
under Grant OCE89-15408.**

**Reproduction in whole or in part is permitted for any purpose of the United States  
Government. This thesis should be cited as: Barry A. Klinger, 1992. Eddy  
Generation at a Convex Corner by a Coastal Current in a Rotating System.  
Ph.D. Thesis. MIT/WHOI, WHOI-92-22.**

**Approved for publication; distribution unlimited.**

**Approved for Distribution:**

  
**James Luyten, Chairman**  
Department of Physical Oceanography

  
**John W. Farrington**  
Dean of Graduate Studies

# EDDY GENERATION AT A CONVEX CORNER BY A COASTAL CURRENT IN A ROTATING SYSTEM

by

Barry A. Klinger

S.B., Massachusetts Institute of Technology  
(1985)

Submitted in partial fulfillment of the  
requirements for the degree of

DOCTOR OF PHILOSOPHY

at the

MASSACHUSETTS INSTITUTE OF TECHNOLOGY

and the

WOODS HOLE OCEANOGRAPHIC INSTITUTION

March 1992

© Barry A. Klinger 1992

The author hereby grants to MIT and to WHOI permission to reproduce  
and to distribute copies of this thesis document in whole or in part.

Signature of Author.....*Barry A. Klinger*.....

Joint Program in Physical Oceanography  
Massachusetts Institute of Technology  
Woods Hole Oceanographic Institution  
March 5, 1992

Certified by.....*John A. Whitehead*.....

John A. Whitehead  
Senior Scientist  
Thesis Supervisor

Accepted by.....*Lawrence J. Pratt*.....

Lawrence J. Pratt  
Chairman, Joint Committee for Physical Oceanography  
Massachusetts Institute of Technology  
Woods Hole Oceanographic Institution

Accession For	
NTIS CRA&I	<input checked="" type="checkbox"/>
DTIC TAB	<input type="checkbox"/>
Unannounced	<input type="checkbox"/>
Justification	
By	
Distribution /	
Availability Codes	
Dist	Avail and/or Special
A-1	

"While the solid appears in itself dead, moved only from without, the liquid and volatile make the impression of independent mobility and vitality..."

-quoted by Ved Mehta, *The Stolen Light*

*Nur ein nar messt wasser.*

[Only a fool measures water.]

-Old Yiddish Saying

# EDDY GENERATION AT A CONVEX CORNER BY A COASTAL CURRENT IN A ROTATING SYSTEM

by  
Barry A. Klinger

Submitted in partial fulfillment of the requirements for the degree of  
Doctor of Philosophy at the Massachusetts Institute of Technology  
and the Woods Hole Oceanographic Institution  
March 5, 1992

## Abstract

Rotating baroclinic and barotropic boundary currents flowing around a corner in the laboratory were studied in order to discover the circumstances under which eddies were produced at the corner. Such flows are reminiscent of oceanic coastal flows around capes. When the baroclinic currents, which consisted of surface flows bounded by a density front, encountered a sharp corner, immediately downstream of the corner an anticyclone grew in the surface layer for an angle of greater than 40 degrees. Varying the initial condition of the flow or the depth of the lower layer did not noticeably affect the gyre's properties except for its growth speed, which was greater when the lower layer was shallower. The barotropic currents were pumped along a sloping bottom, and also formed anticyclonic gyres which quickly attained an approximately steady state. For a given topography, the size of the gyre was proportional to the inertial radius  $u/f$ . Volume flux calculations based on the surface velocity revealed vertical shear which increased with gyre size. Hydraulic models were also applied to flow around gently curving topography to determine the critical separation curvature as a function of upstream parameters.

Thesis Advisor: Dr. J. A. Whitehead

Title: Senior Scientist, Woods Hole Oceanographic Institution

## Table of Contents

<b>Abstract</b> . . . . .	<b>3</b>
<b>Acknowledgments</b> . . . . .	<b>6</b>
<b>1. Introduction</b> . . . . .	<b>8</b>
1.1. Coasts, Currents, Capes, Channels, and Gyres . . . . .	8
1.2. Flow Separation in a Rotating and Non-rotating World . . . . .	20
1.3. Previous Theoretical Studies . . . . .	23
1.4. Plan of the Thesis . . . . .	30
<b>2. Hydraulic Models of Separation From Curved Coastlines</b> . . . . .	<b>32</b>
2.1. Introduction . . . . .	32
2.2. The System of Equations to be Solved . . . . .	36
2.3. Barotropic Flows Over a Flat Bottom . . . . .	41
2.4. Barotropic Flows Over a Sloping Bottom . . . . .	48
2.5. Reduced Gravity Currents . . . . .	53
2.6. Conclusions . . . . .	70
<b>3. Eddies Generated by a Density Front Current at a Sharp Corner     in a Rotating Tank</b> . . . . .	<b>74</b>
3.1. Introduction . . . . .	74
3.2. Apparatus and Procedure . . . . .	77
3.3. Qualitative Behavior and Eddy Growth Rates . . . . .	86
3.4. Interpolation of Fresh Water Velocity Fields . . . . .	102
3.5. Summary and Discussion . . . . .	113
<b>Appendices to Chapter 3</b> . . . . .	<b>121</b>
3.A. Technical Notes on Apparatus . . . . .	121
3.B. Estimation of Interpolation Errors . . . . .	125

<b>4. Barotropic Sloping Bottom Flows Around a Corner in a Rotating Tank . . . . .</b>	<b>127</b>
4.1. Introduction . . . . .	127
4.2. Experimental Apparatus and Procedure . . . . .	130
4.3. Qualitative Observations . . . . .	138
4.4. Rossby Number and Gyre Size . . . . .	143
4.5. Velocity, Transport, and Vorticity Profiles . . . . .	156
4.6. Discussion and Conclusions . . . . .	177
<b>Appendix to Chapter 4 . . . . .</b>	<b>181</b>
4.A. Jitter Removal . . . . .	181
<b>5. Summary and Conclusions . . . . .</b>	<b>184</b>
<b>References . . . . .</b>	<b>190</b>

## Acknowledgements

I would like to thank my advisor, Jack Whitehead, for many lessons in how one actually does science as well as for pushing me into deeper waters so I could swim by myself. Thanks go also to Glenn Flierl, my geophysical fluid dynamics guru and the man responsible for my entering physical oceanography graduate school in the first place, who contributed many ideas to this thesis and gave extensive computer and administrative support at MIT. The rest of my thesis committee—Larry Pratt, Nelson Hogg, and Phil Richardson—helped me refine and focus my thesis with their comments and discussion. Melvin Stern was not officially on my thesis committee, but our many scientific discussions were quite helpful to me. I could hardly have put together any experiments without the help of Robert Frazel, who has presided over the Geophysical Fluid Dynamics Lab since the dawn of time and has a knack for giving one some perspective on life in academia. The data analysis was based on work at the Motion Analysis facility at WHOI; the burden of its upkeep fell on the shoulders of Scott Gallagher, who was kind enough to take time away from his own research to answer my numerous questions about the equipment. Roberta Young and Steve Meacham have been a great help in dealing with the computers at MIT. Anne Marie Michael saved me days of work by helping me with the mysteries of  $\text{\LaTeX}$ ; much of this work was on her own time. Fellow Joint Program students—Dave Walsh, LuAnne Thompson, Sarah Gille, Changshen Chen, Dave Chester, Sarah Green, Molly Baringer, Xiaoming Wang, Lorenzo Polvani, Keith Alverson, Gwyneth Hufford, and many others—have helped keep me sane while also keeping me on my toes with many clever comments and probing questions about my work.

I thank my parents, Linda and Rudy Klinger, and my sister, Elise Klinger, for their decades of faith in me, and my wife, Elise Berliner, whose love, help, and advice was like a ship carrying me over the storm-tossed seas of oceanography grad school.

This work was supported by the National Science Foundation grant OCE 89-15408.





# Chapter 1.

## Introduction

### 1.1. Coasts, Currents, Capes, Channels, and Gyres

A dominant feature of the world's oceans is the ubiquity of eddies. Though the forcing of the general circulation is dominated by the basin-scale patterns of wind stress and surface heating and cooling, much of the energy of ocean currents resides in mesoscale structures, which have a spatial scale on the order of the local internal radius of deformation, and sub-mesoscale features. Since mesoscale eddies in the ocean are thought to be largely a consequence of baroclinic and barotropic instability of larger scale mean currents, much work on eddy generation has concentrated on the instability of geometrically simple currents, such as zonal or circular flows. However, it is also interesting to contemplate the dynamics of other mechanisms which may produce eddies. Laboratory and computer experiments as well as oceanic observations have shown that coastal currents that flow around a convex corner, such as a cape, are capable of generating eddies. In this thesis, we attempt to shed some light on the dynamics governing such eddy generation.

The Mediterranean Outflow is a prime example of a current flowing along a lateral boundary with a convex bend in it (see Figure 1.1.1). This current is a buoyancy-driven flow from the salty, warm Mediterranean to the relatively fresh and cold Atlantic (Ambar, Howe and Abdullah, 1976; Ambar and Howe, 1979a,b; Grundlingh, 1981; Howe, 1982; Madelain, 1970; Thorpe, 1976; Zenk, 1970, 1975, 1980). While the character of the dense plume is dominated by mixing and friction as it descends from the sill at Gibraltar along the continental shelf, by the time it reaches Cape Saint Vincent at the western end of the Gulf of Cadiz (Figure 1.1.1), it has attained a stable depth range marked by salinity and temperature maxima

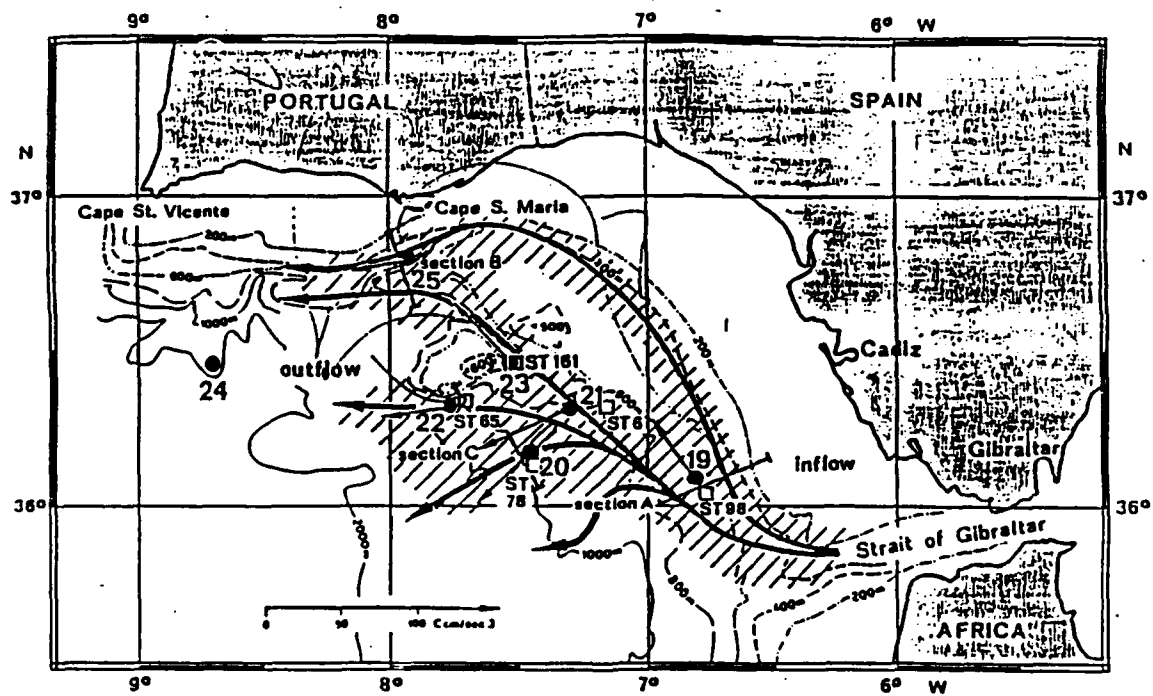


Figure 1.1.1: Flow of Mediterranean Outflow in Gulf of Cadiz (Zenk, 1975, Figure 1).

centered at 1200 m and 800 m (Figure 1.1.2). As the Mediterranean water emerges from the Strait of Gibraltar, it rests completely on the sloping bottom, but by the time it reaches Cape Saint Vincent, the Outflow is bounded both above and below by Atlantic water, with the continental slope acting as a wall rather than a floor. Average current speeds of 20–35 cm/s have been measured in the Mediterranean Outflow in the Gulf of Cadiz, with a current width on the order of 20 km for the flow filament closest to the shore and 60 km wide if we include other westward-flowing filaments (Figure 1.1.1).

Related to the Mediterranean Outflow are meddies, which are anticyclonically circulating subsurface lenses of water with water properties of the Outflow (Armi and Zenk, 1984; Kase and Zenk, 1987; Richardson *et al.*, 1988). A typical meddy has a radius on the order of 50 km, maximum azimuthal current speeds of 20–25 cm/s, and vertical property distributions as shown in Figure 1.1.3. While the maxima in property anomalies and rotation speed are clearly deep in the thermocline (as in the Mediterranean Outflow, at about 1200 m), there is evidence that meddies do have a significant surface vorticity (Kase and Zenk, 1987).

The best studied meddies have all been observed on the order of 1000 km west of Cape Saint Vincent even though the meddy water characteristics are indicative of an origin near Cape Saint Vincent. Swallow (1969) reports a *cyclone* observed in the Gulf of Cadiz. His hydrography also showed a weak lens of salty water reminiscent of a meddy, but drifters placed in it showed no anticyclonic rotation. Sanford (1988, personal communication) reports an anticyclone observed forming off Cape Saint Vincent, but its 30 cm/s velocity maximum was only about 5 km from the center. Armi and Zenk (1984) estimate that it would take 20 days for the main branch and 10 days for the entire current to form a meddy. Richardson *et al.* (1988) estimate that 8 to 12 meddies are formed a year, implying that meddy formation must be happening at least a third of the time.

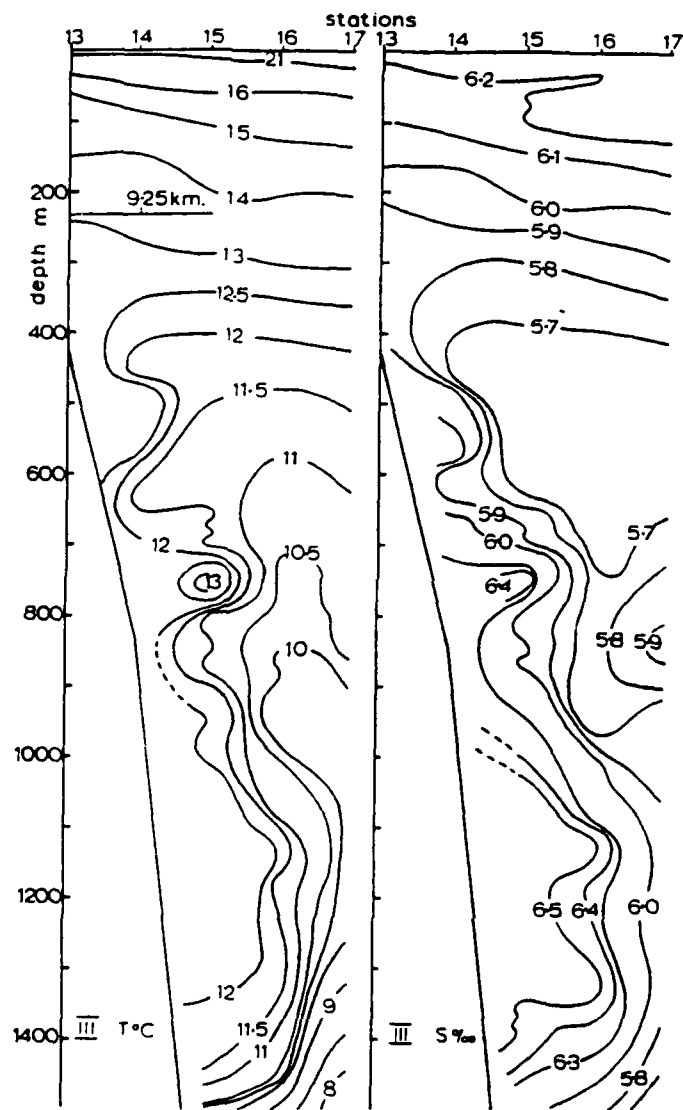


Figure 1.1.2: Cross-shore profile of Mediterranean Outflow along line extending south from about 30 km south of Cape Saint Vincent (Ambar and Howe, 1979a, Figure 5). (a) Temperature, (b) salinity.

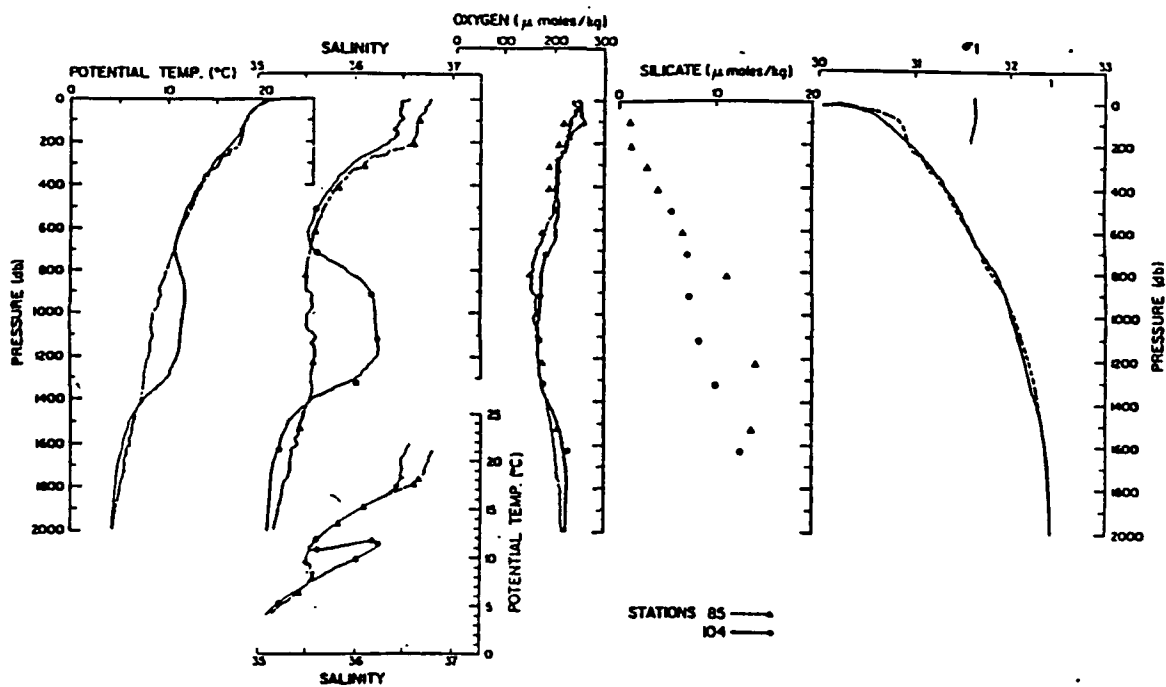


Figure 1.1.3: Vertical profile of properties in a meddy and in a nearby "ambient" water station 85 km away (Armi and Zenk, 1984, Figure 1): potential temperature, salinity, oxygen, silicate, and  $\sigma_t$  vs. pressure, and potential temperature vs. salinity.

D'Asaro (1988) has hypothesized that meddies are generated by the Mediterranean Outflow at Cape Saint Vincent. He considered this an example of eddy generation by a boundary current encountering a corner. Another example is the generation of Beaufort Sea sub-mesoscale vortices by a surface coastal current flowing past Point Barrow on the northern coast of Alaska (Figure 1.1.4). There is better direct evidence of anticyclonic eddy formation at Point Barrow than there is at Cape Saint Vincent. For instance, in the summer of 1971 an occupied ice floe was carried along the coast by the current and after passing Point Barrow executed two anticyclonic loops with approximate radius of 5 km (about a Rossby radius) and approximate period of one day (Figure 1.1.5). Satellite infrared photography during the summer also shows similarly scaled cyclonic and anticyclonic features. In D'Asaro's conception, friction at the inshore edge of the coastal current generates a layer of negative vorticity, as in non-rotating flows, which is the source for the large negative relative vorticity of the anticyclonic eddies. Meddies have smaller negative relative vorticities, with rotation periods at the velocity maximum on the order of a week rather than a day.

There are other theories for the generation of meddies, such as McWilliams' (1985) proposal that they are formed by geostrophic adjustment as the plume descends from the Strait of Gibraltar. The most compelling of these explanations of meddy generation is the work of Kase and Zenk (1987) and Kase, Beckmann, and Hinrichsen (1989). Their models suggest that meddies are broken off from the Mediterranean Outflow by stronger currents above the thermocline in the Atlantic off the coast of Portugal.

A situation which is similar to that of a coastal current flowing around a corner is that of the outflow from a strait which can form a gyre at the mouth of the strait. Such anticyclones have been observed in the Alboran Sea in the western Mediterranean (see Figure 1.1.6 and Lanoix, 1974) and in the outflow of the Tsugaru Sea in Japan (Conlon 1982; Kawasaki and Sugimoto, 1984). The Alboran gyre is fed

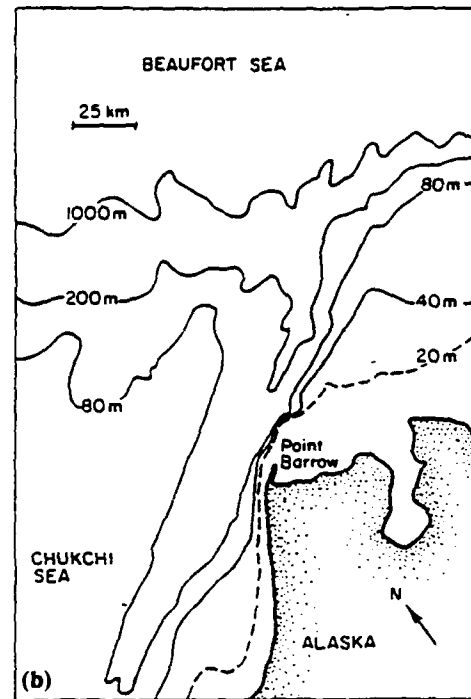
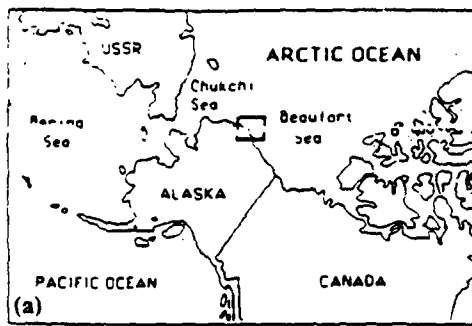


Figure 1.1.4: (a) Location and (b) topography of Barrow canyon and Point Barrow, suspected generation site of Beaufort Sea eddies (D'Asaro, 1988, Figure 1). Contours deeper than 1000 m are not shown.

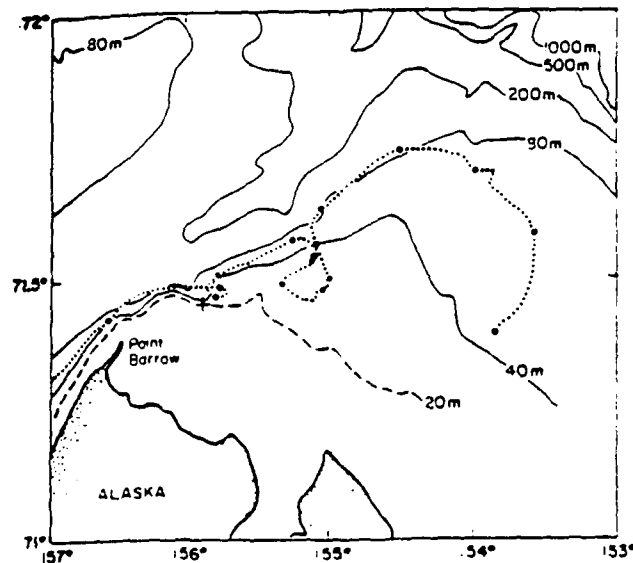


Figure 1.1.5: Track of ice flow showing anticyclonic motion past Point Barrow, August 6-9, 1971, with heavy dots six hours apart (D'Asaro, 1988, Figure 4).



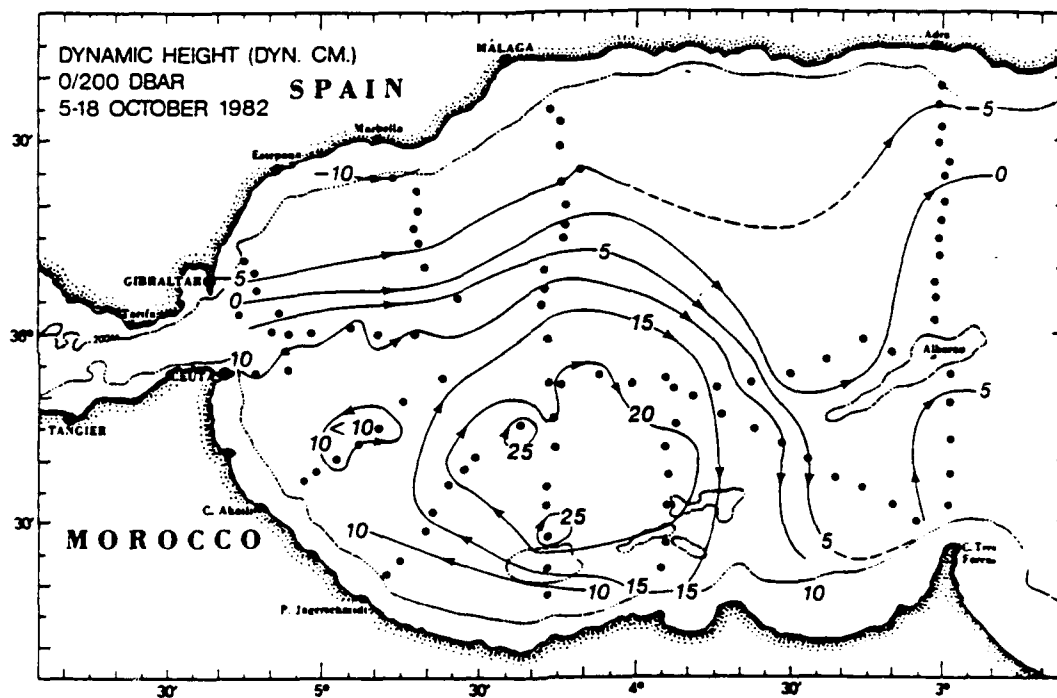


Figure 1.1.6: The Alboran gyre as seen in dynamic height map of western Mediterranean Sea (Donde Va Group, 1984).

by the surface current which flows into the Mediterranean from the Strait of Gibraltar and detaches from a bend in the North African coast. The Tsugaru outflow is also a surface current, which has a seasonal change from a mode that remains attached to the coast and one that forms a gyre. Bormans (1988) reviews the literature on gyres produced by such flows. Numerical models of the Alboran gyre (Loth and Crepon, 1984; Preller, 1985; Werner *et al.*, 1988) reproduced the gyre but did not isolate its cause.

The generation of eddies by a current flowing around a corner has been observed in several laboratory experiments in rotating systems.

Whitehead and Miller (1979) conducted a series of experiments in a rotating channel that opened at either end into a wider basin. The bends in the wall consisted of segments of circles. Initially a dam or gate was placed across the center of the channel, separating salty, dense water on one side from fresh, light water on the other (Figure 1.1.7). When the gate was removed, geostrophic adjustment created a current in each layer moving in opposite directions. The Rossby radius of deformation was varied from run to run, and the radius  $\rho$  of the circular bends in the walls took one of two values for each run. For a Rossby radius  $R$  small compared to the channel width  $W_c$ , the currents had a width of about  $R$  and were concentrated close to the right hand wall looking downstream. For  $R < W_c$ , the current was unstable, producing a series of vortices of both signs, and for  $R > W_c$ , the current veered right to stay near the wall as it emerged from the channel. For  $R > \rho$  the current outside the channel formed an anticyclone between the current and the wall near the channel opening. This eddy grew with time, but stayed attached to the wall. Figure 1.1.8 summarizes results.

Bormans and Garrett (1989) conducted similar experiments in which the fresh current flowed into water which had an ambient surface fresh layer. The relative depths of the two fresh layers controlled the Rossby number of the flow. For flows in

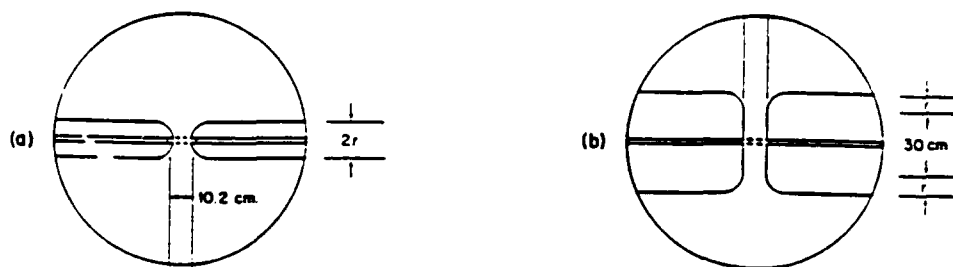


Figure 1.1.7: Laboratory apparatus for experiments in which channel opened into wider basin and flow was initiated by geostrophic adjustment (Whitehead and Miller, 1979, Figure 3).

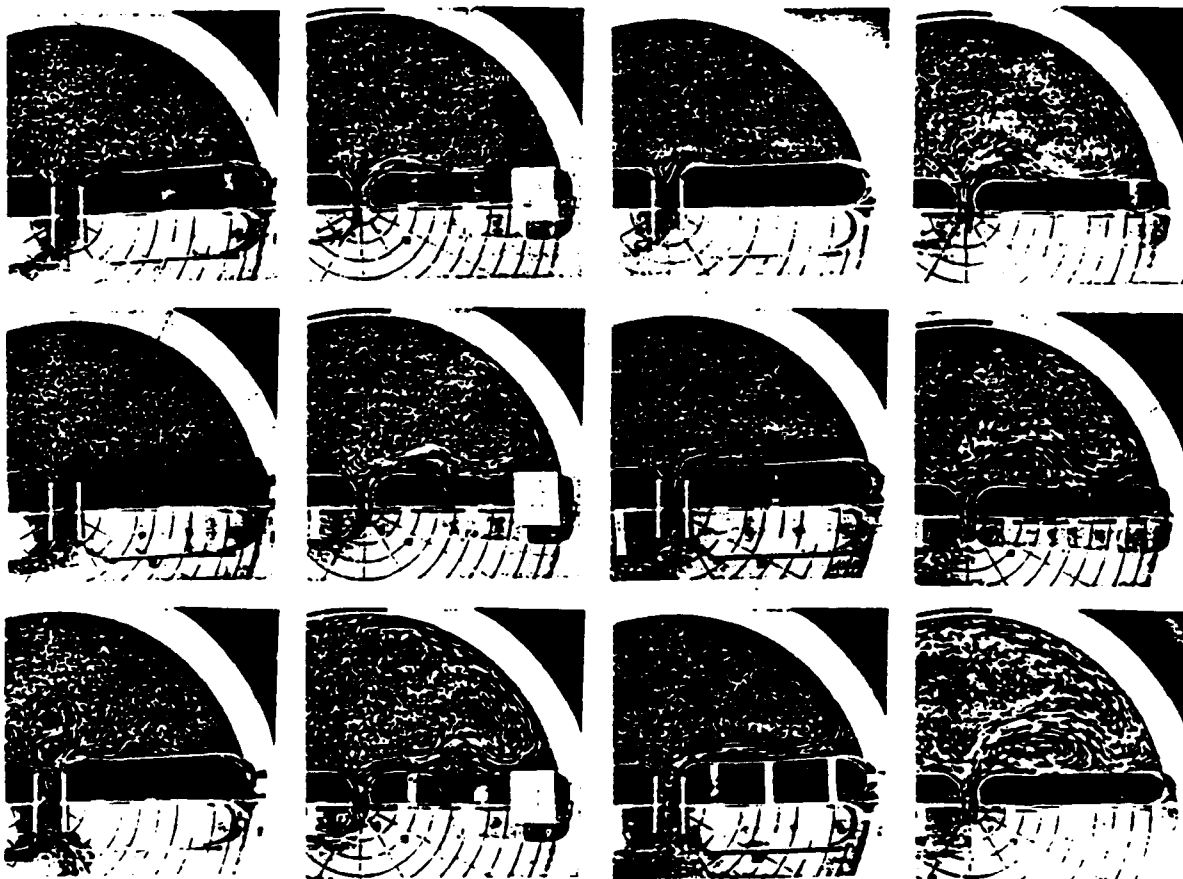


Figure 1.1.8: Representative flow regimes, channel flow into wider basin (Whitehead and Miller, 1979, Figure 4). Photos show surface currents flowing into dark region of tank, with each column a different time sequence. From left to right, shows increasing Rossby radius runs: violently unstable flow, moderate instability, coastal trapped current, and single gyre downstream of corner.

which  $\rho > W_c$ , a gyre was formed when  $u/f\rho > 1$  for velocity scale  $u$  and Coriolis parameter  $f$ . Whitehead and Miller's results were compatible with this relation, since in their flow  $R$  was approximately  $u/f$ . For  $\rho < W_c$ , the distinction between different regimes is not clear. Kawasaki and Sugimoto (1984, 1988) also conducted similar experiments, except they pumped the fresh water into a channel whose mouth had a sharp corner rather than a rounded one. They also controlled the Rossby number of the flow, and found that for Rossby number greater than about .5 a gyre was formed as in the other studies, but no gyre was formed for low Rossby number flows. Primitive equation models of lock-exchange flow from a strait (flow out of the strait at the surface and into the strait at depth) developed an anticyclone for a Rossby number of about .6 (Wang, 1987) but produced a bulge with no apparent anticyclonic rotation for a Rossby number of about .2 (Chao and Boicourt, 1986).

The only study of a rotating coastal current flowing around a corner is that of Stern and Whitehead (1990), who used a pump to create a turbulent barotropic flow next to a straight wall with a sharp corner. The current tended to stay attached to the wall downstream of the bend for small total bend angle and for flows for which the distance of the velocity maxima to the wall were small compared to the current width. For higher corner angles, it separated from the corner in a very different manner from the baroclinic flows emerging from channels. Instead of the current flowing around a single anticyclonic gyre and re-attaching to the wall further downstream, it broke into dipoles which propagated away from the coast and did not re-attach (Figure 1.1.9). In all of the laboratory experiments and in almost all of the numerical studies of strait outflows described above, the flow was baroclinic (or reduced gravity), indicating that the stratification is a decisive factor in determining the nature of the flow separation at the corner, probably due to the stability characteristics of the flows. However, Loth and Crepon (1984) ran a barotropic model which also produced a single gyre.

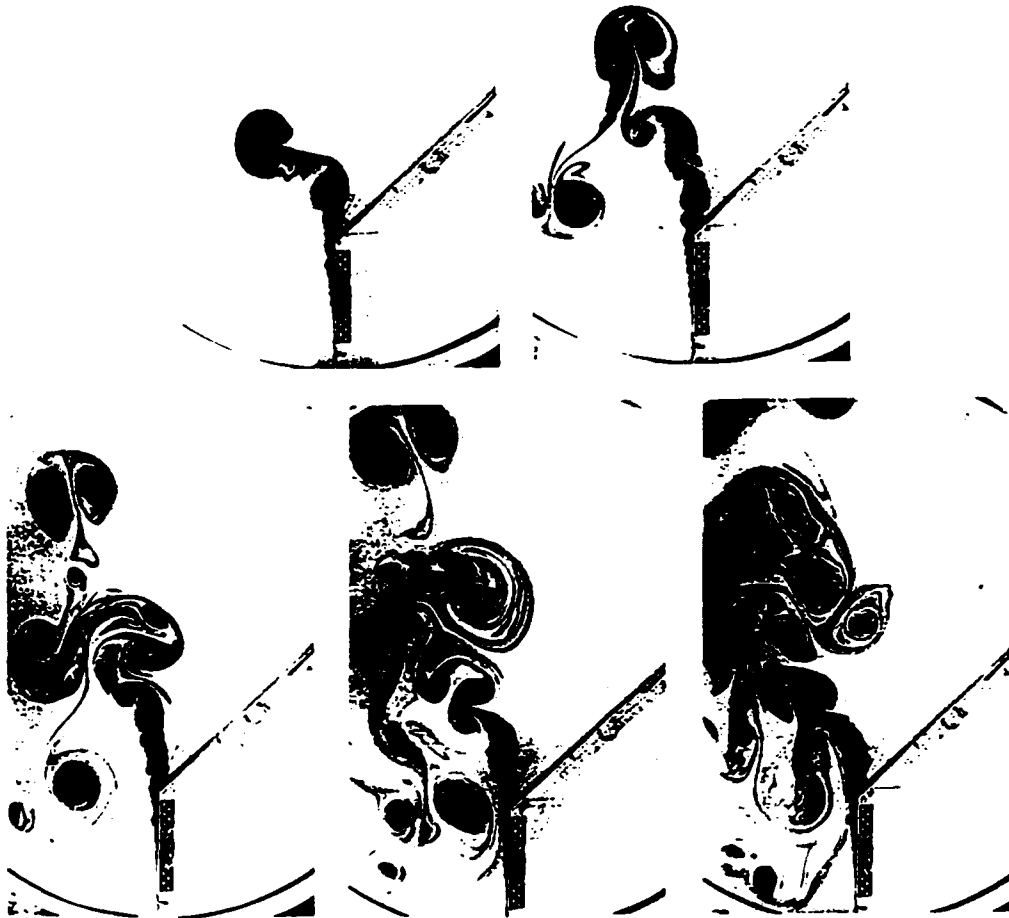


Figure 1.1.9: Top view of dyed barotropic jet which flows along wall and separates at corner of angle  $50^\circ$ . Photographs are 1 min apart, starting at top left and ending at bottom right. The nozzle is 35 cm from the corner (Stern and Whitehead, 1990, Figure 18).

Boyer and Davies (1982), Boyer and Kmetz (1983) and Boyer and Tao (1987) observed the generation of eddies by uniform flow past obstacles in rotating systems. In the first two of these studies, homogeneous fluid flowing past a right circular cylinder produced eddies on the downstream side of the obstacle. In the third, linearly stratified salt water flowed past a wall with a protruding triangular "cape" with linearly sloping sidewalls. This also produced a gyre on the downstream side of the obstacle. Signell and Geyer (1991) performed numerical simulations of high Rossby number, barotropic flow past a headland with similar results.

## **1.2. Flow Separation in a Rotating and Non-rotating World**

Since the late nineteenth century, fluid dynamicists concerned with the lift generated by an air foil, the drag on a moving automobile, the interaction of wind with buildings, or flow through a widening pipe, have studied eddies generated by the separation of a current from the solid object in question (Prandtl, 1957; Batchelor, 1967; Schlichting, 1979). In all those cases, the flow can be thought of as consisting of an inviscid, irrotational flow in most of the fluid domain, with a thin layer of frictionally-dominated vorticity connecting the irrotational flow to the no-slip condition that must be enforced at the solid boundary. There exists a comprehensive body of information about how the presence of the viscous boundary layer produces separation in such non-rotating flows. However, when rotation must be considered, as in geophysical applications, several new elements are added which have the potential to radically change the nature of how a current separates from a boundary.

In addition to the ubiquity of eddies, oceans are also distinguished by the presence of numerous boundary currents. In contrast to non-rotating flows, in which boundary layers are marked by a decrease in flow speeds relative to the rest of the fluid,

ocean currents near a boundary are frequently much stronger than flows in the rest of the neighborhood. In rotating systems, veering induced by the Coriolis force tends to push currents up against a lateral boundary in a number of ways. There are alongshore currents due to coastal upwelling, coastal downwelling, buoyancy sources, and larger scale western boundary currents which can be pushed by the wind or by thermohaline forcing. Any pressure gradient directed perpendicularly to the coast ("cross-shore") will induce a flow parallel to the coast ("alongshore") so that forcing that would induce jets directed away from a boundary in a non-rotating system creates a boundary current when the system is rotating. A more subtle consequence of rotation is that there are wave modes for a wide range of frequencies and wavelengths that propagate along coasts but not into the interior of basins. This is important because the direction that a signal may travel determines where a current will be established when there is some localized disturbance in a density or sea surface height field. Kelvin waves propagate along a coast with the boundary to the right in the northern hemisphere (to the left in the southern hemisphere) if we face in the direction of propagation, so a buoyancy current will propagate in this direction. A similar phenomenon may occur in homogeneous fluid over a sloping bottom, in which case topographic Rossby waves propagate along isobaths.

In non-rotating flows viscosity is ultimately the only source for vorticity in the fluid, and in practice the viscous boundary layers near solid boundaries are the main sources of water parcels that have vorticity. In a rotating system, all water has ambient vorticity due to the rotation itself. In geophysical flows, the vertical component of the background, or "planetary" vorticity (the Coriolis parameter  $f$ ) can be converted to relative vorticity by vertical stretching and compressing of water parcels as well as changes in the latitude of the water parcel. In this study we only look at flows for which the horizontal scale is small enough to ignore latitude variations.

In the limit of relative vorticity  $\zeta$  small compared to  $f$  and friction also small, there are two consequences which combine to constrain homogeneous density flows to approximately follow isobaths. Such flow can not support vertical shears in horizontal velocity, so that we can define a potential vorticity  $q = (f + \zeta)/h$  to characterize an entire column of water from water surface to floor, where  $h$  is the height of this column. Potential vorticity is conserved, so that if a column of water moves across an isobath,  $h$  changes, then  $\zeta$  must change by a corresponding amount in order to keep  $q$  constant. If we have  $\zeta \ll f$ , however, large changes in  $h$  can not be compensated, thus not allowing the water parcel to change its thickness by much. Since isobaths near coasts inevitably tend to parallel the coastline, this provides an additional impetus on fluids with little or no stratification to have strong flows parallel to the coast.

Finally, rotation has a more subtle effect which is due to the presence of the Ekman layer at the base of the fluid. This effect, discovered by Merkin and Solan (1979), will be described at the end of the next section.

These differences between rotating and non-rotating flows can have a number of consequences. In non-rotating two-dimensional flows, for which the most complete work on current separation and eddy generation has been conducted, the viscous boundary layer is the only source for small scale structure in the fluid. Irrotational flow is determined entirely by the boundary conditions, which consist of the shape of the solid boundaries of the domain as well as the distributions of sources and sinks of fluid at the borders of the domain. Such irrotational flow can not support an interior streamfunction maximum (which would produce closed streamlines inside the current) or a geographically localized current. In three dimensional non-rotating flows, a richer vocabulary of motion is allowed, but there is still no special tendency to form flows that stay near lateral boundaries, so that there is nothing to inhibit the separation of a flow from such a boundary. For these reasons the story of eddy



formation at solid boundaries in non-rotating fluids is essentially the story of viscous boundary layer separation. The special features of the rotating fluids described above, namely the ability of rotating fluids to convert vorticity associated with the system's rotation to relative vorticity, as well as the prevalence of isolated boundary currents, presents us with the possibility that the dynamics governing the separation of currents at boundaries in rotating fluids is quite different from the dynamics of flow separation in non-rotating fluids.

### 1.3. Previous Theoretical Studies

Classical theory of two dimensional flow separation begins with the scaling argument that allows us to study a subset of the equations of motion which applies to a thin layer near the wall. Restricting ourselves to steady state flows, and following Batchelor (1967), we assume that everywhere except near the wall, friction is a small effect which can be ignored. In the event of separation, this assumption breaks down, but it is a useful device for discovering when separation must occur. One calculates the solution to the corresponding inviscid problem, which is mathematically more tractable, and then finds a boundary layer solution near the wall in order to satisfy the boundary condition of no flow tangent to the wall at the wall. If to lowest order in the along-wall momentum equation the downstream advection of momentum and cross stream diffusion of momentum are of the same order, then the width scale for the boundary layer is given by  $\delta = \sqrt{\nu/UL} = 1/\sqrt{Re}$ , where  $U$  and  $L$  are the speed and alongstream length scales,  $\nu$  is the viscosity,  $\delta$  is the boundary layer width scale divided by  $L$ , and  $Re \equiv UL/\nu$  is the Reynolds number and must be large if  $\delta$  is to be small. A consequence of this scaling is that in the boundary layer the pressure is approximately independent of the cross-wall coordinate, so that near the wall the pressure is given by the pressure calculated for inviscid flow just outside the boundary layer. Separation can occur when the pressure gradient along the wall is

pushing in the opposite direction of the flow. While this pressure gradient may be just enough to retard the inviscid flow just outside the boundary layer, inside the boundary layer, friction has slowed the flow enough so that the adverse pressure gradient can actually reverse the direction of flow, thus producing a gyre "downstream" of the separation point and forcing fluid from "upstream" to leave the wall. The inviscid flow around a corner accelerates upstream of a corner and decelerates downstream, and it is this deceleration that produces the adverse pressure gradient and hence separation. Similarity solutions for simple cases show that not all adverse pressure gradients produce separation, but the inviscid deceleration must be very small if the boundary layer is to stay attached.

Several authors have discussed rotating separation processes which are different from boundary layer separation in non-rotating fluids. We now review the main features of these studies.

Kubokawa (1991) used a reduced gravity, quasigeostrophic contour dynamics numerical model to simulate flow out of a sea strait into a basin. The outflow consisted of two regions of uniform potential vorticity, with negative quasigeostrophic potential vorticity in the right side of the current (looking downstream) and zero potential vorticity in the left region (see Figure 1.3.1). Contour dynamics is an inherently inviscid formulation of the equations of motion, so there was no friction. Depending on the parameters of the outflow, the flow in the basin took one of three basic states. In all three states, water parcels in the flow eventually veered to the right (the rotation of the system was counterclockwise) as they left the channel mouth and flowed along the edge of the basin to infinity. In one state, the veering was immediate. In another, fluid tended to accumulate just outside the mouth of the channel, forming a bulge of introduced fluid that grew with time, though the component of velocity parallel to the coast was always directed away from the mouth of the channel. Finally, there

was a state in which some of the fluid in the bulge formed an anticyclonic gyre which grew with time.

Kubokawa explained the existence of the bulge and gyre with reference to the volume flux in each region of potential vorticity and to the propagation of waves along the coastal current formed outside the strait. Inside the strait, the current is bounded by the two walls of the strait. Outside, the zero potential vorticity flow is unbounded on the offshore side. Some values of volume flux that are possible in the strait are greater than any possible volume flux far downstream with the boundary conditions described above. This causes fluid to pile up in a bulge. Reverse flow occurs in the bulge when waves on the potential vorticity front travel upstream, which happens for sufficiently large (negative) vorticity. In this problem, the necessity of a coastal current forming from the strait outflow, the cross-stream interface slope, and the resulting formulation of the volume flux expressions and vorticity-front waves are all unique to rotating systems.

While Kubokawa's model produces flows which are similar to those seen in the lab by Kawasaki and Sugimoto (1984, 1988), Bormans and Garrett (1989) and Whitehead and Miller (1979), and his explanation of his contour dynamics results is quite compelling, the model is unable to account for several important features of eddy generation. Since the volume flux condition is based on an asymmetry between upstream flow, which is confined to a channel, and downstream flow, which spreads out over a semi-infinite domain, the explanation is dependent on the existence of the channel upstream of the corner. If the upstream flow is bounded by a free streamline or a density front, as it is in the experiments performed in this thesis, Kubokawa's explanation does not apply. However, the importance of the direction of wave propagation in this theory may carry over to coastal flows, if some other disturbance, perhaps in the initial condition of the flow, plays the role that the volume flux asymmetry plays in the channel outflow case. If such a flow is bounded by a density front,

the waves that must be examined are frontal waves such as those analyzed by Killworth and Stern (1982); Killworth, Paldor and Stern (1984); Kubokawa and Hanawa (1984); and Kubokawa (1986, 1988). Kubokawa's condition also does not take into account local conditions at the corner, such as radius of curvature (taken to be zero in Kubokawa's model) or total corner angle ( $90^\circ$  in his model).

Stern and Whitehead (1990) used contour dynamics to explain the results of their experiments with barotropic coastal currents that separate at a sharp corner. The coastal current consisted of two piecewise regions of non-zero vorticity, with low vorticity on the inshore side of the current and high vorticity on the offshore side (see Figure 1.3.2). In this case the rotation of the current is dynamically irrelevant except insofar as the Taylor-Proudman theorem serves to two-dimensionalize the flow. If we think of the current as being composed of the union of many vortex patches, then when the leading edge, or "nose" of the current encounters the corner with a large enough angle, the corner distorts the velocity field associated with each vortex patch so that the resultant velocity field carries the leading edge of the current away from the wall.

An elegant way of looking at rotating coastal flows is through a class of models which we may call hydraulic theory (Gill, 1977). In such a theory, an inviscid, steady flow is considered in the limit in which alongstream variations are long compared to the width of the current. Such a scaling allows us to ignore alongstream derivatives in the equations of motion, so that the cross-stream structure of the current at any point is governed by a set of ordinary differential equations which only depend parametrically on the downstream coordinate through some quantity such as local topography or coastline curvature. The effect of coastline curvature was studied by Røed (1980) and Ou and de Ruijter (1986) for uniform potential vorticity, reduced gravity flows, and by Hughes (1989) for barotropic currents, with continuous potential vorticity variations, flowing over isobaths that were parallel to the coast. These

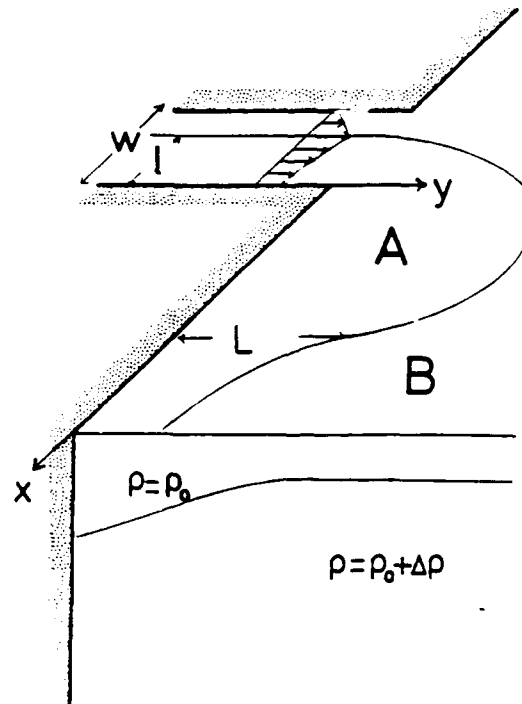


Figure 1.3.1: Configuration for inviscid, quasigeostrophic strait outflow model which produces anticyclones at the corner (Kubokawa, 1991, Figure 2).

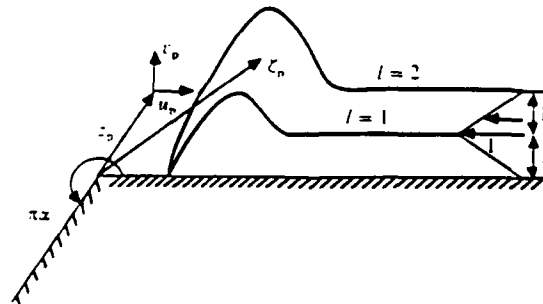


Figure 1.3.2: Initial condition of barotropic jet flowing along a wall towards a sharp corner (Stern and Whitehead, 1990, Figure 5).

currents can be said to separate from the coast when for a given coastal curvature, there is no unidirectional current flowing in a specified direction along the coast that has the appropriate potential vorticity and other conserved quantities prescribed upstream of the region of curved coastline. The reduced gravity currents were found to separate from the coast at a region of positive curvature (a cape) in the sense that the depth of the density interface bounding the flow must become negative if the curvature is greater than a critical value. However, the value of the critical curvature was only found for a single point in parameter space. The barotropic currents separated by undergoing a flow reversal near the coast when the curvature was great enough.

The reduced gravity hydraulic models above are candidate explanations of the separation of baroclinic currents rounding a corner in the dam-break experiments described above. However, the lack of quantitative predictions makes the theory difficult to test. The barotropic theory is somewhat cumbersome to test because it is formulated in such a way that the velocity profile of the current is not made explicit. No laboratory experiments in which steady currents flow around a corner over a sloping bottom have been reported. The hydraulic models also do not tell what kind of separation occurs. In particular, a hydraulic model can not tell whether a gyre is formed when separation occurs or whether the flow simply leaves the coast at some point. Whitehead and Miller (1979) reported that a current impinging on a wall bifurcated at the wall and speculated that a similar effect was causing the corner anticyclone in their experiments; when water that had separated from the wall at the corner returned to the wall, some was forced to flow back towards the corner from the stagnation point. Whitehead (1985) attributes this reverse flow to a consequence of the conservation of momentum.

Cherniawsky and LeBlond (1986) calculated the reduced gravity flow around a sharp corner as an expansion in Rossby number for currents which decayed monotonically to zero speed from the coast. They found that due to upwelling similar to

that found by Røed (1980), the current always separated from the coast upstream of the corner and re-attached downstream, but for moderately small Rossby number (.5 and less), the region was very small compared to either the Rossby radius or the width scale of the current. This indicates that hydraulic models, though formally invalid for small radius of curvature, may still describe phenomena, such as upwelling separation, which actually occur when neglected alongstream derivatives are included. However, no gyre appeared in Cherniawsky and LeBlond's flow, thus warning us to be cautious in concluding that a current which is predicted to separate actually produces an eddy. Cherniawsky and LeBlond neglected time-dependence and friction and produced a solution that is only formally true for small Rossby number, so that any of these idealizations may account for the difference between their model and the experiments and ocean observations described above.

If horizontal (but not vertical) friction is included in a flow model, the scaling of the boundary layer is the same in the rotating and non-rotating cases. This is because the Coriolis term in the alongshore component of the momentum equation is proportional to the cross-shore velocity component  $v$ , but  $v$  is small within the viscous boundary layer due to the condition that no fluid flows through the wall, which must approximately apply to the inviscid flow outside the boundary layer. Modelling the results of Boyer and Kmetz's (1983) experiments on uniform flow past a cylinder, Merkin and Solan (1979) showed that rotation can affect separation of a frictional boundary layer when the effect of the bottom Ekman layer is included. The Ekman flux caused by friction between the floor and the water column is not constrained to have a zero component into side walls. Therefore fluid in the Ekman layer that is flowing towards [away from] a wall must flow down [up] in a "Stewartson layer" close to the wall in order to satisfy continuity. This Stewartson layer, superimposed on the lateral viscous boundary layer, adds another term to the vertically integrated momentum equation near the wall. This term tends to inhibit separation at the wall.

In summary, there are a variety of candidate mechanisms, both viscous and inviscid, steady state and time-dependent, with which to account for gyre formation at a corner, but the actual cause of gyres at a corner is not understood. Werner *et al.* (1988) used a reduced gravity model to try to isolate the dynamics of Alboran Sea gyre. They found that a gyre was only formed when the advection terms in the equations of motion were included and when a no-slip (as opposed to free-slip) boundary condition was imposed. The latter finding differs from the results of Loth and Crepon's (1984) quasigeostrophic model and Speich and Crepon's (1992) primitive equation model, which produced an anticyclone in the Alboran Sea with a free-slip boundary condition. There are also inconsistencies among three different models as to the importance of relative vorticity of the strait outflow; Loth and Crepon needed it to be positive to get a gyre, Preller's (1986) reduced gravity model produced a stronger eddy when the relative vorticity was positive, and Werner *et al.* found that vorticity had little effect on the flow. In all these studies, the strait was only about 4 gridpoints wide, thus limiting resolution.

## 1.4. Plan of the Thesis

In this thesis, gyre formation at a coastline bend is investigated with laboratory experiments and theory. We start by exploring some earlier results on the hydraulic theory of flows around curved coastlines. The main results of the thesis are obtained in the chapters on laboratory results that follow. Experiments are performed to answer some questions regarding eddy formation at a corner by a density current. Further experiments explore a regime of eddy formation in a barotropic fluid which has not been investigated before. While oceanographic examples of flow around capes have various continuous stratifications, there are enough simple questions to be asked about barotropic, reduced gravity, and two-layer currents that we will restrict ourselves to these cases.



In Chapter 2, the hydraulic model of Røed (1980) and Ou and de Ruijter (1986), and a similar model for barotropic currents, are solved for a range of points in the parameter space controlling the flow. The purpose of obtaining the quantitative relationship between the upstream parameters of the flow and the predicted minimum radius of curvature needed for separation is to allow us to compare the predicted radius of curvature with the actual radius of curvature needed for separation in the experiments of Bormans and Garrett (1989).

Chapter 3 describes results from baroclinic experiments that are similar to those of Miller and Whitehead (1979), Kawasaki and Sugimoto (1984, 1988), and Bormans and Garrett (1989). Whereas those experiments involved density currents flowing around corners at the mouth of a channel, in my experiments the left wall of the channel is removed so that the flow is a coastal current upstream of the corner as well as downstream. While earlier experiments found a critical radius of curvature of the corner for which a gyre was produced, these experiments find a critical corner angle for gyre creation. The experiments also explore how different lower layer depths and different initial conditions affect eddy generation. These experiments obtain quantitative data about the current upstream and downstream of corner.

In the barotropic experiments described in Chapter 4, flows of various strengths are pumped over a sloping bottom and around a corner to see if the separation implied by Hughes (1989) actually occurs. In fact eddies are produced by some of these flows for a variety of related topographies, and their characteristics are studied.

Summaries and conclusions are presented in Chapter 5.

## Chapter 2.

# Hydraulic Models of Separation From Curved Coastlines

### 2.1. Introduction

The separation of a coastal current from a curved boundary in a rotating system has been studied but the dynamics has not been explained. Whitehead and Miller (1979) and Bormans and Garrett (1989) performed laboratory experiments in which a current was created by a dam-break and flowed through a channel into a wider basin, where it either stayed attached to the wall outside the mouth of the channel or separated from the wall to form a growing anticyclonic eddy just outside the channel. The corner was rounded, with a radius of curvature which could be varied relative to both the width and the Rossby radius of the current. Bormans and Garrett's experiments suggest that separation occurs when the radius of curvature is less than the inertial radius of the current,  $u/f$  for current speed  $u$  and Coriolis parameter  $f$ . The dependence on the rotation parameter raises the possibility that dynamics unique to a rotating system are involved in the separation of the current.

Røed (1980) and Ou and de Ruijter (1986) gave one possible mechanism for this gyre formation. They studied inviscid, steady state, uniform potential vorticity two-layer flows in which the bottom layer was infinitely deep and hence motionless. Assuming that alongstream variations had a length scale that was long compared to the width of the current allowed them to neglect derivatives with respect to the alongstream coordinate in the equations of motion, so that the partial differential equations became ordinary differential equations with respect to the cross stream coordinate. The only ways in which the curvature of the boundary entered into the equations of motion in this approximation were in a centrifugal term in the force

balance and a curvature term in the potential vorticity equation.

Røed examined a density front (Figure 2.1.1a) along which the current flowed with the wall to its right looking downstream (his and our discussion are confined to systems with counterclockwise rotation), while Ou and de Ruijter studied a current bounded by a wall on its left and a free streamline on its right (Figure 2.1.1c). In both cases, increasing the curvature of the wall, as one traveled downstream from a region of zero curvature, decreased the layer thickness at the wall. At some critical radius of curvature, the thickness became zero. This implies that if a rounded corner has a greater curvature than the critical one, the solution has the physically meaningless property of negative layer thickness at the wall, and it is impossible to have a steady state flow with the current attached to the wall at the bend.

Though these two papers demonstrated that such a behavior exists, they did not show how great a curvature a given upstream flow needs in order to actually separate. In this chapter, I non-dimensionlize the equations somewhat differently than Røed did, and solve for the critical radius of curvature as a function of the two non-dimensional upstream parameters which control the form of the boundary current. This allows us to compare the different flow cases (front and free streamline) illustrated in Figure 2.1.1. A thorough examination of parameter space will investigate the possibility that the current may separate due to a flow reversal rather than a surfacing of the interface. Finally the separation criteria derived here can be compared with the experimental results mentioned above. Ultimately, we would like to see if inviscid, centrifugal upwelling can account for flow separation from a wall in real laboratory and natural systems.

In order to gain a more complete understanding of the influence of curvature in the simplified equations of motion, the long wave approximation is also applied to barotropic flows, both with a flat bottom and a sloping bottom. In such systems the momentum equation becomes unnecessary, and the dynamics is governed

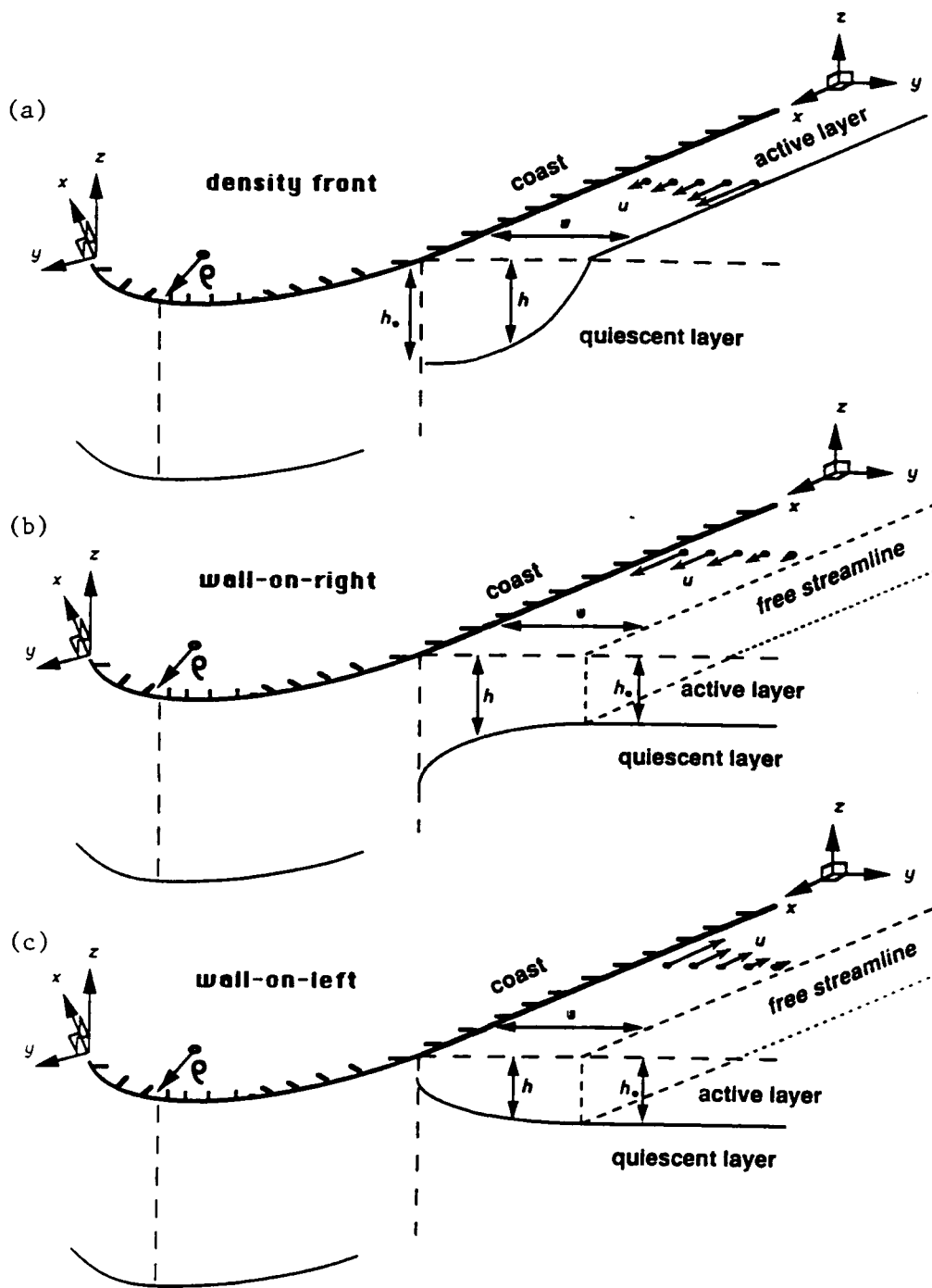


Figure 2.1.1: Upstream current structure for reduced gravity models. (a) Density front case as in R ed (1980). (b) Free streamline case (potential vorticity front only) with wall on the right. (c) Free streamline case with wall on left, as in Ou and de Ruijter (1986).

by the potential vorticity equation alone. For this reason rotation vanishes from the formulation for the flat bottom case, which should display the same dynamics as a two-dimensional, inviscid, non-rotating flow, though rotation reappears in the sloping bottom case through the influence of bottom topography on potential vorticity. In these systems, centrifugal upwelling cannot occur because there is no density interface to upwell. However, it is possible that the current speed at the coast will reverse for a great enough curvature. As in the reduced gravity case (flow above an infinite lower layer), this flow reversal implies that separation of the current from the coast must occur for sufficiently great curvature.

Hughes (1989) showed that a flow reversal does occur for a system with topography that deepens exponentially with distance from a coast and with a potential vorticity distribution profile that is an exponential function of the streamfunction. In this chapter, we look at linear topographic slopes and flow profiles that consist of one or two regions of uniform potential vorticity. This formulation is mathematically more simple than that of Hughes, and permits analytical solutions for both upstream (straight coastline) and downstream (curved coastline) velocity profiles. Hughes' continuously varying potential vorticity is perhaps more realistic, but the equations must be numerically integrated to find the flow profile both upstream and downstream (Hughes, 1989). The simplicity of flows with piecewise uniform potential vorticity should also make it easier to compare the flat bottom, sloping bottom, and reduced gravity systems with each other.

In this chapter, we will first derive the system of equations to be solved for all of the cases described above, as well as the appropriate form of the equations and boundary conditions for each case. Separate sections will deal first with the barotropic flat bottom case, then barotropic sloping bottom case, and finally reduced gravity flows. Though the barotropic sections precede the baroclinic section, the main emphasis of the chapter is on the baroclinic work, because it is the most relevant to real

fluid flows. There are several problematical aspects of the barotropic work which will be discussed below. Most importantly, after I performed the barotropic calculations, analysis of my homogeneous-density laboratory data (see Chapter 4) showed that processes involving vertical shear (which are not included in these shallow water models) were important to the flow separation in homogeneous systems. However, the barotropic results are included here because they do display some interesting nuances of hydraulic theory.

## 2.2. The System of Equations to be Solved

Following Røed (1980), we start with the cross-shore component of the momentum equation, and the conservation of potential vorticity, both in curvilinear coordinates.

$$\frac{uv_x}{1+y/\rho} + vv_y - \frac{u^2}{\rho+y} + fu = -g'h_y, \quad (2.2.1a)$$

$$-u_y + \frac{v_x}{1+y/\rho} - \frac{u}{\rho+y} + f = qh, \quad (2.2.1b)$$

where  $(u, v)$  are the alongshore and cross-shore components of velocity,  $(x, y)$  are coordinates parallel to and perpendicular to the shore,  $h$  is the layer thickness,  $\rho$  is the local radius of curvature of the shore (and the coordinate system),  $f$  is the Coriolis parameter,  $g'$  is the reduced gravitational acceleration, and  $q$  is the potential vorticity. The smaller  $\rho$  is, the larger the curvature, so that for a straight wall,  $\rho = \infty$ , and for a sharp corner,  $\rho = 0$ . The wall is at  $y = 0$ , and for convex curvature  $\rho$  is positive. For the case in which the wall is on the right of the current looking downstream, we have  $u > 0$ , and when the wall is on the left,  $u < 0$ . Now let us non-dimensionalize the equations with  $(u, v)$  scaled by  $(U, V)$ ,  $h$  scaled by  $D$ , and  $(x, y)$  scaled by  $(\rho, W)$ . The non-dimensional continuity equation, which is

$$\left(\frac{DU}{\rho}\right)(hu)_x + \left(\frac{DV}{W}\right)([1 + (W/\rho)y]hv)_y = 0, \quad (2.2.2)$$

implies that  $U/\rho = V/W$ . Using this fact, the non-dimensional version of the momentum and potential vorticity equations above become

$$\left(\frac{U}{fW}\right) \left\{ \delta^2 \left[ \frac{uv_x}{1+\delta y} + vv_y \right] - \delta \frac{u^2}{1+\delta y} \right\} + u = - \left(\frac{g'D}{fUW}\right) h_y \quad (2.2.3a)$$

$$-\delta^2 \frac{v_x}{1+\delta y} + \delta \frac{u}{1+\delta y} + u_y = \left(\frac{Wf}{U}\right) (1 - qh/f), \quad (2.2.3b)$$

where  $\delta = W/\rho$ . If we assume that the Rossby number  $U/fW$  is  $O(1)$  and we neglect  $\delta^2$  terms but keep  $\delta$  terms, then the dimensional equations can be approximated by

$$fu - \frac{u^2}{\rho + y} = -g'h_y, \quad (2.2.4a)$$

$$u_y + \frac{u}{\rho + y} = f - qh. \quad (2.2.4b)$$

These equations are essentially the equations of motion for axisymmetric circular motion. As stated above, these equations, which were also derived by Røed (1980), are much easier to solve than the full equations of motion because they consist of coupled ordinary differential equations in  $y$  rather than partial differential equations in  $(x, y)$ . Alongshore variations in the flow enter parametrically through  $\rho(x)$ . For a barotropic system,  $h(y)$  is determined by the topography, which is known, so only the potential vorticity equation is necessary to determine the velocity profile.

The barotropic system is governed by a single first order differential equation, so one boundary condition must be imposed in order to solve for the motion. Since we are only considering coastal currents, we take the fluid to be motionless far away from the wall. Integration of the vorticity equation (2.2.4b) over a vanishingly small interval in  $y$  shows that  $u$  must be continuous, so that  $u = 0$  on the outer edge of the jet,  $y = w$ . The reduced gravity case is equivalent to a second order differential

equation, so two constants of motion are necessary. For the case of a density front,  $h$  goes to zero at  $y = w$ . In this case the wall must be on the right ( $u > 0$ ). For the free streamline case, the assumption of no motion outside the region of anomalous potential vorticity again tells us that  $u(w) = 0$  as in the barotropic case. Now there is an additional constraint that  $h$  must also be continuous in order to have finite  $u$ , so  $h(w) = h_0$ , where  $h_0$  is the thickness of the stagnant water outside the current. For the front case, we fix  $h_0$ , the layer thickness at the wall, thus supplying a second boundary condition for the equations.

In order to relate the flow structure at various  $\rho$  to the upstream ( $\rho = \infty$ ) flow we need other properties of the flow that are conserved along streamlines. For a given  $\rho$ , we must find the current width  $w(\rho)$  in order to know the flow field. For the barotropic flow, it is sufficient to use the volume flux within each region of uniform potential vorticity,

$$Q_i = \int_a^b u(y)h(y)dy, \quad (2.2.5)$$

where  $a(\rho)$  and  $b(\rho)$  are the minimum and maximum values of  $y$  with the given vorticity. For the reduced gravity case, more information is needed, so we utilize the Bernoulli function, which to the same order of approximation as equations (2.2.4a,b) can be written

$$B = g'h + \frac{1}{2}u^2. \quad (2.2.6)$$

At the end of this section we will review the conditions on  $B$  necessary to close the problem.

The most convenient scaling for the equations is somewhat different for each of the two barotropic problems and the reduced gravity problem. In the flat bottom barotropic case, velocity can be scaled by some velocity  $U$  in the upstream profile, and all lengths can be scaled by the upstream current width  $W$ . Therefore  $u/U$  is a function of position ( $y/W, \rho/W$ ). If the potential vorticity is uniform, there is no



other parameter governing the system. If there are two regions of uniform potential vorticity in the jet, then two parameters are added: the upstream ratio of widths of the two regions,  $W_1/W$  ( $W_1$  is width of region closest to the wall), and another parameter which can be expressed in a variety of ways, including the ratio of the two potential vorticities as well as  $u_0/U$ , which is the ratio of the velocity at the wall to velocity at  $y = W_1$ . With this scaling, the non-dimensional vorticity equation is

$$u_y + \frac{u}{\rho + y} = \frac{\Delta U}{\Delta W}, \quad (2.2.7)$$

where  $\Delta U$  is the non-dimensional change in upstream velocity across a region of uniform vorticity and  $\Delta W$  is the non-dimensional width of the region.

When the topography consists of a linear slope with zero fluid depth at the wall, lengths are scaled as before but speed is scaled by  $Wf$ . For such a flow with potential vorticity  $q$  and bottom slope  $s$ , the parameters are  $\alpha \equiv qWs/f$  for each vorticity, and, if there is more than one vorticity region  $W_1/W$ . Thus there is one non-dimensional parameter for uniform  $q$  and three parameters if there are two values of  $q$ . Specifying the two dimensionless potential vorticities and  $W_1/W$  is equivalent to specifying  $W_1/W$  and the upstream values of  $u(y=0)$  and  $u(y=W_1)$ . If velocity in the sloping bottom problem is scaled with  $U = u(W_1)$  as in the flat bottom case, rotation still appears in the potential vorticity equation in the form of a Rossby number,  $U/fW$ . In contrast, in the flat bottom case  $f$  only appears inside the expression  $f - qD$ , so that "planetary" vorticity is merely a part of relative vorticity in that case. Using different velocity scales as I have done does not affect any quantities besides the magnitude of the velocities. The non-dimensional vorticity equation for this case is

$$u_y + \frac{u}{\rho + y} = 1 - \alpha y. \quad (2.2.8)$$

In the reduced gravity problem,  $h$  is non-dimensionalized by a scale thickness  $h_0$ , lengths are scaled by the Rossby radius  $\sqrt{g'h_0}/f$ , and speed is scaled by the long

gravity wave speed  $\sqrt{g'h_0}$ . For the density front,  $h_0$  is the upstream layer thickness at the wall, and for the free streamline case,  $h_0$  is the upstream thickness at the outer edge of the current. The two non-dimensional parameters governing the system are then the upstream non-dimensional width  $Wf/\sqrt{g'h_0}$  and the non-dimensional potential vorticity,

$$\delta = \frac{q}{f/h_0}. \quad (2.2.9)$$

Switching to non-dimensional variables, the equations of motion become

$$u - \frac{u^2}{\rho + y} = -h_y \quad (2.2.10a)$$

$$u_y + \frac{u}{\rho + y} = 1 - \delta h, \quad (2.2.10b)$$

and  $B$  is non-dimensionalized by  $g'h_0$ , so that

$$B = h + \frac{1}{2}u^2. \quad (2.2.11)$$

At  $\rho = \infty$ , the boundary conditions are simply

$$h(0) = 1, \quad h(W) = 0 \quad (\text{front}), \quad (2.2.12a)$$

$$h(W) = 1, \quad u(W) = 0 \quad (\text{free streamline}), \quad (2.2.12b)$$

The Bernoulli function  $B$  at the streamline adjacent to the coast can be computed upstream, and provides an additional constraint from which to calculate  $w(\rho)$  for finite  $\rho$ . The condition that the front has  $h(0) = 1$  upstream does not hold for finite  $\rho$ , but since the offshore edge of the current is a streamline, the Bernoulli function there can be used instead. To summarize, for flow bounded by a density front we have

$$\text{at } y = 0, \quad h + \frac{1}{2}u^2 = B_0, \quad (2.2.13a)$$

$$\text{at } y = w, \quad h = 0 \text{ and } \frac{1}{2}u^2 = B_1, \quad (2.2.13b)$$

and for the free streamline case

$$\text{at } y = 0, \quad h + \frac{1}{2}u^2 = B_0, \quad (2.2.14a)$$

$$\text{at } y = w, \quad h = 1 \text{ and } u = 0, \quad (2.2.14b)$$

where  $B_0 = B(0)$  and  $B_1 = B(w)$ .

## 2.3. Barotropic Flows Over a Flat Bottom

In this section, we will calculate the flow profile for a region of uniform vorticity, and then calculate the flow for a current consisting of two regions of uniform vorticity. All calculations will be performed in the non-dimensional units introduced in the previous section.

### Uniform Potential Vorticity

When the coast is straight ( $\rho = \infty$ ), equation (2.2.7), the condition that  $u(W) = 0$  and the use of the velocity at the coast as the velocity scale constrain the upstream velocity profile to be simply

$$u(y) = 1 - y. \quad (2.3.1)$$

Then the volume flux  $Q$  (see equation (2.2.5)) is equal to  $1/2$ , and  $\Delta U/\Delta W = 1$  (see equation (2.2.7)).

We can solve (2.2.7) by solving the homogeneous version, which is separable, and then using the method of variation of parameters to solve the inhomogeneous problem. Invoking the outer boundary condition, we find that

$$u = \frac{1}{\rho + y} \left[ \frac{1}{2}(w^2 - y^2) + \rho(w - y) \right]. \quad (2.3.2)$$

Since we always have  $y < w$ , the current never reverses, so there is never any separation. For completeness, let us find  $w$ , which we do by integrating the volume flux (equation (2.2.5)) from  $y = 0$  to  $y = w$  and setting the quantity equal to its upstream value:

$$\frac{1}{4}\rho^2 + \frac{1}{2}(\rho + w)^2 \left( \ln \frac{\rho + w}{\rho} - \frac{1}{2} \right) = \frac{1}{2}, \quad (2.3.3)$$

which can be rewritten using  $w' = w/\rho$ :

$$1 + (1 + w'^2) [2 \ln(1 + w') - 1] = 2/\rho^2. \quad (2.3.4)$$

The variation of  $w$  with  $\rho$  can be displayed by calculating  $\rho$  as a function of  $w'$  in equation (2.3.4) and plotting  $w = w'\rho$  against  $\rho$ . The current width decreases monotonically as  $\rho$  decreases from  $\infty$ . Changes in  $w$  are small unless the radius of curvature becomes small compared to the upstream current width, in which case the long wave approximation has already broken down. For all  $\rho$ ,  $u(y)$  is a monotonic function with a maximum at  $y = 0$ , where  $u = w(1 + \frac{1}{2}w/\rho)$ , and  $u(y = 0)$  increases as the radius of curvature decreases.

The qualitative features of these results can be explained by examining equation (2.2.7). As the boundary curvature increases, the centrifugal term  $u/(\rho + y)$  increases from zero, forcing the shear term  $\partial u/\partial y$  to decrease. Since for this flow,  $\partial u/\partial y < 0$ ,  $|\partial u/\partial y|$  must increase. Meanwhile the volume flux must remain constant. If the shear is approximated with  $u(0)/w$ , and the flux by  $Q = u(0)w$ , then  $u(0)/w = u(0)^2/Q = Q/w^2$ , so that as curvature increases the shear, the current becomes faster and narrower. This analysis has an implicit assumption that the shear is about the same for all  $y$ , which happens to be true for all  $\rho$  for which  $w$  was calculated.

### Two Regions of Uniform Potential Vorticity

The constraint of uniform potential vorticity limits the range of currents which can be modelled. More important, it is conceivable that it limits the range of

behavior which our ideal current displays. By looking at a current which is divided into two regions of uniform potential vorticity, we obtain a crude model of currents which have cross stream vorticity gradients, while we retain the mathematical apparatus of the last section, which allows us to treat the problem analytically except for actually finding the roots of the equations for width.

Let  $0 < y < w_1$  be the "inner" region of constant vorticity, and  $w_1 < y < w$  be the "outer" region. Far upstream, ( $\rho = \infty$ ), we set  $w_1 = W_1$ ,  $w = 1$ ,  $u(0) = u_0$ ,  $u(W_1) = 1$ , and  $u(1) = 0$  ( $W_1$  and  $u_0$  are given), so that

$$u = u_1 = \frac{1 - u_0}{W_1} y + u_0, \quad y < W_1 - 1 \quad (2.3.5a)$$

$$u = u_2 = \frac{1 - y}{1 - W_1}, \quad W_1 < y < 1. \quad (2.3.5b)$$

We can then solve equation (2.2.7) for  $u_1$  and  $u_2$ , as in the uniform vorticity case, using the appropriate expressions for potential vorticity in each region and the requirements that  $u_2(w) = 0$  and  $u_1(w_1) = u_2(w_1)$ . We obtain

$$u_1 = \frac{1}{\rho + y} \left\{ \frac{1 - u_0}{W_1} \left[ \frac{1}{2} y^2 + \rho y - \frac{1}{2} w_1 (w_1 + 2\rho) \right] + \frac{1}{2} \frac{(w - w_1)(w + w_1 + 2\rho)}{1 - W_1} \right\}, \quad (2.3.6a)$$

$$u_2 = \frac{1}{1 - W_1} \frac{1}{\rho + y} \left[ \rho(w - y) + \frac{1}{2}(w^2 - y^2) \right]. \quad (2.3.6b)$$

Is there a flow reversal at the wall? The condition that  $u_1(0) < 0$  can be written

$$\frac{w_1}{W_1} \left( 1 + \frac{1}{2} \frac{w_1}{\rho} \right) > w \left( 1 + \frac{1}{2} \frac{w}{\rho} \right). \quad (2.3.7)$$

Equation (2.3.7) is the analogue of the shear argument for currents of uniform potential vorticity, but here flow reversal is dependent on two width parameters rather than one. We cannot tell whether or not this condition is satisfied until we find  $w_1(\rho)$

and  $w(\rho)$ , but since  $w_1 < w$ , the condition can be satisfied only if  $w_1$  increases faster than  $w$  as  $\rho$  decreases from  $\infty$ .

In order to find  $w_1$  and  $w$ , we must use the conservation of volume flux. Integrating (2.3.5a) and (2.3.5b), we find that

$$Q_1 = \frac{w_1}{4W_1}(1 - u_0)(w_1 + 2\rho) + \frac{1}{2} \left[ \frac{(w - w_1)(w + w_1 + 2\rho)}{1 - W_1} - \frac{1 - u_0}{W_1}(w_1 + \rho)^2 \right] \ln \frac{\rho + w_1}{\rho}, \quad (2.3.8a)$$

$$Q_2 = \frac{1/2}{1 - W_1} \left[ (\rho + w)^2 \ln \frac{\rho + w}{\rho + w_1} - \frac{1}{2}(w - w_1)(w + w_1 + 2\rho) \right], \quad (2.3.8b)$$

and we integrate (2.3.4a) and (2.3.4b) to get  $Q_1 = \frac{1}{2}W_1(1 + u_0)$  and  $Q_2 = \frac{1}{2}(1 - W_1)$ . Equations (2.3.8a) and (2.3.8b) constitute a transcendental system for  $w_1$  and  $w$  in terms of the parameters  $W_1$ ,  $u_0$ , and  $\rho$ , but the dimension of the system can be reduced because (2.3.8a) is a quadratic in  $w$ , so that we can find an analytical expression for  $w(w_1; W_1, u_0, \rho)$ . This expression can then be inserted into (2.3.8b), leaving a single transcendental equation  $Q_2(w_1; W_1, u_0, \rho) - Q_2(W_1, u_0, \rho = \infty) = 0$  which can be easily solved numerically.

The currents studied by Hughes (1989) displayed conjugate states, in which two currents with the same potential vorticity distribution (as a function of stream function) and the same volume flux could have different velocity profiles. One state was relatively narrow and fast and consisted of flow that was supercritical with respect to the lowest mode waves on the potential vorticity gradient (that is, the wave speed was not great enough to allow the wave to propagate upstream against the tendency of the current to advect the wave downstream) while the wide and slow state was subcritical (the wave could propagate upstream). The narrower of the two profiles would become even more narrow as the curvature increased, while the wider of the two currents would grow wider with curvature until a flow reversal developed. The currents studied here also exhibit conjugate states. For an upstream current defined

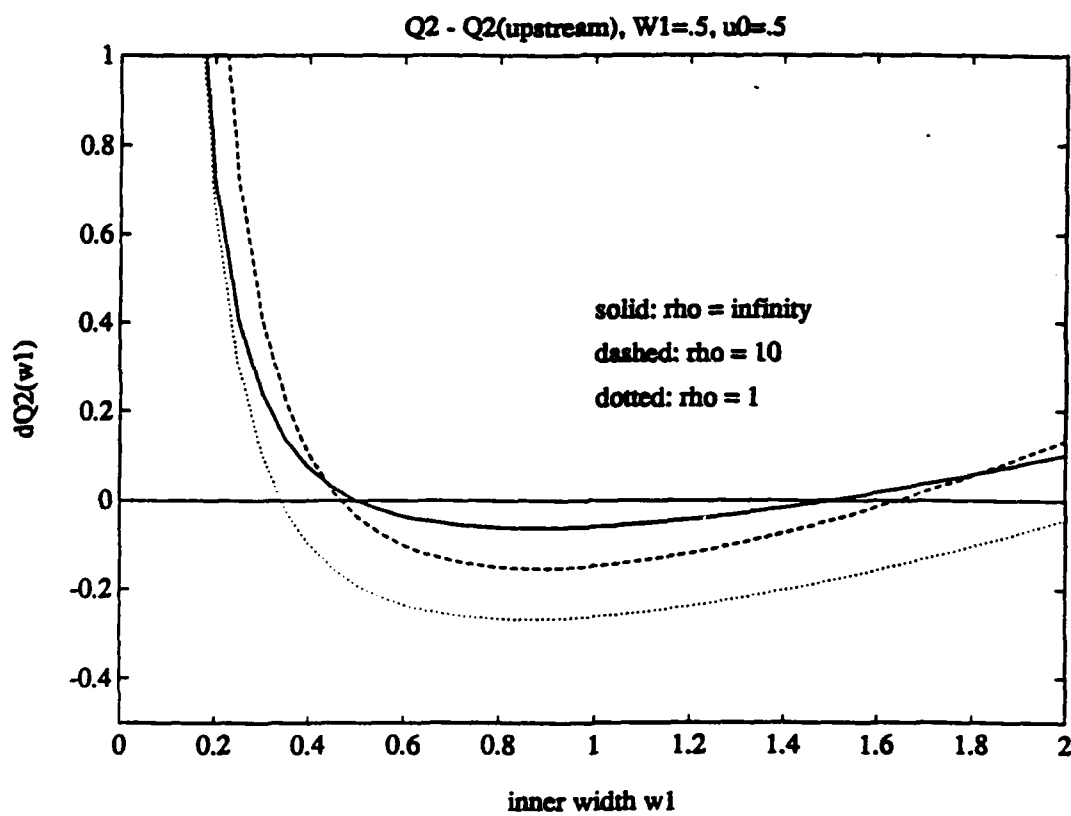


Figure 2.3.1: Difference between upstream and downstream transport  $Q_2$  as a function of inner width  $w_1$  for  $\rho = \infty, 10$ , and  $1$ , for barotropic, flat bottom current consisting of two regions of uniform potential vorticity. For all curves,  $W_1 = .5$  and  $u_0 = 0$ .

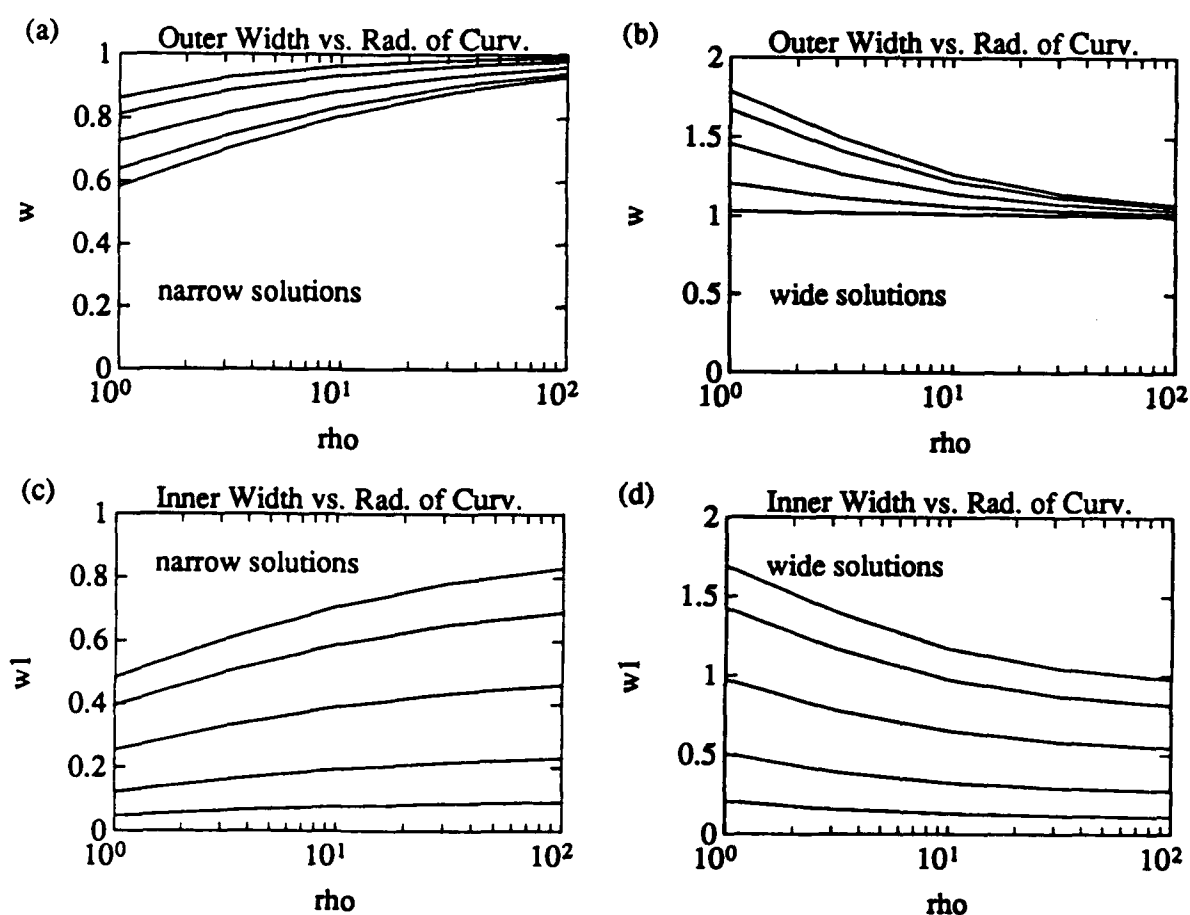


Figure 2.3.2: Inner and outer widths ( $w_1, w$ ) as functions of radius of curvature  $\rho$  for  $u_0 = 0$  and  $W_1 = .1, .25, .5, .75$ , and  $.9$ . Values calculated at  $\rho = 100, 10^{3/2}, 10, 10^{1/2}$ , and  $1$ . (a) Outer width  $w$ , narrow solutions. (b) Outer width  $w$ , wide solutions. (c) Inner width  $w_1$ , narrow solutions. (d) Inner width  $w_1$ , wide solutions.



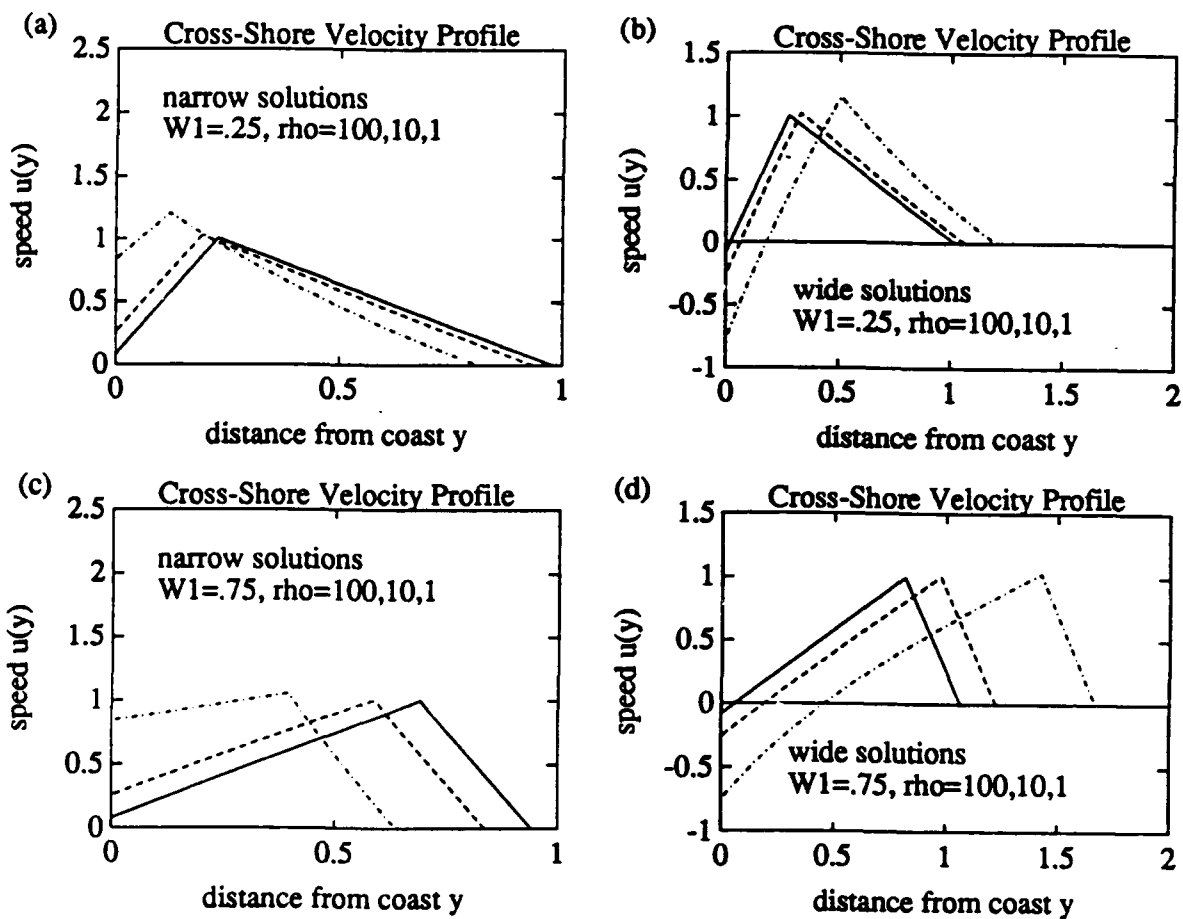


Figure 2.3.3: Cross-shore profiles of alongshore component of velocity for radius of curvature  $\rho = 100, 10$  and  $1$ . For decreasing  $\rho$ , the currents become narrower in the narrow solution case and wider in the wide solution case. For all currents,  $u_0 = 0$ . (a) Narrow solutions,  $W_1 = .25$ . (b) Wide solutions,  $W_1 = .25$ . (c) Narrow solutions,  $W_1 = .75$ . (d) Wide solutions,  $W_1 = .75$ .

by equations (2.3.5a,b), with inner width  $W_1$  and outer width of 1, there is a conjugate current with the same inner and outer vorticities and the same  $Q_1$  and  $Q_2$ . This current has inner and outer widths  $w_1$  and  $w$  given by  $w_1 = (1 + u_0)/(1 - u_0)$  and  $w = 1 + 2u_0W_1/(1 - u_0)$ , and is a wider current. However, for all parameter values, the speed at the wall is  $u_1(0) = -u_0$ , while  $u(w_1) = 1$ . Therefore the wide conjugate state has an upstream flow reversal for  $u_0 > 0$ , and is excluded from consideration because we are only interested in flows which are unidirectional when  $\rho = \infty$ . Figure 2.3.1 shows  $\Delta Q_2 = Q_2(w_1, \rho) - Q_2(\rho = \infty)$  for  $\rho = \infty, 10$ , and 1 when  $W_1 = .5$  and  $u_0 = .5$ . Solutions to the equations of motion occur at the two values of  $w_1$  for which  $\Delta Q_2 = 0$ . As in Hughes (1989), the narrow current gets more narrow as curvature increases. When  $u_0 = 0$ , the minimum in  $\Delta Q_2(w_1)$  is tangent to the  $w_1$  axis, so that as we travel from a region of no curvature to one of finite curvature, the flow can either narrow or it can widen. Widths  $(w_1, w)$  as a function of radius of curvature  $\rho$  for several upstream inner widths  $W_1$  are shown in Figure 2.3.2.

As shown in Figure 2.3.3, the narrowing mode of the current merely increases its speed as the curvature increases, while the widening mode develops a flow reversal at the wall. The equations of motion in this approximation do not tell us which mode an actual current would pick. For  $u_0 \neq 0$ , there are two states upstream rather than one (see Figure 2.3.1), and solving equations (2.3.8a,b) for a wide range of points in  $(W_1, u_0)$  space shows that the narrow state always narrows as curvature increases, with  $u(0)$  increasing and no separation occurring.

## 2.4. Barotropic Flows Over a Sloping Bottom

We can find an exact solution of the differential equations which govern the flow of a coastal current for the case in which fluid depth increases exponentially with distance from the coast. This was the topography used by Hughes (1989) with

numerical solutions of a more complicated potential vorticity distribution. However, there is no analytical expression for the volume flux integrals with such topography, so that we restrict ourselves to the simpler case of a linearly sloping bottom, as introduced in section 2.

### Uniform Potential Vorticity

Equation (2.2.8), the non-dimensional vorticity equation for topography given by  $h(y) = sy$ , can be solved using the same technique with which we integrated equation (2.2.7) in section 3. For uniform potential vorticity, the resulting solution is

$$u = \frac{1}{\rho + y} \left[ \frac{1}{3} \alpha (w^3 - y^3) - \frac{1}{2} (1 - \alpha \rho) (w^2 - y^2) - \rho (w - y) \right], \quad (2.4.1)$$

while the upstream velocity profile is

$$u = \left[ \frac{1}{2} \alpha (1 - y^2) - (1 - y) \right]. \quad (2.4.2)$$

The upstream velocity profile is a parabola, with  $u(1) = 0$ ,  $u(0) = \frac{1}{2} \alpha - 1$ , and the local extremum in  $u$  given by  $u_m = (1 - \alpha)^2 / 2\alpha$  at  $y = 1/\alpha$ . The potential vorticity parameter  $\alpha \equiv qWs/f$  (where  $q$ ,  $W$ , and  $f$  are dimensional quantities) can be thought of as the ratio of the depth of the fluid at the outer edge of the current to the depth of a motionless fluid with the same potential vorticity. When the bottom is flat, there is no difference between flows with the coast on the right or on the left, but this symmetry is broken by the sloping bottom. For flow with the coast on the right looking downstream, we have  $u > 0$ , which occurs for  $\alpha > 2$ , and for flow with the coast on the left,  $\alpha < 0$ . Finally, we can complete the connection between the potential vorticity parameter  $\alpha$  and the shape of the velocity profile by noting that as  $\alpha$  decreases from either positive or negative infinity,  $u_m/u(0)$  increases from one to infinity. Since  $u_m$  is essentially the Rossby number of the system, the minimum

possible Rossby number for this current is  $1/4$  for the coast on the right and 2 for the coast on the left.

The upstream volume flux (equation (2.2.5)) is given by  $Q = \frac{1}{2}(\alpha/4 - 1/3)$ , where  $Q$  has been non-dimensionalized by  $fsW^3$ . A given upstream volume flux can be attained by only one current with a given potential vorticity and a positive width, though there is a negative width solution that is physically meaningless (the flat bottom uniform potential vorticity case also has a second, negative width solution). For finite  $\rho$ , inserting equation (2.4.1) into equation (2.2.5) yields

$$Q = \frac{1}{4}\alpha w^4 + \frac{1}{3}\left(\frac{4}{3}\alpha\rho - 1\right)w^3 + \frac{1}{4}\rho\left(\frac{1}{3}\alpha\rho - 3\right)w^2 - \frac{1}{2}\rho^2\left(1 + \frac{1}{3}\alpha\rho\right)w + \frac{1}{6}\rho\left[-2\alpha w^3 - 3(\alpha\rho - 1)w^2 + 6\rho w + 3\rho^2 + \alpha\rho^3\right]\ln\frac{\rho + w}{\rho}. \quad (2.4.3)$$

I solved the above equation, using the known upstream value of  $Q$ , for  $\alpha$  set equal to 2, 2.25, 2.5,..., 5, for  $\rho$  ranging from  $10^4$  to 1. In this range,  $w$  showed only a very weak dependence on  $\rho$ . In every instance  $w$  decreased as  $\rho$  decreased, but stayed above .9. As the width of the current decreases, the velocity must increase in order to maintain the same volume flux, and for all values of  $\alpha$  tested, speed at the wall increases. The behavior of the system was similar for  $\alpha$  equal to 0, -1 and -2, values for which the current has the wall on the left rather than on the right.

### Two Regions of Uniform Potential Vorticity

As in section 3, we now look at currents consisting of two regions of uniform potential vorticity,  $(\alpha_1, \alpha_2)$ . The upstream velocity profile is

$$u_1 = \frac{1}{2}\left[\alpha_2 + (\alpha_1 - \alpha_2)W_1^2 - \alpha_1 y^2\right] - (1 - y), \quad (2.4.4a)$$

$$u_2 = \frac{1}{2}\alpha_2(1 - y^2) - (1 - y), \quad (2.4.4b)$$

and for finite  $\rho$ ,

$$u_1 = \frac{1}{\rho + y} \left[ \frac{1}{3} \alpha_2 (w^3 - w_1^3) + \frac{1}{3} \alpha_1 (w_1^3 - y^3) - \frac{1}{2} (1 - \alpha_2 \rho) (w^2 - w_1^2) - \frac{1}{2} (1 - \alpha_1 \rho) (w_1^2 - y^2) - \rho (w - y) \right], \quad (2.4.5a)$$

$$u_2 = \frac{1}{\rho + y} \left[ \frac{1}{3} \alpha_2 (w^3 - y^3) - \frac{1}{2} (1 - \alpha_2 \rho) (w^2 - y^2) - \rho (w - y) \right]. \quad (2.4.5b)$$

It is convenient to relate  $\alpha_1$  and  $\alpha_2$  to parameters which are easier to visualize, such as the upstream velocity at various values of  $y$ . If the upstream speeds at the coast and at  $y = W_1$  are  $(u_0, u_m)$ , then

$$\alpha_1 = \frac{2}{W_1^2} (u_0 - u_m + W_1), \quad (2.4.6a)$$

$$\alpha_2 = \frac{2u_m}{1 - W_1^2} + \frac{2}{1 + W_1}. \quad (2.4.6b)$$

If the current has the wall on the right ( $u > 0$ ) then  $\alpha_2 > 0$  and if in addition  $u_m$  is larger than  $u_0$  by a wide enough margin,  $\alpha_1 < 0$ . If the wall is on the left, the sign of  $\alpha_2$  is not obvious, but  $\alpha_1$  will be positive if  $u_m$  is sufficiently larger than  $u_0$ .

Upstream, the volume flux is

$$Q_1 = W_1^2 \left[ \frac{1}{4} \alpha_2 - \frac{1}{2} + \frac{1}{3} W_1 - \frac{1}{8} \alpha_2 W_1^2 \right] + \frac{1}{8} (\alpha_1 - \alpha_2) W_1^4 \quad (2.4.7a)$$

$$Q_2 = W_1^2 \left[ \frac{1}{4} \alpha_2 - \frac{1}{2} + \frac{1}{3} W_1 - \frac{1}{8} \alpha_2 W_1^2 \right] - \frac{1}{6} + \frac{1}{8} \alpha_2. \quad (2.4.7b)$$

Whichever side the coast is on, there are two states with the same potential vorticity and volume flux in each region. The additional state, which is the wider of the two, always has the water near the coast flowing in the opposite direction of the flow near  $y = W_1$ , so that only the narrower state is of interest. The expressions for downstream

volume flux are somewhat complicated:

$$Q_1 = A \left( P_1 - \rho \ln \frac{\rho + w_1}{\rho} \right) + \rho \left( P_2 + \rho^2 \ln \frac{\rho + w_1}{\rho} \right) \\ + \frac{1}{2}(1 - \alpha_1 \rho) \left( P_3 - \rho^3 \ln \frac{\rho + w_1}{\rho} \right) - \frac{1}{3} \alpha_1 \left( P_4 + \rho^4 \ln \frac{\rho + w_1}{\rho} \right) \quad (2.4.9a)$$

$$Q_2 = \left( \frac{1}{3} \alpha_2 w^3 - \frac{1}{2} [1 - \alpha_2 \rho] w^2 - \rho w \right) \left( \Delta P_1 - \rho \ln \frac{\rho + w}{\rho + w_1} \right) \\ + \rho \left( \Delta P_2 + \rho^2 \ln \frac{\rho + w}{\rho + w_1} \right) + \frac{1}{2} (1 - \alpha_2 \rho) \left( \Delta P_3 - \rho^3 \ln \frac{\rho + w}{\rho + w_1} \right) \\ - \frac{1}{3} \alpha_2 \left( \Delta P_4 + \rho^4 \ln \frac{\rho + w}{\rho + w_1} \right), \quad (2.4.9b)$$

where

$$A \equiv \frac{1}{3} \alpha_2 w^3 - \frac{1}{2} (1 - \alpha_2 \rho) w^2 - \rho w + (\alpha_1 - \alpha_2) \left( \frac{1}{3} w_1^3 + \frac{1}{2} \rho w_1^2 \right), \quad (2.4.10)$$

and

$$P_N \equiv \sum_{n=0}^{N-1} (-1)^n \frac{\rho^n w_1^{N-n}}{N-n} \quad \text{and} \quad \Delta P_N \equiv \sum_{n=0}^{N-1} (-1)^n \frac{\rho^n (w^{N-n} - w_1^{N-n})}{N-n}. \quad (2.4.11)$$

Neither equations (2.4.8a) nor (2.4.8b) can be solved for either  $w_1$  or  $w$ , so the two equations must be solved together numerically for the widths. This was done for values of  $(W_1, u_0, u_m)$  on a rectangular grid in parameter space:  $W_1 = .25, .5$ , and  $.75$ , and  $u_0$  and  $u_m$  were set equal to  $.5, 1, \dots, 5$  and  $-.5, -1, \dots, -5$ . For all these values, as the curvature increased, the current grew narrower and the speed at the coast increased. This is consistent with the results of Hughes (1989) and those described above, in that the narrower of the two conjugate states does not separate from the coast. The behavior of the piecewise uniform potential vorticity current differs from the currents studied by Hughes by not having a wide, uni-directionally flowing mode along a straight coast.

## 2.5. Reduced Gravity Currents

### Upstream Flow

For  $\rho = \infty$ , we drop the centrifugal terms in equations (2.2.10a,b) and they become the linear, constant coefficient equations

$$u = -h_y \quad (2.5.1a)$$

$$u_y = 1 - \delta h, \quad (2.5.1b)$$

the general solution of which is

$$h = \frac{1}{\delta} + A_1 \sinh y\sqrt{\delta} + A_2 \cosh y\sqrt{\delta} \quad (2.5.2a)$$

$$u = -\sqrt{\delta}(A_1 \cosh y\sqrt{\delta} + A_2 \sinh y\sqrt{\delta}). \quad (2.5.2b)$$

This solution is valid for  $\delta \neq 0$ . We will only look at currents for which  $\delta > 0$ .

For the free streamline case, inserting (2.5.2) into the boundary conditions yields the solution

$$h = \frac{1}{\delta} [1 + (\delta - 1) \cosh \sqrt{\delta}(W - y)] \quad (2.5.3a)$$

$$u = \frac{\delta - 1}{\sqrt{\delta}} \sinh \sqrt{\delta}(W - y). \quad (2.5.3b)$$

Since  $\sinh$  is a monotonic function, the velocity varies monotonically from zero at the edge of the current to a maximum absolute value at the wall. If  $\delta > 1$  then  $u(0) > 0$  and the wall is on the right of the current, and if  $\delta < 1$ ,  $u(0) < 0$  and the wall is on the left. The thickness also varies monotonically, with the interface sloping upwards approaching the wall for  $u < 0$  and sloping downwards approaching the wall for  $u > 0$ . For one region in the  $\delta < 1$  half of the  $(W, \delta)$  parameter plane, the layer thickness at

the wall is negative and hence there is no physically meaningful flow possible. This situation is somewhat akin to the case of separation due to curvature, which also has the density interface surfacing. Substituting equation (2.5.3a) into the inequality  $h(0) < 0$ , we find that the invalid region is given by

$$W > \frac{1}{\sqrt{\delta}} \cosh^{-1} \left( \frac{1}{\delta - 1} \right). \quad (2.5.4)$$

For the upstream free streamline case, contours of  $h(0)$ , and  $u(0)$  in the  $(W, \delta)$  plane are given in Figures 2.5.1 and 2.5.2.

For the front case, the boundary conditions yield the solution

$$h = \frac{1}{\delta} + \frac{1}{\delta} \frac{(\delta - 1) \sinh \sqrt{\delta}(W - y) - \sinh y \sqrt{\delta}}{\sinh W \sqrt{\delta}} \quad (2.5.5a)$$

$$u = \frac{1}{\sqrt{\delta}} \frac{(\delta - 1) \cosh \sqrt{\delta}(W - y) + \cosh y \sqrt{\delta}}{\sinh W \sqrt{\delta}}. \quad (2.5.5b)$$

The flow at the outer edge of the front is positive for any  $\delta$ , so we only look at the case in which the flow is positive everywhere.  $u(0)$  is negative in the region of the  $(W, \delta)$  plane in which  $h(0)$  is negative in the free streamline case, so in both cases, the same region in parameter space is excluded from our consideration. In other respects, the dependence of the upstream flow on the parameters is quite different in the two cases. Contour plots of  $u(0)$  and  $u(W)$  are shown in Figures 2.5.3a and 2.5.3b.

It is also possible to have a local extremum in  $u(y)$  in the case of a front. Inserting equations (2.5.1b) and (2.5.5) into the condition  $u_y(y_e) = 0$ , we obtain

$$\coth y_e \sqrt{\delta} = \coth W \sqrt{\delta} + \left( \frac{1}{\delta - 1} \right) \frac{1}{\sinh W \sqrt{\delta}}. \quad (2.5.6)$$

For this extremum to be within the bounds of the current, we must have  $0 < y_e < W$ , or  $\coth W \sqrt{\delta} < \coth y_e \sqrt{\delta} < \infty$ . This is satisfied for  $\delta > 1$ . Inserting (2.5.6) into the expression for  $u_{yy}$ , we can show that for any  $(W, \delta)$  with an extremum in  $u(y)$ ,



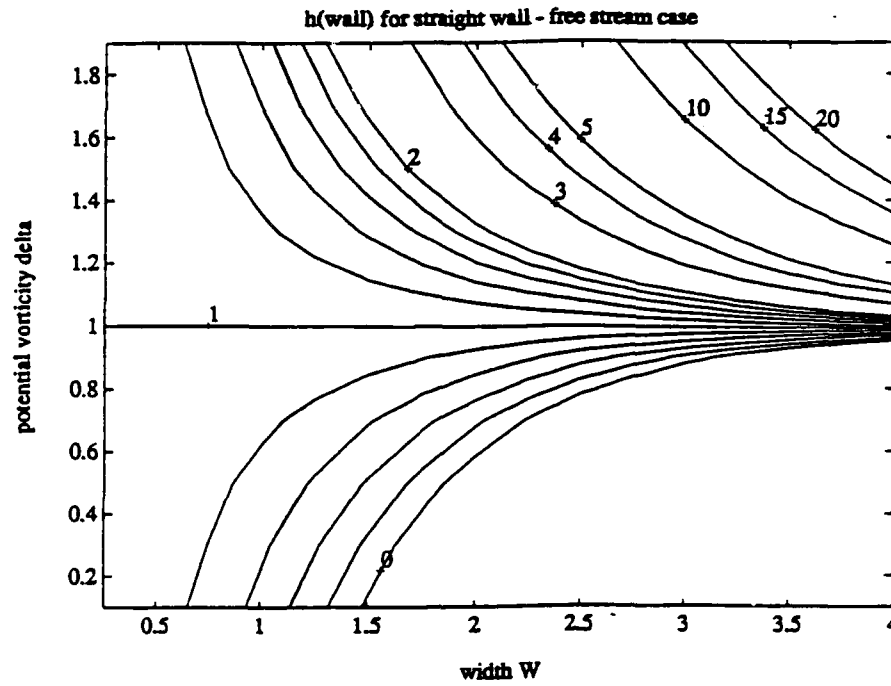


Figure 2.5.1: Contours of layer thickness at the wall  $h(0)$  at  $\rho = \infty$  as function of upstream width  $W$  and potential vorticity  $\delta$  for the free streamline case.

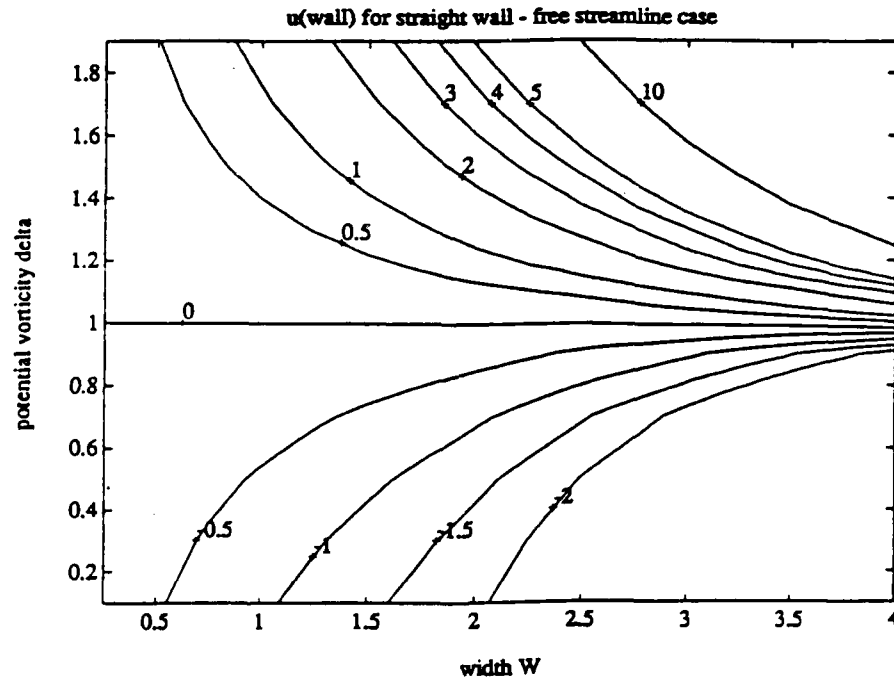


Figure 2.5.2: Contours of velocity at the wall  $u(0)$  at  $\rho = \infty$  as function of upstream width and potential vorticity for the free streamline case.

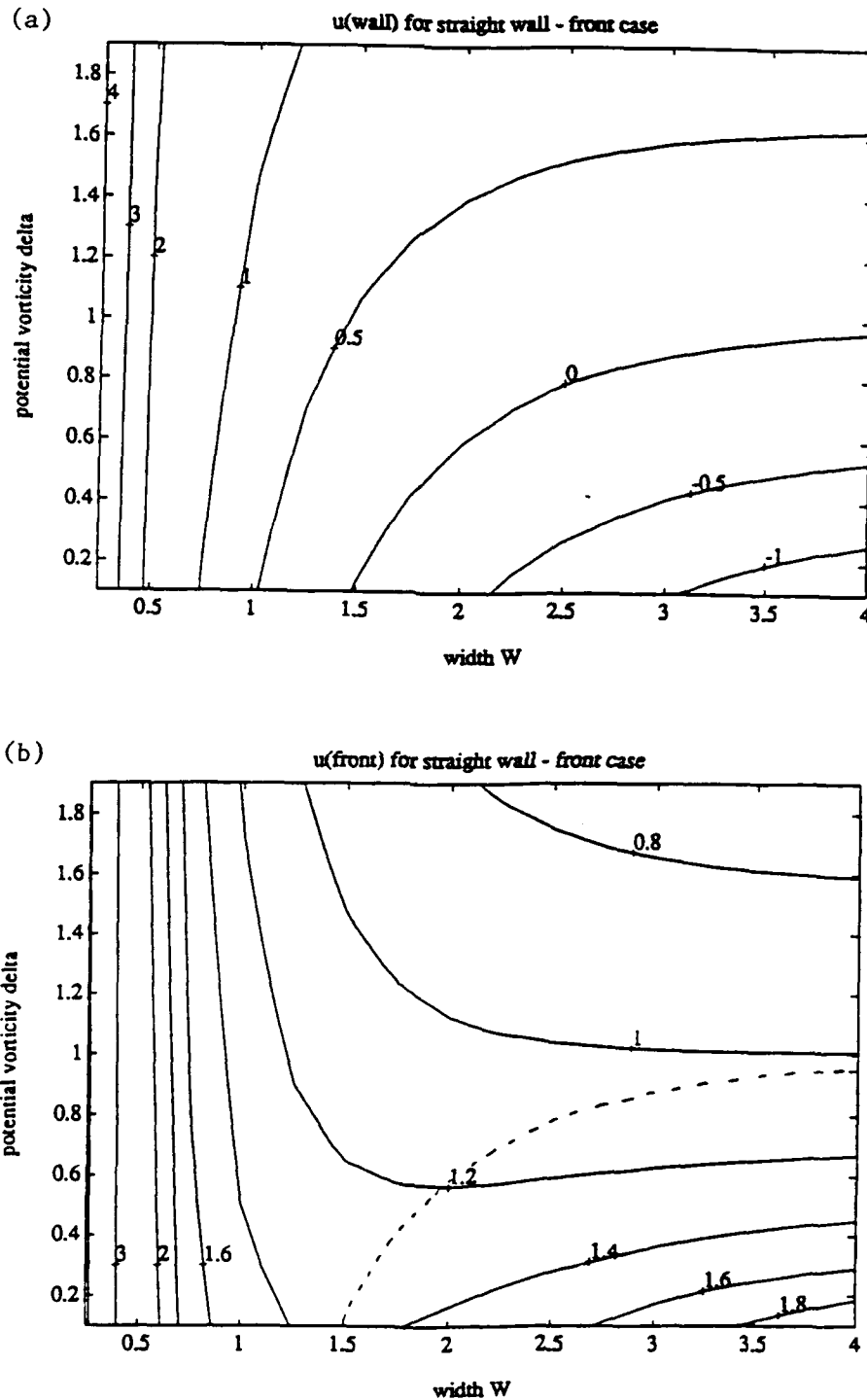


Figure 2.5.3: Contours of velocity at  $\rho = \infty$  as function of upstream width and potential vorticity for the density front case. (a) Velocity at the wall. (b) Velocity at the outer edge of current. Parameter values below dashed line in (b) do not have valid upstream flow.

$u_{yy} > 0$ , so the extremum is always a local minimum. As with the other case,  $h(y)$  is always monotonic.

For the free streamline case, the Bernoulli function at the wall is

$$B_0 = 1 - \frac{1}{2}\delta + \frac{1}{2\delta}(1 + [\delta - 1] \cosh W\sqrt{\delta})^2. \quad (2.5.7)$$

For the front, the Bernoulli function at the wall is

$$B_0 = 1 + \frac{1}{2\delta} \frac{([1 - \delta] \cosh W\sqrt{\delta} - 1)^2}{\sinh^2 W\sqrt{\delta}}, \quad (2.5.8)$$

and at the outer edge of the current is

$$B_1 = \frac{1}{2\delta} \frac{(\cosh W\sqrt{\delta} + \delta - 1)^2}{\sinh^2 W\sqrt{\delta}}, \quad (2.5.9)$$

Contours of  $B(0)$  for the free streamline case are plotted in Figure 2.5.4. Contours for  $B(0)$  and  $B(W)$  for the front case have the same shape as contours for  $u(0)$  and  $u(W)$ , since  $h(0) = 1$  and  $h(W) = 0$  for all  $(W, \delta)$ .

### Downstream Flow and Separation

For finite  $\rho$ , equations (2.2.4) were integrated using a fourth order Runge Kutta method with uniform step size (Press *et al.*, 1986). (I also attempted to find an analytical approximation to the solution using a Taylor expansion, but the complexity of the resulting expression and the slowness of convergence made this approach less attractive than a simple numerical solution). For both cases of the flow, there are two boundary conditions at the outer edge of the current and one at the wall. For this reason, the equations were transformed to a new coordinate  $t = w - y$ , so that

$$\frac{dh}{dt} = u - \frac{u^2}{\rho + w - t} \quad (2.5.10a)$$

$$\frac{du}{dt} = -1 + \frac{u}{\rho + w - t} + \delta h, \quad (2.5.10b)$$

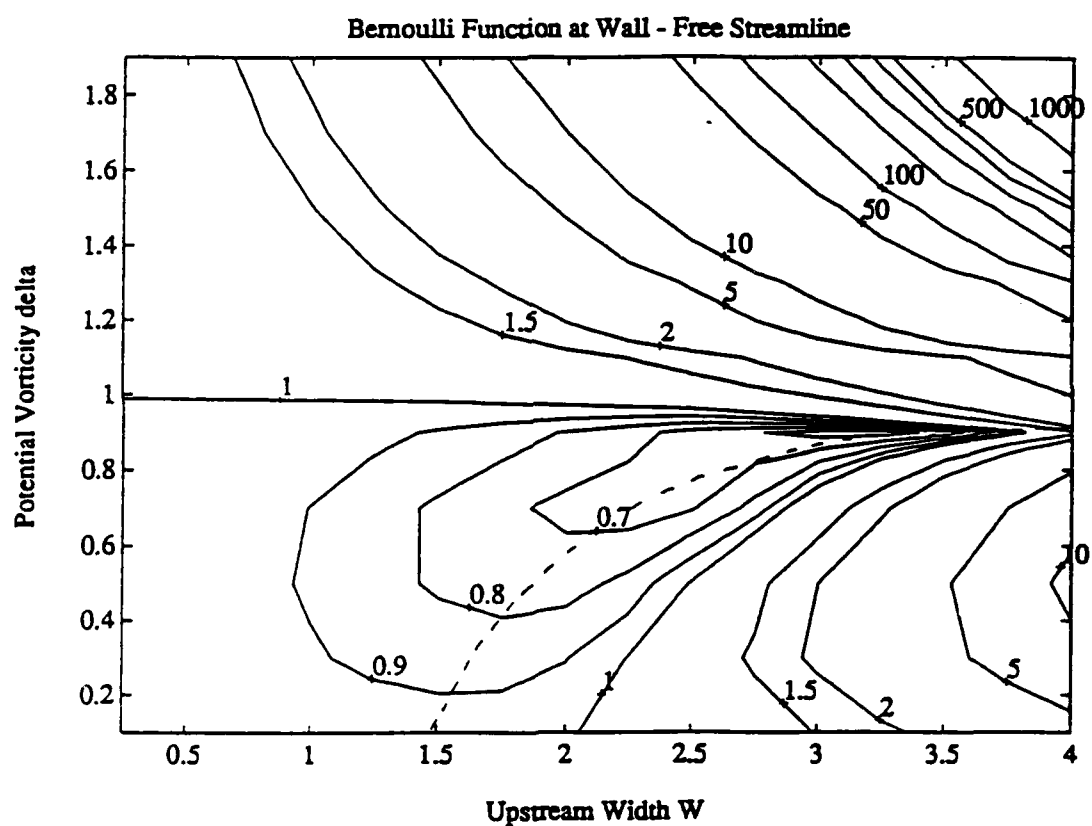


Figure 2.5.4: Contours of Bernoulli function at the wall at  $\rho = \infty$  as function of upstream width and potential vorticity for the free streamline case. The part of parameter space below the dashed line is not physically meaningful.

and they were integrated from  $t = 0$  with the "initial conditions" from the equations (2.2.13) or (2.2.14). Rather than solving given a certain value of  $\rho$ , the equations were solved given  $r = \rho + w$ , since  $w$  was not known before the equation was solved. For every step in  $t$ , the quantity  $h + \frac{1}{2}u^2 - B_0$  was tested for a zero crossing. When this happened, the current value of  $t$  was taken to be  $w$ , and  $\rho = r - w$  was found. This algorithm stops the integration prematurely if  $B = B_0$  for some  $0 < t < w$ . It can be proved that this does not happen for the free streamline case unless  $h(0) < 0$  at  $\rho = \infty$ . I was not able to prove that it does not happen for the front case, but I examined  $B(t)$  at a number of points in the  $(W, \delta)$  plane, and it had only one zero crossing in all of them.

For a given  $(W, \delta)$ , when I decreased  $r$ ,  $\rho$  and  $h(0)$  decreased also. For a small enough  $r$ ,  $h$  would become negative in the course of the integration, but  $h + \frac{1}{2}u^2 - B_0$  would never change sign, so that there was no solution consistent with the wall boundary condition, even allowing for a negative layer thickness. In order to get a lower bound on  $r$  and  $\rho$  for separation, I ended the integration in this case when  $(h + \frac{1}{2}u^2 - B_0)^2$  reached a local minimum, which always occurred if  $h(t) < 0$ . This allowed me to define  $w$  and  $\rho$  as above. I took this value of  $\rho$  to be a lower bound for  $\rho_c$ , while the smallest value of  $\rho$  with  $h(0) > 0$  was the upper bound for  $\rho_c$ . To refine estimates  $\rho_c$  for a certain  $(W, \delta)$ , a computer routine kept bifurcating the interval between a lower and upper bound for  $r$  until the interval between the corresponding upper and lower  $\rho$  was below a certain distance. This process was repeated on a grid in the  $(W, \delta)$  plane with  $W$  between .25 and 4.00 (grid spacing = .25) and  $\delta$  between .1 and 1.9 (grid spacing = .2). The step in  $t$  was  $W/10^4$ , and the threshold for the final interval in  $\rho$  was .0005.

The resulting function  $\rho_c(W, \delta)$  is wildly different for the two cases. For the free streamline case (see Figure 2.5.5), as upstream width increases, the current is more likely to separate (critical radius of curvature *increases*). As potential vorticity

goes to 1 from either side (the interface slope goes to zero), the current becomes less likely to separate. For the front, the critical radius of curvature is almost independent of the potential vorticity, and it *decreases* as upstream width increases (see Figure 2.5.6). For  $W \leq 1$  we have  $\rho_c$  very roughly equal to  $.7/W$ .

For the free streamline flow, the separation radius of curvature goes to infinity as the upstream layer thickness at the wall goes to zero. This makes intuitive sense, since the interface depth has to make a relatively small excursion in order to induce separation. In fact, comparison of Figures 2.5.1 and 2.5.5 shows that contours of upstream depth at the wall look very similar to contours of critical radius of curvature. In Figure 2.5.7,  $\rho_c$  is plotted against the cross stream change in interface depth at  $\rho = \infty$ ,  $|h(y = 0) - 1|$ . This plot shows that most of the variation in  $\rho$  with the upstream parameters can be explained in terms of the upstream height. The relation is especially striking for the  $\delta > 1$  case, in which a greater  $|h - 1|$  makes the current *easier* to separate even though the interface must travel *further* to come up to the surface at the wall. A similar relation holds for  $\rho_c$  plotted against upstream velocity at the wall (Figure 2.5.8). If we average the velocity over the width of the current upstream, we obtain  $\bar{u} = (h(0) - 1)/W$  for the free streamline case and  $\bar{u} = 1/W$  for the front case. Thus the free streamline critical radius of curvature is roughly proportional to the volume flux, and the front critical radius of curvature, at least for small upstream width, is roughly proportional to average velocity. Care must be taken in reviewing these results because equations (2.2.10a,b) upon which these results are based are derived with the assumption that  $w/\rho$  is small. The value of this parameter is contoured in Figure 2.5.9, which shows that for the free streamline case, the approximation is only valid for both  $W$  and  $\delta$  large or for the upstream depth at the wall small, while for the front case, it is only valid for small  $W$  (at  $W = .25$ ,  $w/\rho$  is around .3 for all  $\delta$ ).

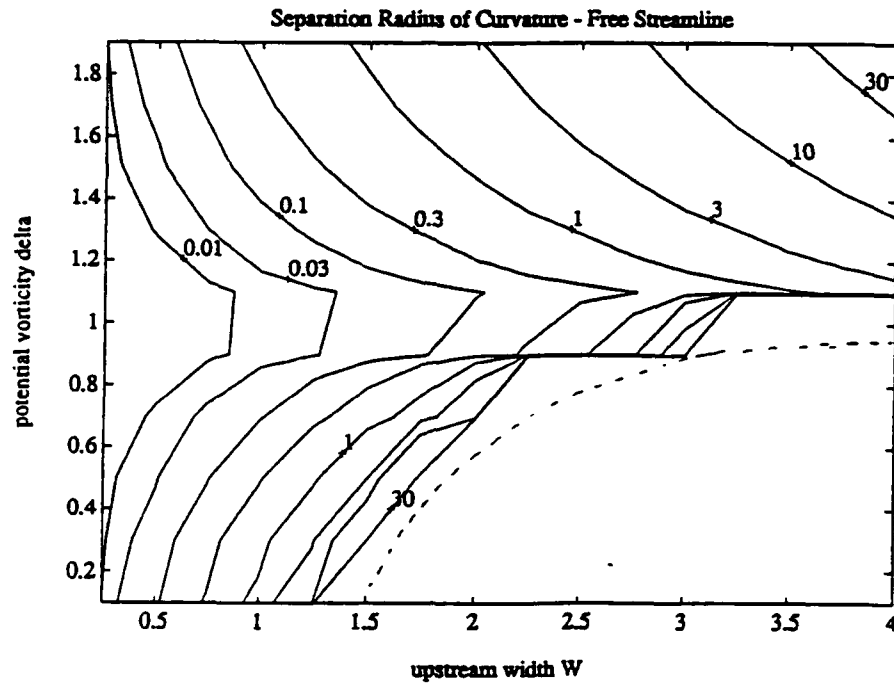


Figure 2.5.5: Contours of critical radius of curvature  $\rho_c$  for separation as function of upstream width  $W$  and potential vorticity  $\delta$  for the free streamline case.

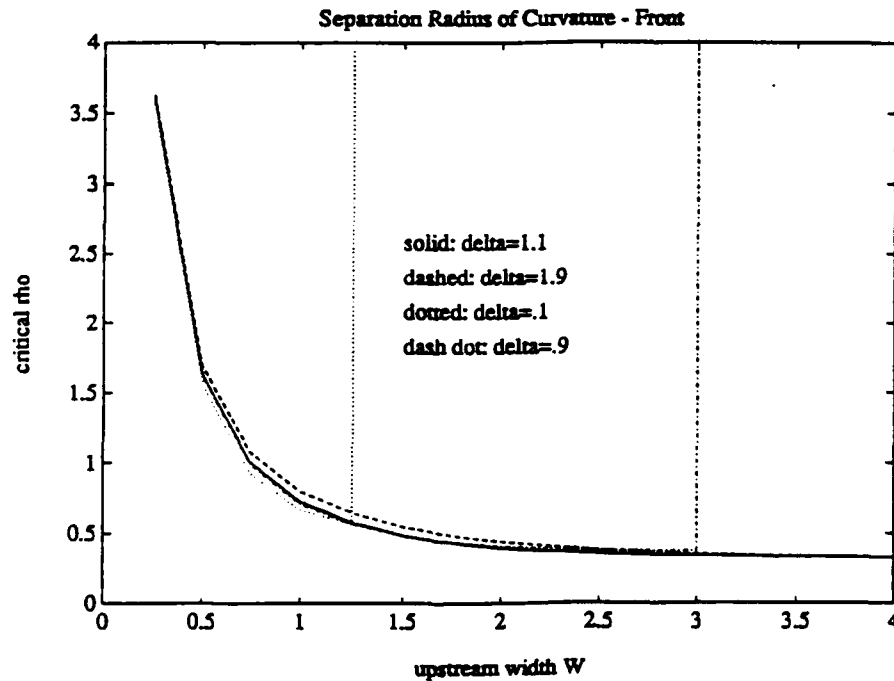


Figure 2.5.6: Critical radius of curvature for separation as a function of upstream width for various values of potential vorticity for the front case.

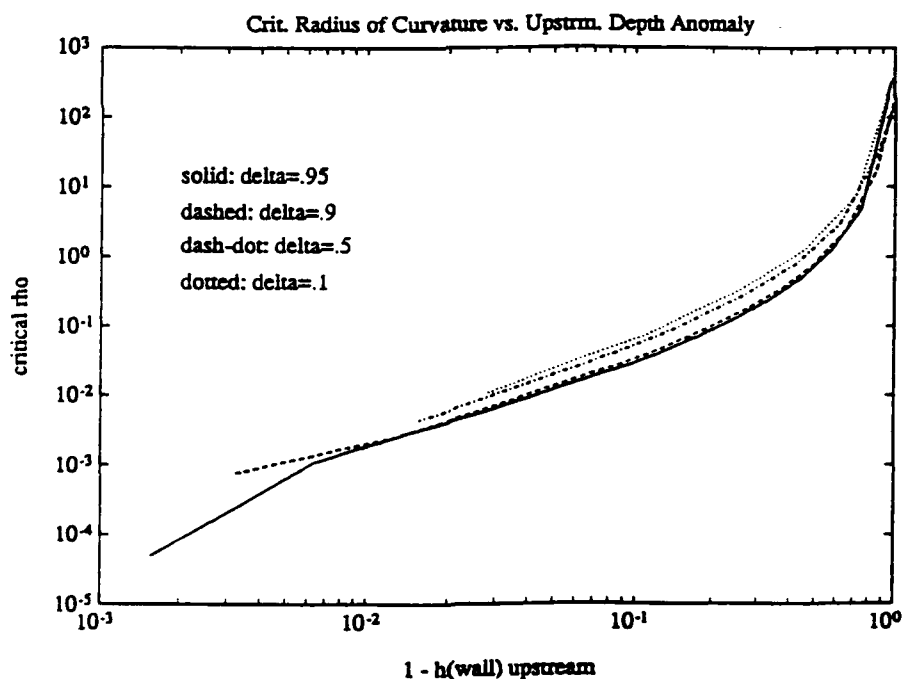
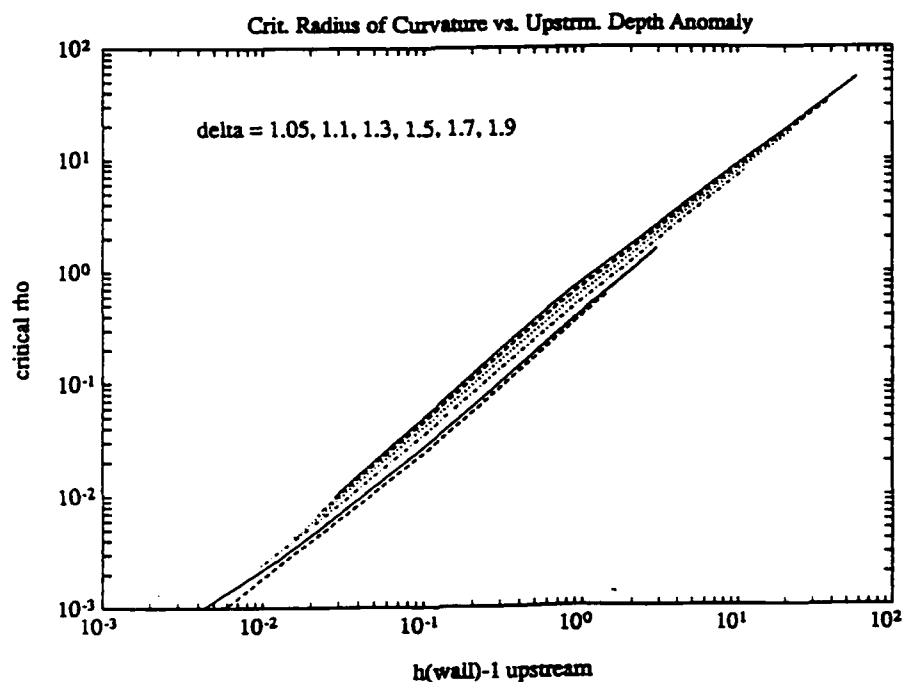


Figure 2.5.7: Critical radius of curvature for separation for free streamline case as a function of difference between upstream wall depth and free streamline depth for various potential vorticity values, log-log coordinates. (a) Wall on the right. (b) Wall on the left.



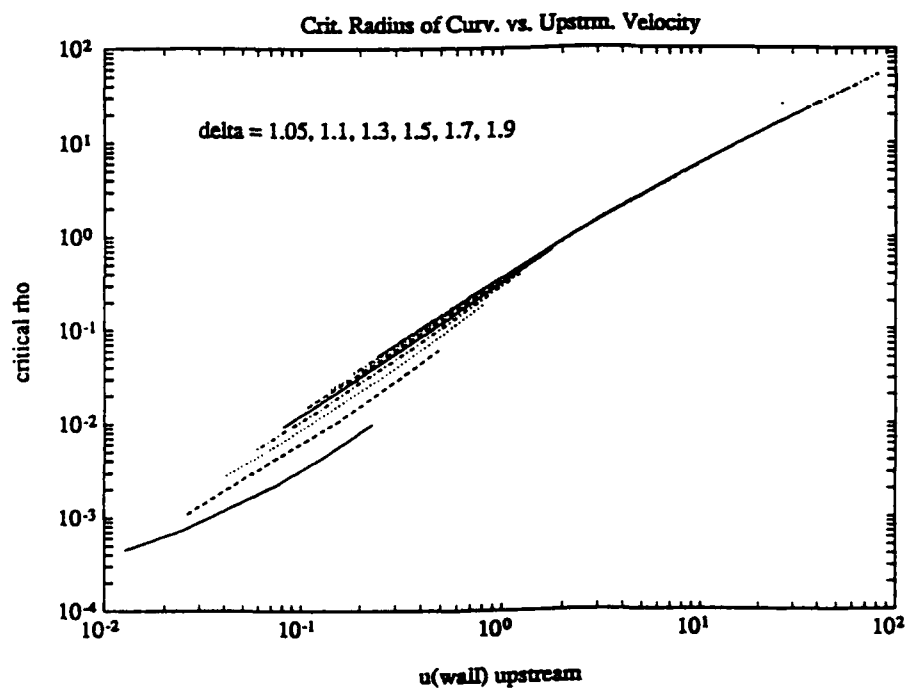


Figure 2.5.8: Radius of curvature for separation for free streamline case as a function of upstream velocity at the wall.

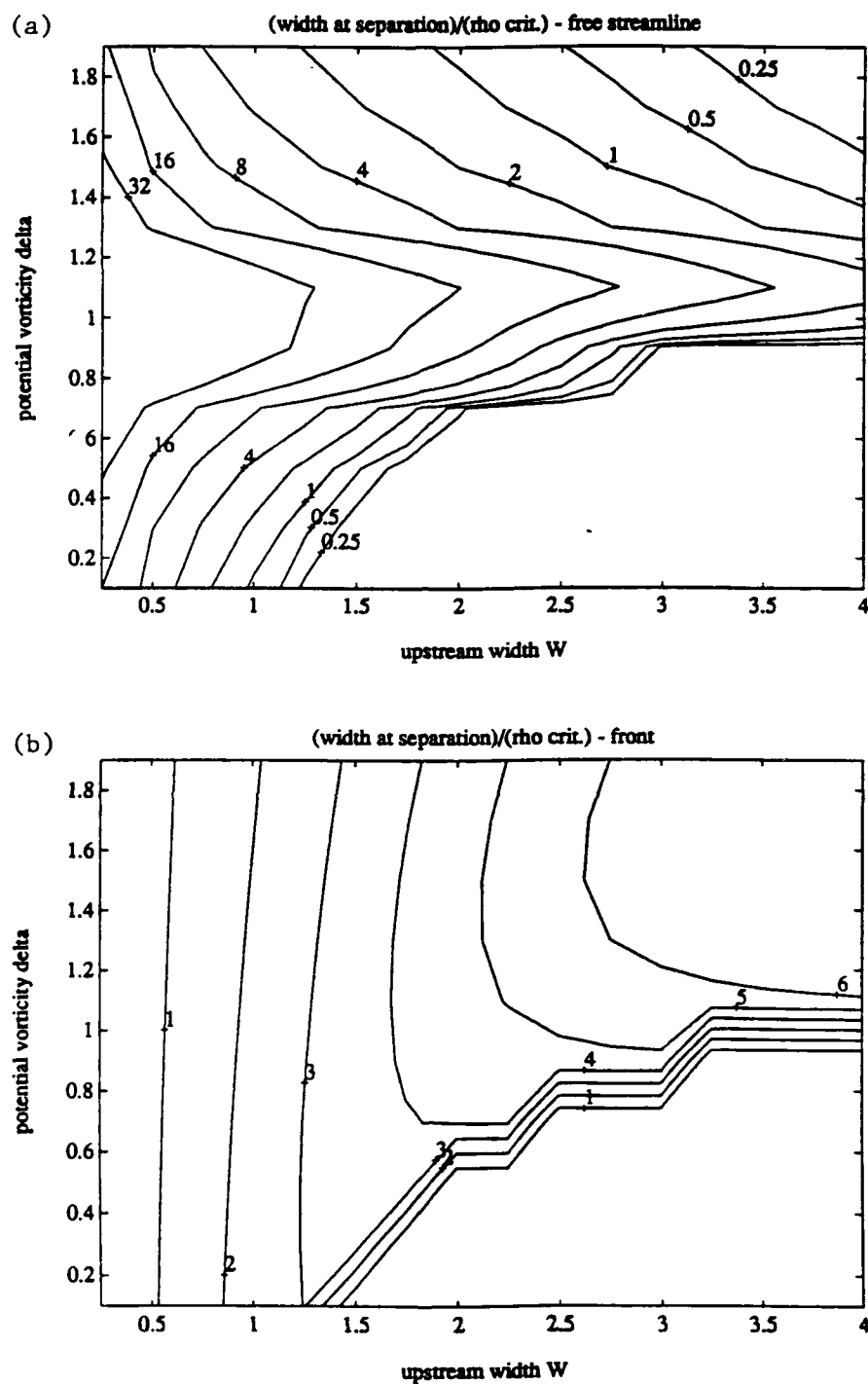


Figure 2.5.9: Contours of width of current divided by critical radius of curvature for separation,  $w/\rho_c$ , as a function of upstream width and potential vorticity. (a) Free streamline case. (b) Front case.

Cross-stream current profiles for straight wall and for critical curvature are shown for selected depth profiles in Figure 2.5.10. Though the depth profiles were forced to undergo great changes by the coastal curvature, the velocity did not change much. The current can either narrow or widen as the wall reaches its maximum curvature. Figure 2.5.11 shows  $w/W$  for  $\rho = \rho_c$  for the two cases.

Røed found the separation radius of curvature for a single value of potential vorticity and wall Bernoulli function. I converted his nondimensional units into mine to confirm that our results are consistent. Røed used a dimensionless potential vorticity equivalent height  $\hat{h}_\infty = 2/\delta$  and a dimensionless Bernoulli function parameter  $\hat{H}_r = 2B_0$ , and found a non-dimensional separation radius of curvature  $\rho_s$ , which is related to my separation radius  $\rho_c$  by  $\rho_s = \sqrt{\delta}\rho_c/2$ . For  $\hat{h}_\infty = 4.0$  and  $\hat{H}_r = 2.4$  we have  $\delta = .5$  and  $B_0 = 1.2$ , which gives  $W = 1.039$  (also  $W = 5.122$ , but that is a physically invalid solution). Røed found that  $\rho_s = .23$ , corresponding to  $\rho_c = .65$ , while I found that  $\rho_c = .66$  for a front. Thus they agree reasonably well (if we know  $\rho_s$  to within  $\pm .005$ , then we only know  $\rho_c$  to within  $\pm .01$ ). Ou and de Ruijter only solved for a separation radius of curvature given a non-zero velocity at the outside edge of the current, so his results are not directly comparable with mine.

Bormans and Garrett (1989) offered a simple rule, which is consistent with laboratory data, for deciding when a current in a two-layer system forms a gyre at a curved coast. If the (dimensional) inertial radius  $u/f$  ( $u$  is some characteristic velocity) is smaller than the radius of curvature of the corner,  $\rho$ , the current will stay attached, while if it is larger the current will separate. This criterion is equivalent to the scaling argument that the curvature term in the approximation to the cross-stream momentum equation (equation (2.2.4a)) is the same size as the geostrophic term. Physically, this corresponds to a centrifugal force at the corner that is strong enough to counteract the Coriolis force in order to pull the density interface up to the surface. This scaling argument only applies to flows with the wall on the right

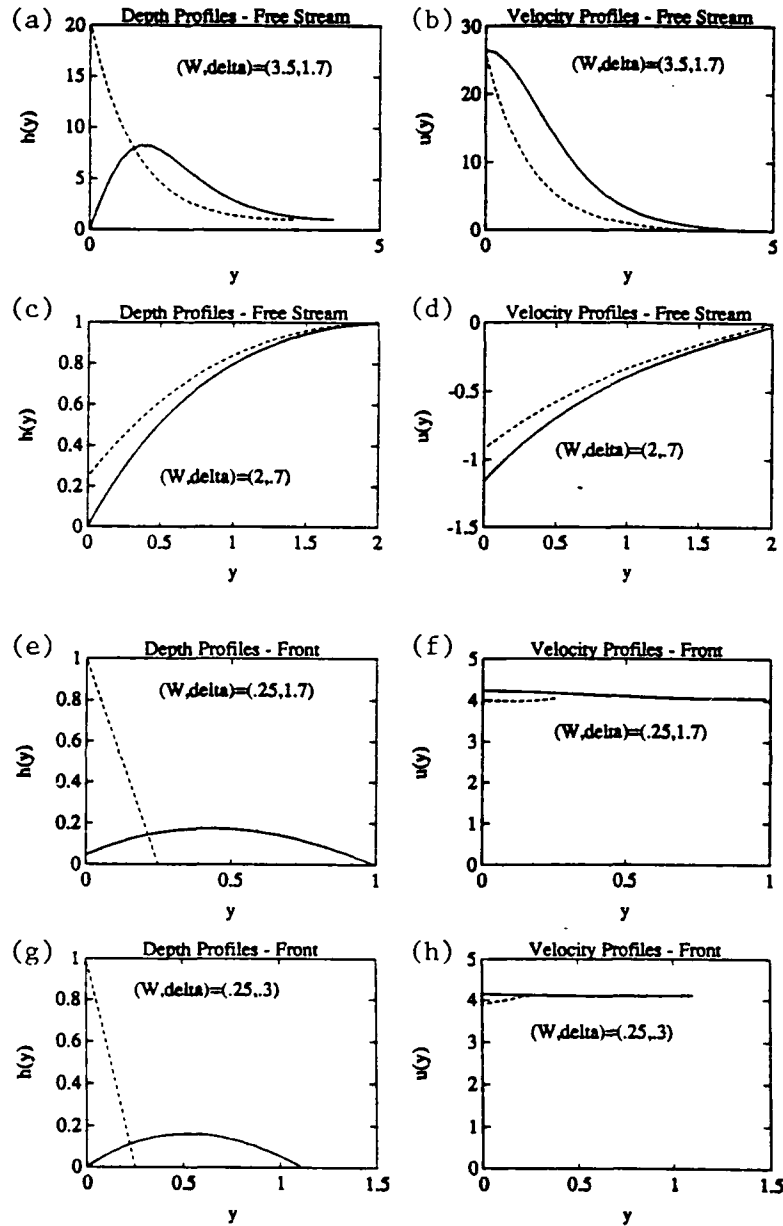


Figure 2.5.10: Depth and velocity profile for selected flows, at critical radius of curvature (solid curve) and zero curvature (dashed curve). Free streamline flows are shown in: (a) depth,  $(W, \delta) = (3.5, 1.7)$ , (b) speed,  $(W, \delta) = (3.5, 1.7)$ , (c) depth,  $(W, \delta) = (2, .7)$ , (d) speed,  $(W, \delta) = (2, .7)$ . Density front flows are shown in: (e) depth,  $(W, \delta) = (.25, 1.7)$ , (f) speed,  $(W, \delta) = (.25, 1.7)$ , (g) depth,  $(W, \delta) = (.25, .3)$ , (h) speed,  $(W, \delta) = (.25, .3)$ .

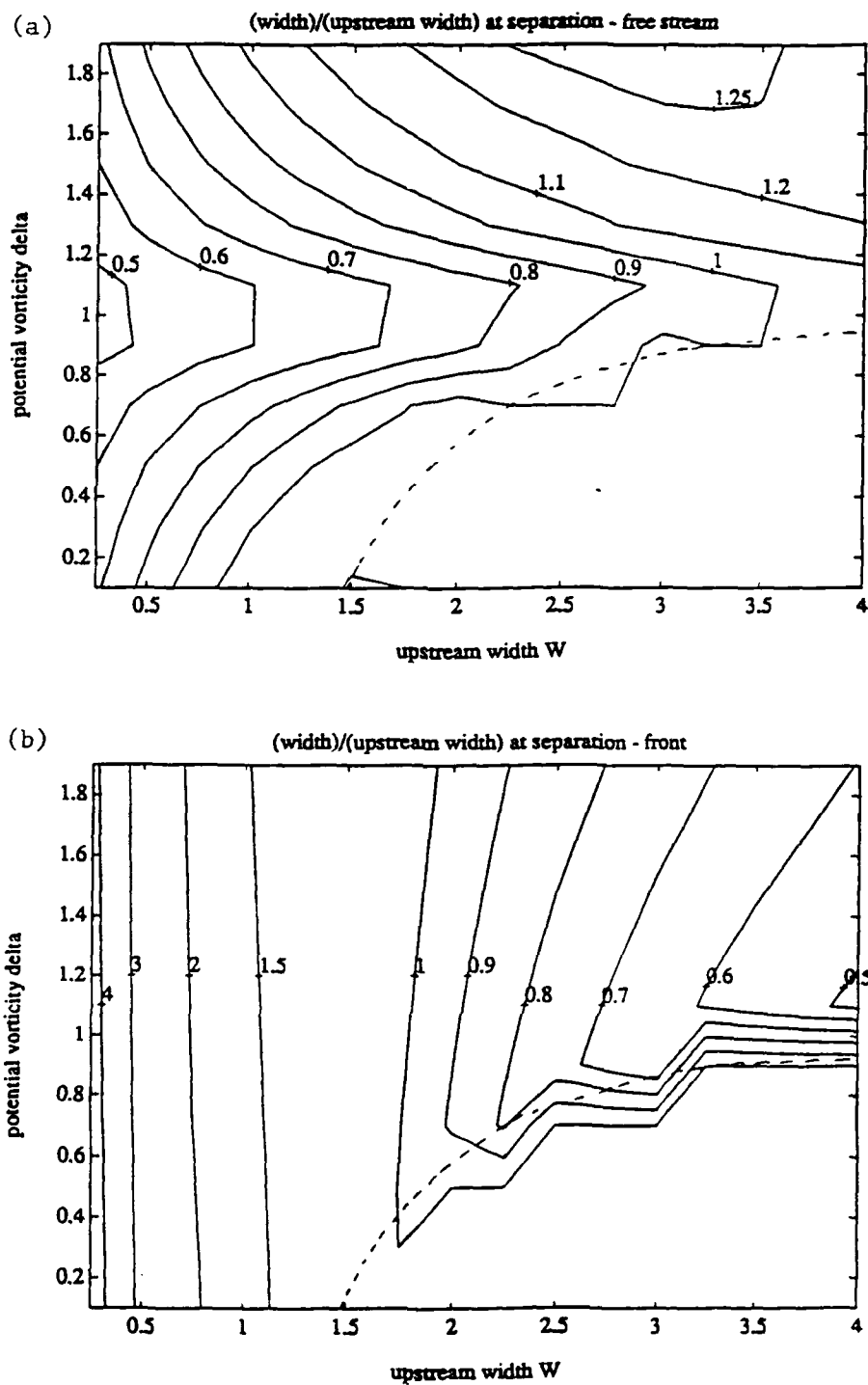


Figure 2.5.11: Contours of width of current at separation scaled by upstream width as a function of upstream width and potential vorticity. (a) Free streamline case. (b) Front case.

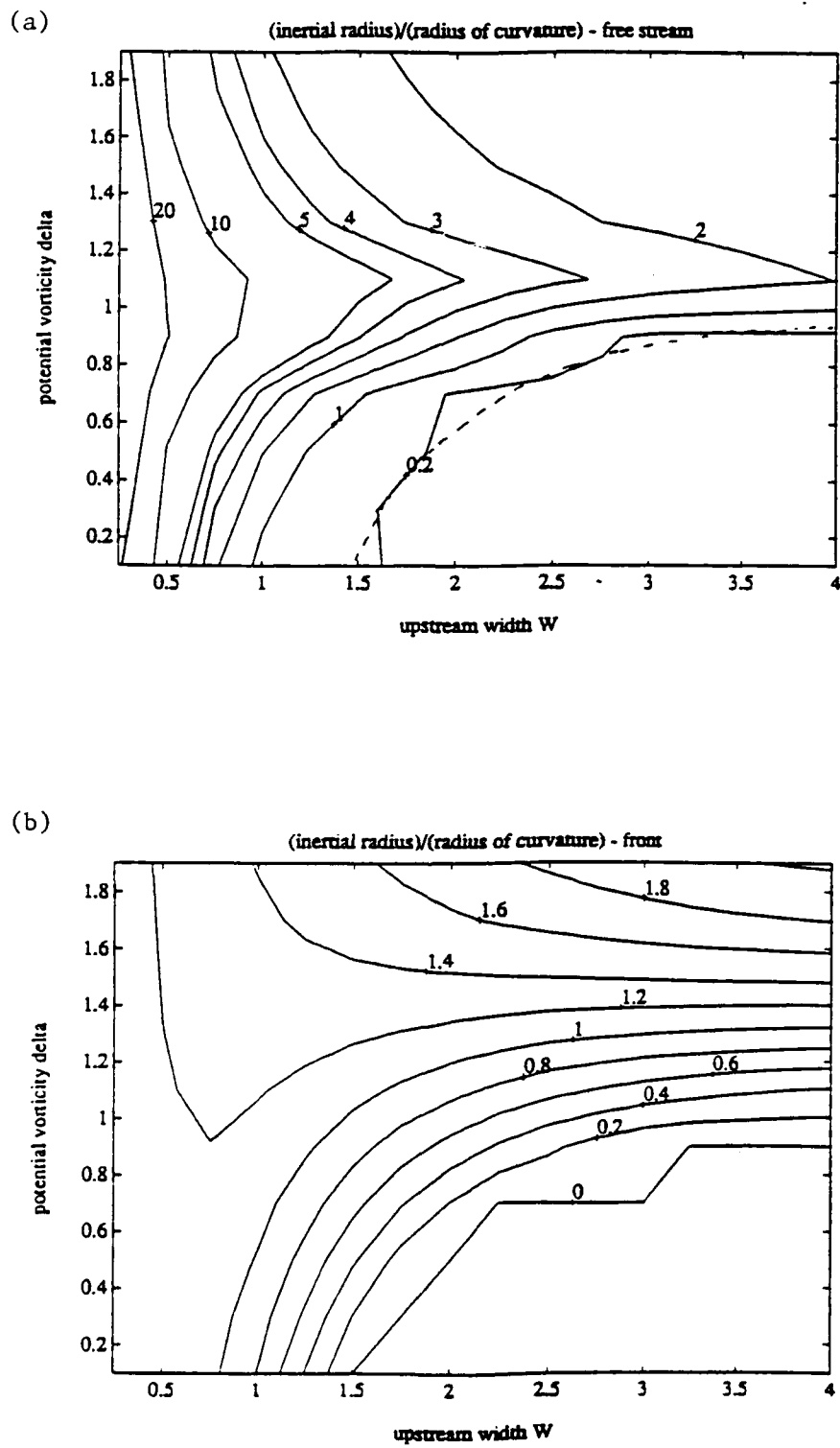


Figure 2.5.12: Contours of proposed separation parameter  $u/\rho_c$  as a function of upstream current width and potential vorticity for  $u = u(0)$ . (a) Front case. (b) Free streamline case.

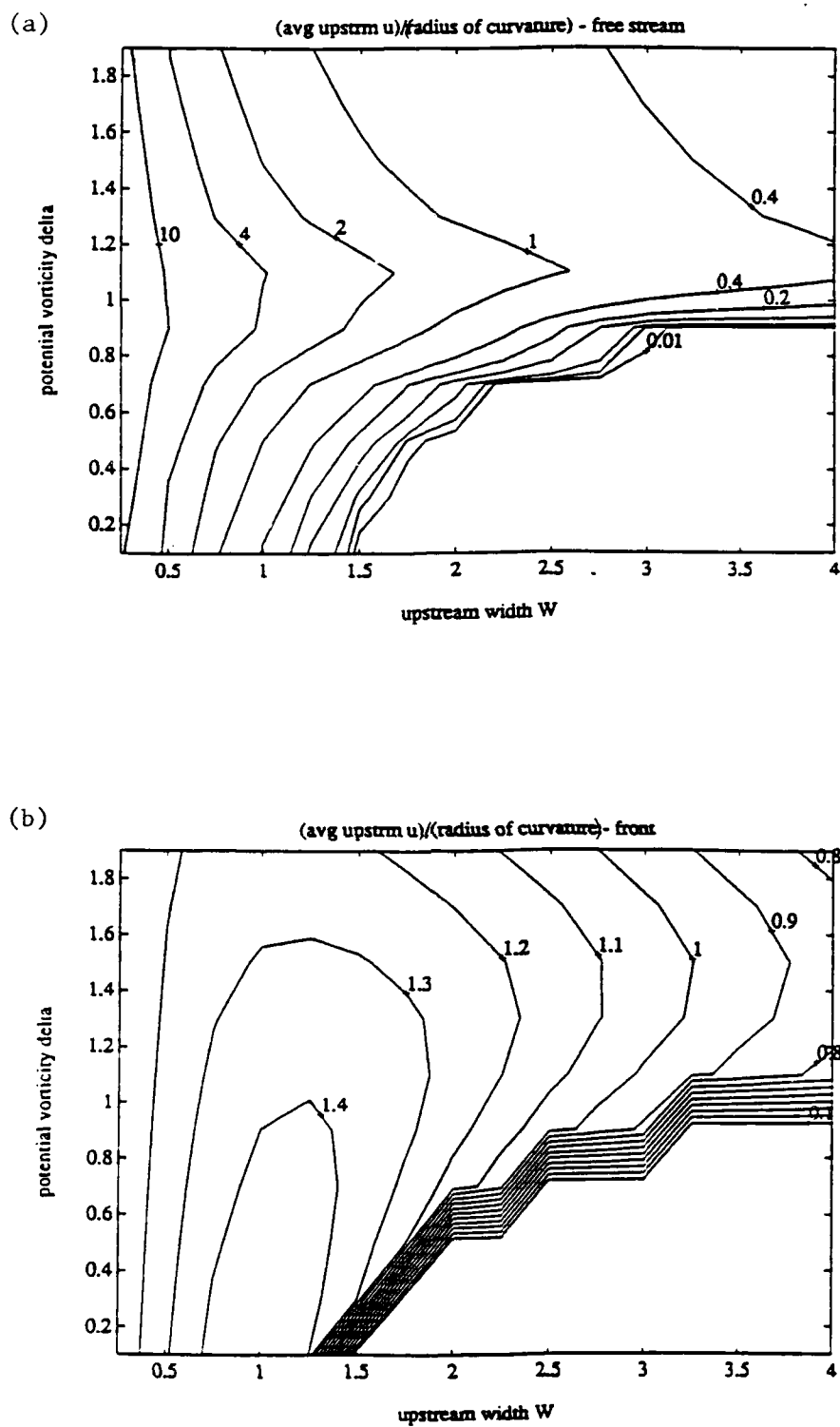


Figure 2.5.13: Contours of proposed separation parameter  $u/\rho_c$  as a function of upstream current width and potential vorticity for  $u = \bar{u}$ . (a) Front case. (b) Free streamline case.

of the current, since when the wall is on the left, the interface is rising towards the wall anyway, so that a small perturbation in the force balance may be sufficient to carry the interface the rest of the way up to the surface. In the non-dimensional formulation of this chapter, the criterion becomes  $u/\rho < u/\rho_c = 1$ . Bormans and Garrett did not specify the location in the flow of the velocity which they used to scale the flow. Strictly speaking, the scaling argument above applies to the velocity at the point of separation, but the separation criterion would be most useful if it could be applied to the flow upstream of the corner in order to predict the behavior of the current at the corner. This still leaves several possible choices for the appropriate  $u$ . Contours of  $u/\rho_c$  for two such choices are shown in Figures 2.5.12 and 2.5.13. In Figure 2.5.12,  $u$  is taken to be the upstream value of  $u(0)$ , while in Figure 2.5.13 it is  $\bar{u}$ , the cross stream average of  $u$  upstream defined above. For the front, letting  $u = \bar{u}$  gives  $u/\rho_c \approx 1$ , and letting  $u = u(0)$  gives a  $u/\rho_c$  which ranges from about 2 down to 0 near the region where there is a flow reversal near the wall at  $\rho = \infty$ . Free streamline flows show large variations in  $u/\rho_c$  everywhere in parameter space.

## 2.6. Conclusions

Barotropic and baroclinic coastal currents were modelled with an inviscid, hydraulic approximation in which alongstream variations in the flow quantities only appear parametrically. Given a simple flow upstream, where the coast was straight, the flow was computed downstream where the coast curved with radius of curvature  $\rho$  in order to see if and under what circumstances the current would be forced to separate from the coast, either due to a flow reversal in the barotropic cases or a surfacing of the density interface in the reduced gravity cases.

The barotropic flows investigated in this study never underwent separation. This is in contrast to the behavior of the barotropic currents studied by Hughes (1989).



In Hughes' currents, potential vorticity decreased exponentially with streamfunction, and fluid depth increased exponentially with distance from the wall. The flows in this study had piecewise uniform potential vorticity and fluid depths that were either uniform or proportional to distance from the coast. The discrepancy between Hughes' results and mine probably stems from the fact that he only found flow reversal for the wider of the two possible states which exist for a given potential vorticity and volume flux, while the wide state of the currents studied here was removed from consideration because it always had a flow reversal even for zero curvature.

Several differences between Hughes' model and mine could account for the difference between his upstream wide states (subcritical with respect to vorticity wave propagation) and mine: my depth profile went to zero at the wall while his did not, my bottom slope was uniform while his increased as one travelled offshore, and I had a piecewise uniform potential vorticity distribution while his was smoothly-varying. In order to isolate which factor was most important for the qualitative difference in the flow direction of the wide state, I calculated the  $\rho = \infty$  cross-stream profiles of currents which had piecewise uniform potential vorticity, uniform bottom slope, and finite depth at the wall. This system has another nondimensional parameter in addition to the parameters for the barotropic systems studied in Sections 3 and 4:  $\gamma = h_0/sW$ , the ratio of depth at the wall to depth at the outer edge of the current (in Section 3,  $\gamma = \infty$ , and in Section 4,  $\gamma = 0$ ). Arbitrarily restricting ourselves to the  $\gamma = 1$  case, we find that for some (but not all) values of potential vorticity when the current is flowing with the wall on the left (as in Hughes' case), both the wide and narrow states are unidirectional. This shows that the assumptions of piecewise uniform potential vorticity and linear bottom slope do not by themselves preclude the flow reversal found by Hughes. The actual behavior of these  $\gamma \neq 0$  flows in places where the coastline is curved was not explored because by the time these results were obtained, full analysis of the barotropic data had indicated that the shallow water

equations, upon which the analysis in this chapter is based, break down when a gyre is formed.

Røed (1980) and Ou and de Ruijter (1986) showed that uniform potential vorticity, reduced gravity currents separated from a curved coast when the density interface surfaced at the coast. They did not record separation due to flow reversal for the case of convex curvature studied here, though Røed did show flow reversal in a bay. The survey of parameter space undertaken in this chapter confirmed that the upwelling of the interface is the only mode of separation available for this system. The qualitative difference in the separation characteristics of barotropic flows with different potential vorticity and depth profiles raises the question of whether giving a reduced gravity flow non-uniform vorticity could cause it to separate from a cape by developing a flow reversal as in some of the barotropic flows.

The reduced gravity systems studied by Røed (1980) and Ou and de Ruijter (1986) are governed by the non-dimensional potential vorticity and non-dimensional upstream (zero curvature) width, and by the form of the outer boundary condition. Over a range these parameters, I found the critical radius of curvature for which the thickness of the layer at the wall goes to zero. A coastline with a sharper curve than this critical curvature will not support a steady boundary current with the given upstream parameters, and presumably some kind of separation will occur at the coast.

The dependence of the critical curvature on the parameters is very different for the  $h = 0$  outer boundary condition (front case) and the  $u = 0$  outer boundary condition (free streamline case). For the front, the dimensionless critical radius of curvature for the front is roughly proportional to  $1/W$ , which is the average upstream velocity  $\bar{u}$ , in the range of relatively small  $W$  for which the long wave approximation applies. For the free streamline case, the critical radius depends most strongly on the volume flux  $\bar{u}W$ : it is proportional to the flux for positive velocities, and is a

more complicated function that monotonically increases with volume flux for negative velocities.

These results yield ambiguous agreement with experimental results, which show that the dimensional  $\rho_c$  ought to be the inertial radius  $u/f$  (Bormans and Garrett, 1989). If we base the radius of curvature on the upstream velocity at the wall, the latter relation does not hold for either case solved here, though it is correct to within about a factor of two for a front with  $\delta > 1$  (which has monotonic  $u(y)$ ). If we use the average upstream velocity, Bormans and Garrett's relation does approximately hold for the case of the front, because the dimensional version of the expression for critical radius of curvature calculated in this chapter is  $\rho_c = .7\bar{u}/f$ . For the free streamline case, the corresponding expression is  $(\bar{u}/f)(W/R)$ , where  $R$  is the Rossby radius  $\sqrt{g'h_0}/f$  based on the current depth at the free streamline. Bormans and Garrett's data included upper layer currents which flowed into either unstratified ambient water (the density front case) or two-layer stratification (free streamline case), and their value of  $\rho_c$  remained independent of  $W/R$  despite variations in  $W/R$  by a factor of 7.

The great difference between the results for density front and free streamline flows, even when both have the coast to the right of the current, show that the form of the outer boundary condition is important in determining the conditions under which the current will separate at a curved section of coast. In the experiments of Whitehead and Miller (1979) and Bormans and Garrett (1989), the width of the flow was controlled by the channel width (relative to the Rossby radius of the system), which implies a different boundary condition for the upstream flow than either the free streamline or the density front case. Unfortunately, in the laboratory it is much more difficult to control the (non-dimensional) width and potential vorticity of a true coastal current like those studied in this chapter in order to probe parameter space.

## Chapter 3.

# Eddies Generated by a Density Front Current at a Sharp Corner in a Rotating Tank

### 3.1. Introduction

Previous studies have examined eddy generation by density currents which emerge from a counterclockwise rotating channel, turn to the right, and flow along the wall outside the channel. In some circumstances, the current overshoots the corner and re-attaches to the wall to the right of the channel, generating an anticyclone in between. Presumably, the formation of a gyre is not dependent on the existence of the channel's left wall, so that if we remove it, leaving a coastal current both upstream and downstream of the corner, the same processes would still form a gyre. Therefore the first purpose of the experiments described in this chapter was to confirm that this was indeed the case. This was shown to be true (see below), so that we can assume that studies of flows leaving a channel and studies of boundary currents flowing around corners are interchangeable. In this spirit, the experiments described in this chapter are designed to continue the investigation of baroclinic currents which produce a gyre at a corner.

Bormans and Garrett (1989) showed that a current characterized by a speed  $u$  traveling around a curved coast with a radius of curvature  $\rho$  in a rotating system with Coriolis parameter  $f$  produces an anticyclone at the corner if  $u/f\rho > 1$ . We will look at a similar geometrical parameter for a system which in all cases has a sharp corner ( $\rho = 0$ ). In such a system, the angle between the walls upstream and downstream of the corner plays a role that is analogous to the radius of curvature in Bormans and Garrett's system. Together, radius of curvature and corner angle control

the magnitude of the perturbation from straight, parallel flow which a current must undergo to follow a bend in a coastline. A bend in some real stretch of coast bordering the Earth's ocean, such as Cape Saint Vincent on the Iberian Peninsula, would be characterized by both the angle between the coast upstream and downstream of the corner and by the radius of curvature. The experiments in which radius of curvature was varied and these new experiments, in which corner angle is varied, represent two simple limits which can be used to gain insight into the more general case.

In the new experiments, fresh water was made to flow into relatively dense salty water, where the intrusion flowed along a vertical wall and around a corner. The angle of the corner was varied from run to run. The flow was produced by a dam-break between the homogeneous salty water and a region with a fresh layer floating on top of a salty one, as in Bormans and Garrett. In these runs, the corner was sharp to about .1 cm, compared to a current width on the order of 10 cm.

We also conducted one run in which the current was made to flow with the wall on the left of the current looking downstream, instead of on the right. This also produced a gyre, which is qualitatively described below. Different methods of generating the flow, such as using a pump instead of a dam-break, were also used, with similar results. In addition, some runs were conducted with a sloping side-wall, since real oceanic boundaries are never vertical, and with water with an ambient stratification into which a current was forced.

It is possible that the eddies generated at a corner are formed because there is no steady-state solution to the equations of motion which allow a flow to remain attached to the coast at the corner, or because such an attached flow is unstable at the corner. In dam break experiments such as the ones described above, the flow was initiated upstream of the corner and propagated as a tongue of fluid that approached the corner. Since the eddy appears as soon as the nose reaches the corner, the experiments leave open the possibility that the initial interaction of the nose with

the corner is responsible for producing the eddy. It would be desirable to know if eddy generation can be explained by exploring the dynamics of a steady current, or if the nose is responsible for the eddy. To do this, I conducted experiments in which the fresh water was initially confined to a region adjacent to the coast both upstream and downstream of the corner. Thus the leading edge of the current was initiated downstream of the corner, and the existence of an eddy in these runs would prove that the interaction of the leading edge with the corner is not a crucial factor in determining whether an eddy is formed.

In most of the runs, the intrusion had a maximum thickness that was small compared to the depth of the ambient water so that motions in the salty layer would be sluggish compared to the fresh water. In some runs, the thickness of the two layers was of the same order, so that the contribution of the lower layer flows to the motions in the upper layer could be emphasized. Unless otherwise noted, the discussion below will not include these runs.

The velocity field was traced by surface drifters, which were interpolated to create grids of velocity, from which depth, potential vorticity, and volume flux of the fresh water flow were mapped. This data gives us a more detailed picture of the currents which are being studied, and profiles upstream of the corner can be used as a measure of the reproducibility of conditions upstream of the corner. If there is a critical corner angle for eddy formation, it is likely that flow around a corner with a subcritical angle (no gyre produced) will exhibit a quantitative dependence on the corner angle. As the critical angle is approached from below, the flow profile could show signs of incipient gyre formation. Therefore the details of the flow pattern in gyreless runs were examined to give further insight into the processes at work when a gyre is produced.

## 3.2. Apparatus and Procedure

### General Description

Most of the experiments were conducted in June and July 1990, in the 2.13 m diameter rotating tank at the Coastal Research Laboratory at WHOI. Initial experiments with a 90° corner angle were conducted in November 1989. The tank was divided by walls into two regions, areas A1 and A2 (see Figure 3.2.1). Both regions were filled with salty water, the tank was made to rotate, and fresh water was slowly fed into region A1 to form a surface layer there. A gap in a wall separating A1 and A2 was sealed with a watertight dam (the "short dam"), which was removed to initiate a surface flow of fresh water into A2 and a weaker bottom flow of salt water into A1. The fresh water intrusion traveled along "the first wall," around a corner, down "the second wall," and then around the rim of the tank. The gap was 12.5 cm, 20 cm, or 5 cm wide in the initial runs with a 90° corner angle, and 9.3 cm wide in the rest of the runs. The different gap widths were originally used to see if any aspect of the flow could be controlled by the gap width, but this parameter had little effect on the flow.

For the "long dam" runs, the gap was left open and a removable Plexiglass wall was suspended parallel to the first and second walls, extending from the gap to the rim. This extended the region A1, which initially contained a fresh surface layer, into a channel along the first and second walls (see Figure 3.2.2). When the suspended wall was removed, the fresh water in the channel adjusted (as in a geostrophic adjustment process) to form a current along the first and second walls, while more fresh water was pulled through the gap to continue feeding the current. Figure 3.2.3 shows corner angles which were used for all three variations of the experiment: deep lower layer/short dam, deep lower layer/long dam, shallow lower layer/short dam.

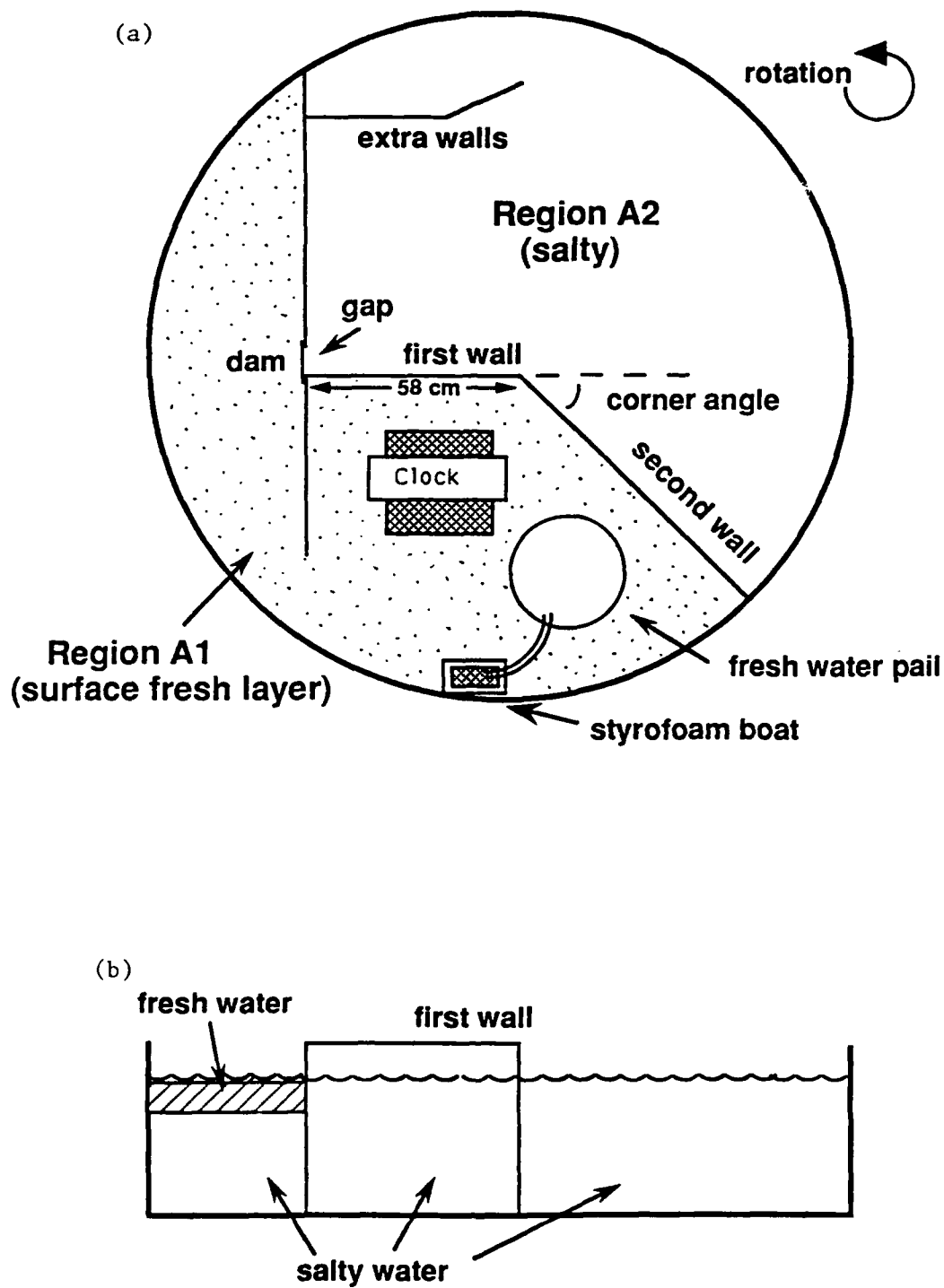


Figure 3.2.1: Experimental apparatus, dam-break flow, short dam. (a) Top view of tank. (b) Side view of tank.



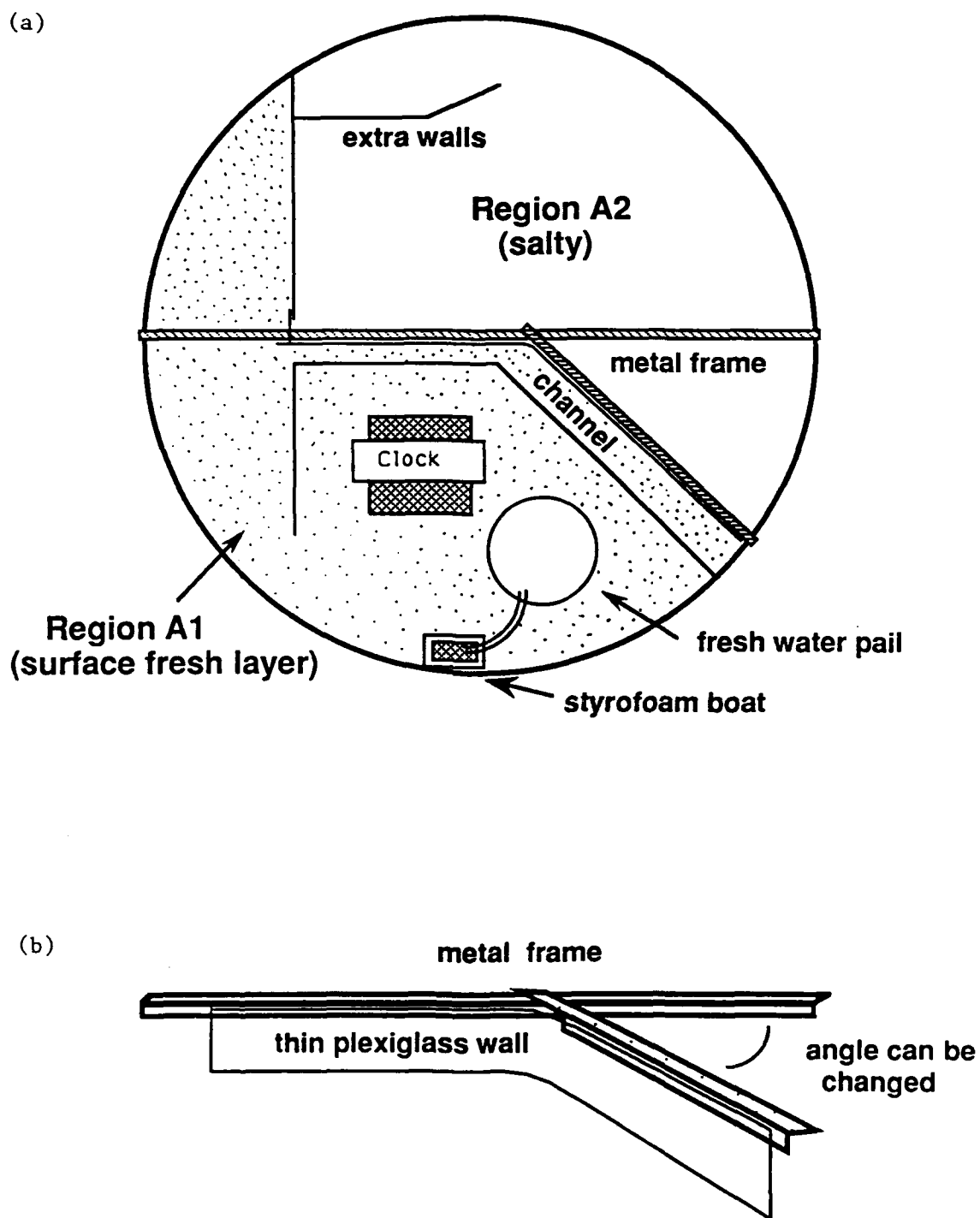


Figure 3.2.2: Experimental apparatus, dam-break flow, long dam. (a) Top view of tank. (b) Perspective view of long dam.

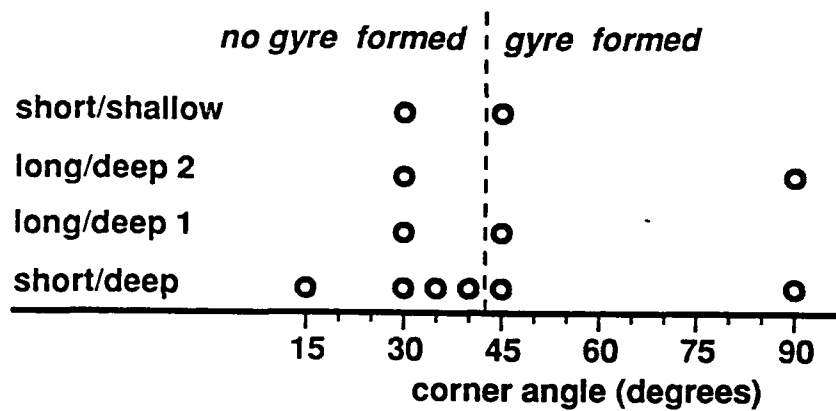


Figure 3.2.3: Parameter synopsis for experiments, showing corner angle and type of run, where "short/deep" is short dam, 32 cm deep lower layer; "long/deep" is long dam, 32 cm deep lower layer; and "short/shallow" is short dam, 4-6 cm deep lower layer. "Long/deep 1" refers to the first long dam, which formed a channel 10 cm wide, while "long/deep 2" refers to the second long dam, with a channel 4 cm wide.

In the run with the wall on the left of the flow, the initial stratifications of area A1 and A2 were reversed: A1 was filled with homogeneous salt water, while a cap of fresh water was added to the surface of A2. Even though the stratification was different, when the dam was removed, the velocity signal propagated as a nonlinear Kelvin wave along the first wall towards the corner. However, the direction of the actual current was reversed, since the fresh water was pulled by gravity from region A2 to region A1. Corresponding to the direction of flow, the density interface must rise rather than sink as the wall is approached from offshore. The run was conducted with a corner angle of  $90^\circ$ .

### Flow Visualization

The flow field was visualized by white paper and cardboard disks strewn on the surface during the run. Most of the pellets were .64 cm in diameter, but some were .32 cm wide. The initial  $90^\circ$  runs were recorded from above by a co-rotating color video camera, and the other runs were recorded from above by a co-rotating  $512 \times 512$  pixel black-and-white CCD camera whose signal was fed via sliprings to a VHS format video cassette recorder. A monitor was connected to the VCR so I could watch the experiment from the co-rotating frame in real time. The video data for the velocity field was transferred to computer with the "ExpertVision" motion analysis system, a commercially available package which digitized the position of the centroid of each surface drifter in a number of video frames in a given time interval. Each velocity vector at a given time was computed from the difference between a drifter position one frame before and one frame after the time, with the vector locations given by the average of these two positions.

In the initial  $90^\circ$  experiments, the fresh water was dyed red and the salty water was not dyed. In the rest of the runs, the fresh water was dyed almost black so that it would be clearly identifiable, and the salty water was made a light blue so that

it was dark enough to contrast with the white pellets and light enough to contrast with the darker fresh water.

### Density and Rossby Radius

All runs had rotation periods of approximately 15 s. The temperatures of the fresh water and the salty water were within  $.5^{\circ}$  C of each other before the fresh water was fed into the tank and even closer by the time the run was conducted. For all runs, the water temperature was between  $19.5^{\circ}$  and  $21.5^{\circ}$ . The fresh water layer was given an initial thickness of 4 cm, which was small enough to maintain a large ratio of bottom layer thickness to top layer thickness in the tank, and large enough for the surface and bottom Ekman layers of the freshwater intrusion to be thin compared to the mean depth of the intrusion. A small aspect ratio (fresh layer depth divided by current width) was desired to give the hydrostatic approximation some validity, so the current width was made as large as possible. Given the size of the tank, it was convenient to make the density current width, which is on the order of one Rossby radius, about 10 cm. In order to obtain an internal Rossby radius of 10 cm with a fresh layer 4 cm deep, the salty layer needed to have a density of  $1.0163 \text{ g/cm}^3$ . The actual densities were between  $1.0160$  and  $1.0180 \text{ g/cm}^3$ . The corresponding gravity long wave speed was 8–9 cm/s in most of the runs (all parameter values are shown in Tables 3.2.1 and 3.2.2). In the initial  $90^{\circ}$  runs, the density difference was somewhat weaker, giving a Rossby radius of only about 8.4 cm and a long wave speed of 7.1 cm/s.

For all experiments, a density sample was drawn from the surface of the fresh layer before the run, and from the surface of the fresh water flowing near the intersection of the second wall and the rim of the tank after a few minutes of flow. During one run (shallow lower layer,  $45^{\circ}$  corner angle run), flow samples were extracted by syringe at several depths in the fresh current instead of just at the surface (see Figure 3.2.4b). Similarly, samples from several depths in the fresh layer were extracted

Table 3.2.1. Parameter Chart, Dam Break Experiments

run	$\theta$	$h_1$	$h_2$	period	$\rho_{2a}$	$\rho_{2b}$	$\rho_{1a}$	$\rho_{1b}$	gap
Short Dam, Deep Lower Layer									
a1	90°	4.5	32.0	14.54	1.0110 <sup>a</sup>	n.m.	n.m.	.9980 <sup>a</sup>	12.5
a2	90°	4.0	32.0	14.92	1.0110 <sup>a</sup>	n.m.	n.m.	.9980 <sup>a</sup>	20.0
a3	90°	4.0	32.0	15.39	1.0111	n.m.	n.m.	.9981	5.0
h3	30°	4.3	31.6	14.87	1.0172	1.0172	.9988	.9988	9.3
h5	15°	4.4	31.8	14.81	1.0163	1.0172	.9986	.9983	9.3
h6	45°	4.5	32.8	14.85	1.0170	1.0182	.9988	.9984	9.3
h11	35°	4.0	32.0	15.26	1.0163	1.0167	.9979	.9978	9.3
h12	40°	4.1	31.7	15.15	1.0159	1.0167	.9986	.9987	9.3
h13	90°	4.3	31.6	14.96	1.0173	1.0173	n.m.	.9984	9.3
avg		4.2	31.9	14.97	1.0167 <sup>b</sup>	1.0172 <sup>b</sup>	.9985 <sup>b</sup>	.9984 <sup>b</sup>	
rms		0.2	00.4	00.26	0.0006 <sup>b</sup>	0.0005 <sup>b</sup>	.0004 <sup>b</sup>	.0004 <sup>b</sup>	
Long Dam, Deep Lower Layer									
h1	90°	4.0 <sup>a</sup>	32.0 <sup>a</sup>	14.89	1.0163	1.0166	n.m.	.9980	10.
h2	30°	4.0	32.0	15.17	1.0169	1.0170	.9985	.9984	10.
h4	15°	4.6	31.7	14.79	1.0160	1.0170	.9985	n.m.	10.
h8	45°	4.5	31.3	14.97	1.0174	1.0175	.9982	.9982	4.
h10	30°	4.3	31.8	14.92	1.0166	1.0166	.9977	.9974	4.
Short Dam, Shallow Lower Layer									
h7	45°	3.0	4.7	14.85	1.0165	n.m.	.9985	.9981	9.3
h9	30°	3.2	4.4	15.06	1.0155	n.m.	.9987	.9982	9.3

$\theta$  is corner angle,  $h_1$  and  $h_2$  are upper and lower layer depths in reservoir region of tank before flow begins, "period" is rotation period of tank,  $\rho_{2a}$  and  $\rho_{2b}$  are measurements of lower layer density near top of layer and near bottom of layer,  $\rho_{1a}$  and  $\rho_{1b}$  are measurements of upper layer density measured near end of second wall during run and inside reservoir before run, and "gap" is width of gate for the short dam runs and width of long dam channel just outside gap for long dam runs (for which the gate width is 9.3 cm for all runs). All units cgs. Depth measurements are accurate to about .5 cm and density measurements are accurate to about .0002 g/cm<sup>3</sup>.

<sup>a</sup> Estimate.

<sup>b</sup> Statistics from experiment h only.

n.m. Not measured.

Table 3.2.2. Derived Parameters, Dam Break Experiments

run	$\theta$	$\delta$	$f$	$g'$	$c$	$R_D$
Short Dam, Deep Lower Layer						
a1	90°	.14±.02	.864	12.7	7.6±.5	8.7±.5
a2	90°	.13±.02	.842	12.7	7.1±.4	8.4±.5
a3	90°	.13±.02	.817	12.7	7.1±.4	8.7±.5
h3	30°	.14±.02	.845	18.0	8.8±.5	10.4±.6
h5	15°	.14±.02	.849	17.3	8.7±.5	10.3±.6
h6	45°	.14±.02	.846	17.8	8.4±.5	9.9±.6
h11	35°	.13±.02	.823	18.0	8.5±.5	10.3±.6
h12	40°	.13±.02	.829	17.0	8.3±.5	10.1±.6
h13	90°	.14±.02	.840	18.5	8.9±.5	10.6±.6
avg		.14	.839	17.8 <sup>a</sup>	8.6 <sup>a</sup>	10.3 <sup>a</sup>
rms		.005	.014	.5 <sup>a</sup>	.2 <sup>a</sup>	.2 <sup>a</sup>
Long Dam, Deep Lower Layer						
h1	90°	.12±.02	.844	17.9	8.5±.5	10.0±.6
h2	30°	.12±.02	.828	18.0	8.5±.5	10.2±.6
h4	15°	.15±.02	.850	17.2	8.9±.5	10.5±.6
h8	45°	.14±.02	.839	18.8	9.2±.6	11.0±.7
h10	30°	.14±.02	.842	18.5	8.9±.5	10.6±.6
Short Dam, Shallow Lower Layer						
h7	45°	.64±.08	.846	17.6	7.3±.4	8.6±.5
h9	30°	.73±.09	.834	16.5	7.2±.4	8.7±.5

$\theta$  is corner angle,  $\delta = h_1/h_2$  is ratio of upper layer to lower layer depth,  $f$  is Coriolis parameter,  $g' = g\Delta\rho/\rho$ , (where  $g$  is acceleration due to gravity (980 cm<sup>3</sup>/s),  $c = \sqrt{g'h_1}$  is the upper layer gravity wave speed, and  $R_D = c/f$  is the upper layer Rossby radius.  $\rho$  is the upper layer density measured during the run, and  $\Delta\rho$  is the difference between the upper layer density during the run and the lower layer density before the run; in runs a1, a2, a3, h1 and h13, the upper layer water density was not measured during the run so the measurement before the run was used. For all runs, the estimated error in  $g'$  was .3 cm<sup>3</sup>/s, and the error in  $f$  was at most .006 s<sup>-1</sup>. All units cgs.

<sup>a</sup> Statistics from experiment h only.

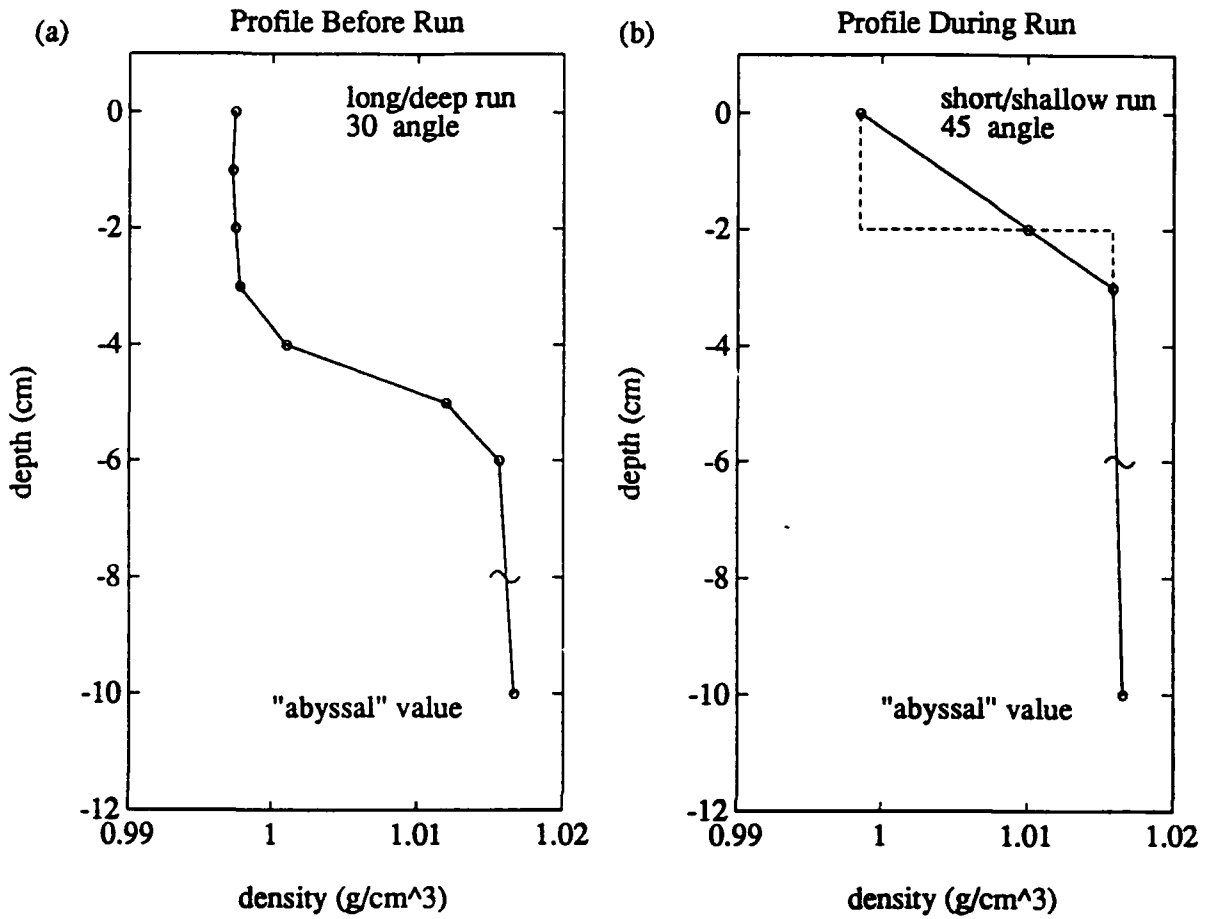


Figure 3.2.4: Density profiles as a function of depth. (a) Long dam, deep lower layer, 30° angle; fresh reservoir before dam removed. (b) Short dam, shallow lower layer, 45° angle; end of second wall during run. Dashed line shows sharpest pycnocline compatible with data.

before the flow began in the long dam, 30° corner angle run (see Figure 3.2.4a). The reservoir profile shows a pycnocline primarily between 4 cm and 5 cm depth, while the outflow profile had a pycnocline primarily between the surface and 3 cm depth. The density profiles give an upper bound on the amount of mixing that took place in the reservoir and in the fresh outflow. The dashed curves in Figure 3.2.4 show the sharpest pycnoclines compatible with the data.

Though efforts were made to make the salty layer homogeneous, the density of a sample drawn from the bottom few centimeters was typically .0002 to .0010 g/cc greater than the surface density of the layer before spin-up. At worst this is about 6% of the density difference between the fresh layer and the salty layer, and is also spread out over a depth range that is about thirty times greater.

For more detailed notes on the apparatus, see Appendix 1.

### **3.3. Qualitative Behavior and Eddy Growth Rates**

#### **Short Dam, Deep Lower Layer**

The short dam, deep lower layer experiments established that a baroclinic coastal current could generate an anticyclonic gyre at a corner like the gyre produced by baroclinic outflow from a channel. The angle of the corner was varied in order to find a critical angle for gyre formation and to discover if any other features of the flow were dependent on the corner angle.

In all three runs with a ninety degree corner angle, a narrow density current intruded into the salty water along the first wall, overshoot the break in the wall by several centimeters, returned and traveled along the second wall. Within a few seconds (as soon as pellets could be strewn over the area), an anticyclone was observed next to the second wall at the corner. Pellets coming from upstream were captured



by the vortex and typically traveled around it a few times before continuing along the second wall. The anticyclone grew in size and propagated away from the corner, moving diagonally from both walls (Figure 3.3.1). As the eddy moved away from the corner there was evidence of a new anticyclone forming at the corner. The current weakened slowly as the reserve of fresh water ran down, but the flow was fairly strong for at least six minutes. This was about the time the nose of the current took to circumnavigate the perimeter of the active region of the tank.

In the runs with gate widths  $W_g$  of 12.5 cm and 20 cm, and possibly in the  $W_g = 5$  cm run as well, a weak cyclone was observed to accompany the anticyclone as it propagated away from the corner (visibility was dependent on the spacing of surface pellets). The cyclone was in the salty layer and was presumably the lower-layer counterpart to the upper layer anticyclone, but was weaker due to the relatively large depth of this layer. The lower layer flow must form a boundary current against the wall underneath the surface current, even though the lower layer current flows with the wall on its left (looking downstream), because the Kelvin wave that initially establishes the current travels with the wall on its right as it propagates away from the gap connecting regions A1 and A2. The lower layer cyclone provides a likely mechanism for the eddy to drift away from the coast, because the cyclone and anticyclone pair form a heton, which will tend to drift in the observed direction due to mutual advection of the vortices by the velocity fields associated with each other's vorticity anomalies. In the  $W_g = 20$  cm run, a cyclone with a diameter of at most 29 cm also emerged from the current considerably upstream of the corner, as if generated by an instability. There was some sign of a similar cyclone in the  $W_g = 5$  cm run; this may have been less visible due to undersampling of the flow field with surface drifters.

In each run, the dye formed two regions. Adjacent to the walls was the deeply dyed inner region, which included the fastest currents, while the outer region was lightly dyed and had much smaller velocities. This outer region appeared to be

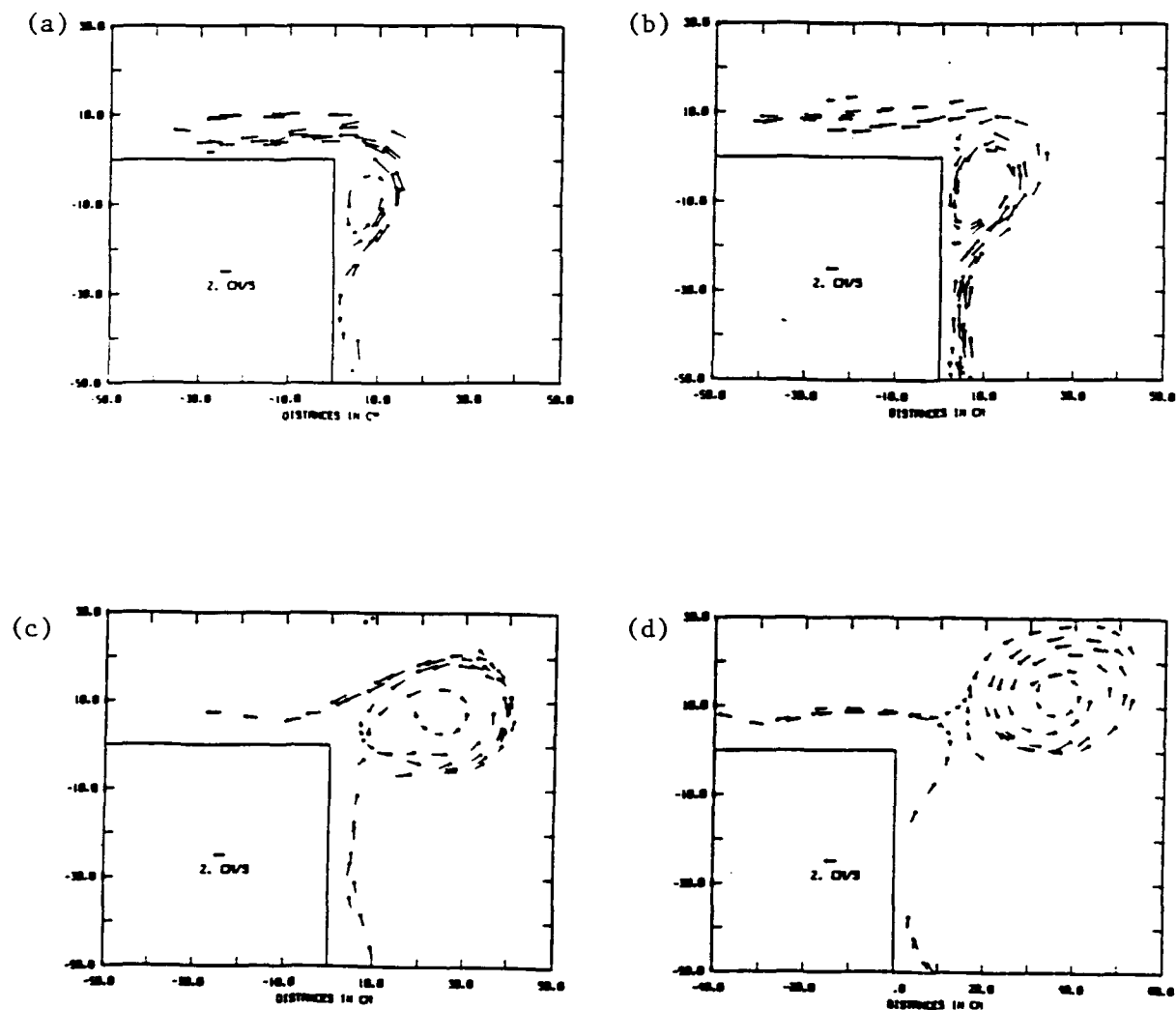


Figure 3.3.1: Velocity field for various time intervals during short dam, deep lower layer,  $90^\circ$  angle run with 12.5 cm wide gap. Velocity vectors for all runs are from digitized paths of videotaped surface drifters. The tail of each vector, marked by a small box, shows position of velocity measurement. In this and all subsequent plots of velocity fields, distances are in cm and apparent length of vector in cm gives speed in cm/s. (a) 33–60 sec after flow began, every third second. (b) 63–90 sec. (c) 123–150 sec. (d) 183–210 sec.

only on the order of a millimeter deep. Once the nose passed the corner, there was no sign of any surfacing of the density interface, as indicated by lightening of the dye, near the corner. In most of the runs, the dye was so dark that the interface needed to almost surface in order to become perceptibly lighter, but in the runs with a short dam and  $90^\circ$  corner angle and in some of the runs in which the current was forced by pumping rather than a dam-break, the dye was light enough so that any decrease in the thickness of the dye should have been apparent. In all the runs, the current width, as measured near the middle of the first wall, was about the same when delimited by high current speeds and by dark dye: about 10 cm. The nose propagated along the first wall at an average speed of about 4 cm/s for the first run and about 6 cm/s for the other two.

Runs with corner angles of  $15^\circ$ ,  $30^\circ$ ,  $35^\circ$ , and  $40^\circ$  did not separate at the corner. The current travelled around the corner and continued along the second wall and along the rim of the tank (see Figure 3.3.2). The  $35^\circ$  and  $40^\circ$  runs produced a stagnation region at the intersection of the second wall and the rim of the tank. This region developed reverse flow along the second wall — essentially an anticyclone at the downstream end of the second wall. The upstream edge of the anticyclone grew towards the corner over time, while the gyre widened. This is evidence that there were quantitative changes in the flow along the second wall due to the corner, but it is likely that no eddy would have developed had the second wall been much longer. A  $45^\circ$  angle did produce a gyre at the corner (Figure 3.3.3). This grew more slowly than the  $90^\circ$  runs. Though no experiments were performed with a corner angle greater than  $90^\circ$ , a wall protruding from the rim of the tank downstream of the second wall provided a  $180^\circ$  angle around which the current flowed. The eddy generated here was qualitatively the same as the one at the  $90^\circ$  corner (see Figure 3.3.2).

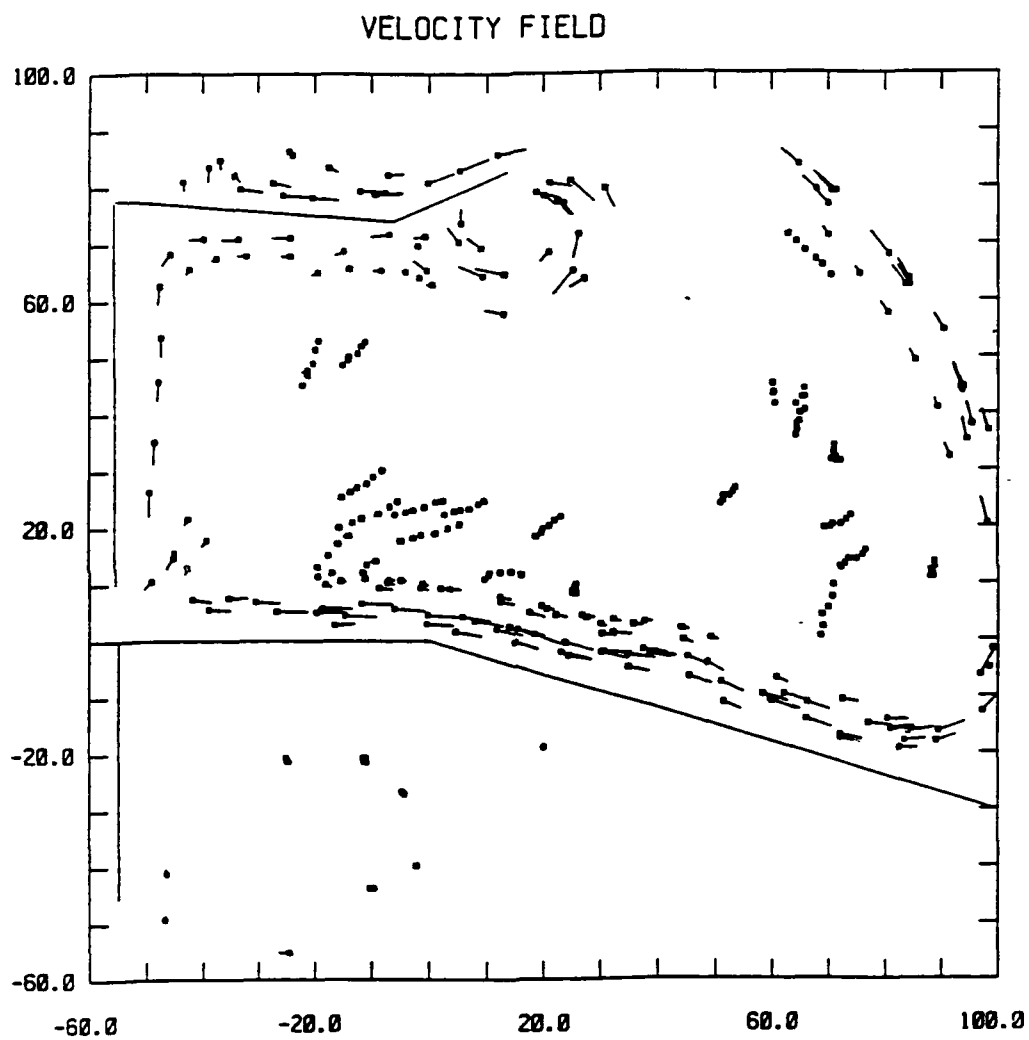


Figure 3.3.2: Velocity field in which no eddy was formed, short dam, deep lower layer run with  $30^\circ$  corner angle. Data comes from every fifth second in the interval 125–150 sec after flow began.

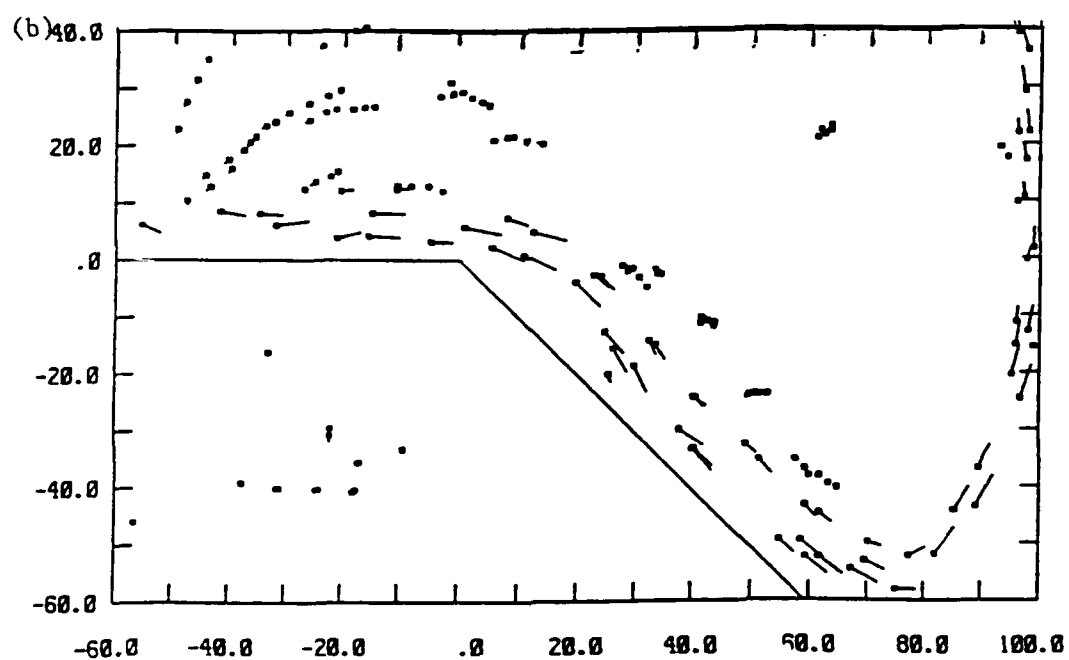
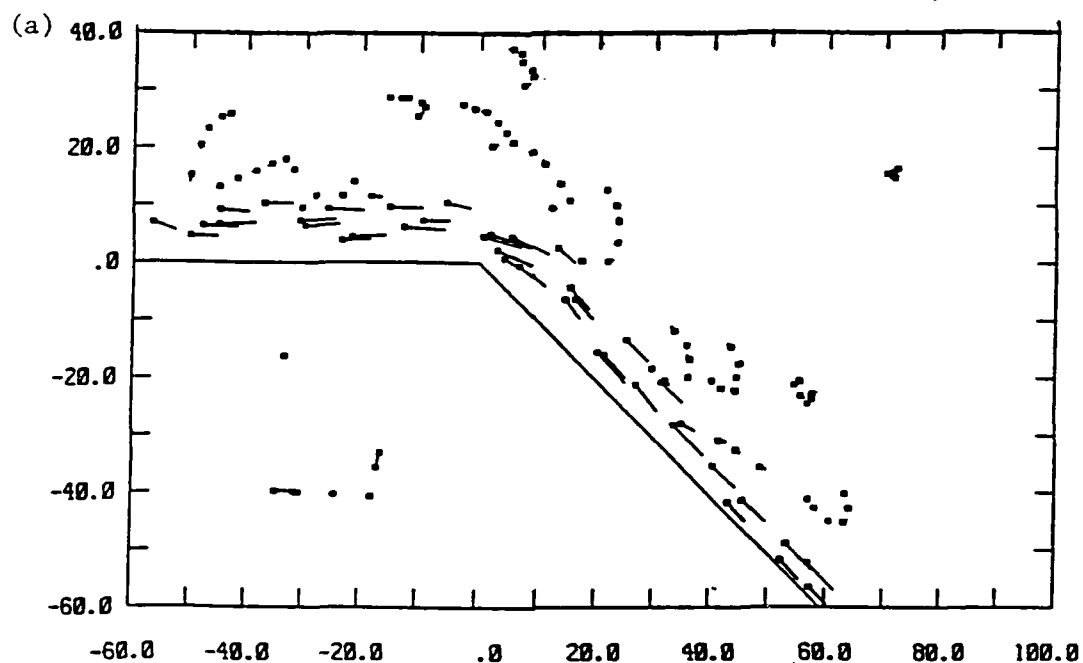
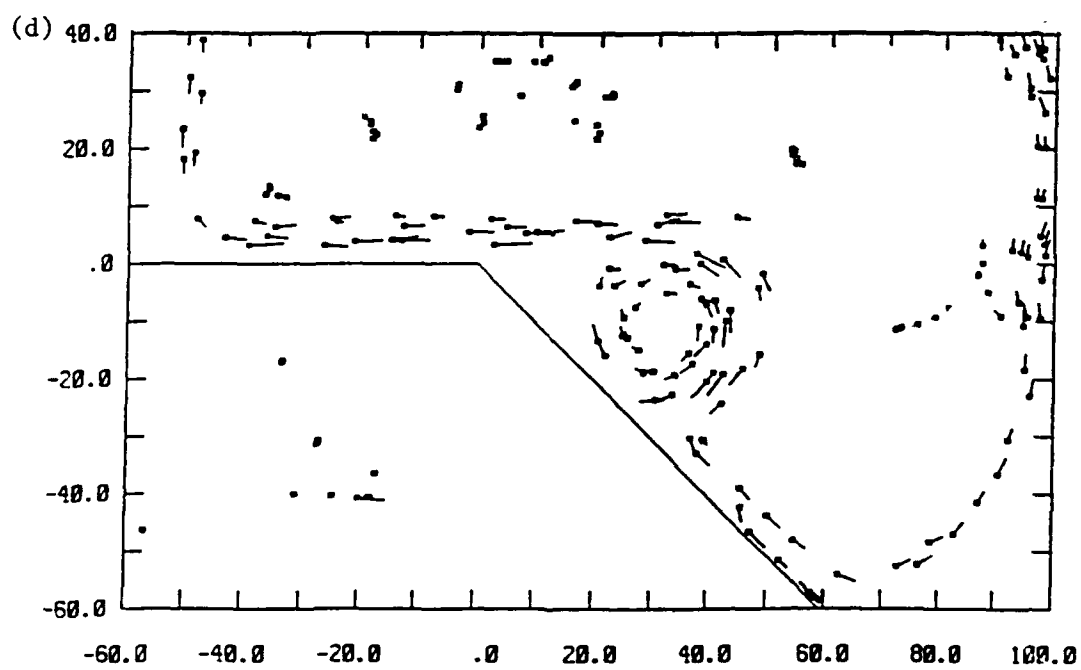
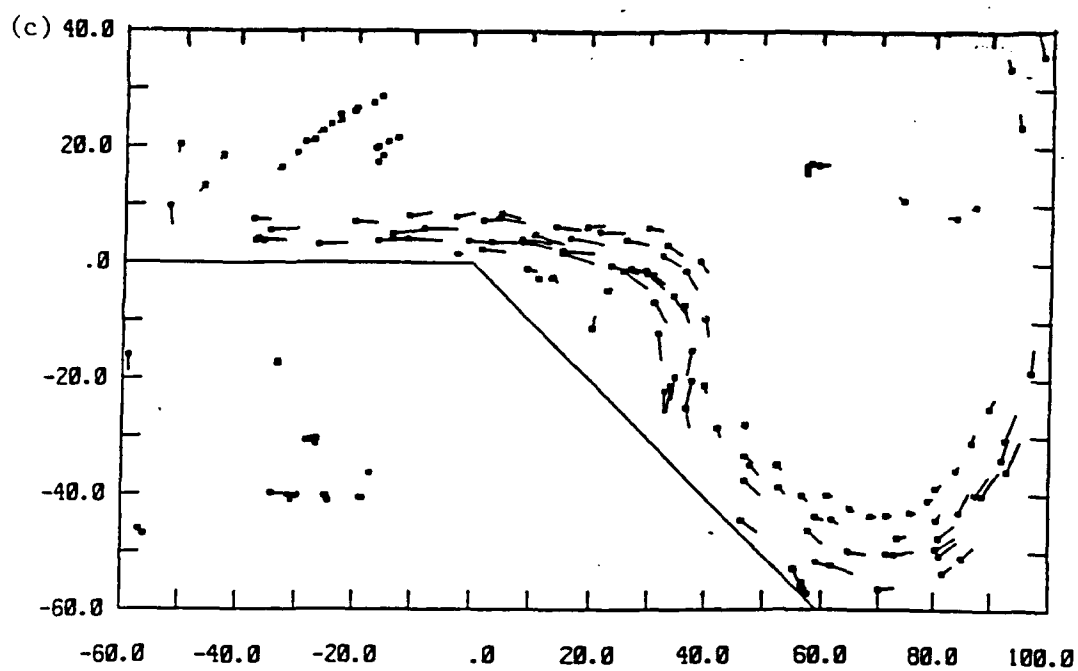


Figure 3.3.3: Velocity fields showing growth of eddy in short dam, deep lower layer run with  $45^\circ$  corner angle. Data from every fifth second in each time interval shown. (a) 5-30 sec after flow began. (b) 65-90 sec. (c) 125-150 sec. (d) 185-210 sec.



### Long Dam, Deep Lower Layer

The long dam experiments were the runs in which fresh water was initially contained along the whole length of the first and second walls so that the nose of the current would not interact with the corner. The purpose of this experiment was to see if the interaction of the nose with the corner was a necessary condition for eddy formation.

For a ninety degree corner angle, the long dam run behaved qualitatively the same as the short dam runs described above. Just downstream of the corner, an anticyclone formed, grew, and drifted away from the walls. Once it was away from the walls, another anticyclone formed. This too drifted away from the walls, and a third anticyclone formed, though by this time the current had circumnavigated the tank and was feeding itself at the upstream end of the first wall. The flow along the first wall was somewhat different than flow in the short dam runs. When the Plexiglass wall was removed, geostrophic adjustment caused the fresh water to immediately spread out from the channel width of 10 cm to a width of about 20 cm. This was seen not only in the dye pattern, but in the velocity field as traced by the paper pellets. Fresh water leaving the reservoir through the 9 cm wide gap tended to veer away to the left from the first wall, perhaps forming a cyclone along the first wall.

The 30° and 45° runs were repeated with the long dam forming a channel only 4 cm wide. When the dam was removed, geostrophic adjustment only spread the flow to a width of about 10 cm. Thus water leaving region A1 did not need to veer to the left, and flow along the first wall was parallel to the wall. The flows were the same as in the 30° and 45° short dam runs: no corner eddy at 30°, eddy at 45°. As in the 35° and 40° runs with the short dam, the run with no corner eddy had a disturbance at the end of the second wall which grew into a large anticyclone.

### Short Dam, Shallow Lower Layer

Runs with  $30^\circ$  and  $45^\circ$  angles were also repeated for a short dam and shallow lower layer. As in the other runs, a gyre formed at  $45^\circ$  but not at  $30^\circ$ . The gyre tended to drift downstream along the second wall. The streamlines along the second wall in the  $30^\circ$  degree run developed a single-crested wave which grew over 20 cm wider than the steady-state current and propagated downstream from about 40 cm downstream of the corner (Figure 3.3.4). When it reached the end of the wall, an anticyclone was visible between the wall and the crest.

In all the dam-break experiments that are described here, there was no unstable mode which produced a street of eddies either upstream or downstream of the corner. This is in contrast to the observations of Whitehead and Miller (1979), who reported strong instability in the channel when the width of the current was much smaller than the channel width. This may be because their arrangement was more favorable to baroclinic instability than mine, since their layer depths were equal while my top layer was relatively shallow. However, in the shallow lower layer runs, this asymmetry is not so strong. Another factor that may have destabilized Whitehead and Miller's flows was the large aspect ratio, which was about one in their unstable flows and less than  $1/2$  in my experiments. Flows with a high aspect ratio are susceptible to instability due to nonhydrostatic modes (Whitehead, 1990, personal communication).

### Flow With Wall to Left

The run in which the wall was on the left side of the current (looking in the flow direction) produced a coastal current on the order of a Rossby radius wide, and this generated an eddy just downstream of the right angle corner. As in the other experiments, the flow separated from the wall at the corner, flowed around a



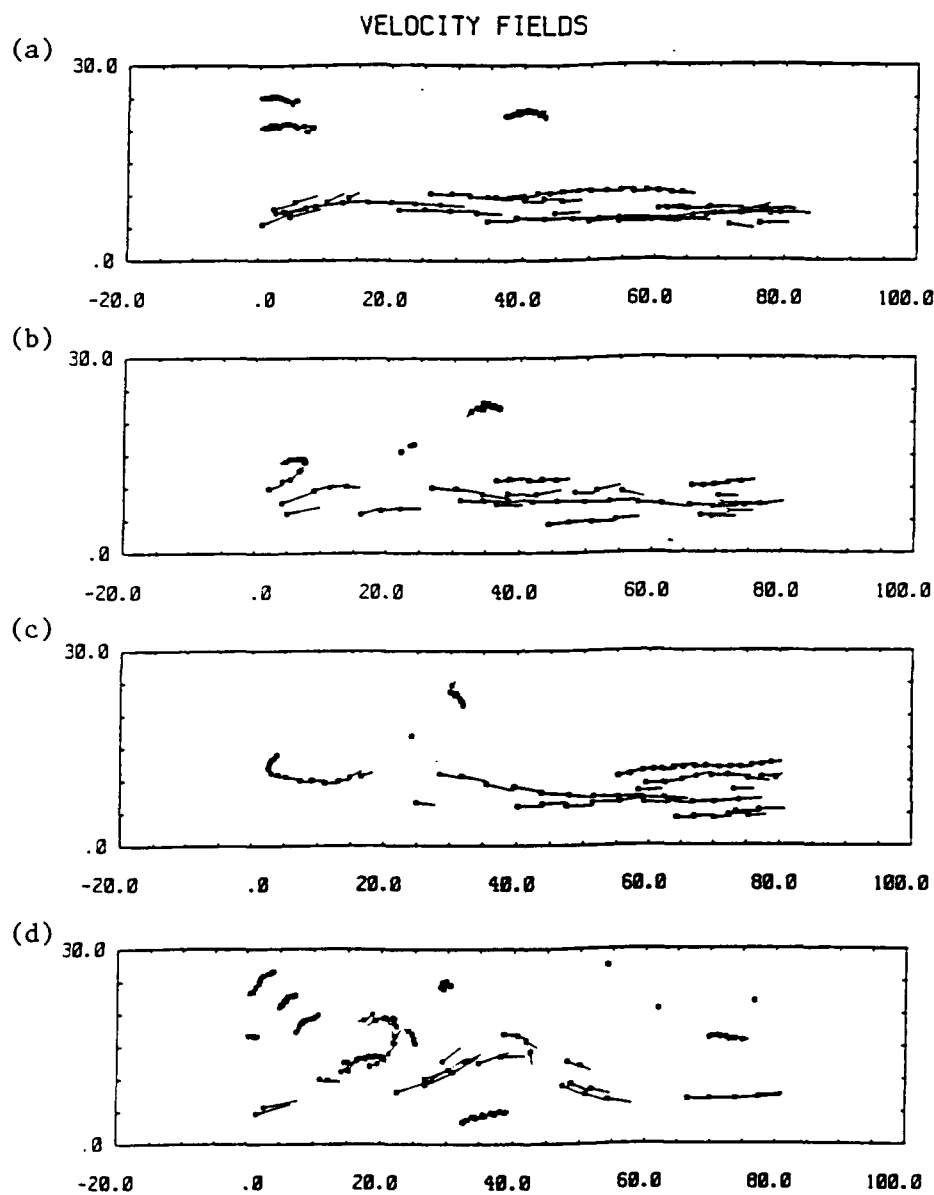
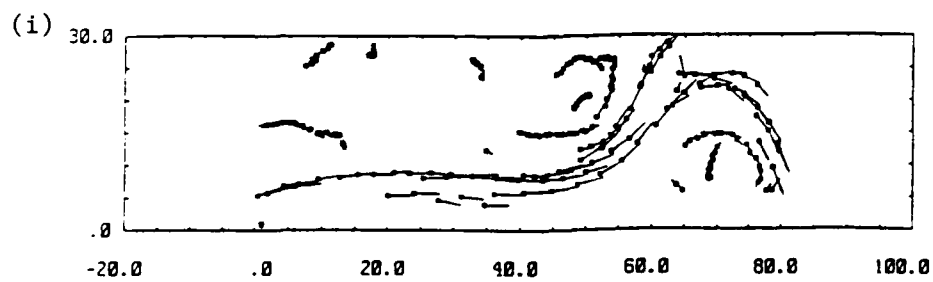
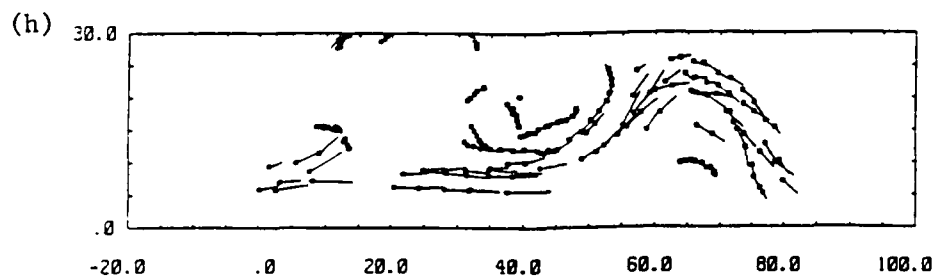
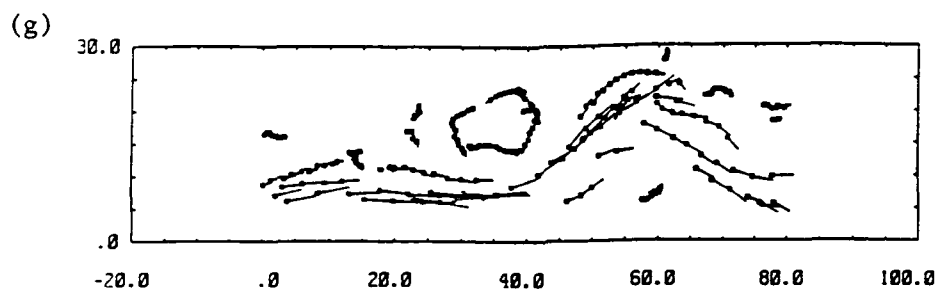
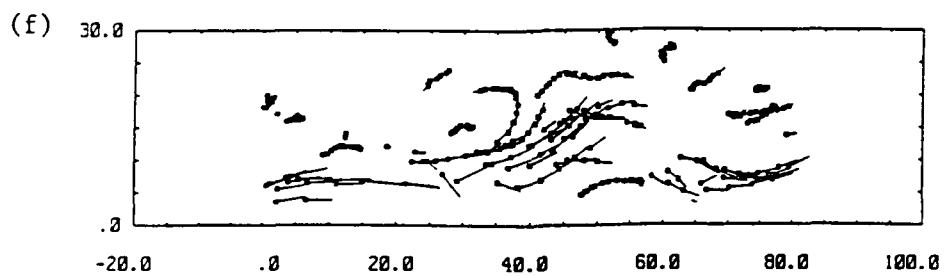
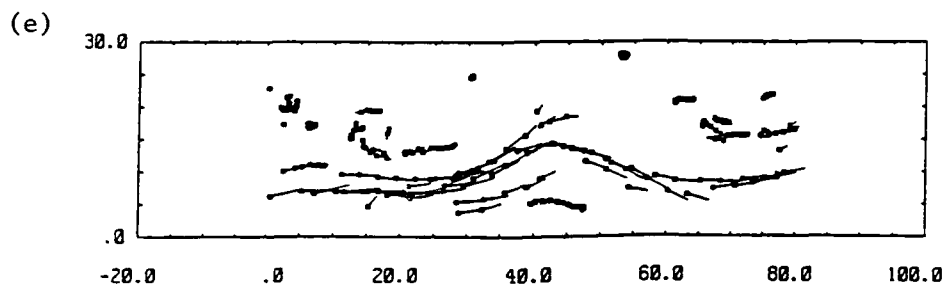


Figure 3.3.4: Velocity field along second wall for short dam, shallow lower layer run with  $30^\circ$  corner angle, in which solitary wave grows and propagates downstream. In each plot, vectors are shown for every second in a fifteen-second interval. (a) 46–60 sec after flow began. (b) 61–75 sec. (c) 76–90 sec. (d) 91–105 sec. (e) 106–120 sec. (f) 121–135 sec. (g) 136–150 sec. (h) 151–165 sec. (i) 166–180 sec.



gyre which grew with time, and re-attached to the wall downstream of the corner. Due to the opposite direction of flow relative to the wall, the gyre in this case was cyclonic rather than anticyclonic. An interesting difference between this run and the rest of the experiments was the behavior of the density interface just downstream of the corner. The dye looked noticeably lighter there than in the rest of the fresh layer, indicating that the interface was surfacing. This is reminiscent of the mechanism proposed by Røed (1980), which was applied to the case of a current with the wall on the left by Ou and de Ruijter (1986). However, it is most likely that the interface surfacing in the lab was a simple consequence of the cyclonic flow in the surface eddy, which causes the interface to rise as a consequence of geostrophy.

#### Pumped Flow, Sloping Bottom, Topography

Runs in which fresh water was pumped into ambient salty water produced an eddy for a sufficiently large corner angle as in the dam-break experiments. A  $90^\circ$  corner angle produced a similar eddy when the wall was sloped rather than vertical. The chief difference between the pumped-flow eddies and the dam-break eddies is that the former do not drift away from the coast. The pumped-flow gyre probably does not drift away because it is not accompanied by a lower layer cyclone, since the cyclones observed in the dam-break experiments were a consequence of lower layer flow around the corner. Therefore no heton-like structure was formed to allow the eddies to drift away from the coast.

In some runs, the original water in the tank consisted of a salty layer capped by a fresh layer. More fresh water was pumped into the top layer. The resulting flows were complicated by cyclonic eddies produced on the outer edge of the current. Some of the introduced fluid propagated away from the walls in the form of eddy dipoles, but some water rounded the corner and formed an anticyclonic gyre.

## Eddy Evolution and Motion

The evolution of the gyre, including its growth rate, is a key physical parameter defining the eddy. Propagation of the eddy away from the coast is an issue that is somewhat tangential to this study, but is interesting because it provides a mechanism for eddies generated near coasts to be found in the ocean's interior. Therefore, some simple measurements of the eddy evolution and motion were made.

The gyre completely separated from the coastal current and propagated away from the coast in the  $90^\circ$  corner angle runs in both the long dam and short dam case. When the corner angle was only  $45^\circ$ , however, the gyre did not drift away. Therefore there may be two critical angles which describe the current's interaction with a corner. The first critical value marks how large an angle must be in order to generate an eddy, and the second value marks a minimum angle for which the eddy can leave the coast. The eddy drift critical angle may be a function of the upper and lower layer depth ratio.

The separation of the anticyclone from the coast in the short dam experiments with a  $90^\circ$  corner angle was most clearly observed in the run with a gap width of 12.5 cm. There was a clear break in the dye field between the eddy and the coastal current, and subsequently all pellets in the coastal current flowed along the wall without being captured by the eddy (see Figure 3.3.1). According to dye measurements, this eddy was 36 to 40 cm in diameter, or about four times the width of the coastal current. The anticyclones in other runs were of a similar size. From 60 to 210 s after the gate was removed, the eddy's leading edge, as traced by the dark dye, moved away from the corner at .22-.37 cm/s, and it followed a linear path from the corner that made a  $31^\circ$  angle with the direction parallel to first wall. After this period the drift slowed to only .04 cm/s, perhaps due to interaction with the perimeter of the tank.

The anticyclone that formed at the corner was seen to be accompanied by a weak cyclone in most of the  $90^\circ$  runs and in the  $45^\circ$  runs with shallow lower layer and with the long dam. It probably also existed in the  $45^\circ$  run with a short dam and a deep lower layer, but was not seen due to gaps in coverage by surface drifters.

The eddy growth speeds for the  $45^\circ$  runs were estimated from the digitized trajectories of surface drifters. Several parameters, including the width and length of the region of closed streamlines marking the anticyclone, characterize the size of the eddy, but a particularly clear measure of eddy size in this data set is the excursion of streamlines from their upstream distance from the coast as they travel around the anticyclone downstream of the corner. Particle trajectories which began upstream of the corner and continued downstream of the corner were selected. Upstream of the corner, the distance of each trajectory from the first wall was measured, and downstream of the corner, the distance of the trajectory from the second wall was measured. Particle paths upstream of the corner were approximately parallel to the first wall. The streamline excursion was defined to be the difference between the average distance of a trajectory from the first wall and the maximum distance of the trajectory from the second wall. The distance from the corner, along the second wall, of this maximum was used as a measure of the length of the gyre (it is actually about half the length of the full gyre). These measures of gyre width and length are shown as a function of time in Figure 3.3.5. The time at which such a measurement occurs is actually spread over several seconds, but the measurement was assigned to the time at which the particle was furthest from the second wall. This is the most reasonable time choice because the maximum excursion is the most time-dependent parameter of the flow.

Gyre growth was calculated for the short dam/deep lower layer run, the long dam/deep lower layer run, and the short dam/shallow lower layer run. In all three, the gyre width and length grew linearly with time. Therefore the parameter that

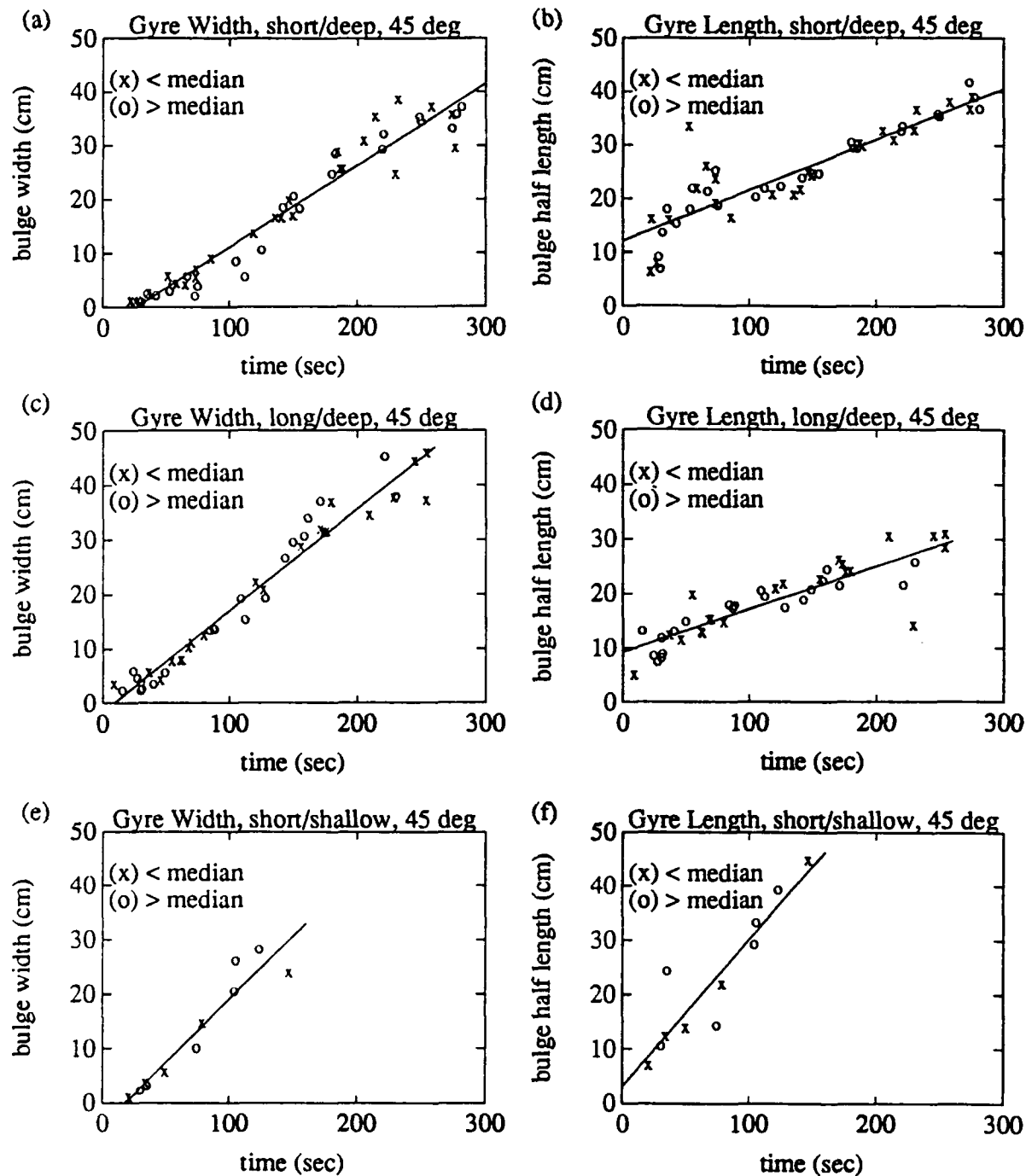


Figure 3.3.5: Width and half length of eddy as a function of time (flow began at  $t = 0$ ), for runs with corner angle of  $45^\circ$ . "x" indicates trajectory whose upstream distance from the wall is less than the median for the data set, and "o" indicates trajectory with upstream distance greater than the median. (a) Width, short dam/deep lower layer run. (b) Half length, short dam/deep lower layer run. (c) Width, long dam/deep lower layer run. (d) Half length, long dam/deep lower layer run. (e) Width, short dam/shallow lower layer run. (f) Half length, short dam/shallow lower layer run.

characterizes the growth is not an exponential growth rate (which would have units of 1/s), but a growth speed (cm/s). In the short dam/shallow lower layer run, the gyre slowly drifted away from the corner along the wall, and this drift was included in the length growth speed. There was a possibility that different streamlines would undergo different excursions downstream of the corner, for instance if a water parcel slowed down and spread out as it passed around the gyre. In Figure 3.3.5, different symbols were used for streamlines with distances from the first wall of less than the median value of all trajectories in the data set and for those further than the median. These show that there was no trend in excursion distance with upstream streamline position. For each run, a least squares fit to a straight line was performed for all the length and width data. The estimated variance in the measurements, based on the sum of squares of differences between the data and the linear fit, was 3 cm for the width and 3 to 5 cm for the length. This is larger than the estimated uncertainty in the measurements, which should be less than .5 cm/s (see next section), but this large variance does not invalidate the least squares fit. It merely shows that the approximately laminar flow of these experiments is perturbed by turbulence which produces the observed jitter in the particle trajectories.

The slope of the line fitting the data for each of the three runs is shown in the first column of Table 3.3.1. Since different runs have somewhat different values of reduced gravity and upper layer depth, it is more appropriate to compare the non-dimensional growth speed, which is scaled by the upper layer gravity wave speed,  $c = \sqrt{g'h}$ , where  $h$  is upper layer depth and  $g'$  is reduced gravity. Since this expression for gravity wave speed is strictly true only for an infinitely deep lower layer, an even better scale factor may be the two-layer wave speed,  $c_2 = \sqrt{g'hh_2/(h+h_2)} = \sqrt{g'h/(1+\delta)}$ , where  $h_2$  is the lower layer depth and  $\delta = h/h_2$ . Both expressions are tabulated in Table 3.3.1. When scaled with either of these two quantities, the growth speeds for both width and half length are about the same for the two runs with a deep lower layer, and considerably faster for the shallow lower layer run. The shallow lower layer

Table 3.3.1. Eddy Growth Speeds for 45° Runs

run	speed	c	speed/c	$\delta$	speed/c <sub>2</sub>
Width					
short/deep	.152±.005	8.4±.5	.018±.001	.14±.02	.019±.001
long/deep	.187±.006	9.2±.6	.020±.001	.14±.02	.021±.001
short/shallow	.233±.029	7.3±.4	.032±.004	.64±.08	.041±.005
Half Length					
short/deep	.095±.007	8.4±.5	.011±.001	.14±.02	.012±.001
long/deep	.078±.007	9.2±.6	.008±.001	.14±.02	.009±.001
short/shallow	.270±.046	7.3±.4	.037±.007	.64±.08	.047±.009

"Speed" is the raw growth speed of the width or half length of the eddy,  $c$  is the gravity wave speed for the upper layer,  $\delta$  is the ratio of upper layer to lower layer thicknesses, and  $c_2$  is the gravity wave speed for the two layer system. All units cgs.

run width grows about 60% faster than the other runs when scaled by the reduced gravity wave speed and grows twice as fast as the others when scaled by the two-layer wave speed. The shallow lower layer run half length grows by an even greater factor of about four or five times faster for scaling by reduced gravity or two-layer wave speed. All growth speeds are a factor of about 20 to 70 smaller than the maximum particle speeds in the current.

### 3.4. Interpolation of Fresh Water Velocity Fields

I estimated velocity profiles across the current at several positions upstream and downstream of the corner. From this data, I calculated rough estimates of cross-stream profiles of upper layer depth and potential vorticity, as well as estimates of volume flux and entrainment.



The raw surface velocity field from float tracks or streaks is highly irregular in space and time. In order to compute cross-shore profiles of velocity, a linear smoothing and interpolation scheme was used. The velocity field along each wall was interpolated to a regular grid by taking a weighted average of all nearby velocity vectors, with closer vectors having greater weight:

$$(u, v) = \frac{\sum \exp(-(\delta_x/L_x)^2 - (\delta_y/L_y)^2)(u_j, v_j)}{\sum \exp(-(\delta_x/L_x)^2 - (\delta_y/L_y)^2)},$$

where  $(u_j, v_j)$  are the data velocity vectors (downstream and cross stream components),  $(u, v)$  is an interpolated velocity,  $\delta_x$  and  $\delta_y$  are the distances between the grid position and the  $j^{\text{th}}$  data position (alongshore and cross-shore components), and  $L_x$  and  $L_y$  are length scales of the weighting function. The summations are over  $j$ .

The error in the velocity measurements depends on the windage on the drifters, the fact that the drifters are solid and are lighter than the surrounding fluid, and surface tension effects on the drifters (especially interactions between the drifter and either another drifter or a wall). Previous laboratory experience indicates that the rms variation from all these errors is not much less than .1 cm/s and probably not greater than about .4 cm/s. In a series of spin-up experiments in a smaller circular tank, velocities derived from surface pellet trajectories showed departures from the expected velocity field with an rms average on the order of .1 cm/s. We assume that the velocities of the surface drifters represent the depth-independent velocity of a layer of homogeneous density, but in reality there are small vertical variations in density due to temperature gradients and large variations from interfacial mixing, while the surface velocity includes the wind-induced Ekman velocity which is confined to the top millimeter of the surface. The wind-induced velocity is small compared to the speed of the density current. The velocity at the top of a shear layer can be thought of as the maximum velocity in a region of vertical shear, or as a scale velocity for an idealized homogeneous layer that would display similar behavior to the actual pycnocline.

In addition to the errors in the layer velocity as measured by the pellet velocity, there are also errors associated with interpolating from the pellets to grid points. If all the velocity measurements used to calculate velocity at some grid point made up a set of independent measurements of the same quantity, a simple propagation of errors formula could be applied to find the error of the grid point velocity. In reality, spatial variations in the velocity field cause the expectation value of the error at the grid point to be smaller for pellet positions that are closer to the grid point location. In Appendix 2, I describe a crude method for using a measure of how many data points are close to a grid point to determine the error at the grid point.

### Short/Deep Velocities

Velocities were interpolated to rectangular grids that were parallel to the first and second walls. Velocity data was binned into consecutive thirty second intervals to make six to eight maps for each run along each wall. The alongshore and cross-shore weighting length scales ( $L_x, L_y$ ) were (4 cm, 1 cm). The alongshore scale was on the order of the distance traversed by a pellet in the time interval used to measure its velocity, while the cross-shore scale was on the order of a pellet diameter.

I attempted to determine whether the current speed should be scaled by the reduced gravity wave speed for the upper layer,  $c = \sqrt{g'h}$  or the two-layer wave speed  $c_2 = \sqrt{g'h/(1 + \delta)}$ , based on upper layer thickness  $h$  and ratio between upper and lower layer thicknesses  $\delta$ . The maximum alongshore speed was recorded for each cross-shore profile along the first wall in the short dam runs for corner angles of  $15^\circ$  to  $45^\circ$ . Selected values scaled by both the upper layer wave speed and the two-layer wave speed are displayed in Table 3.4.1. The non-dimensional maximum speed of the current is on the order of .5 to .8 of the gravity wave speed, depending on the time and position of the maximum speed. The ratio of the non-dimensionalized speeds for the deep lower layer run and the shallow lower layer run should be unity

**Table 3.4.1. Cross-Stream Maximum Speeds**

Cross-Stream Maximum Speed Scaled  
by Upper Layer Gravity Wave Speed

t\ x	<u>deep</u>		<u>shallow</u>	
	-45	-5	-45	-5
t1	.77	.68	.67	.50
t2	.67	.52	.62	.44

Cross-Stream Maximum Speed Scaled  
by Two Layer Gravity Wave Speed

t\ x	<u>deep</u>		<u>shallow</u>	
	-45	-5	-45	-5
t1	.82	.73	.87	.65
t2	.71	.55	.81	.56

Values based on maximum alongstream speed at profiles at -45 cm and -5 cm upstream of corner. Deep run data is averaged from short dam runs with 15°, 30°, 35°, 40° (deep lower layer), and 45° corner angle. Shallow run data is averaged from short dam runs with 30° and 45° corner angle (shallow lower layer). t1 is period 31 to 60 sec after flow began and t2 is period 181 to 210 sec after flow began.

if the correct scale factor is used. This ratio was calculated for the maximum speeds measured at profiles at 5, 15, 25, 35, and 45 cm upstream of the corner at six different 30 sec intervals. Due to noise in the measurements, there was quite a bit of variation in this ratio. For speeds scaled by the upper layer wave speed, the ratio ranged from .8 to 1.7, with an average of 1.1 and a sample standard deviation of .1. Using the two-layer wave speed, the ratio ranged from .7 to 1.4, with an average of .9 and a standard deviation of .1. Since both scales yield a ratio just about a standard deviation away from unity, it is impossible to say which, if either, quantity provides the correct velocity scale. Both are possible based on the observations.

The reproducibility of the upstream flow in the short dam, deep lower layer runs is indicated in Figure 3.4.1, which shows the average and standard deviation velocities along the first wall in two time intervals. A similar plot (Figure 3.4.2) is shown for velocities along the second wall for the short dam, deep lower layer runs which did not produce eddies at the corner. An ideal current of uniform potential vorticity that is bounded by a surface front would have velocity increasing monotonically with distance from the coast; the laboratory currents are slower on the outer edge due to mixing. Taking the average over the whole flow field of the ratio of velocity standard deviation to velocity average for each point in the flow field, we obtain a measure of the reproducibility of the flow. Both upstream and downstream of the corner, the average value of this ratio is around .2 to .3 for data taken during various time intervals after flow began. The ratio is about 10-20% smaller upstream of the corner than downstream. This figure is somewhat misleading, however, because the run-to-run variations upstream of the corner are heavily weighted by large fractional variations at the outer edge of the current, where the velocity is small so the noise is relatively large. Therefore it is fruitful to look more closely at disaggregated subsets of the data.

Downstream of the corner, there is a tendency for the flow to be slower near the wall for larger corner angles. To get a clearer measure of this variation, I plotted maximum speed and speed at the wall as a function of corner angle for various cross-shore sections. As Figure 3.4.3 shows, the cross-shore maxima of flow speed parallel to the second wall were always around 5 cm/s and had no strong trend with angle. Five centimeters downstream of the corner, the velocity near the wall is almost as great and relatively independent of angle. Further downstream (15, 25, 35 and 45 cm) the wall speed is fairly flat in the first minute after the flow reached the corner, but a clear trend is visible in most of the plots of wall velocity versus angle for the next two minutes.

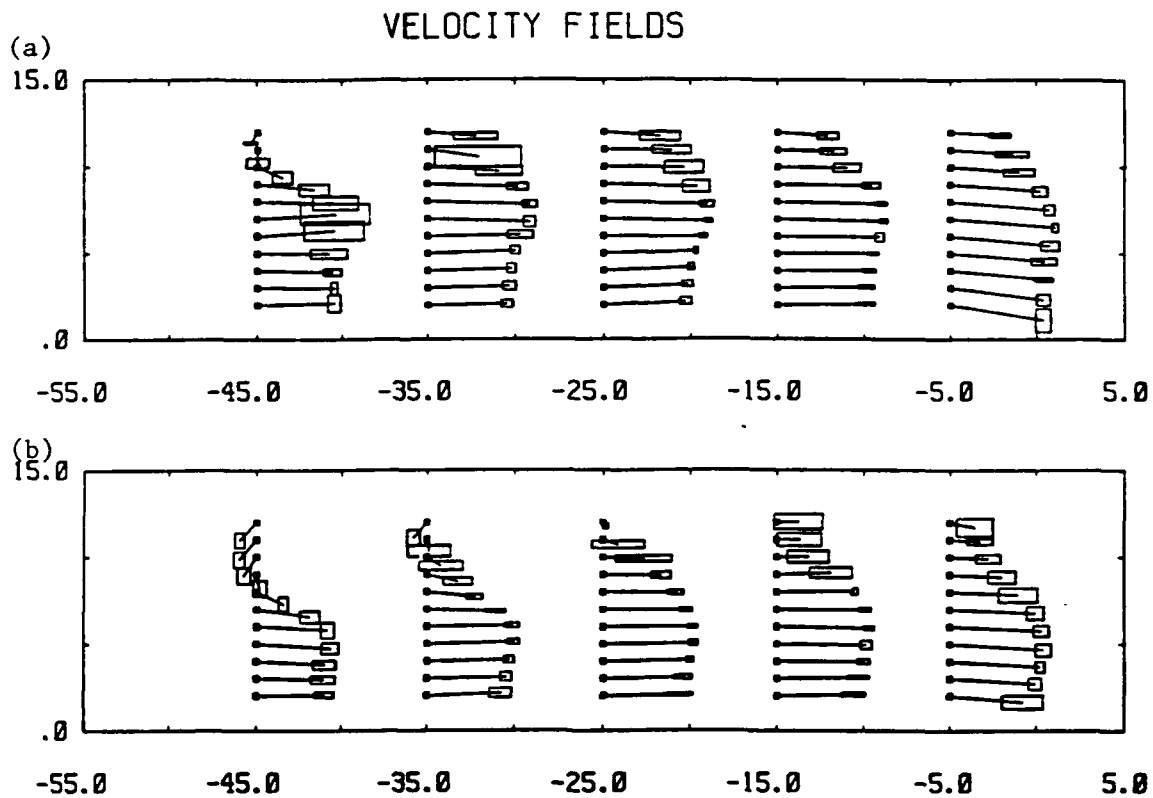


Figure 3.4.1: Interpolated velocity fields upstream of corner for runs with short dam and deep lower layer. Vectors show velocity averaged over the runs ( $15^\circ$ ,  $30^\circ$ ,  $35^\circ$ ,  $40^\circ$ , and  $45^\circ$  corner angle), and rectangles at heads of vectors show standard deviations. (a) 31-60 sec after flow began. (b) 121-150 sec.

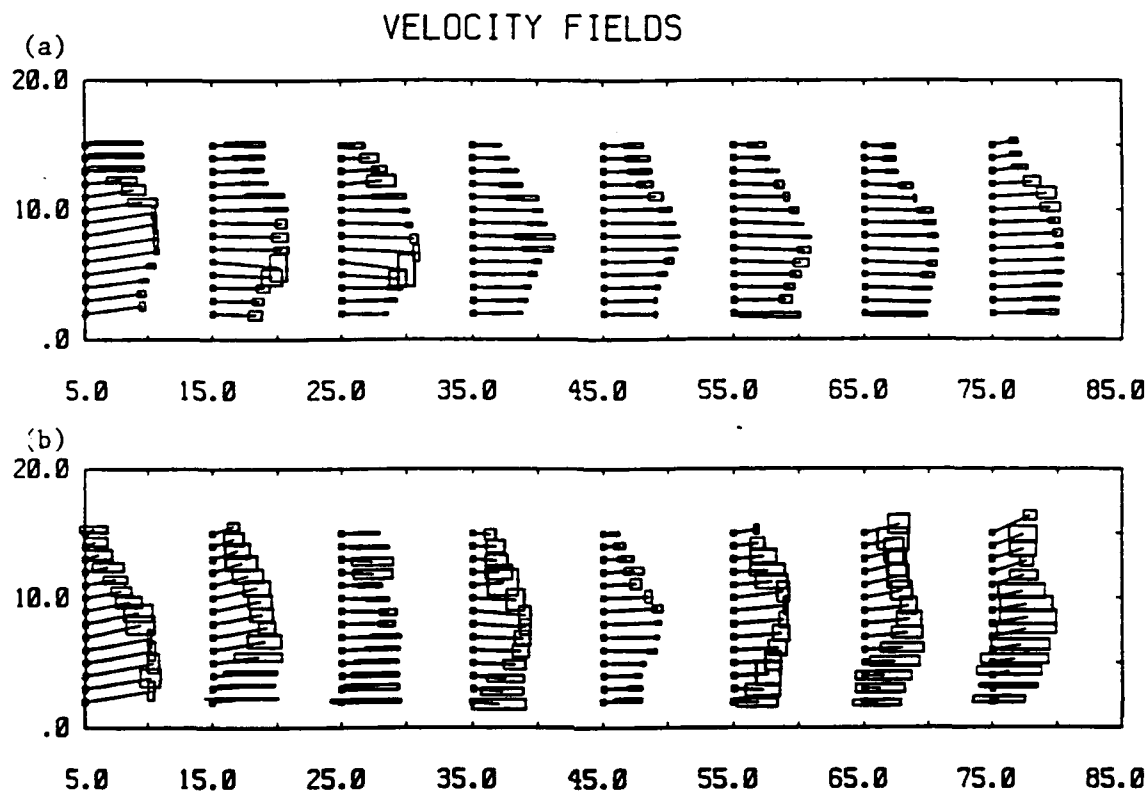


Figure 3.4.2: Interpolated velocity fields downstream of the corner for runs with short dam and deep lower layer. Vectors show velocity averaged over runs in which no eddy formed ( $15^\circ$ ,  $30^\circ$ ,  $35^\circ$ , and  $40^\circ$  corner angle) and rectangles show standard deviations. (a) 61-90 sec after flow began. (b) 151-180 sec.

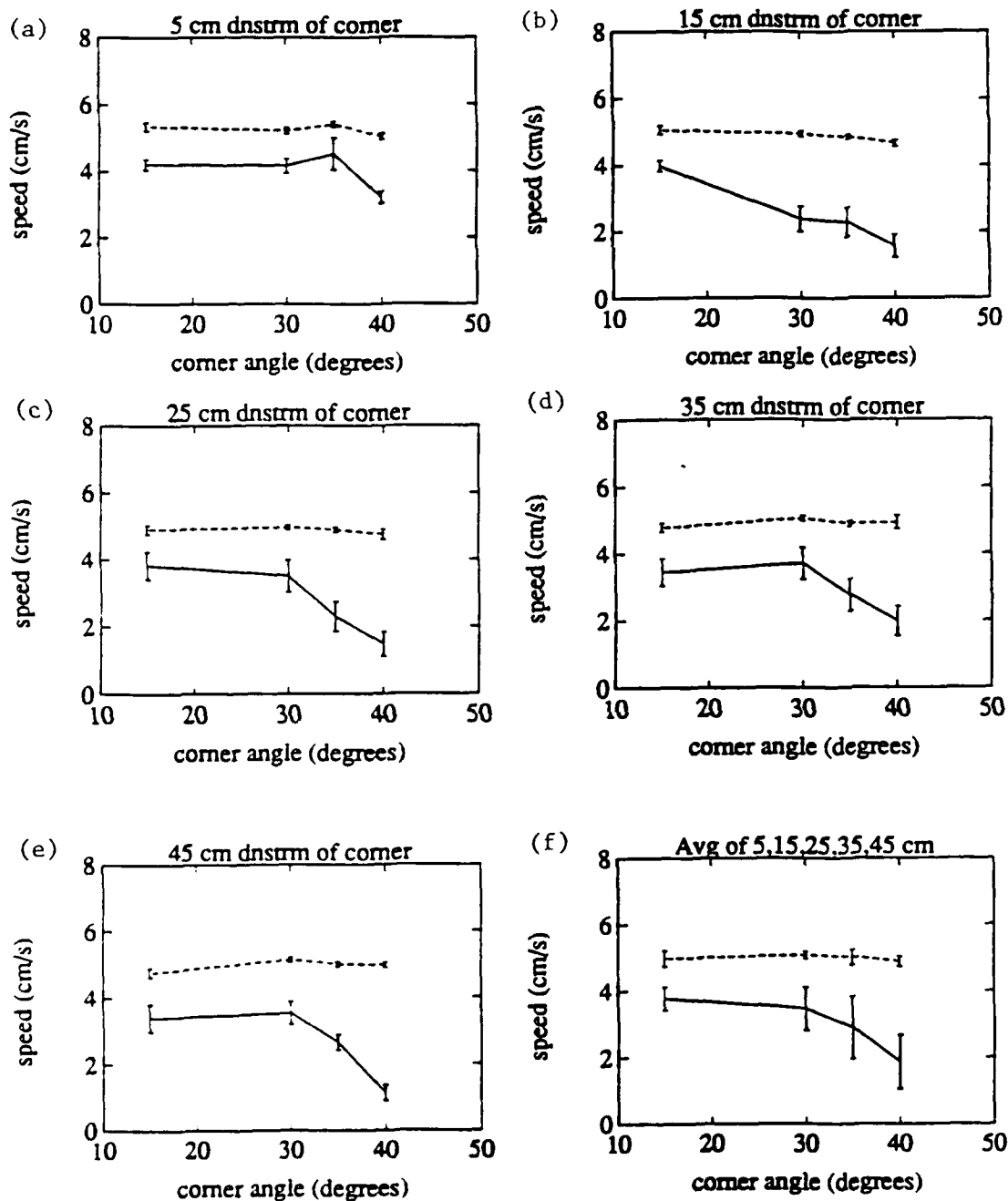


Figure 3.4.3: Maximum speed (dashed line) and speed near the wall (solid line) as a function of corner angle for sections downstream of the corner in short dam, deep lower layer runs in which no eddy formed ( $15^\circ$ ,  $30^\circ$ ,  $35^\circ$ , and  $40^\circ$  corner angle). Speeds are taken from interpolated velocity maps in time interval 91–150 sec after flow began. Error bars denote estimated errors except in (f), where they denote standard deviations. (a) 5 cm downstream of corner, (b) 15 cm, (c) 25 cm, (d) 35 cm, (e) 45 cm, (f) average of 5 to 45 cm.

These results are intriguing, because the trend is probably linked to the gyre formation process. For a large enough angle, the speed actually becomes negative at the wall and an anticyclone forms. Decreasing wall speeds for increasing angles of less than this critical angle may be a sign of the system moving towards eddy formation as the angle increases. It is also an interesting asymmetry between the flow upstream and downstream of the angle. Similar plots for velocity along the upstream wall (Figure 3.4.4) show relatively flat curves, though with large components of noise.

### Top Layer Depth

A naive estimate of the depth of the fresh-salt interface upstream of the corner was made from the velocity measurements. This calculation assumed geostrophy, no mixing, uniform density within each of two layers, and no motion in the lower layer. The depth is obtained by integrating the geostrophic relation for the velocity component parallel to the wall:

$$fu = -g' \frac{dh}{dy} ,$$

using the boundary condition that  $h = 0$  at  $y = 15$  cm (the wall is at  $y = 0$ ). Using the same assumptions, the volume flux as a function of the layer thickness at the wall is  $Q = \frac{1}{2}(g'/f)H^2$ .

The dam break produced a counterflow underneath the fresh layer current. Since the interface slope is proportional to the vertical difference in velocities, and since the lower layer has flow in the reverse direction to the upper, ignoring the lower layer flow would cause us to underestimate the depth of the interface. In all the deep lower layer runs, this lower layer flow should only be about one eighth the upper layer flow, since that is the ratio of the two depths.

For the dam break runs, contours of depth near the wall as a function of position along the first wall (horizontal coordinate) and time (vertical coordinate) are



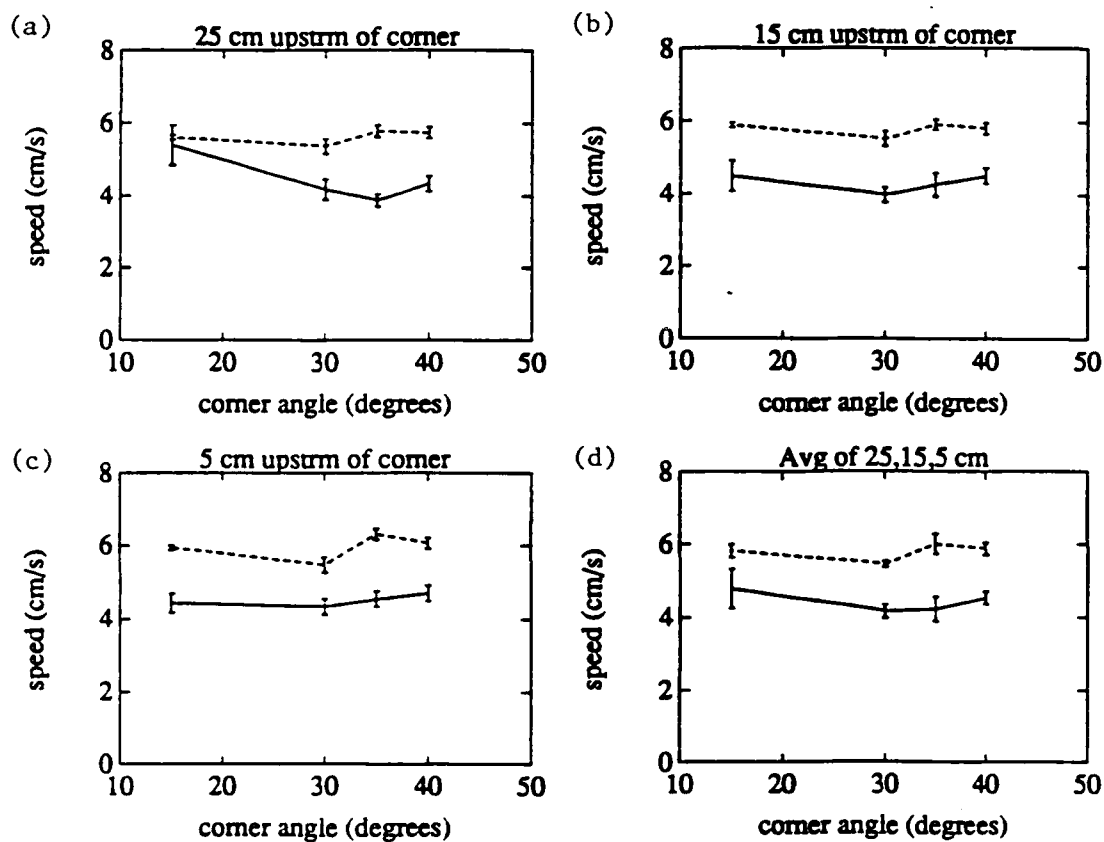


Figure 3.4.4: Maximum speed (dotted line) and speed near the wall (solid line) as a function of corner angle for sections upstream of the corner in short dam, deep lower layer runs in which no eddy formed ( $15^\circ$ ,  $30^\circ$ ,  $35^\circ$ , and  $40^\circ$  corner angle). Speeds are taken from interpolated velocity maps in time interval 61–120 sec after flow began. Error bars denote estimated errors except in (d), where they denote standard deviations. (a) 25 cm upstream of corner, (b) 15 cm, (c) 5 cm, (d) average of 25 to 5 cm from corner.

shown in Figure 3.4.5. The data is fairly noisy, but it tends to confirm the expectation that depth increased downstream due to mixing and decreased with time as the system ran down. Mixing increased the calculated interface depth and volume flux in two ways. There was an actual increase in volume flux as entrained water was added to the flow, while there was an apparent increase in volume flux because the nominal value of  $g'$  overestimated its actual value downstream, where it decreased. From 45 cm upstream of the corner to 25 cm upstream of the corner, transport increased 10–190% in various runs, with most increases in the 60–100% range. From 25 cm to 5 cm upstream of the corner, transport increased by 0–20%. Thus near the gap from which the fresh water flowed, volume fluxes into the top layer due to entrainment were substantial compared to the transport of the current, though within a few current widths of the corner the entrainment is small.

### 3.5. Summary and Discussion

A series of experiments were performed in which currents were generated by a dam-break between a homogeneous salty region of the rotating tank and a region capped with a fresh surface layer. The current flowed along a pair of straight walls which were joined at a convex corner, the angle of which was varied from run to run in order to find a critical angle, if one existed, for gyre formation. In the first runs, the lower layer depth was initially eight times greater than the upper layer thickness, and the fresh intrusion began when a short dam upstream of the corner was removed. In these short dam, deep lower layer (“short/deep”) runs, no gyre was formed at the corner for a corner angle of  $40^\circ$  or less. At  $45^\circ$ , an anticyclonic gyre grew while staying near the corner. At  $90^\circ$ , an anticyclone formed immediately and tended to drift away from the wall into the interior of the basin. When this happened, a second and sometimes a third gyre grew from the corner to take the place of its predecessor. In all cases in which a gyre was formed, the current flowed around the

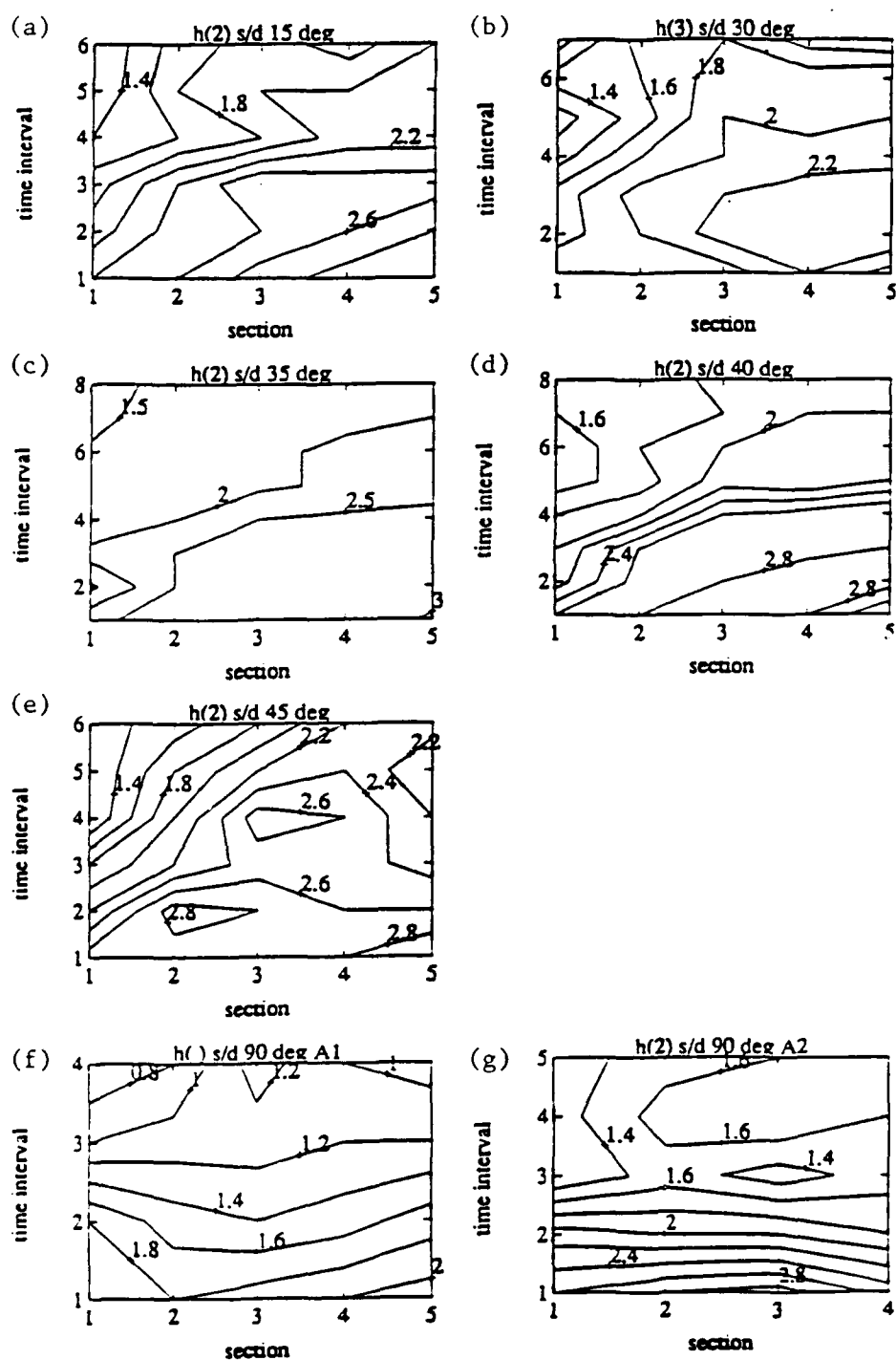


Figure 3.4.5: Contours of depth near the wall as a function of distance along the first wall (horizontal axis) and time (vertical axis), for short/deep runs. Sections are 45, 35, 25, 15 and 5 cm upstream of corner. Time intervals are 6–30 sec, 31–60 sec, etc., after flow began. (a)  $15^\circ$  angle, measured 2 cm from wall. (b)  $30^\circ$ , 3 cm. (c)  $35^\circ$ , 2 cm. (d)  $40^\circ$ , 2 cm. (e)  $45^\circ$ , 2 cm. (f)  $90^\circ$  (12.5 cm gap), various distances close to the wall. (g)  $90^\circ$  (20 cm gap), 2 cm.

gyre, re-attached to the wall downstream of the corner, flowed along the wall to where the wall intersected the rim of the tank, and continued around the rim.

The velocity profile of the current upstream of the corner was roughly the same from run to run, showing no trend with corner angle. Downstream of the corner, the velocity profile showed interesting changes as the critical angle for eddy formation was approached from below. There was little change with corner angle in the cross-shore maximum in the speed of the current, but the velocity near the wall decreased as the corner angle increased. This is a hint that eddy formation should be conceptualized as the limit in which the speed at the wall is not only lowered but is actually reversed.

Experiments with a relatively shallow lower layer showed eddy generation characteristics that were similar to the deep lower layer runs. The critical angle for gyre formation was between  $30^\circ$  and  $45^\circ$ , which is consistent with the results of the "deep" runs. However, the eddy in the "shallow" run grew significantly faster than the "deep" run gyres, and tended to propagate away from the corner along the wall. The shallow lower layer run for which no gyre appeared at the corner also produced a solitary disturbance in the streamlines several current widths downstream of the corner. This wave propagated downstream while growing into an anticyclone similar to the corner eddies.

"Long dam" experiments, in which the leading edge or nose of the current was initiated downstream of the corner so that the two did not interact, demonstrated the same behavior as the short dam experiments. When the corner angle was  $30^\circ$ , no gyre was formed; when the angle was  $45^\circ$  a gyre grew downstream of the corner; at a  $90^\circ$  angle a gyre grew and drifted away from the wall. Before the long dam experiments were conducted, there was evidence both for and against the hypothesis that the gyres were not caused by dynamics specific to the nose of the current. The claim that the interaction of the nose with the corner is not a key factor in producing

the anticyclones was supported by the fact that a second eddy formed when the first eddy drifted away in the  $90^\circ$  run. However, it was possible that the eddies would not have formed if the current had not already been deformed by the first eddy. On the other hand, it was obvious in the  $90^\circ$  angle runs, at least, that the current initially overshot the corner, turned sharply around, and immediately bifurcated into a gyre and a boundary current along the second wall, so that the nose appeared to be responsible for the initiation of the first gyre. The long dam experiments showed that the nose is not crucial to the genesis of a corner eddy. This is in contrast to separation of a barotropic current from a wall, which Stern and Whitehead (1990) modeled with a time-dependent model of the nose of the current.

If the baroclinic eddy were generated by the leading edge of the current as in the barotropic case, the dynamics of anticyclone genesis would be complicated by the short alongshore length scale at the nose of the current, where the current is perpendicular to the isobars. Perhaps more importantly, a mechanism that will produce eddies from either a steady current or an intrusion will have wider oceanographic application than one that needs specialized initial conditions. It is possible that the initiation of the current in both the long and short dam runs is somehow responsible for forming or not forming anticyclones. However, since the behavior of the flow looks so similar for such different initial conditions, it is likely that time-independent features are more important, and we should be able to explain gyre formation in terms of whether non-separating, steady flow around the corner is possible for various angles.

What is the essential dynamics of the eddy generation? One possible cause is that as water rounds a corner, the centrifugal force due to the curvature of streamlines makes the water unable to conserve volume flux, potential vorticity, and energy while remaining attached to the wall, and so separation ensues. This phenomenon was reproduced in Chapter 2 with a simple model which was only applicable to gently curving coastlines. This hydraulic model produced a separation due to upwelling of

the density interface which was consistent with some of Bormans and Garrett's (1989) experimental results for a curved corner but not consistent with others. As described in Chapter 1, some numerical models (Chao and Boicourt, 1986 and Kubokawa, 1991) and laboratory experiments (Kawasaki and Sugimoto, 1984) have indicated that gyre formation at a sharp right angle corner may be inhibited by the upstream properties of the flow, such as the Rossby number or the potential vorticity distribution. My experiments show that even a current which has an upstream flow profile that could potentially form an eddy, and which satisfies Bormans and Garrett's curvature criterion, will depend on a further geometrical parameter for eddy generation, namely the angle of the corner. These results point out the limits of hydraulic theory, though they leave open the possibility that if we were to solve the short wave (and mathematically more difficult) analogue of the hydraulic approximation, separation would occur at a sharp corner for large enough angle and Rossby number. The experiments showed that the flow near the wall downstream of the corner decreased as the separation angle was approached from below. *This is strong evidence that the most important effect of the corner is to slow down the flow rather than pull up the interface.* This effect could result because frictionally-induced cross-stream variations in the potential vorticity of the current produces different behavior than that exhibited by the uniform vorticity currents in Chapter 2, or because the viscous boundary layer widens downstream of the corner.

If the eddy generation is caused by viscous boundary layer separation, we might expect the effect of varying either coastline radius of curvature (for a given large corner angle) or corner angle (for a given infinitesimal radius of curvature) to be quite similar. Increasing the perturbation in the coastline shape in either case would increase the alongstream velocity gradients close to the wall, which would increase the adverse pressure gradient downstream of the corner and make the current more prone to separate. Nonrotating flow tends to separate from sharp corners even if the angle is moderately small (as in the  $30^\circ$  runs in the laboratory experiments),

but the Ekman friction effect described by Merkin and Solan (1979) could inhibit separation. If a steady state, inviscid process were responsible for the separation, the curvature and angle could influence the flow in different ways. One possibility is that the curvature determines whether there is separation, while the angle determines whether the current reattaches to the wall in such a way that all the water flows away from the corner (no gyre formed) or some water returns (gyre formed). Whitehead (1985) argued that any steady current impinging on a wall must bifurcate at the wall, but his discussion was based on the assumption of parallel flow towards the wall at infinity. Any current reattaching to the wall in the lab would not satisfy this assumption. The fact that not even a small degree of separation is visible when the corner angle approaches the critical (separation) value from below makes this picture of the behavior at the corner less attractive.

Another possibility is that the corner eddy is a soliton-like instability which is being stimulated in the inviscid time-dependent equations of motion by fluid rounding the corner. Similarly, while the long-dam experiments showed that very different initial conditions can produce the same behavior, it is possible that almost any initial condition, by virtue of not being an exact steady-state solution to the equations of motion, would produce a growing disturbance even if there exists a time-independent state which does not separate at the corner. Kubokawa (1991) explained the generation of eddies from a current flowing out of a channel in terms of a quasigeostrophic model in which waves on a potential vorticity front were responsible for the anticyclone, but in his model the eddy formation was dependent on the asymmetry between the upstream condition (flow confined to a channel) and the downstream condition (no outer wall). In order for a disturbance to be trapped at the corner in the coastal flows studied in this thesis, the wave speed would have to be negative (propagation opposite to the flow direction), or at least very small, downstream of the corner as well as positive upstream of the corner.

The possible importance of a wave-like cause is hinted at by other waves seen along the second wall. In the run with a shallow lower layer and a 30° corner angle, the solitary instability that propagated downstream away from the corner developed an anticyclone similar to the corner eddies. The corner eddy that grew in the 45° shallow lower layer run also slowly drifted downstream. In contrast, the corner eddies for the deep lower layer runs do not drift downstream. However, the wave behavior is different for different layer-thickness ratios, but the eddy behavior at the corner is qualitatively similar.

The fact that the shallow lower layer run eddy width has a higher non-dimensional growth speed than the deep lower layer run eddies is another indication that the thickness of the lower layer can cause quantitative changes in the eddy behavior. If the growth speed is scaled by the upper layer reduced gravity wave speed, the shallow run eddy grows about fifty percent faster than the deep run eddy. The shallow eddy growth is twice as fast as the deep run growth if the two-layer wave speed is used instead. This is evidence that something like a locally trapped baroclinic instability may play a role in the creation of the eddy. The role of baroclinicity in the dynamics of a coastal front is poorly understood. Therefore, let us pause to review baroclinic instability in a classical quasigeostrophic, two-layer flow in a channel.

Baroclinically unstable modes typically disappear in a two-layer system when one of the layer thicknesses becomes very great compared to the other. As the depth ratio  $\delta = h_1/h_2$  goes to zero, the growth rate decreases to zero. The instability becomes weaker because coupling between potential vorticity anomalies in the thin layer and motion in the thick layer become weaker as the difference between the thicknesses increase. Mathematically, this is illustrated in the relatively simple case of a system with no horizontal shear. Pedlosky (1982) calculates the imaginary part of the linear wave speed, which is proportional to the instability growth rate and can



be written

$$c_i = \frac{1}{2} U_s \frac{\sqrt{4\delta - \kappa^4}}{\delta + \kappa^2 + 1},$$

where  $U_s$  is the difference between the basic state speeds in the two layers and  $\kappa = K\sqrt{g'h_1}/f$ , where  $K^2 = k^2 + l^2$  is the square of the wavenumber. Fixing all other quantities, as  $h_2$  increases,  $\delta$  decreases to zero, and  $c_i$  decreases until it becomes zero, at which point the wave becomes stable. Other factors, such as Ekman friction, can ensure that as  $\delta$  goes to zero, there are no unstable waves. The factor of  $U_s$  in the expression for  $c_i$  provides another path through which  $\delta$  can affect the growth of the wave, because the adjustment process which produces the upper layer flow will cause the lower layer flow to be larger (thus making  $U_s$  larger) when  $\delta$  increases to one.

A more relevant model than two-layer quasigeostrophic flow is the two-layer frontal instability theory of Kubokawa (1988), in which the lower layer is assumed to be deep compared to the upper layer, which has a jet of zero potential vorticity. Unlike a quasigeostrophic flow, a frontal system does not need to have the potential vorticity gradient change sign in order for an instability to develop. In Kubokawa's system, the instability is caused by the coupling of a frontal wave with a Rossby wave on the potential vorticity gradient in the lower layer. In this model, both growth rates and cross-jet speeds are scaled by a factor of  $\delta^{3/2}$ . This is too strong a dependence on  $\delta$  to fit the results of the experiments, but quantitative agreement should not be expected, since the experiments differ from the theory in having a shallow lower layer, non-zero potential vorticity in the jet, and an eddy whose perturbation on the flow is not small compared to the basic state flow. More importantly, Kubokawa's system has a motionless lower layer. In the laboratory, the lower layer velocity is not known. If there were no friction the potential vorticity in the lower layer would be uniform, but friction may impose a potential vorticity gradient on the flow.

While the difference in growth rates implies that baroclinicity causes the eddy to grow faster, it does not prove that an active lower layer is essential to eddy

formation. The model of Werner *et al.* (1988), for instance, does not have an active lower layer, but it does produce a gyre. The active lower layer probably is necessary for drift of the eddy away from the corner, because it is likely that the drift is caused by heton-like coupling between the upper layer anticyclone and the lower layer cyclone.

## Appendices to Chapter 3

### 3.A. Technical Notes on Apparatus

#### The Long Dam

The long dam was held in place by a metal frame placed across the top of the tank (Figure 3.2.2b). The tank was spanned by a two meter "angle" piece, which has an "L" shaped cross section. A second "angle" was screwed to the center of the first, and could be adjusted to lie parallel to the second wall. A thin sheet of Plexiglass, 30.3 cm wide, was screwed into the first piece of metal and clamped to the second so that it hung into the water, reaching to a depth of about 18 cm. Tension from the frame bent the Plexiglass into the appropriate angle near the corner. The Plexiglass was readjusted on the frame for each corner angle so that the region of curvature of the Plexiglass wall extended up to 5 to 15 cm upstream and downstream of the corner, and so that tension did not pull the Plexiglass too close to the corner itself. Because different lengths of wall were needed parallel to the second wall for different corner angles, a second piece of Plexiglass was taped over the first in order to extend the removable wall all the way to the rim. A thick (about one cm) Plexiglass rectangle with a vertical slit cut in it was taped to the tank perimeter near the second wall, so that the removable wall fitted snugly in the slit. Silicone grease was rubbed on the slit to stop fresh water from leaking out of the channel. The wall was removed by two or three people picking up the ends of the metal frame.

#### Two Different Long Dams

In the first three long dam runs, the gap end of the removable Plexiglass wall was fitted to a greased slit in the permanent Plexiglass wall, about 1 cm from

the gap. The channel width ranged from about 10 cm near the ends and the corner up to 14 cm about 20 cm downstream of the corner. The last two long dam runs had a channel width of only about 4 cm. In these, the removable wall extended into the middle of the gap between A1 and A2. To close the gap outside of the removable wall, a piece of thin Plexiglass was taped to the removable wall and stuck with grease into the metal bracket behind the permanent Plexiglass wall.

### Walls

The first and second walls were made of aluminum, 43 cm tall and less than 1 mm wide. They were taped to the bottom of the tank in the "back," on the A1 side of the walls. The walls were carefully taped to each other on both sides at the corner. This arrangement allowed the corner to make a sharp angle which could be changed from run to run without re-taping the two walls to each other. The second wall needed to be a different length for different corner angles in order to reach the rim of the tank, so it consisted of two metal pieces taped tightly together. A "zero<sup>th</sup>" wall, also of aluminum, was taped at the beginning of the first wall (see Figure 3.2.1). One further wall was needed to separate A1 from A2 (see Figure 3.2.1). This was made out of 7/16 inch thick (1.1 cm) Plexiglass (45 cm tall).

Once the fresh water flow is started by the dam release, it eventually makes its way around the rim of the tank and along the Plexiglass wall, until it intercepts its own tail at the beginning of the first wall. Though data collected after this point is not necessarily useless, interpreting it is somewhat complicated. Therefore I taped another wall, consisting of two pieces of metal taped together, to the Plexiglass wall near the rim (see Figure 3.2.1a). For a current traveling at 4 cm/s, the 68.5 cm of extra wall causes the current to traverse an extra 137 cm in about 34 sec. Since it only takes a few minutes to traverse the whole perimeter, this is a useful gain in duration of the experiment.

## Watertight Seals

The short dam was held in place by metal brackets on either side of the gap. Silicone grease along the edge of the dam prevented fresh water from seeping through. The brackets were originally glued or taped in place in various runs. The dam only reached down to a depth of 20–25 cm for the deep lower layer experiments, so that no horizontal pressure gradients could develop between region A1 and A2 in the salty water. Similarly, water could seep underneath the walls in several places. Since the tank floor sloped up within a couple of centimeters of the rim, the permanent Plexiglass wall and the second wall did not reach all the way to the rim. Small pieces of Plexiglass were taped to the walls and rim in order to prevent fresh water from leaking out of A1.

In runs with a shallow lower layer, extra Plexiglass pieces were taped at appropriate depths between the rim of the tank and both the second wall and the permanent Plexiglass wall in order to prevent relatively low-lying fresh water escaping region A1. For reasons which are still unclear, the seal between the permanent Plexiglass wall and the rim of the tank leaked fresh water. There was also a pulsation in region A1 near the leak. A patch of blue (salty) water would appear by the rim at the same phase in just about every revolution of the tank. It is possible that this was mixing the two layers enough to allow water to escape underneath the seal between the rim and the wall. Fresh water also seemed to be leaking under the dam. At times there was significant motion near the first wall due to the outflow, but the layer was extremely thin (probably as little as .1 cm), and was probably dynamically irrelevant once the dam was removed.

### Fresh Layer

A twenty-gallon (approximately 80-liter) plastic pail was placed on a milk crate behind the first and second walls. This was filled with tap water to be siphoned to the surface of region A1 to form the fresh layer. The water filtered through foam rubber glued to a styrofoam frame floating on the surface. The foam rubber forced the fresh water to have a low flow rate, so that mixing with the ambient salt water was minimized.

It was difficult to directly measure the thickness of the opaque fresh layer even before the current was made to flow, so I estimated it from geometrical considerations. From the areas of regions A1 and A2, the thickness of the fresh layer could be calculated from the rise in the water surface when the fresh water was initially fed into the tank: if  $H_1$  is the fresh layer depth,  $dH$  is the change in total depth, and  $A_1$  and  $A_2$  are the areas of the two regions,  $A_1 H_1 = (A_1 + A_2) dH$ .

### Unwanted Motion

In all the runs there was some difficulty with motion in the fresh layer before the dam was removed. The first five experiments had fairly slow motions (perhaps .2 cm/s) after waiting one to two hours between inserting the water and conducting the run. For run 6, I waited over five hours to let flow settle down, and it actually seemed somewhat worse. I suspected that the initial cyclonic flow was due to the flow of fresh water as it filled the reservoir, but the anticyclonic flow later observed could have been caused by windage on the rotating tank. However, a glass plate placed over the main reservoir in some runs seemed to have little if any effect on the flow. A 6.5 cm diameter cylinder was fixed to the end of the *zeroth* wall (Figure 3.2.1a) in order to replace the sharp edge with a rounded contour; this did not seem to discourage the anticyclonic gyre from forming in the main reservoir.

A final suspect is anticyclonic flow in the bottom layer. Covering the surface with fresh water squashes water columns in the lower layer, so water in that layer must acquire negative relative vorticity to conserve potential vorticity. However, for  $H = 32$  cm,  $f = .84$  /s, and kinematic viscosity  $\nu = .01$  cm<sup>2</sup>/s, the Ekman spindown time  $H/\sqrt{\nu f}$  is only about 6 minutes. In most of the experiments I waited over an hour after filling the top layer, to no avail.

Average speeds in the fresh water gyres in each run ranged from .2 to .4 cm/s, with standard deviations of .03 to .25 cm/s in each gyre, and the gyres' major and minor axes were in the 10 to 50 cm range. The average relative vorticity associated with the speed and size of drifter paths around the gyres — *i.e.*, the vorticity the gyre would have if it were in solid body rotation — is on the order of  $4\pi/T = 4u/D$ , where  $T$  = one gyre rotation period,  $u$  = average speed, and  $D$  = average diameter. For the fresh water gyres, this vorticity ranged from .02 to .08 /sec, or up to one-tenth of the Coriolis parameter (most of the vorticity estimates were in the range .03–.05 /sec). This would have introduced a small modification to the assumption that the potential vorticity of the fresh outflow was  $f/H$ . The speeds of surface pellets in the salty layer in the minute preceding the beginning of the flow had an average of about .1 cm/s and a standard deviation of .05 to .1 cm/s in each run of experiment H.

### 3.B. Estimation of Interpolation Errors

The errors in velocity calculated at points on a rectangular grid are due to errors in the original irregularly distributed velocity measurements and to errors caused by the interpolation process. A statistical simulation of the data was used to estimate the error at grid points.

In general, the error that is generated in interpolating is a function of the position of all the data points relative to the grid point and to the spatial variations of the field that is being measured. Rather than explicitly estimate the complexities of the error variations, for each velocity field I found an empirical relationship between the expected error and  $D$ , the denominator in the interpolation formula in Section 4.  $D$  is the sum of weights of all the data used in interpolating to a given grid point, and is large when there are many velocity measurements close to the grid point. Thus  $D$  is a rough index of how close actual data is to any grid point, and there should be a tendency for the interpolation error to decrease when the data is closer to the grid point.  $D$  is also a useful index because it must be calculated for each grid point even if no estimate is made.

For each run, the upstream interpolated velocity field for one time interval was selected as representative for the run. I pretended that this was a true (errorless) velocity map. Ten realizations of simulated "data" were created from the velocity map by randomly eliminating about half the data points and adding Gaussian noise to the rest. Each "data" field was remapped (using the interpolation formula) on to a grid, and difference fields were made by subtracting each of the remapped fields from the original mapped field. These differences represented the "errors" between the original "true" map and the maps based on the noisy "data" fields. I made scatter plots of the absolute values of the errors against  $D$ . As expected, the range of errors decreased as  $D$  increased. Looking at the  $u$  and  $v$  velocity error components separately, I binned the data into intervals in  $D$  and took the velocity error which was greater than two thirds of the errors in that  $D$  interval to be the characteristic error  $E$  of the interval. Thus for any map done for the same run, this relation between the error and  $D$  was used to estimate errors for each interpolated velocity. In practice this estimate of  $E(D)$  did not include high enough  $D$ 's (corresponding to several velocity measurements very close to two grid points), so a curve of the form  $E_0\sqrt{D}$  was appended to the empirical  $E(D)$ .



## Chapter 4.

# Barotropic Sloping Bottom Flows Around a Corner in a Rotating Tank

### 4.1. Introduction

What happens when a barotropic current flowing along a sloping bottom encounters a convex corner? Can the current continue along the coast with no qualitative change, does a gyre form, or can a more radical separation of the current from the coastline occur? These questions were addressed in a series of laboratory experiments.

Flows of Rossby number of  $O(.1)$  to  $O(1)$  were produced by pumping water along a sloping surface in a rotating tank at different flow rates. The bathymetry shallowed towards the coast, and the flow was oriented with the shore to the right looking downstream. Preliminary experiments were conducted with a sharp corner and water depth that went to zero at the coast. As described in Section 3, these experiments showed that an anticyclonic gyre can form downstream of the corner. Later runs examined how coastal water depth, radius of curvature of the corner, and Ekman number influence formation of a gyre. Velocity fields were obtained from videotapes of surface drifter motions.

The conservation of potential vorticity for a homogeneous, hydrostatic fluid demands that an inviscid fluid must flow along isobaths in the low Rossby number limit, because changes in the thickness  $h$  of a fluid parcel must be accompanied by proportional changes in the absolute vorticity  $f + \zeta$  ( $\zeta = v_x - u_y$ ). Water circulating in a gyre must undergo significant changes in thickness as it changes its distance from the coast, implying that the current must have large relative vorticity (Rossby

number not small) or significant friction or both when a gyre is produced. When the Rossby number is no longer small, however, the Taylor-Proudman theorem no longer holds, so that vertical shears are permitted in the water column and water near the surface no longer needs to follow isobaths. In the transition from a low Rossby number regime to a regime of Rossby number of order unity, it is not clear beforehand whether horizontal shears ( $\zeta$ ) or vertical shears will be more important in allowing the flow to cross isobaths.

The existence of vanishing layer depth at the shore in the initial experiments complicated the dynamics because the Ekman layer thickness was not small compared to the depth of the water in part of the current. It was even possible that the gyres in the preliminary experiments were caused by frictional processes near the coast that only occur in a regime in which the depth goes to zero at the wall. Therefore I conducted experiments with finite depth at the coast in order to accomplish two goals. The first was to confirm that gyre formation occurred even when the depth did not vanish at the wall. The second was to see how gyre formation was affected by the relative change in the lower layer depth across the width of the current. Based on the reasoning above, I expected that a system with a smaller relative depth change ( $H_w/(H_e - H_w)$ , where  $H_w$  is depth at the coast and  $H_e$  is depth at the outer edge of the current) would produce a gyre more readily.

The Ekman number of the flow was varied in order to get a crude measure of the importance of bottom friction to the formation of a gyre. The Ekman number is defined by  $E = \nu/fH^2$ , where  $\nu$  is viscosity,  $f$  is the Coriolis parameter, and  $H$  is a depth scale, and was varied by changing the rotation rate. Viscosity may play a role in two aspects of the problem. As discussed in the introduction, it is possible that the formation of the gyre is due to the separation of a viscous boundary layer at the shore. For a non-rotating system, this behavior is governed by the Reynolds number  $Re$ , though the behavior becomes independent of  $Re$  for large  $Re$ . However, Merkin

and Solan (1979) showed that for flow past a cylinder in a rotating system, Ekman friction inhibits separation through its influence on the Stewartson layer. While they kept  $E$  fixed for their calculations of separation, it is plausible that in their theory  $E$  would affect the condition for eddy generation. Unfortunately, while a dependence of eddy formation on  $E$  would imply that friction is important, the absence of such a dependence does not prove that vertical friction is irrelevant. Nevertheless, it is interesting to see if some Ekman number effect does emerge in the experiments. Varying Ekman number by changing  $f$  also allows us to better understand the effect of relative depth change described in the above paragraph. Varying  $H_w$  changes both the relative depth change and the Ekman number, so understanding the influence of the Ekman number will allow us to isolate the effect of relative depth change.

Another interesting aspect of the Ekman number relates to the size of the gyre. A key difference between the baroclinic anticyclones described in Chapter 3 and these barotropic anticyclones is that the baroclinic gyres slowly grow until they are stopped by the walls of the tank, whereas the barotropic gyres reach an equilibrium size within a few rotation periods. It is possible that the increased vertical friction due to proximity to the bottom of the tank limits the growth of the gyre in the barotropic case. If this is true, then the eddy size should vary with Ekman number.

Finally, since Hughes (1989) and I (see Chapter 2) have calculated the breakdown of inviscid flow along a curved coastline of sufficiently large radius of curvature, it is interesting to see how such a system behaves in the laboratory. This is the reason for performing experiments with a rounded corner in addition to the sharp corner experiments. Independent of inviscid theory, the dependence of gyre formation on the details of the local bathymetry of the corner is interesting in its own right and is important if the laboratory experiments are to be applied to the real ocean.

## 4.2. Experimental Apparatus and Procedure

I did several preliminary runs with the same geometry. The two meter tank was filled with fresh water, and fresh water was pumped from a reservoir into the tank along an inclined wall/floor with a slope ( $= dz/dx$ ) of unity. The floor was taped to a second sloping floor to make a ninety degree angle—that is, the isobaths all made a right angle turn (see Figures 4.2.1 through 4.2.3). This angle was sharp to within 1-2 mm. The far end of the second floor was joined to the perimeter of the tank at a right angle. Flow rates were measured by a flow meter through which the injected water ran on its way from the reservoir. The flow was visualized in the same way as the baroclinic experiments, with the intruding water dyed a dark blue and quarter inch (.64 cm diameter) white paper pellets strewn on the surface. Both the floor of the tank and the sloping bottom were painted white and the ambient fluid was dyed light blue to contrast with both the dark intruding flow and the white pellets. The runs were all imaged from above by a co-rotating CCD camera and recorded on VHS format videotape. Pellet paths were digitized by an image analysis system, and pseudo-Eulerian velocity fields were calculated from the paths as in Chapter 3.

In the first run, the intruding water was pumped through the surface of the ambient water via a box with a permeable (foam) bottom. This was to allow a relatively laminar current to flow from water percolating into the tank from above. For all pumping rates, this arrangement produced a wide, sluggish current with a Rossby number considerably smaller than one, so for all the subsequent runs, the current was driven by a jet emerging from a tube taped to the first floor. The tube was fixed so that the jet was approximately parallel to an isobath as it emerged from the tube. Contours of constant fluid thickness are actually more dynamically relevant than isobaths. This thickness is affected by the centrifugal sloping of the water surface. Since the length scale of this surface slope is large compared to the

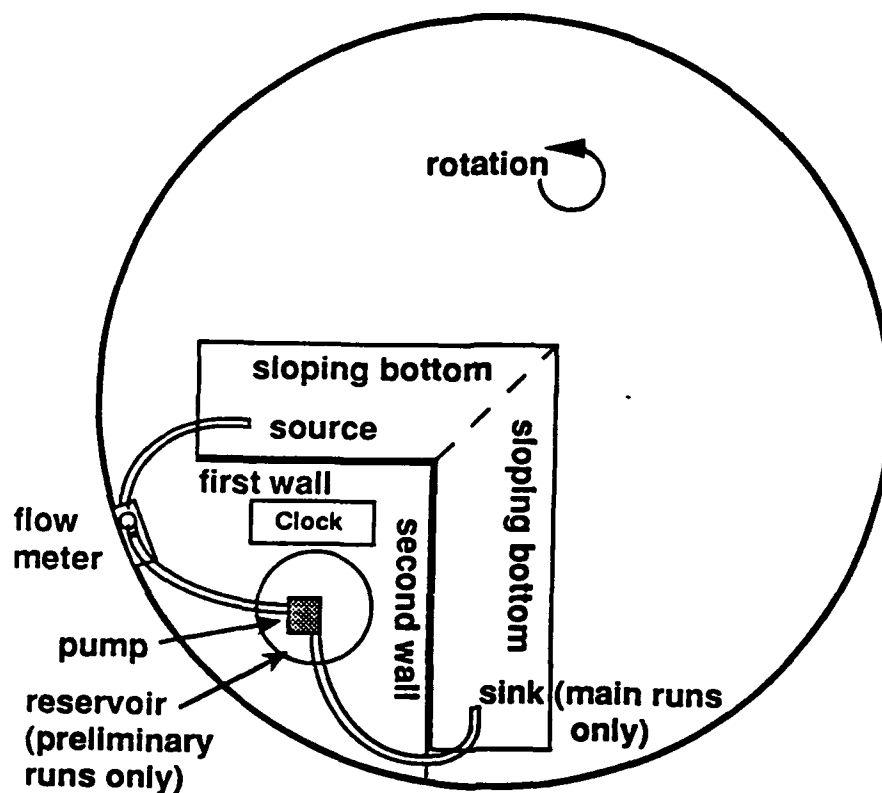


Figure 4.2.1: Apparatus as viewed from above, showing arrangement for preliminary and main experiments. For preliminary experiments, sloping bottom region was 17 cm wide; for main experiments, it was 20 cm wide.

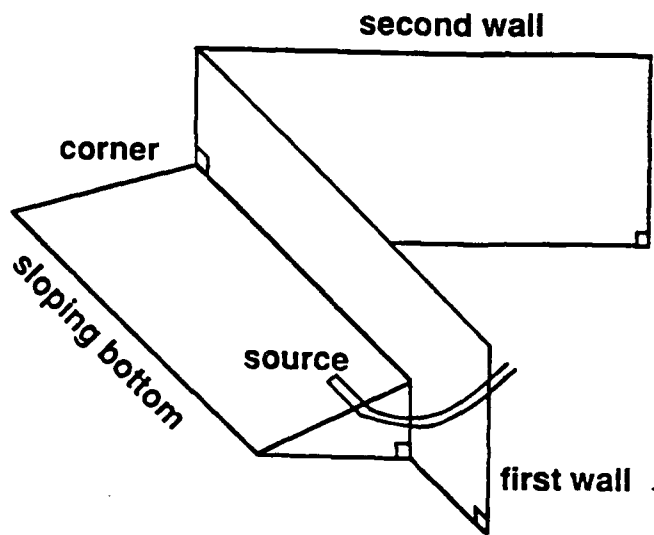


Figure 4.2.2: Perspective view of topography, main experiments. Note that perspective is from upstream of source looking down along the first wall.

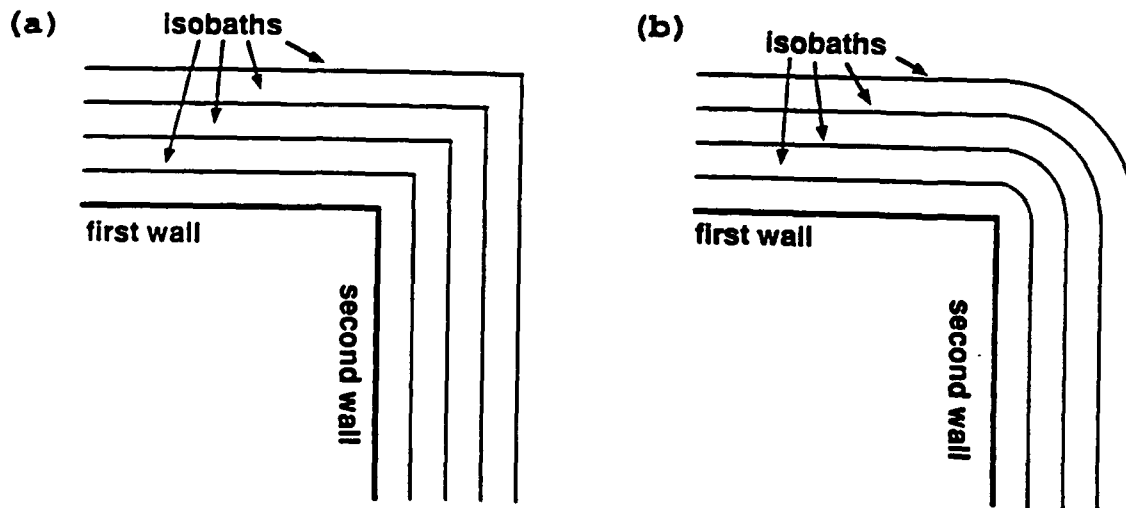


Figure 4.2.3: (a) Apparatus as viewed from above, sharp corner main experiments. (b) Apparatus as viewed from above, rounded corner main experiments.

width of the current, especially in the center of the tank where the region of interest lay, this is a small effect that merely transforms the isobaths from straight lines to slightly curved contours.

For each run, the fluid in the tank was spun up to a state of (counterclockwise) solid body rotation, and the experiment began when the pump was turned on. Typically there was an initial burst of water at high flow rate which was followed by vacillating fluxes as I adjusted the flow rate by tightening a clamp on the tube leading from the reservoir. Once the flow rate settled on a predetermined value, the flow continued at the same rate (to within about ten percent) for several minutes. The flow rate was then changed to a new value, several more minutes of observations were taken, and the process was repeated for several different flow rates.

In the preliminary experiments, the flow rate was varied from 6.7 to 133 cm<sup>3</sup>/s with a rotation period of 15 sec (Table 4.2.1). The high flow rate runs (33 to 133 cm<sup>3</sup>/s) were repeated with the tube fixed further from the shore (horizontal distance of 5.7 cm from the coast to the center of the tube at the beginning of the run as opposed to 2.6 cm) in an attempt to see if changes in the upstream current profile affected the gyre and the low flow rate runs (6.7 to 27 cm<sup>3</sup>/s) were repeated with a 64 sec rotation period. The distance from the tube to the shore increased during the course of each run as water from the reservoir raised the water level in the tank.

The rest of the barotropic experiments were conducted a year later, using a similar geometry. In these experiments, water level in the tank was kept constant by pumping water in a closed circuit from a sink at the end of the second floor to a source at the beginning of the first floor (Figure 4.2.1). The bottom had a slope of .5 (making an angle of 26.6° with the horizontal), instead of 1 (45°), and vertical sidewalls were fixed to the shoreward edge of the sloping bottom (Figure 4.2.2). Table 4.2.2 summarizes the parameters of these experiments.

Table 4.2.1. Preliminary Experiments Parameter Synopsis

run	$f$	Flow Rate	$D_i$	$D_f$	Duration	Eddy
1a	.83	67	-	-	306	N
b	.83	133	-	-	229	N
c	.83	17-33	-	-	n.m.	N
2a	.83	33	2.6	2.9	240	Y
b	.83	67	2.9	3.4	240 <sup>a</sup>	Y
c	.83	133	3.4	4.0	120 <sup>a</sup>	Y
d	.83	25	4.0	4.1	≥240	Y
3a	.84	33	5.7	5.9	150	Y
b	.84	67	5.9	6.2	210	Y
c	.84	133	6.2	7.1	180	Y
d	.84	<33	7.1	7.1	n.m.	*
4a	.84	7	2.6	2.6	53	N
b	.84	13	2.6	2.7	240	N **
c	.84	27	2.7	2.9	180	Y
5a	.20	13	2.9	3.0	240 <sup>a</sup>	Y
b	.20	27	3.0	3.2	240 <sup>a</sup>	Y
c	.20	7	3.2	3.3	≥360	Y ***

$f$  is the Coriolis parameter,  $D_i$  and  $D_f$  are initial and final distances of center of source tube from coast as the water level rises in the course of each run, "duration" refers to length of time a given flow was maintained, and "eddy" tells whether a gyre was seen or not.  $f$  is in  $s^{-1}$ , flow rate in  $cm^3/s$ ,  $D_i$  and  $D_f$  in cm, and duration in sec.

<sup>a</sup> Measurement approximate (good to about 5 sec). All other duration measurements accurate to within about 1 sec.

n.m. Not measured.

\* Not enough pellets to tell if there is a gyre.

\*\* Some sign of very narrow (<2 cm) gyre.

\*\*\* Initially gyre present, but this is remnant from previous flow rate and soon disappears, leaving some signs of return flow near the wall.



Table 4.2.2. Parameter Summary For Main Runs

Sharp Corner Experiments				Rounded Corner Experiments			
Run	$H_w$	$T$	$f$	Run	$\rho$	$T$	$f$
1	0	15	.838	Tube Source			
2	0	30	.419	3	0	15	.838
3	0	60	.209	4	0	30	.419
4	1.5	15	.838	5	0	60	.209
5	1.5	30	.419	6	2.5	15	.838
6	1.5	60	.209	7	2.5	30	.419
7	4	15	.838	8	2.5	60	.209
8	4	30	.419	Diffuse Source			
9	4	60	.209	11	0	15	.838
10	4	7.5	1.676	12	0	30	.419
11	8	15	.838	13	0	60	.209
12	8	30	.419	14	4	15	.838
13	8	60	.209	15	4	30	.419

"Run" is original number for run; some runs excluded from analysis;  $H_w$  is depth of water at corner,  $T$  is rotation period of tank,  $f = 4\pi/T$  is Coriolis parameter;  $\rho$  is radius of curvature of shore. All units cgs.

For the sharp corner experiments, the first and second floors were taped together as in the preliminary experiments (Figure 4.2.3a). Sharp corner experiments were performed for depths at the coast of 0 to 8 cm. For each value of  $H_w$ , the tank was rotated at periods of 15, 30 and 60 sec (as well as 7.5 sec for  $H_w = 4$  cm), and the current was pumped at flow rates of 5 to 30 cm<sup>3</sup>/s. The source and sink tubes each had an inner diameter of 1.27 cm (outer diameter 1.9 cm), with the center of the mouth of the source tube 5.2 cm from the first wall and the center of the sink tube mouth 5.0 cm from the second wall. For the rounded corner experiments (Figure 4.2.3b), the sharp corner was replaced by a thin, pie-shaped piece of Plexiglas, which was taped to the first and second floors so that tension forced it into the approximate shape of a cone.

All the rounded corner runs had  $H_w = 0$ . In these experiments, the corner is characterized by the radius of curvature of the coast which can be easily varied by adjusting the water level in the tank. Experiments were conducted with the same source/sink arrangement as the sharp corner experiments, with a radius of curvature of 0 and 4 cm. In order to resolve flow features better, the rounded corner experiments were also performed with a wider current, which was produced by a diffusing source that was 2.8 cm tall and extended from 4 cm to 14 cm from the coast. These experiments were conducted with corner radii of curvature of 0 and 4 cm. In these wide current experiments a single piece of mylar, which was paper thin and less rigid than the Plexiglas, covered the cone and forty centimeters of straight bathymetry to either side of the cone. This improved the approximation to a cone and covered over discontinuities of  $O(1 \text{ mm})$  in depth where the Plexiglas was joined to the rest of the sloping bottom.

It is important to note that there are several factors which define the sharpness of the corner. One is the size of the region over which the isobaths turn from being parallel to the coast upstream of the corner to being parallel to the coast downstream. It is this parameter that is changed from the sharp corner experiments to the rounded corner ones. In the sharp corner runs, the isobaths change direction within a distance of about 1 mm. In the rounded corner runs, the isobaths turn in a pie-shaped region, so that the distance an isobath takes to turn increases leaving the coast. Thus in an experiment in which the rounded corner has zero coastal radius of curvature  $\rho$ , the zero depth isobath turns in a space on the order of 1 mm, like the sharp corner topography, but other isobaths turn with an arc length proportional to the distance of the isobath from the coast. Therefore, even the  $\rho = 0$  case of the rounded corner topography has a more rounded corner than the sharp corner topography.

Adding a localized sink to the apparatus, instead of letting the depth increase with time, is potentially a major change in the dynamics of the experiment because

the downstream condition on the flow is changed. However, for zero depth at the coast, the system exhibited the same behavior with and without the sink. This is probably because the current in the no-sink case is inhibited from leaving the slope region of the tank until it reaches the perimeter of the tank, effectively creating a sink-like boundary condition at the end of the second floor. The case of finite depth at the coast is more strongly affected by the presence of a sink downstream. In the flat-bottomed experiments of Stern and Whitehead (1990), which we can consider to be the limit of a sloping bottom experiment for which  $H_w/(H_e - H_w)$  goes to infinity, the current globally separated from the coast at a  $90^\circ$  corner, *i.e.*, there was no reconnection further downstream. In those experiments there was no sink. There must be a critical value of the relative depth change at which the flow pattern switches from the anticyclone regime to the global separation regime. Clearly the constraint of removal of fluid at the downstream end of the second wall will affect this transition. However, here we are examining the role of the depth ratio in the anticyclone regime, not the transition from one regime to another. If the presence of a sink inhibits global separation, that is an advantage in isolating the dynamics of this particular regime.

In order to get a cleaner signal in digitizing positions of the white surface pellets, the walls and sloping bottom were painted black. This was especially important for improving flow visualization at the inshore and offshore edges of the current. No dye was used, so that all data from these runs derives from pellet paths. For the sharp corner experiments, the video pictures had a wide field of view and large (.64 cm diameter) pellets were used, while for the wide current rounded corner experiments, a smaller field of view allowed smaller (.32 cm diameter) pellets to be resolved. To reduce windage on the pellets, a co-rotating transparent plastic sheet was placed about thirty centimeters above the rim of the tank during the wide current rounded corner experiments. The sheet was about the same diameter as the tank, and the space between the sheet and the tank rim was partially covered, with gaps left through which I could throw pellets into the tank during the experiments.

### 4.3. Qualitative Observations

For flows in which the current volume flux was above a critical value, an anticyclone formed just downstream of the corner. After a brief adjustment time at the beginning of the flow, the gyre persisted in an approximately steady state. The size of the gyre increased with increasing flow rate. The behavior of the current at the corner for a strongly sloping bottom is similar to the behavior of a baroclinic front (see Chapter 3). Both generate a strong anticyclonic gyre just downstream of the corner. This is in contrast to barotropic currents over a flat bottom (Stern and Whitehead, 1990), which break into both cyclones and anticyclones of approximately equal strength and completely separate from the coast at the corner. Barotropic flows are apparently stabilized by the sloping bottom, perhaps due to the influence of topography on the form of the potential vorticity. A jet with velocity going to zero on the inner and outer edge, and with continuous shear, must have the cross-jet gradient of relative vorticity change sign. For a flat-bottom flow, this is equivalent to the cross-jet potential vorticity gradient changing sign, which is a necessary condition for instability. For a jet flowing over a sloping bottom, the potential vorticity gradient does not necessarily change sign if the relative vorticity does. For a current with the coast to the right looking downstream, the relative vorticity gradient is positive on the inshore edge and negative on the offshore edge, while the potential vorticity gradient due to the factor of  $1/H$  ( $H$  is thickness of the layer) is negative throughout the current. For small Rossby number and large relative layer thickness, the topography component dominates the relative vorticity term. Velocity measurements from the sloping bottom jets seemed to indicate reversing potential vorticity gradients near the coast in some, but not all, of the runs, but the magnitude of the measurement error in this region was large. The sloping bottom may have a more subtle stabilizing influence when this factor is combined with friction or nonlinearities in linearly unstable waves.

In the first of the preliminary runs, the dyed current driven by water percolating through foam rubber at the surface was about 20 cm wide at the initial flow rate of  $67 \text{ cm}^3/\text{s}$  and widened to about 30 cm at the higher flow rate. The dye went around the corner with the flow following isobaths. Initially there was a narrow layer (1 cm or less) of reverse flow next to the shore just downstream of the corner. This reverse flow decreased with time until invisible. Increasing the flow rate increased the width of the current along the first wall more than it increased the speed, so that a higher flow rate did not lead to a higher Rossby number.

The currents issuing from a horizontal tube were narrow (less than 10 cm) and fast compared to the current fed from above. Increasing the flow rate increased the Rossby number in these runs. Return flow was seen offshore of the jet, forming a narrow, cyclonic, "L" shaped gyre parallel to the first and second walls. This was probably due to turbulent entrainment at the source of the jet pulling ambient water in the tank towards the source. At flow rates greater than  $13 \text{ cm}^3/\text{s}$  in the preliminary 15 sec rotation period experiments, an anticyclone was visible just downstream of the corner. The size of the anticyclone did not change appreciably with time for a given flow rate, but the higher the flow rate, the wider the anticyclone (Figure 4.3.1a shows the same behavior in the main runs). Changing the flow rate did not introduce any notable transient effects. When the flow rate changed, the gyre did not drift or break up, it merely changed its size. For some flow rates, the gyre was so large that it extended out beyond the edge of the sloping bathymetry region. This did not introduce any qualitative changes in the behavior of the current unless the gyre became so large that it interacted with the perimeter of the tank.

When the flow rate was  $6.7 \text{ cm}^3/\text{s}$ , virtually all the intruding fluid formed a narrow cyclonic recirculation gyre along the first wall, with very little motion along the second wall. At  $13 \text{ cm}^3/\text{s}$ , most of the flow continued past the corner, with no gyre clearly visible (see Figure 4.3.1b for the same behavior in main experiments), but

with signs of a very thin anticyclone along the second wall shown by pellets touching the wall just downstream of the corner (not visible in figure).

The experiment with a 60 sec rotation period shows qualitatively similar behavior to the 15 sec period runs, but for a given flow rate the 60 sec rotation period gyre is larger than the 15 sec rotation period gyre. This pointed to the possibility that the gyre characteristics are controlled by the Rossby number.

The presence or absence of a gyre downstream of the corner in the preliminary experiments is summarized in the last column of Table 4.2.1.

Also of note was the behavior of the dyed water when it reached the end of the second wall, which intersected the rim of the tank in the preliminary experiments. The water continued to flow along the perimeter of the tank for several current widths, but eventually an eddy which propagated away from the perimeter formed at the nose of the current, causing the current to separate from the outer rim of the tank. A similar process occurs in the simpler case of a jet flowing along a straight vertical wall in a rotating tank (see Stern and Whitehead, 1990).

The dye and the pellet trajectories provided two ways to visualize the flow. Along the first wall, pellets from the undyed offshore region were clearly pulled into the dyed region near the mouth of the tube. Pellets in the dyed current left the dyed region but did not penetrate very deeply into the offshore region; instead they recirculated in a narrow gyre. Another place where pellets were seen leaving the dyed region was at the beginning of the second wall, where faster pellets would continue in the same direction they were travelling along the first wall instead of turning the corner. This was the most dramatic cross-dye flow, because pellets left the dyed region at right angles. In both regions where pellets left the dyed region, some tendrils of dye were seen, indicating the presence of turbulent mixing. The fact that in the region of most dramatic pellet escape some pellets stayed within the dyed water mass

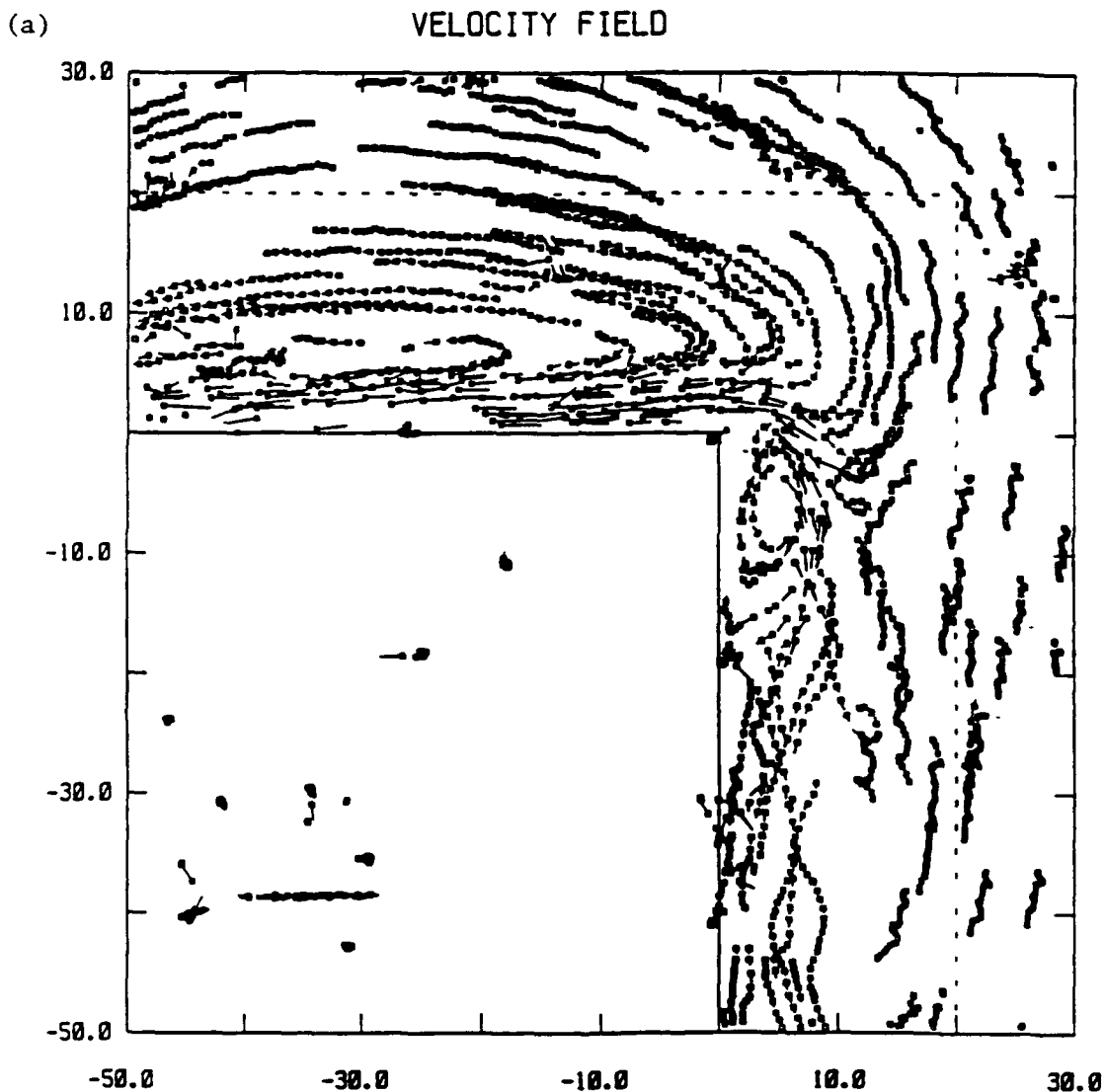
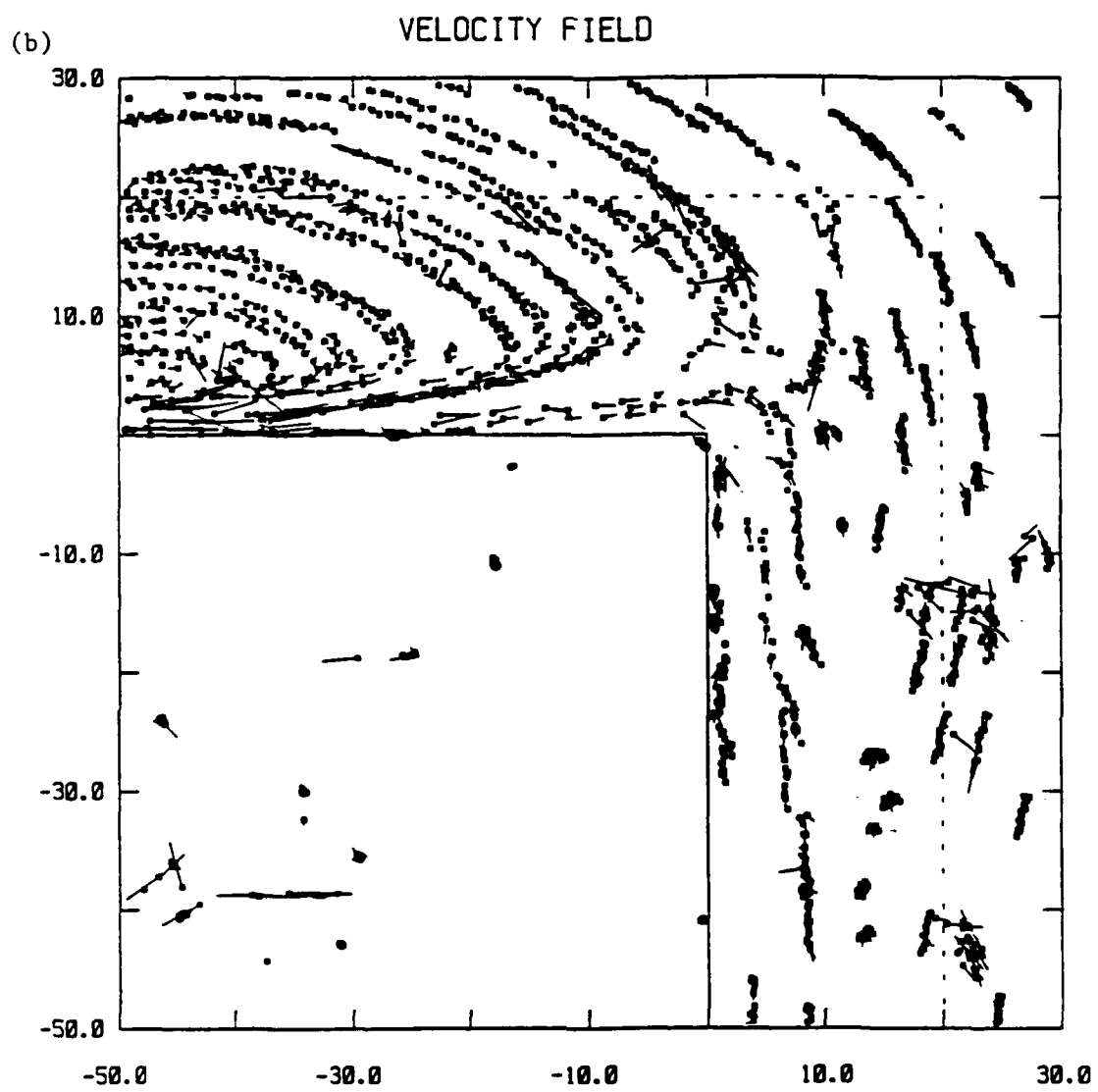


Figure 4.3.1: Flow fields derived from paper pellets floating on surface, for two runs in main experiments, sharp corner, depth at coast  $H_w = 0$ , rotation period  $T = 15$  sec. Axes of figure show distances in cm; small boxes mark tails of vectors; speeds are given by length of vectors in cm (on scale of figure) divided by velocity scale factor  $v_s$ . Velocity field includes all data taken at given intervals for given duration. Solid lines denote coast, dotted lines mark deepest isobath of sloping bottom. Upstream Rossby number  $Ro$  is defined in Section 4. (a)  $Q = 25 \text{ cm}^3/\text{s}$ ,  $v_s = 2$ , every 1 sec, 60 sec interval,  $Ro = 1.52 \pm .18$ . (b)  $Q = 10 \text{ cm}^3/\text{s}$ ,  $v_s = 2$ , every 5 sec, 120 sec interval,  $Ro = .27 \pm .06$ .





also points to turbulent mixing as a cause of the escape. However, it is possible that the cross-dye flow of pellets is caused by differences between the flow patterns in the surface Ekman layer and at depth.

The main experiments exhibited the same qualitative behavior as the preliminary runs, despite differences such as the presence of a mass sink, non-zero depth at the coast, and varied bathymetry at the corner (Figures 4.3.1, 4.3.2 and 4.3.3). However, in runs with a larger coastal depth, there was a tendency for the flow to be less steady, with cyclonic eddies appearing at the outer edge of the current. The absence of a gyre in the low flow runs was also more ambiguous than in the original experiments. These runs showed occasional signs of a barely resolvable layer of reverse flow when pellets which were stuck to the coast just downstream of the corner sometimes moved back towards the corner. In the rounded corner runs with coastal radius of curvature  $\rho = 4$  cm, runs in which the streamlines separated but were not displaced by very much from the coast had no gyre present between the separated streamlines and the coast (Figure 4.3.3a).

#### 4.4. Rossby Number and Gyre Size

Since the size of the gyre seemed to increase with current speed and with rotation period ( $1/f$ ), I plotted measures of gyre size as a function of Rossby number  $Ro$  upstream of the corner.

Various measures of length and velocity scales may be used to define a Rossby number. The width of the shear layer adjacent to the coast and the width of the region of strong flow are both reasonable length scales, but in order to utilize a relatively unambiguous measurement I took the width of the current to be the distance from the coast to the point offshore where the flow reverses direction. This width includes streamlines that are part of the recirculation gyre, and so will lead

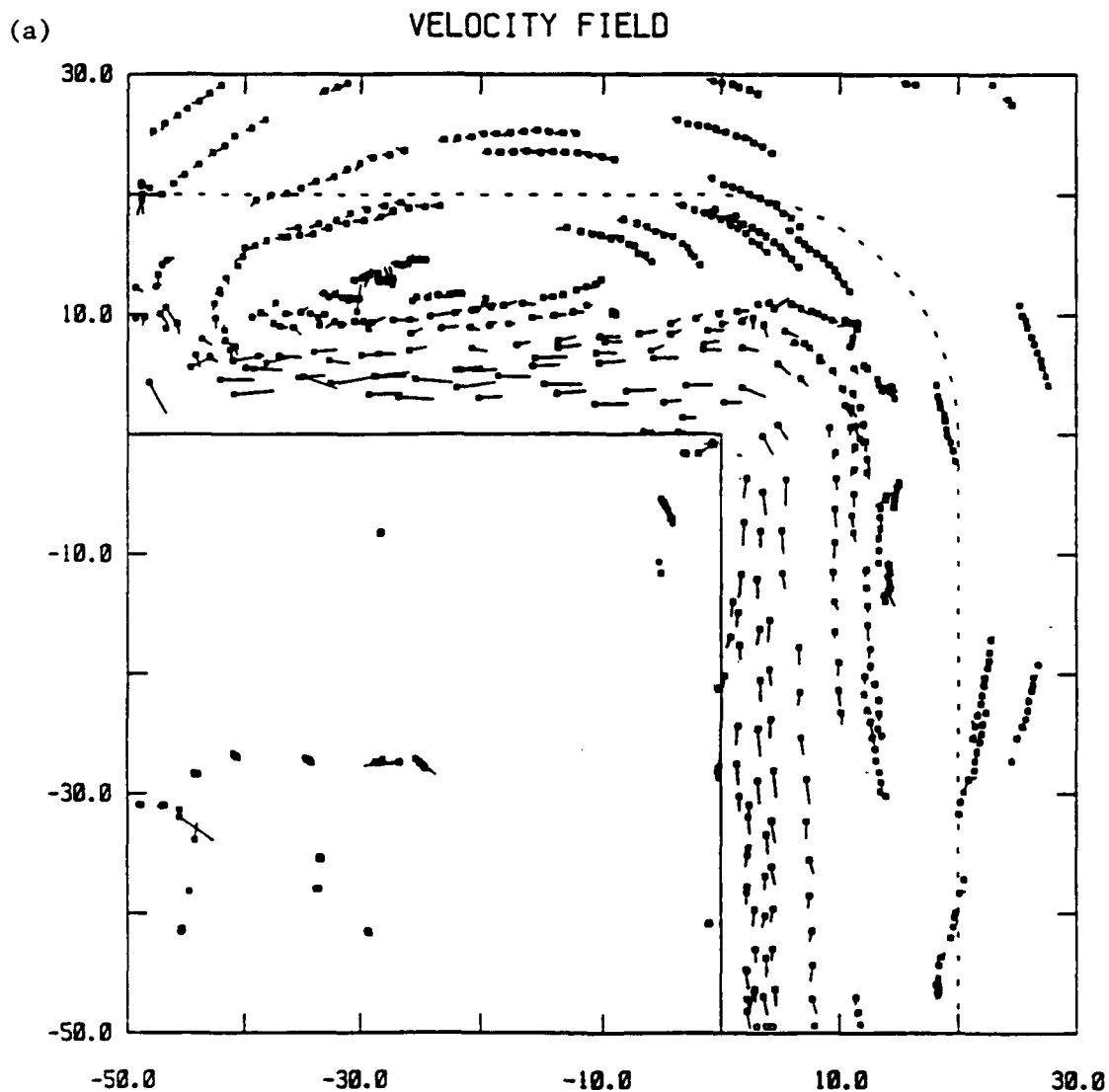
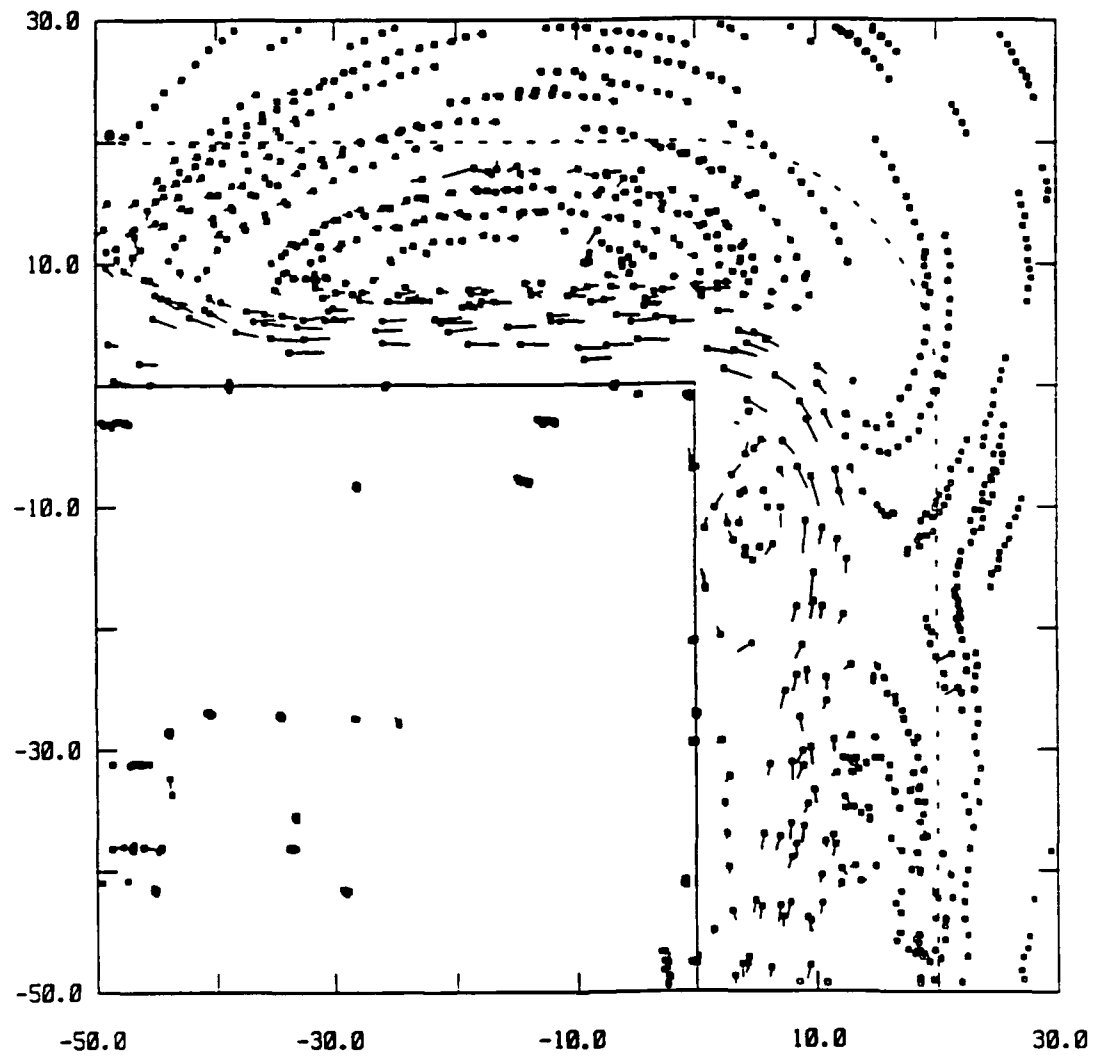


Figure 4.3.2: Flow fields, as in 4.3.1, for main experiments, rounded corner, coastal radius of curvature  $\rho = 0$ , rotation period  $T$ . (a)  $T = 15$  sec,  $Q = 15 \text{ cm}^3/\text{s}$ ,  $v_s = 4$ , every 10 sec, 120 sec interval,  $Ro = .08 \pm .01$ . (b)  $T = 15$  sec,  $Q = 33 \text{ cm}^3/\text{s}$ ,  $v_s = .5$ , every 2.5 sec, 30 sec interval,  $Ro = .82 \pm .08$ .

(b)

# VELOCITY FIELD



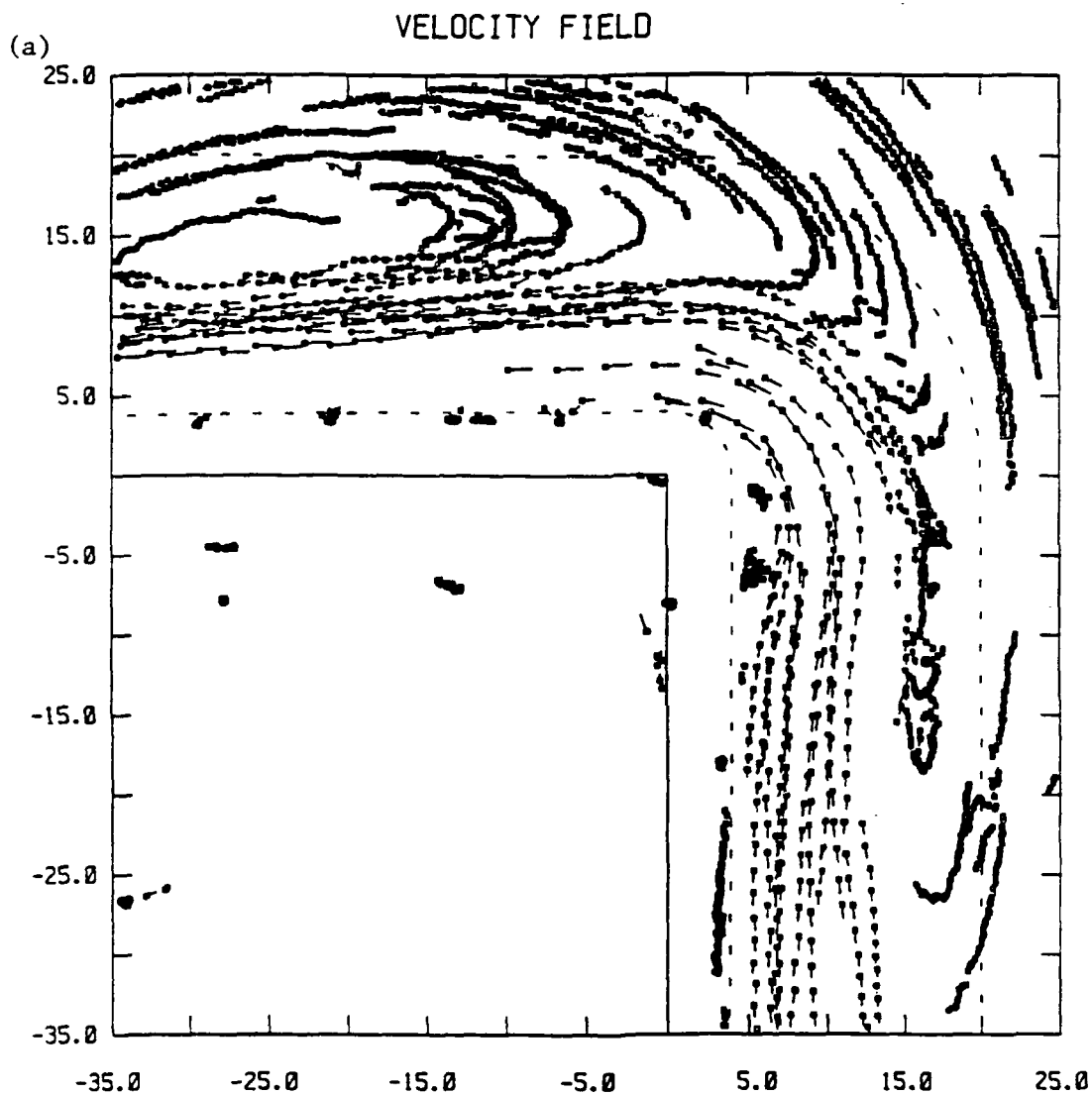
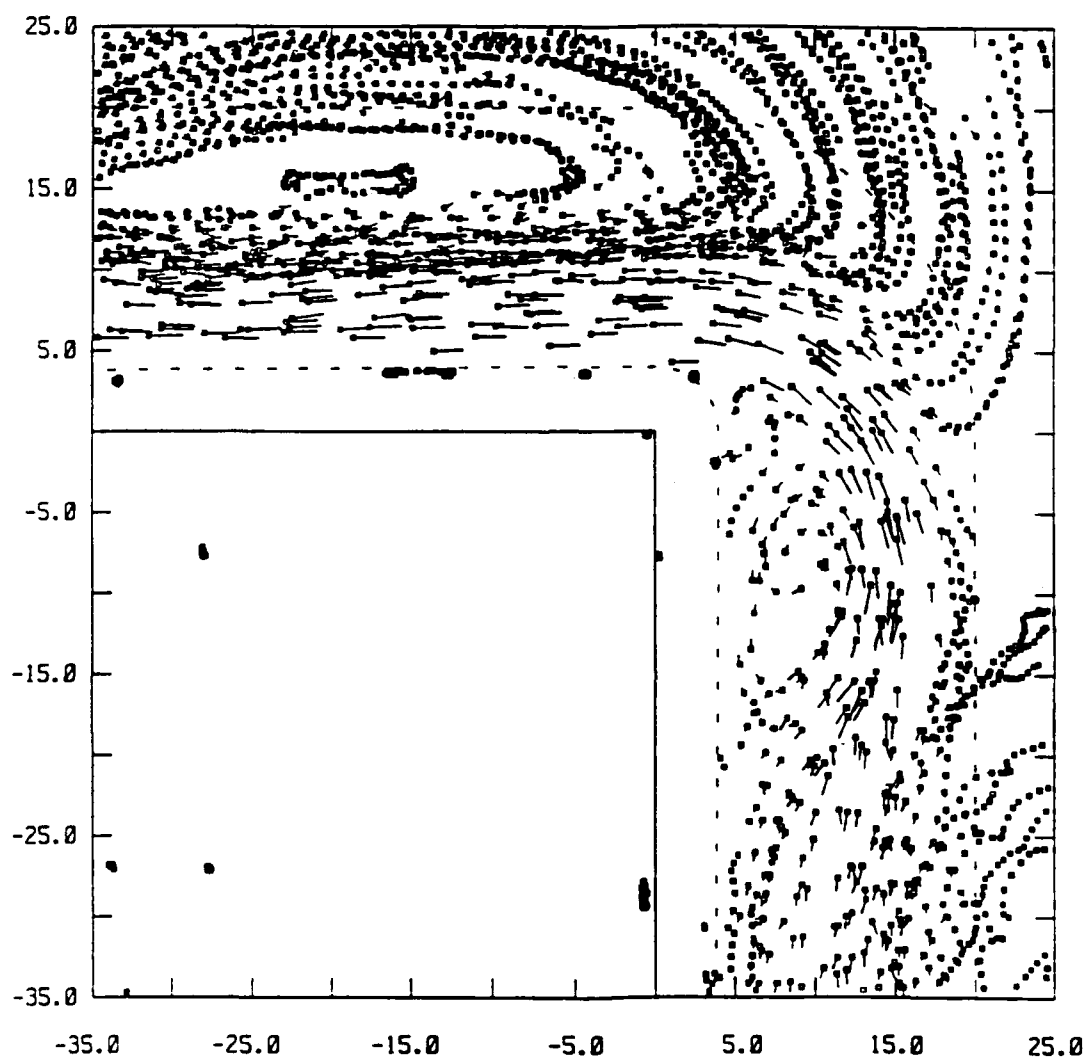


Figure 4.3.3: Flow fields, as in 4.3.1, for main experiments, rounded corner, coastal radius of curvature  $\rho = 4$  cm, rotation period  $T = 15$  sec. Solid lines denote walls as in other flow field plots, and dashed lines near walls show estimated position of coast. (a)  $Q = 30 \text{ cm}^3/\text{s}$ ,  $v_s = .5$ , every 1 sec, 60 sec interval,  $Ro = .41 \pm .06$ . (b)  $Q = 50 \text{ cm}^3/\text{s}$ ,  $v_s = .25$ , every 1 sec, 60 sec interval,  $Ro = .89 \pm .05$ .

(b)

# VELOCITY FIELD



to a lower value of  $Ro$  than the other measures of width. The current width defined this way also varies along the length of the first wall. I measured the width 25 cm upstream of the corner, where this width was near its minimum value. The velocity scale was set by the maximum value of the alongshore component of velocity found along the first wall within 25 cm of the corner.

Of several possible measures of gyre size, we will use the position of the gyre center, which is a distinct point bounded by the smallest closed streamlines in the gyre. The "gyre half width" is the distance from the coast to the gyre center, and the "gyre half length" is the distance along the coast from the corner to the gyre center. These distances  $(x_c, y_c)$  are divided by the upstream width of the current (defined in the previous paragraph) to obtain the "scaled" half width and half length  $(x_s, y_s)$ .

The measurement of Rossby number and gyre parameters was based on the velocity field as traced by surface pellets. For the wide current experiments, motion artifacts were removed from the path data (see Appendix). No further processing was done to the velocity fields before parameters were estimated. Positions of flow reversals were bracketed by the closest couple of velocity vectors pointing in opposite directions.

The upstream width and velocity measurements, which were used in computing upstream Rossby numbers, are plotted in Figure 4.4.1. These plots show that over most of the range of speeds, the current width was approximately constant, but for the wide current runs, the width increases significantly for speeds less than 1 cm/s. There is also some tendency for lower rotation rate currents to be wider. The sharp corner experiments with different values of  $H_w$  had width ranges which were similar though not identical to each other (6 to 9 cm for  $H_w = 0$  and 6 to 8 cm for  $H_w = 4$  cm), as did the rounded corner experiments with different values of  $\rho$  (9 to 19 cm for  $\rho = 0$  and 10 to 16 cm for  $\rho = 4$  cm). I do not know what accounted for the observed variations in widths. If we take the depth at the outer edge of the

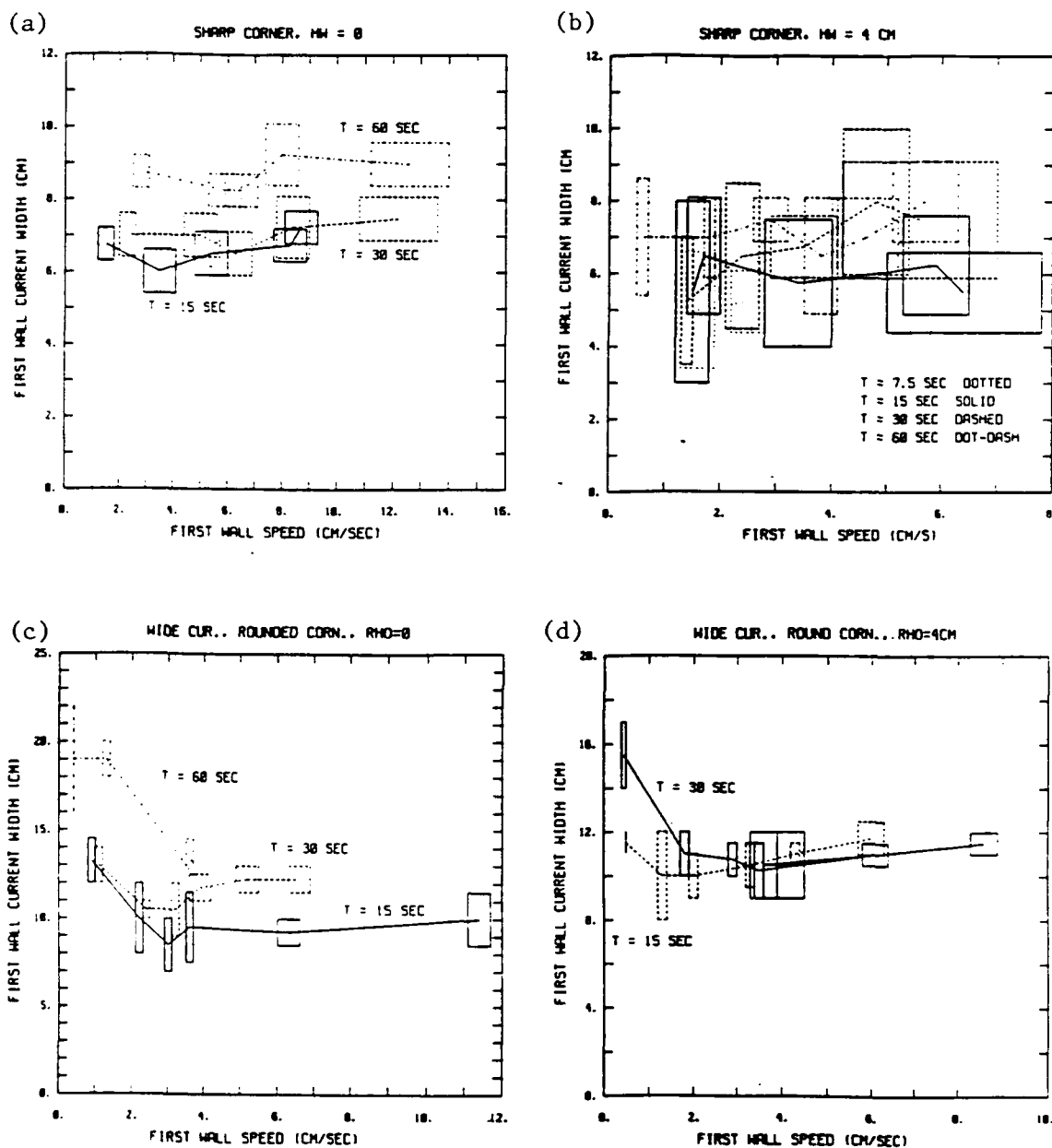


Figure 4.4.1: Upstream width (distance from coast to flow reversal 25 cm upstream of the corner) *vs.* upstream maximum speed (alongshore component of current along first wall measured within 25 cm of the corner). (a) Sharp corner experiments,  $H_w = 0$ . (b) Sharp corner experiments,  $H_w = 4$  cm. (c) Wide current rounded corner experiments,  $\rho = 0$ . (d) Wide current rounded corner experiments,  $\rho = 4$  cm.

current to be the scale for the Ekman number, and we use a current width of 7 cm for the narrow current experiments and 12 cm for the wide current experiments, then  $E$  ranges from  $10^{-3}$  to  $4 \times 10^{-3}$  for the narrow current experiments with  $H_w = 0$ , from  $2 \times 10^{-4}$  to  $10^{-3}$  for the  $H_w = 4$  cm experiments, and from  $3 \times 10^{-4}$  to  $10^{-3}$  for the wide current experiments.

In all plots, box size for each data point indicates estimated measurement error. Error in width measurements arises from the uncertainty in actual particle positions and from uncertainty in locating the exact position of flow reversal between neighboring velocity measurements. Velocity errors come from uncertainty in particle positions. For narrow current runs, I assumed the position errors to be  $\sigma = .2$  cm, and for the wide current runs, I took  $\sigma = .1$  cm.

A clear picture emerges in the variation of gyre half width with Rossby number (Figure 4.4.2). The sharp corner experiments spanned a Rossby number range of approximately .2 to 4 and the rounded corner experiments spanned a Rossby number range of approximately .1 to 1.4. For a given  $H_w$  and  $\rho$ , the scaled width was approximately proportional to Rossby number ( $x_s = ARo$ ), and the scaled length increased approximately linearly with Rossby number, with even the thinnest gyres having length on the order of a current width. With the exception of the slowest rotation runs of the sharp corner experiment with  $H_w = 0$ , the rotation rate did not seem to affect the relation between gyre width and Rossby number, implying that the gyre size is not very sensitive to Ekman number. Since both  $x_s$  and  $Ro$  have a factor of upstream width in common, the gyre width is given by the relation  $u/fx_c = 1/A \equiv B$ . This implies that for any gyre, a sort of Rossby number derived from the gyre size and upstream speed must be a constant which is independent of the upstream flow parameters. This relation between the inertial radius  $u/f$  and the gyre half width  $x_c$  is similar to the criterion of Bormans and Garrett (1989) for the generation of a gyre by a baroclinic current emerging from a channel with a rounded



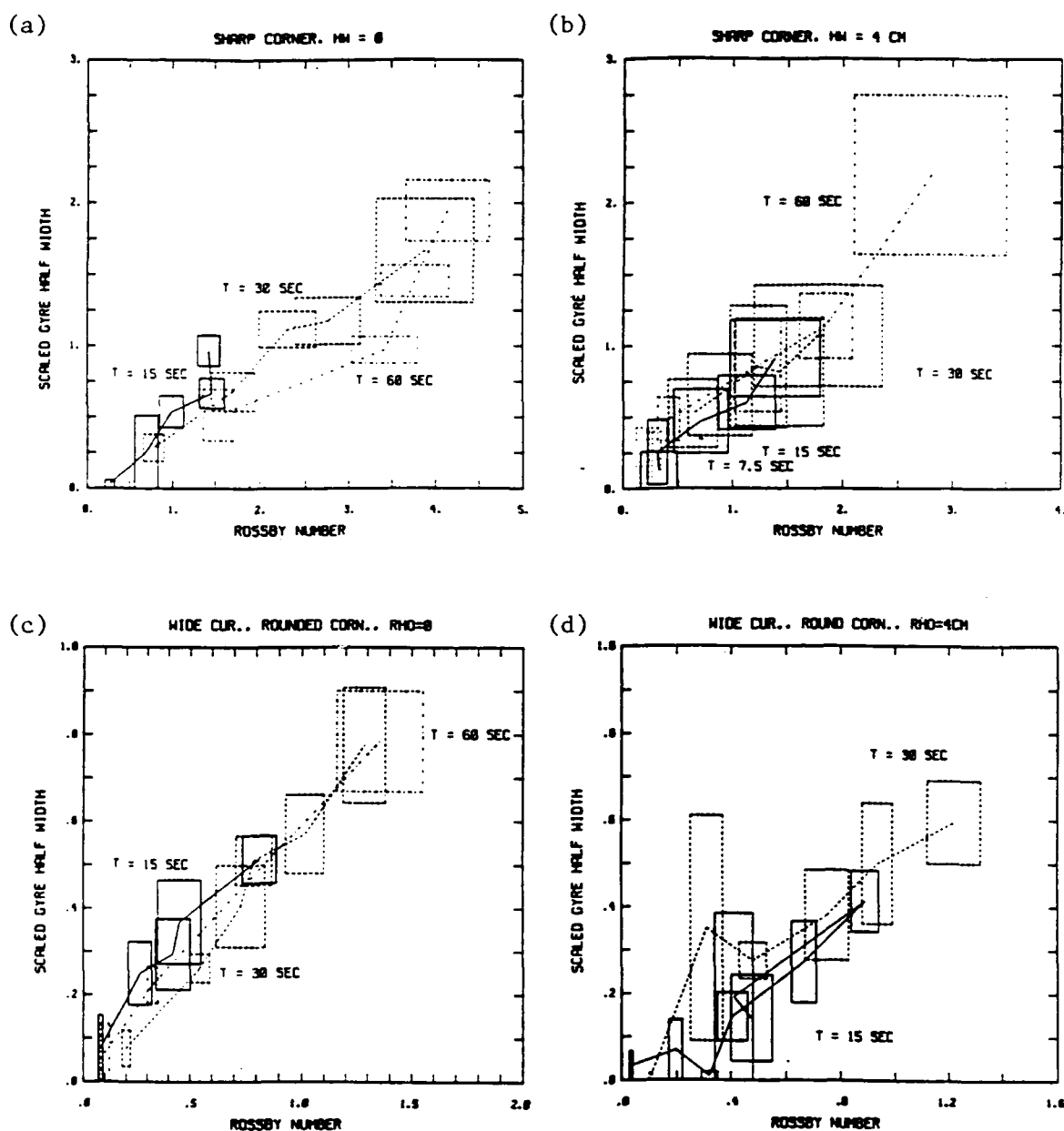


Figure 4.4.2: Scaled gyre half width (distance from coast to gyre center) vs. upstream Rossby number. (a) Sharp corner experiments,  $H_w = 0$ . (b) Sharp corner experiments,  $H_w = 4$  cm. (c) Wide current rounded corner experiments,  $\rho = 0$ . (d) Wide current rounded corner experiments,  $\rho = 4$  cm.

corner. In their observations, the critical length scale was given by the radius of curvature  $\rho$  of the corner. In our barotropic case, the gyre half width is related to the radius of curvature of the jet where it circumnavigates the gyre.

This gyre radius Rossby number,  $B$ , was calculated for different geometries, and for different rotation periods. Assuming that a set of runs are all characterized by the same value of  $B$ , then  $B$  can be estimated by taking a weighted average of the measured values of  $B$  for all the runs,

$$\overline{B} = \frac{\sum B_i / \sigma_i^2}{\sum 1 / \sigma_i^2} \quad (4.4.1)$$

which is characterized by a measurement error of

$$\sigma_{\overline{B}} = \frac{1}{\sqrt{\sum 1 / \sigma_i^2}}, \quad (4.4.2)$$

where  $(B_i, \sigma_i)$  are individual measurements and their errors as derived by propagating the measurement errors in  $u$  and  $x_c$  (errors in  $f$  are negligible). Measurements in which the gyre extended beyond the region of sloping bottom were excluded, since the absence of bottom slope could change the relation between gyre size and current speed. Runs in which the gyre was very narrow ( $\leq 2.5$  cm) and the error in half width was the same order as the half width were also excluded.

Statistics for  $\overline{B}$  can be found in Table 4.4.1. After measurements were excluded as described above, there were only a few data points for each rotation rate in each experiment (see column "N" in Table 4.4.1b). Out of the ten cases for which statistics were compiled, in all but one the sample standard deviation of the individual measurements was comparable to the average estimated measurement error of the data points. Therefore the actual scatter in the data is roughly consistent with the estimated errors. Figure 4.4.3 displays the dependence of  $B$  on rotation period for the four combinations of geometrical parameters studied. There is no significant trend with rotation period  $T$  in any of the cases except for the sharp corner experiment

Table 4.4.1a. Gyre Radius Rossby Number for Different Geometries

Corner	Param	$\bar{B}$	$\sigma_{\bar{B}}$	$N$	$\langle \sigma_i \rangle$	$\sigma$
Preliminary Experiments (slope=1)						
sharp	$H_w = 0$	1.40	.07	4	.16	.71
Narrow Currents						
sharp	$H_w = 0$	2.06	.08	12	.63	.54
sharp	$H_w = 4$	1.26	.12	13	.72	.43
round	$\rho = 0$	1.93	.08	4	.49	.38
Wide Currents						
round	$\rho = 0$	1.54	.07	9	.23	.31
round	$\rho = 4$	1.74	.17	3	.58	.95

Table 4.4.1b. Gyre Radius Rossby Number for Different Geometries as a Function of Rotation Period

Narrow Currents						Wide Currents					
$T$	$\bar{B}$	$\sigma_{\bar{B}}$	$N$	$\langle \sigma_i \rangle$	$\sigma$	$T$	$\bar{B}$	$\sigma_{\bar{B}}$	$N$	$\langle \sigma_i \rangle$	$\sigma$
Sharp Corner, $H_w = 0$ cm (slope=1)						Rounded Corner, $\rho = 0$ cm					
15	1.28	.07	3	.14	.28	15	1.41	.08	4	.20	.23
64	2.86	.22	1	.22	—	30	1.78	.11	4	.24	.22
Sharp Corner, $H_w = 0$ cm						60	1.46	.28	1	.28	—
15	1.66	.12	4	.90	.55	Rounded Corner, $\rho = 4$ cm					
30	2.26	.14	5	.45	.25	15	2.78	.93	1	.93	—
60	2.86	.22	3	.58	.47	30	1.68	.17	2	.41	.60
Sharp Corner, $H_w = 4$ cm											
7.5	1.11	.82	2	1.2	.38						
15	1.66	.26	5	.87	.51						
30	1.29	.25	3	.50	.34						
60	1.22	.10	3	.29	.12						
Rounded Corner, $\rho = 0$ cm											
30	1.93	.08	4	.49	.38						

$T$  is the tank rotation period,  $\bar{B}$  is the weighted average of the gyre Rossby number  $u/fx_c$ ,  $\sigma_{\bar{B}}$  is estimated error in  $\bar{B}$ ,  $N$  is the number of measurements,  $\langle \sigma_i \rangle$  is the average error of  $\sigma_i$ 's, and  $\sigma$  is sample standard deviation of individual measurements of  $B$ . Measurements for which there was both a small  $x_c$  ( $\leq 2.5$  cm) and a large error in  $x_c$  (on the order of  $x_c$ ) were excluded from statistics. Bottom slope = .5 unless otherwise noted. All units in c.g.s.

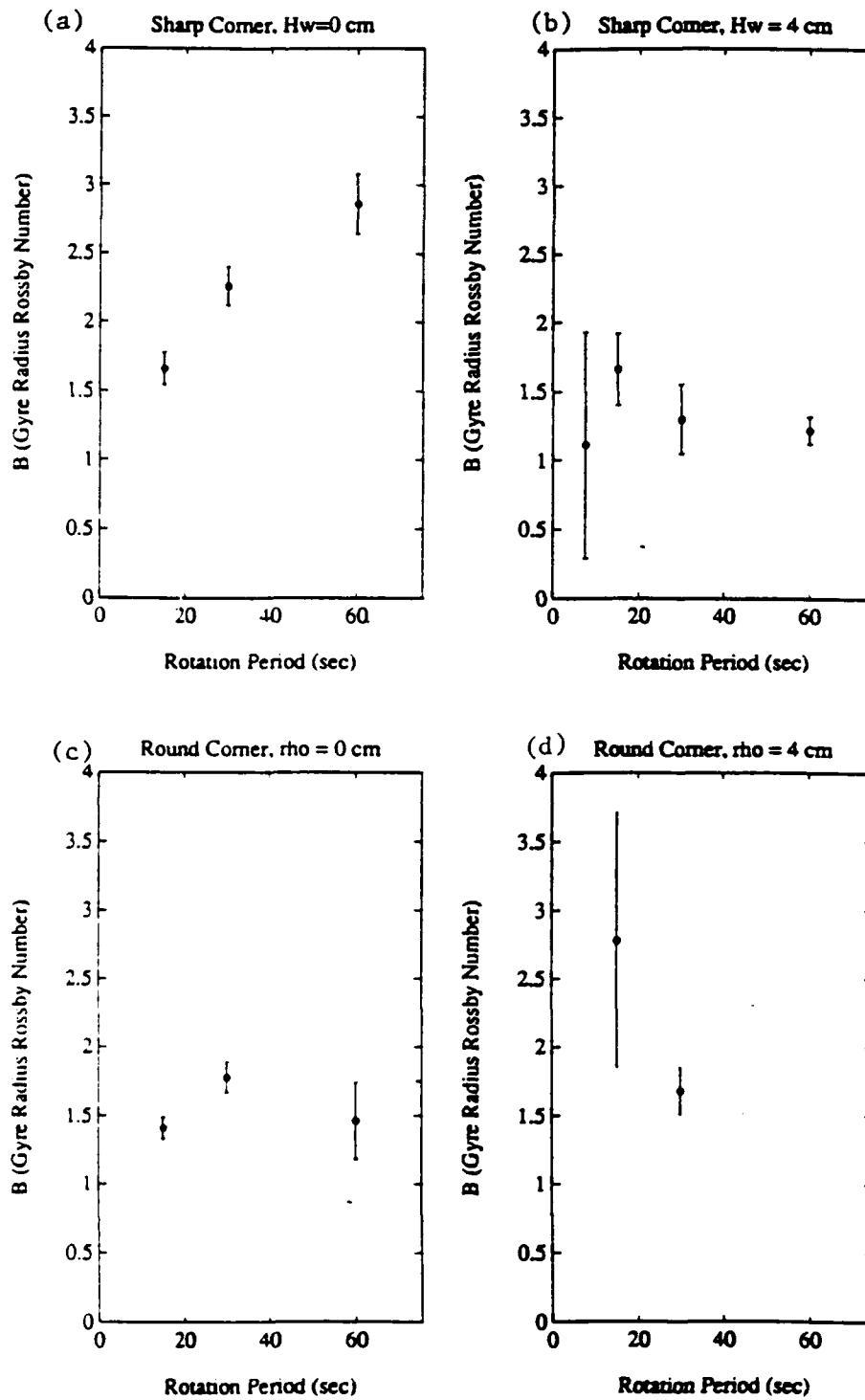


Figure 4.4.3: Gyre radius Rossby number ( $B = u/fx_e$ ) as a function of tank rotation period, for different geometrical parameters. The data and error bars come from Table 4.4.1b, columns 2 and 3. (a) Sharp corner experiments,  $H_w = 0$ . (b) Sharp corner experiments,  $H_w = 4$  cm. (c) Wide current rounded corner experiments,  $\rho = 0$ . (d) Wide current rounded corner experiments,  $\rho = 4$  cm.

with  $H_w = 0$ , for which the gyre radius Rossby number increased with  $T$ . This trend also appeared in the preliminary experiments, which had the same geometry but had a bottom slope of  $s = 1$  instead of  $s = .5$  and had no sink downstream of the corner, though in that case only one run with a long rotation period was in the proper size range to calculate  $B$ . Even though the distribution of  $B$  values in this case is wide compared to the size of the estimated error bars, the fact that the trend does not appear in any of the other cases casts doubt on whether it is a real physical effect. If the trend were real, it would imply that larger Ekman numbers cause the gyre to be smaller. In other words, the less friction, the wider circle the current must make before it returns to the coast.

Ignoring possible Ekman number influence for now, we can examine the data in the four geometrical cases without regard to rotation rate (see Table 4.4.1a). Again, the sample standard deviation of  $B$  for each case is consistent with the average error estimate of individual values of  $B$ . As depth at the coast decreases, and hence the relative change in thickness of the current decreases, then  $B$  decreases, so that the gyre gets larger. This confirms the hypothesis framed in the introduction to this chapter: the smaller the relative change in depth across the current, the larger the cross-shore excursion the current can make. Varying the coastal radius of curvature had hardly any effect on the gyre size, but for  $u/f \leq \rho$  no gyre formed even though the streamline displacement increased with  $u/f$ . Comparing the results of the sharp corner experiment with  $H_w = 0$  and the rounded corner experiment with  $\rho = 0$  (for which  $H_w = 0$  also) produces mixed results. For a narrow current produced by the same tube as was used in the sharp corner runs,  $B$  for the rounded corner experiment was only slightly less than for the sharp corner run, while the rounded corner run with a wide current produced by a diffusing source had a significantly smaller  $B$ . Thus larger eddies tend to form at the rounded corner for the wide current than at either a sharp or rounded corner for the narrow current. Since the Ekman number of a wider current is lower, this data adds to the intermittent evidence, described

above, that friction inhibits the size of the gyre. Differences in the upstream velocity profile may instead be responsible for the difference between the wide and narrow jets. The vertical profile of velocity is unknown (see the following section), but the scaled horizontal profiles of narrow and wide currents are not dramatically different (see Figures 4.5.2 and 4.5.4).

## 4.5. Velocity, Transport, and Vorticity Profiles

Velocity measurements were interpolated to a regular grid in order to produce a sharper picture of the currents studied in these experiments. Velocity profiles were compared from run to run as a measure of their reproducibility. The surface velocity multiplied by the depth of the water ( $uH$ ) was integrated across sections to estimate volume flux through various sections. Since this flux should have a zero divergence, it serves as a consistency check on the assumption that the whole water column travels with a depth-independent velocity. If the assumption is true, surface velocity measurements can also be used to map cross-stream profiles of the potential vorticity  $q$  and alongstream variations in  $q$ .

I studied the flow fields most intensively in the wide current, rounded corner runs with  $\rho = 0$  and rotation period of 15 s, for which flow rate and Rossby number increased from run "a" to run "e." Velocity profile sections 1 to 3 were perpendicular to the first wall and located 20 cm, 10 cm, and 0 cm, respectively, upstream of the corner. Sections 4 through 9, perpendicular to the second wall, were located 0 cm to 50 cm downstream of the corner at 10 cm intervals. There were enough velocity measurements, and the alongshore variations had a long enough length scale, that a good estimate of the velocity profile could be obtained for each section by using all measurements within 2.5 cm upstream and downstream of the section without regard to the measurements' alongshore positions. Data was collected over the whole

slope region, *i.e.* within 20 cm of the coast. Typically there were several velocity measurements within most 1 cm sub-intervals of this range, with the greatest gaps in coverage sometimes occurring within about 1 cm of the coast and in the region of slow return flow offshore of the jet.

The profiles of alongshore and cross-shore components of velocity ( $u, v$ ) were estimated independently of each other using linear least squares fits to fourth to seventh order polynomials in cross-shore distance  $y$ . No-slip and no flow through the coast were built into the fits by setting the constant terms equal to zero. The polynomials were an appropriate model of the data based on subjective criteria: the polynomial estimates were always close to the average value of the nearest data points and they usually seemed to follow the trend in the data well in each region of the fit. High order polynomial fits are notorious for having extraneous wiggles between data points, but the velocity fits rarely showed this phenomenon except in the reverse flow region of some profiles in which there were large gaps in  $y$  between measurements. Polynomials also give inappropriate results for extrapolation, so the fits were not extended past the range of the data. For each  $u$  or  $v$  profile to be fit, the least squares calculation was computed for polynomials of increasing order starting at fourth order. The order of the polynomial was chosen on the basis of the change in  $\chi^2$ , which is the average sum of squares of residuals. If  $\chi^2$  of a polynomial of order  $M$  was less than 1.01 times  $\chi^2$  of the next polynomial, the  $M$ th order polynomial was chosen. In regions of sparse data, a few of the resulting fits showed oscillations which I believed to be unphysical, and I re-did the least squares fit with a (generally lower order) polynomial which had a smoother profile in the region in question. Velocity measurements ( $u$  and  $v$ ) and accompanying polynomial fits for selected profiles in two runs are shown in Figure 4.5.1.

(a)

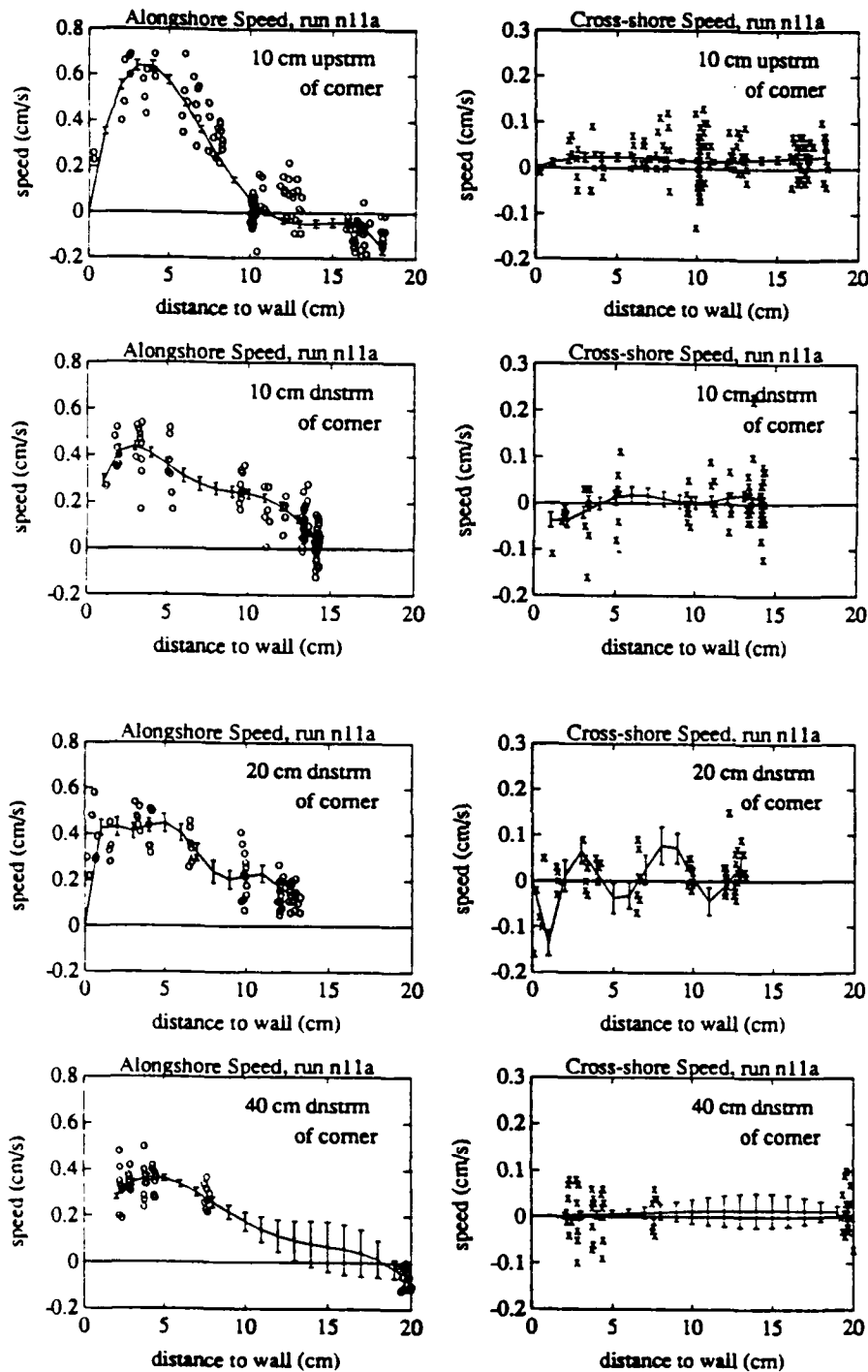
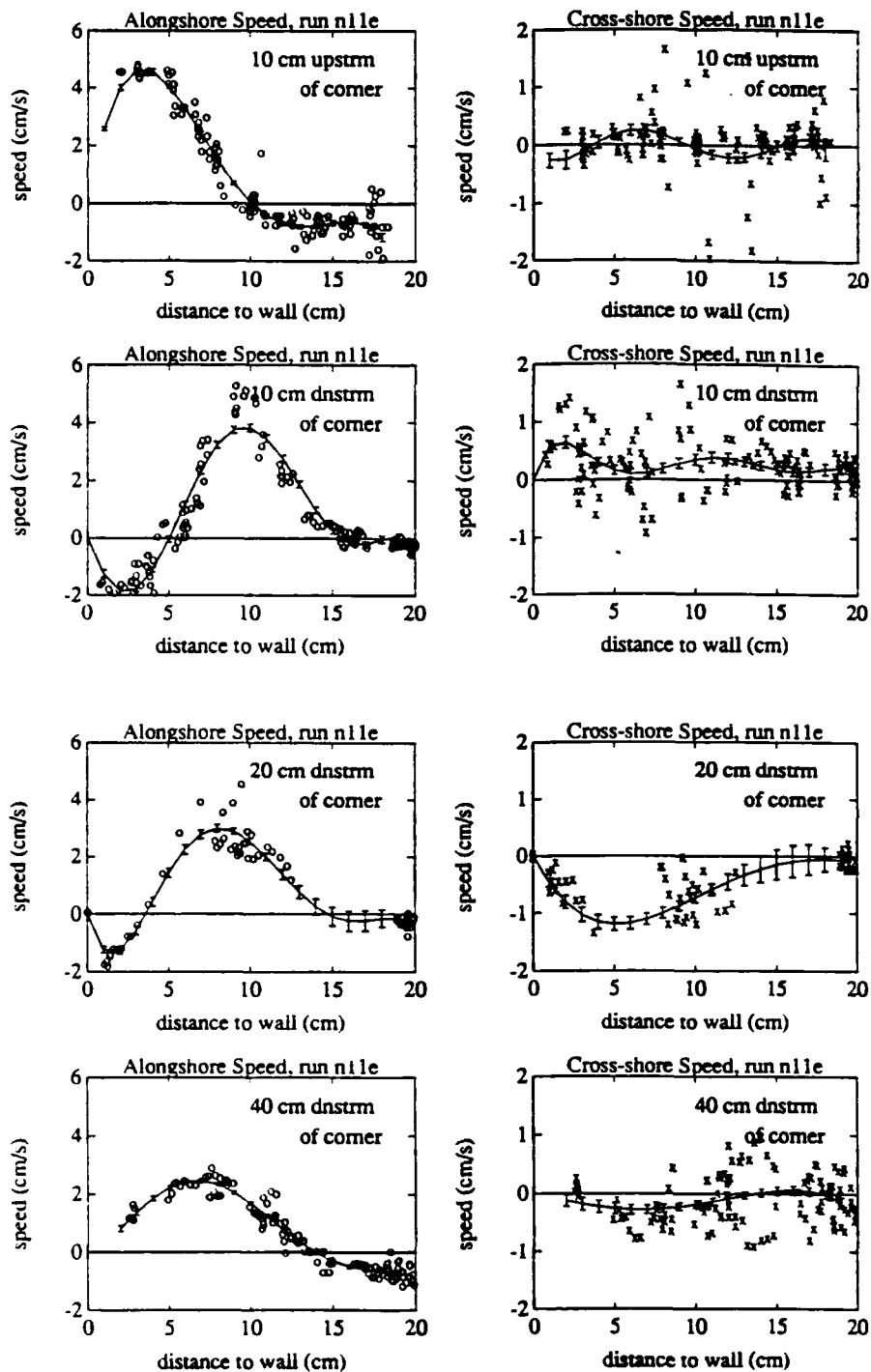


Figure 4.5.1: Measurements and polynomial fits of alongshore and cross-shore components of cross-shore velocity profile for two flow rates in rounded corner,  $\rho = 0$ , 15 sec rotation period experiment. For each run,  $u$  and  $v$  profiles are displayed at 10 cm upstream of corner, and at 10 cm, 20 cm and 40 cm downstream of corner. (a)  $Ro = .08 \pm .01$ . (b)  $Ro = .82 \pm .08$ .



(b)



An explicit analytical fit to a velocity profile is convenient because it is easy to compute derivatives and integrals, such as the volume transport,

$$T = \int_0^y u H dy' \quad (4.5.1)$$

( $y$  is cross-shore coordinate) and the  $\partial u / \partial y$  term needed for potential vorticity, as well as their estimated errors. The covariance matrix of the polynomial coefficients is given by the standard error formula for a linear regression (Press *et al.*, 1986). These error terms are then propagated, taking care to retain both variance and covariance terms, to estimate the errors in  $u$ ,  $v$ ,  $T$  and  $\partial u / \partial y$ , which are functions of the coefficients and offshore distance. The error estimated in this way is based on the assumption that the given polynomial is a valid model for the actual velocity profile. In reality the polynomial consists of the first few terms of the Taylor series of the true profile. The other terms of the Taylor series, which are neglected in using a polynomial, contribute an extra error term which we can expect to be small when the polynomial provides a good fit to the data based on the criteria listed above. To apply the formula to find the covariance matrix, the "instrumental error" of the measurements must be known. Rather than use the estimated measurement error, I used the observed variance of the data,

$$s^2 = \frac{1}{N - M} \sum_{i=1}^N [u_i - u(y_i)]^2, \quad (4.5.2)$$

for  $N$  data points  $(y_i, u_i)$  fit by  $M^{\text{th}}$  order polynomial  $u(y)$ .  $s^2$  includes both measurement error and turbulence in the real flow field. For each run,  $s$  was about 10% of the peak velocity, and was about the same for  $u$  as it was for  $v$ . Assuming the average error in pellet positions is 1 mm for the wide current runs,  $s$  was two to three times larger than the estimated measurement error. Estimated errors in the assumed polynomial fit were typically several times smaller than  $s$ , except in regions of sparse data. This is not surprising, because the expected error in an estimate based on

several data points is typically less than the scatter in the data. In order to compare velocity profiles for different flow rates,  $u$  in each run was scaled by the maximum  $u$  in the first section of the run (20 cm upstream of the corner). As illustrated in Figures 4.5.2a and 4.5.2b, the scaled velocity profiles upstream of the corner are almost identical from run to run. Figures 4.5.2e and 4.5.2f illustrate the generation of reverse flow near the coast and the displacement of the velocity maximum for increasing Rossby number. The profiles in Figure 4.5.2e are taken near the widest part of the gyre, where the strongest current is approximately parallel to the coast. The profile of this current is approximately the same, except for its displacement from the coast, for all the current strengths (and associated gyre sizes) except the smallest. The sections furthest downstream are roughly similar (Figures 4.5.2g,h) from run to run. Figures 4.5.3a,b,c show that the scaled upstream currents in the rounded corner,  $\rho = 0$  runs with 30 s rotation periods are similar to the 15 s rotation period runs. Upstream currents for the sharp corner,  $H_w = 0$  experiments are narrower than the flows shown in 4.5.2 and 4.5.3, but they have a profile shape that is roughly similar to the wider flows, though the narrow flow measurements display greater variation from run to run (see Figure 4.5.4).

Plots of alongshore transport profiles (Figure 4.5.5) imply that the slow counterflow offshore of the coastal current carries almost as much volume flux back towards the current source as the current carries. The low current speeds in the offshore region are offset by the relatively great depth there. In most of the profiles, the peak value of transport was roughly constant from section to section for most sections. However, there is a noticeable peak in section 5 (10 cm downstream of the corner), which has an increasingly anomalous peak transport for increasing Rossby number runs. This is better illustrated in Figure 4.5.6a, which shows that the transport peak is roughly constant from section to section for each run, except for section 5 in the high Rossby number runs. If continuity is to be obeyed by the fluid, the anomalously high transport peak 10 cm downstream of the corner should

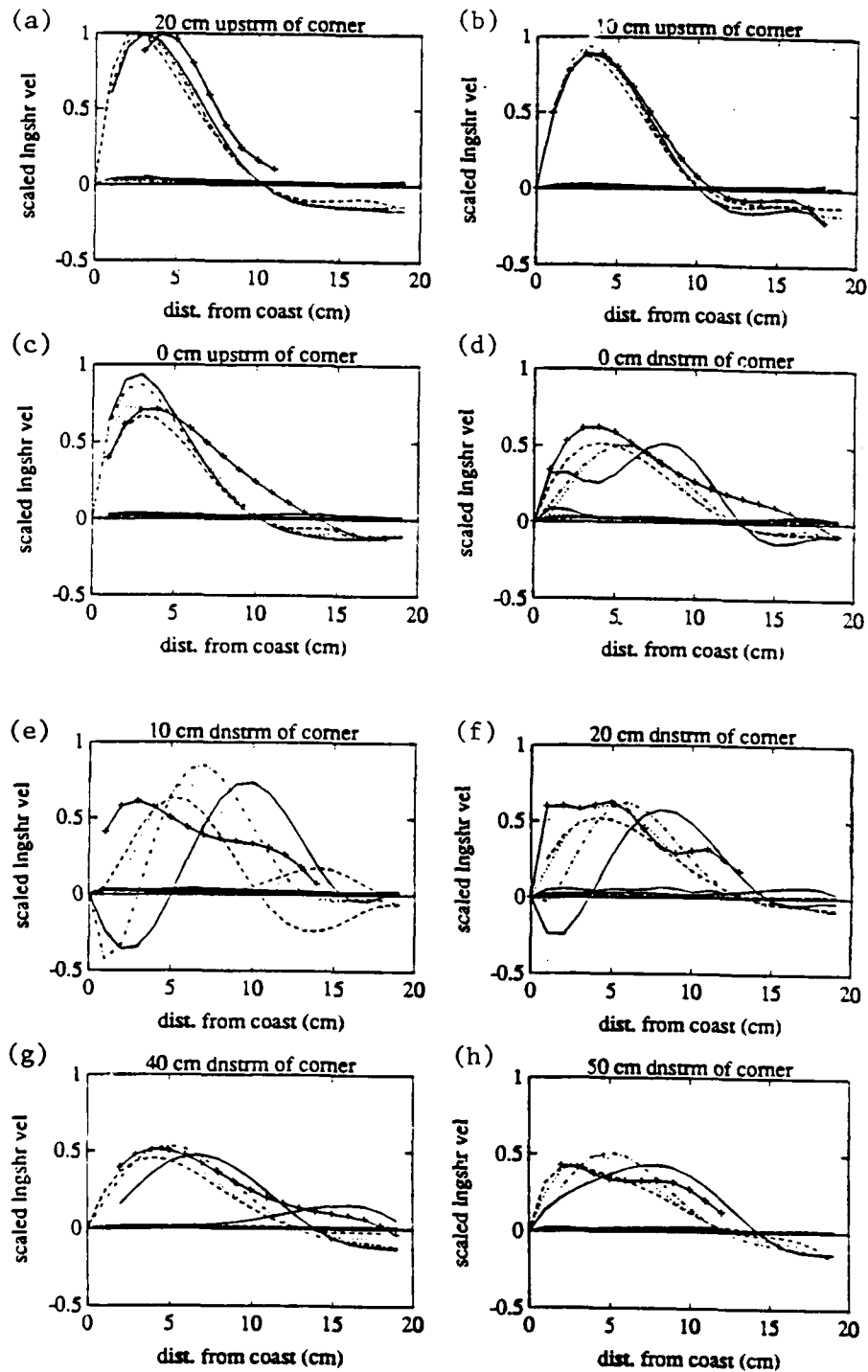


Figure 4.5.2: Alongshore component of velocity scaled by maximum in first section profile for five flow rate runs of rounded corner,  $\rho = 0$ , 15 sec rotation period experiment. In order of increasing flow rate, the runs are represented by a solid line marked by plus signs, a dashed line, a dot-dash line, a dotted line, and a plain solid line. The smaller-value curves show corresponding error estimates. Plots (a) through (c) are profiles perpendicular to first wall and located 20, 10 and 0 cm, respectively, upstream of the corner. Plots (d) through (h) show profiles perpendicular to second wall and located 0, 10, 20, 40 and 50 cm downstream of the corner.

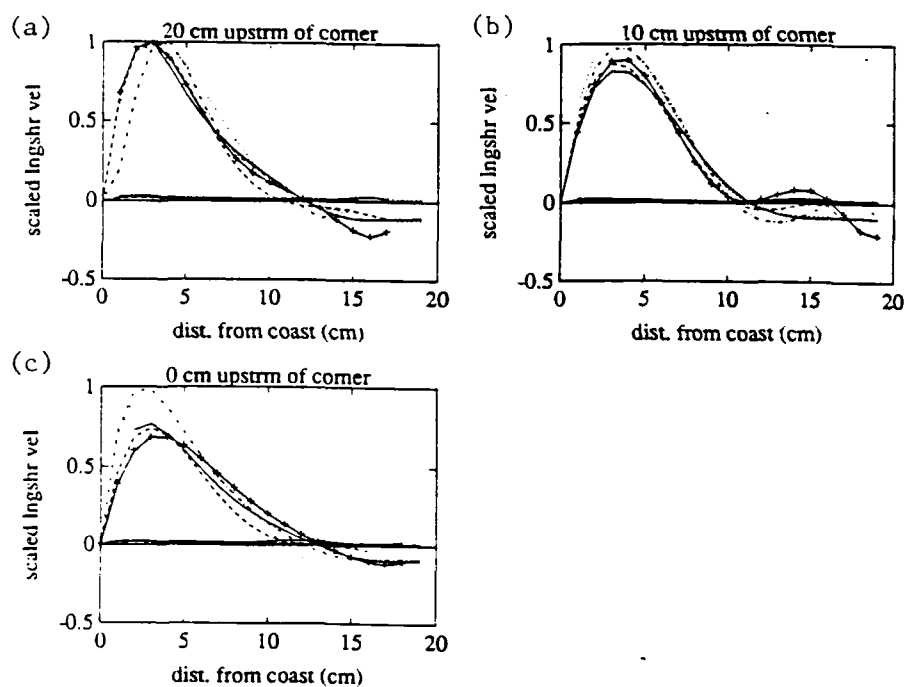


Figure 4.5.3: Same as 4.5.2, for rounded corner,  $\rho = 0$ , experiments with 30 sec rotation periods. Only profiles adjacent to first wall are shown.

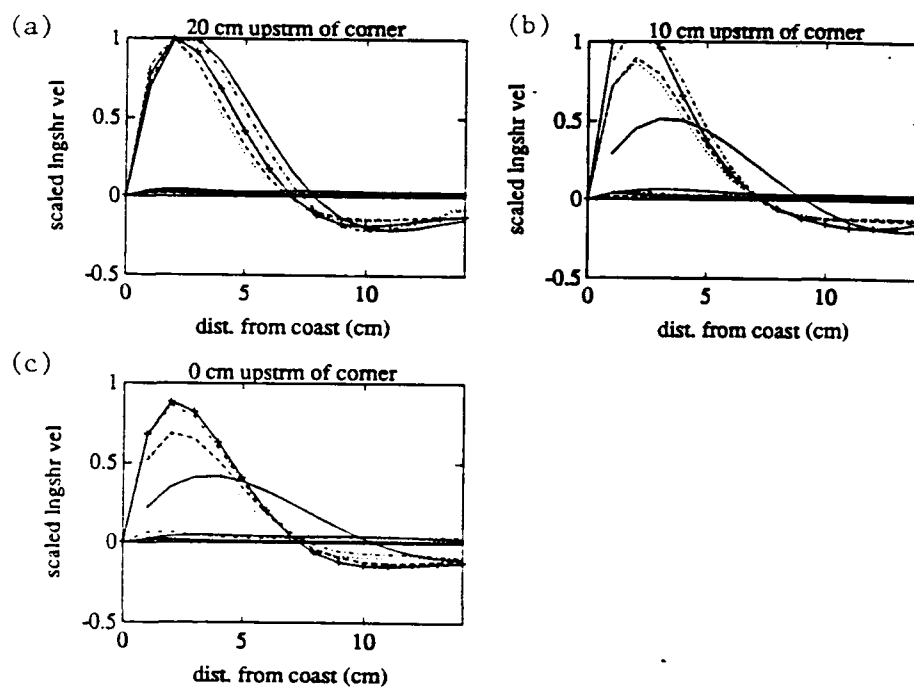


Figure 4.5.4: Same as 4.5.2, for sharp corner,  $H_w = 0$ , experiments with 15 sec rotation periods. Only profiles adjacent to first wall are shown.

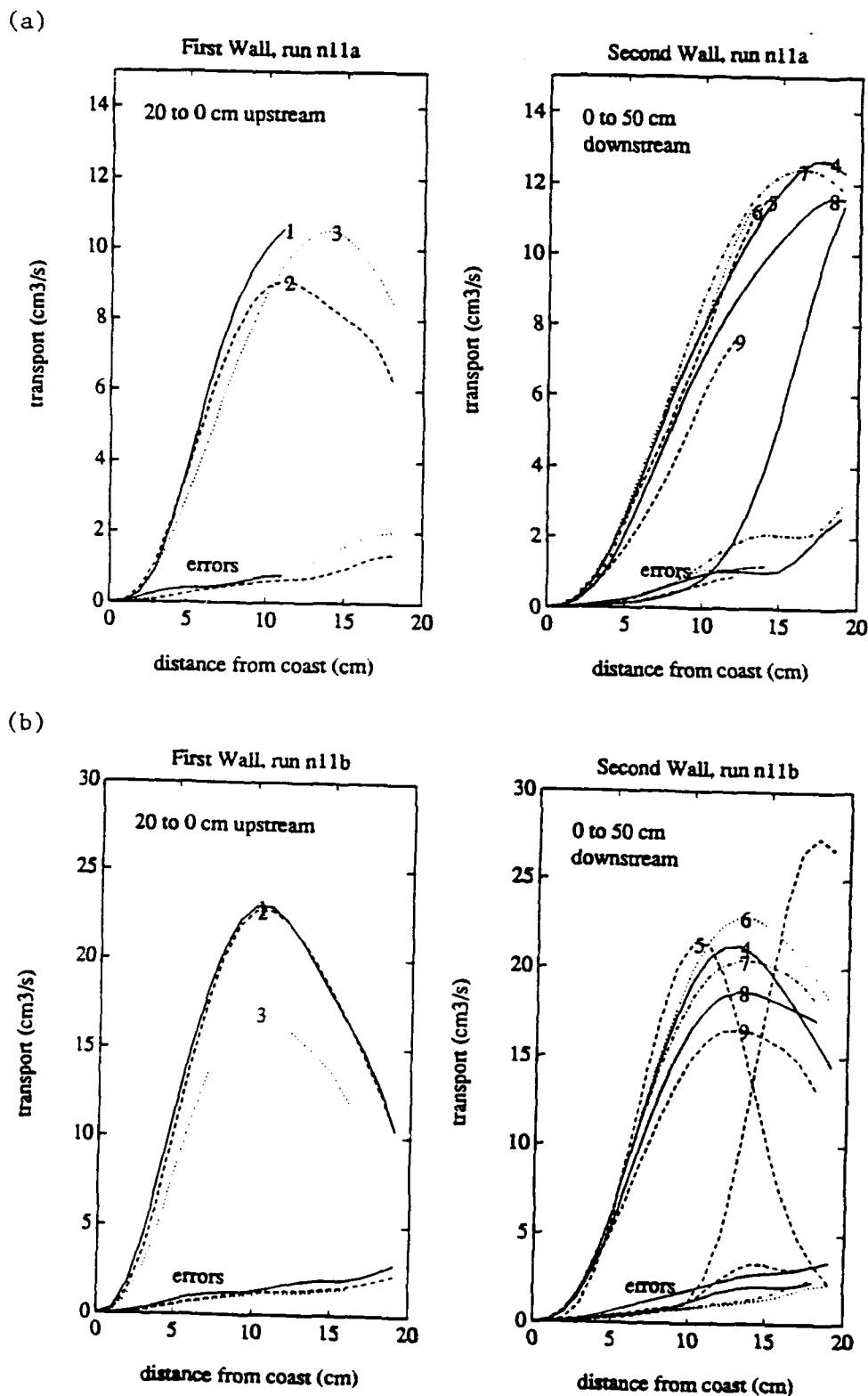
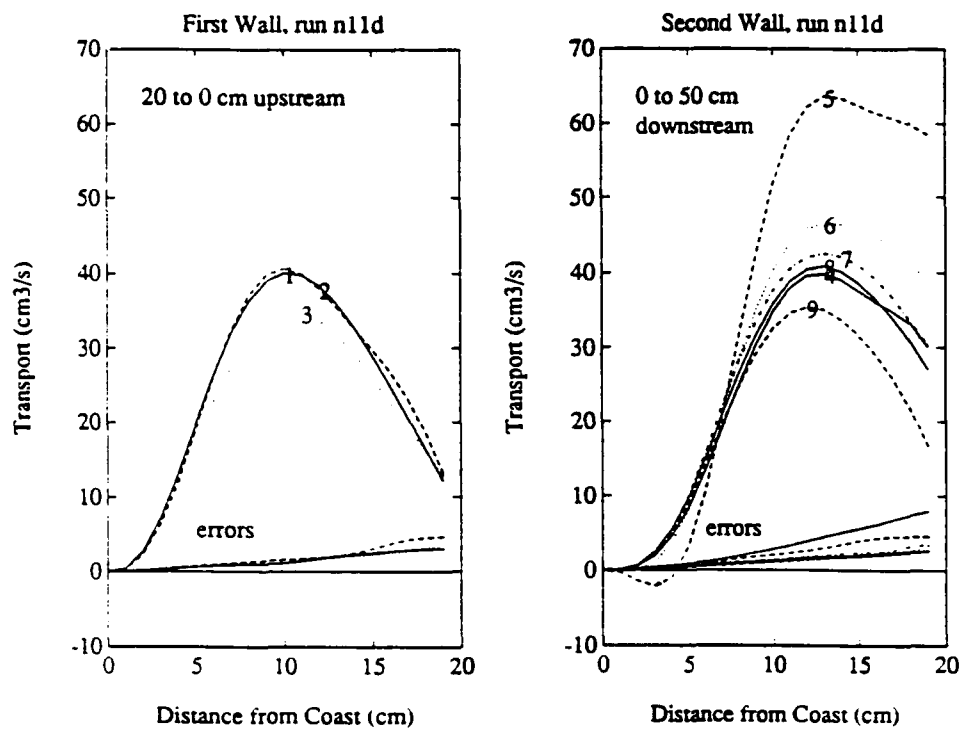
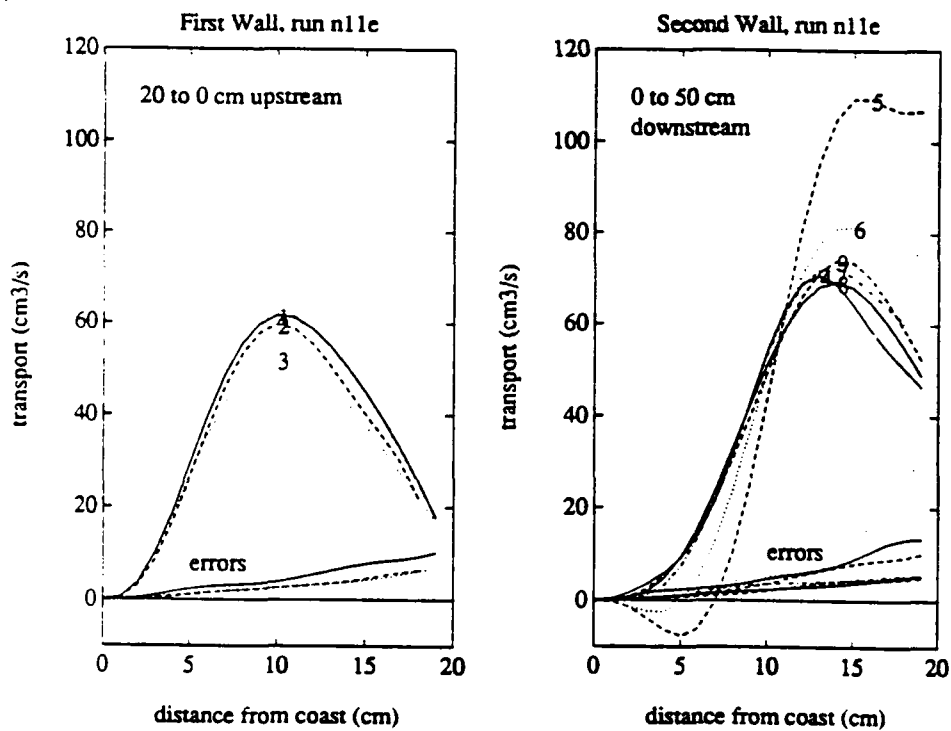


Figure 4.5.5: Profile in  $y$  of the integral of the alongshore volume transport between the coast and  $y$  for experiments with rounded corner,  $\rho = 0$ , and 15 sec rotation period. Plots at left show profiles upstream of corner, at right show profiles downstream (see text for exact locations). Figures (a) through (d) represent five runs with increasing source flow rates.

(c)



(d)





be associated with a cyclonic gyre offshore of the peak. As shown in Figure 4.3.2b, there is no sign of such a cyclonic gyre. Also no significant peak in the cross-stream maximum of the flow speed is apparent in a graph of the flow maximum from section to section (Figure 4.5.6b).

These facts raised the possibility that volume transport as computed from the surface velocity field is not conserved in the presence of a strong gyre. In order to test this hypothesis, the continuity equation was explicitly tested in rectangular cells downstream of the corner. The area integral of the continuity equation for our system is

$$\int_1 uHdy - \int_2 uHdy + \int_3 vHdx + \int_4 vHdx = S, \quad (4.5.3)$$

where the integrals are around the sides of a rectangle and  $S$  is a source term. For perfectly measured time- and depth-independent flow, we should have  $S = 0$ . In reality,  $S$  is made non-zero by measurement error, turbulence, and vertical variations in horizontal velocity. Both measurement error and turbulence were incorporated into the error estimates, so that source or sink terms greater than the estimated error indicate the presence of vertical shear.

The cells of integration were 5 cm by 5 cm. Integration over such a relatively large cell sacrifices horizontal resolution but reduces the error relative to the signal. The integrals in  $y$  were computed from differences in the alongshore transport  $T$ . Integrals in  $x$  were evaluated using values of  $v$  linearly interpolated between cross-shore sections. The results for a run with almost no sign of a gyre, for a run with a moderately sized gyre, and for a run with a large gyre are shown in Figures 4.5.7 to 4.5.9. The diagrams show the fluxes through each side of the rectangular cell and the net flux out of the cell. Accompanying each flux diagram is a similar figure showing the estimated errors.

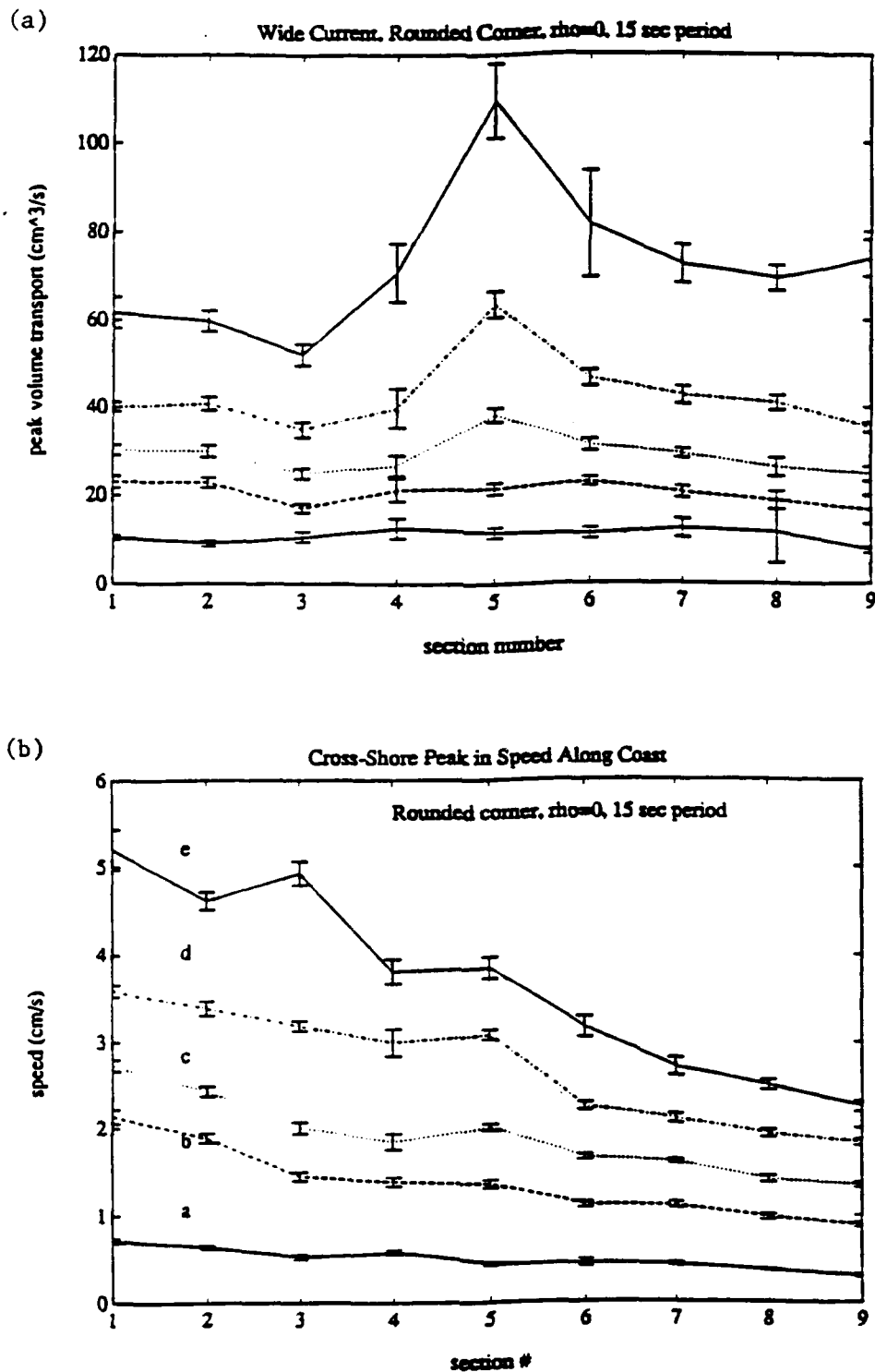


Figure 4.5.6: Cross-shore maxima in transport integral and current speed, as a function of along-shore position of sections (see text for actual section locations), for runs profiled in figure 4.5.5. (a) Maximum in transport integral. (b) Maximum in speed.

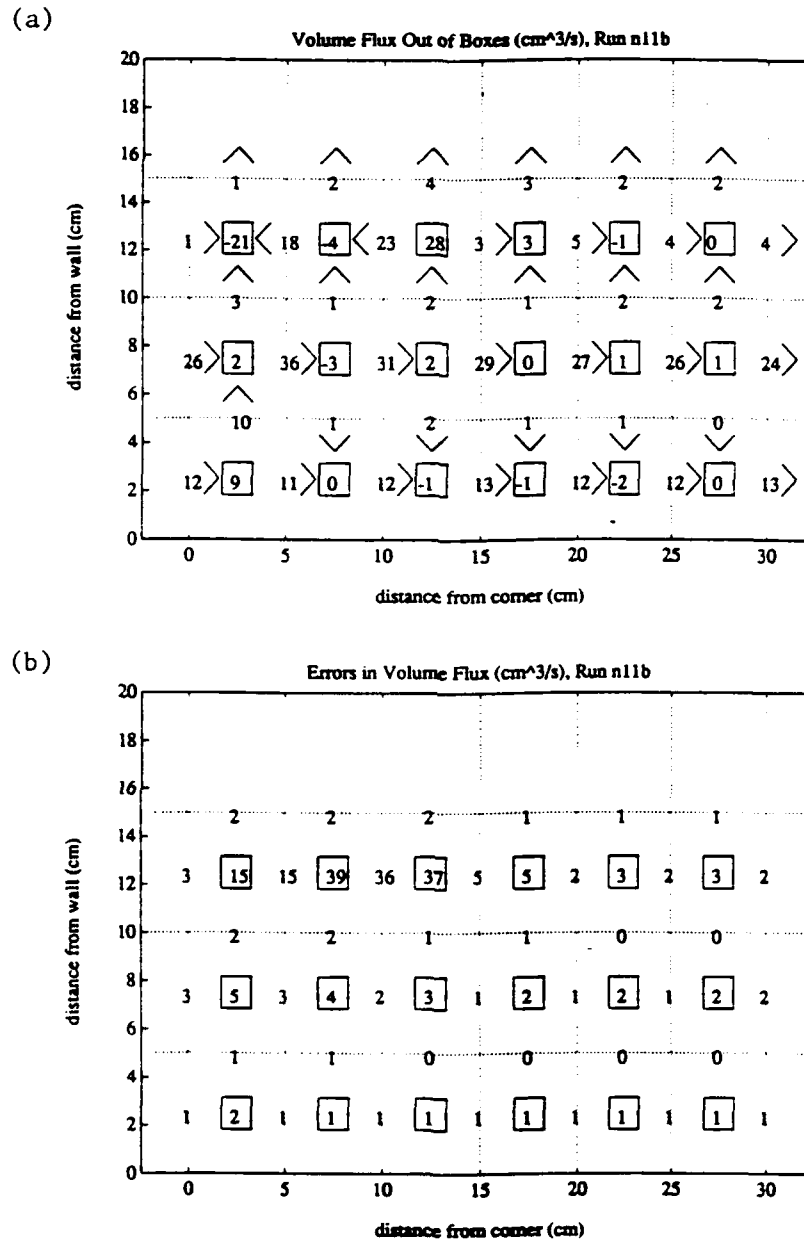
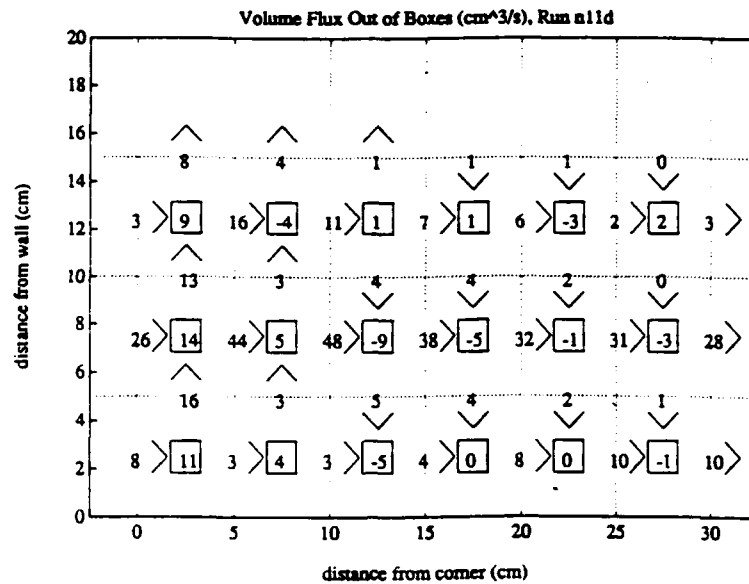


Figure 4.5.7: Volume flux out of rectangular cells for low flow run, rounded corner experiment with  $\rho = 0$  and 15 s rotation period. In this case, all displayed numbers are twice their actual value. (a) Map of fluxes downstream of the corner, where the horizontal and vertical coordinates represent alongshore and cross-shore distances, with the corner at (0,0). Dotted lines indicate boundaries of integration cells. Numbers with arrow superimposed on the boundaries show the magnitude (in  $\text{cm}^3/\text{s}$ ) and direction of volume transport. Each number in a box represents total flux out of cell, so that positive values represent net flow out of box and negative values represent net flow into box. (b) Error estimates associated with each quantity shown in (a).

(a)



(c)

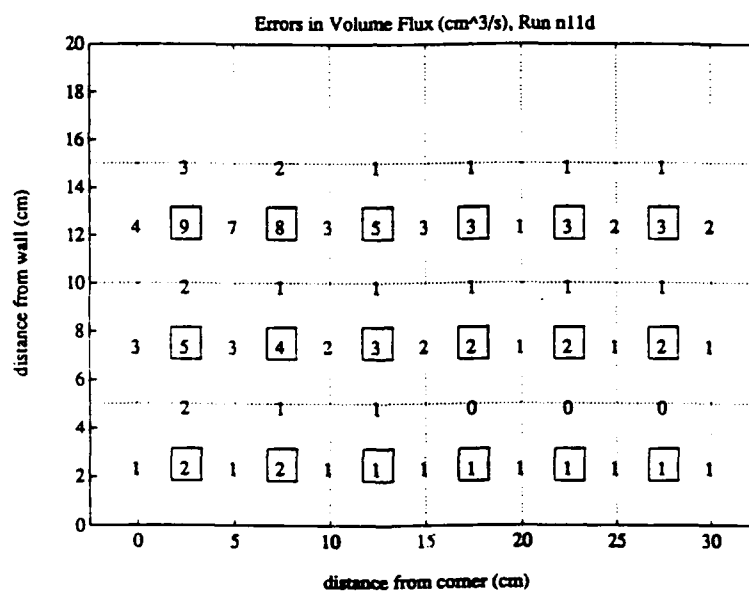
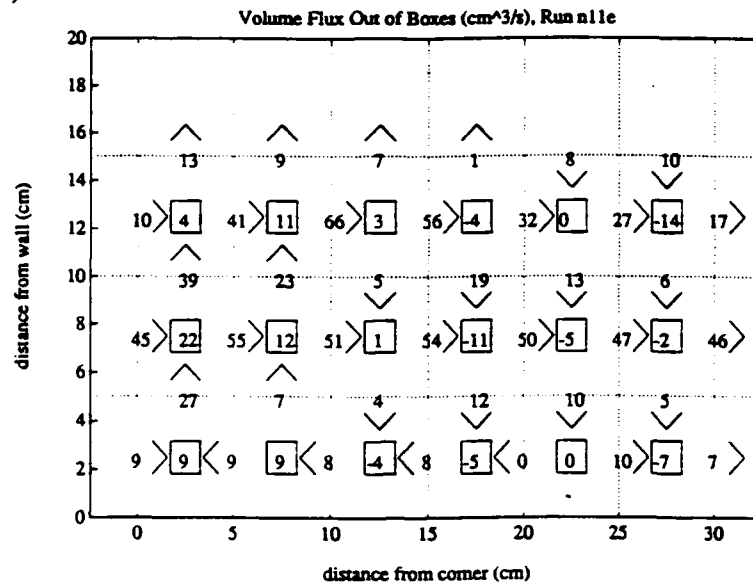


Figure 4.5.8: Same as 4.5.7, for moderate flow run, in which gyre is visible.

(a)



(b)

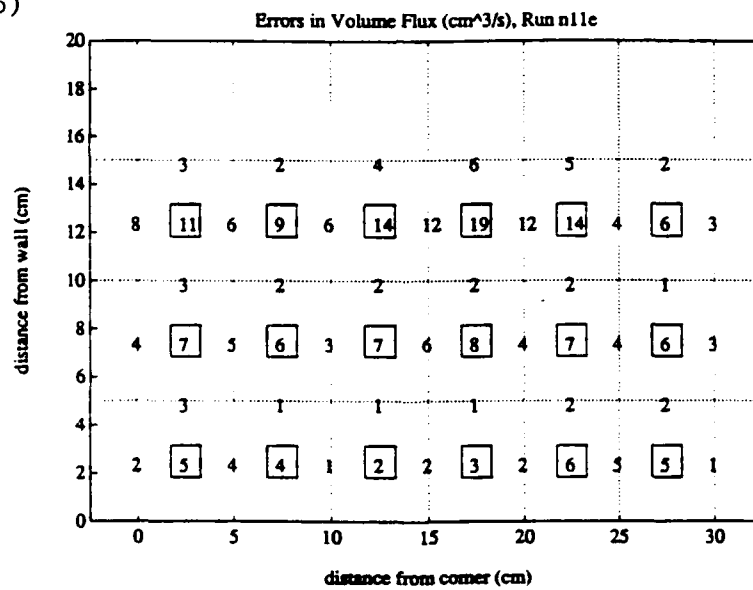


Figure 4.5.9: Same as 4.5.7, for high flow run, in which gyre is visible.

When no eddy is apparent (Figure 4.5.7), the only cell with a flux imbalance much greater than the noise is the one adjacent to the corner. In the rest of the cells within 10 cm of the coast, both the source term and the errors are about 10% of the throughflow. In cells farthest from the coast, the flux terms are dominated by noise. In Figure 4.5.8, the eddy is still too small to produce a reverse transport in cells adjacent to the coast, but the large offshore fluxes near the corner and the significant onshore fluxes a few cells downstream show a clear separation of the axis of the stream from the coast and return to the coast downstream. Where  $v$  is large and positive (offshore transport), there appears to be a source, and where  $v$  is large and negative, there appears to be a sink. The same tendency, with even larger source and sink terms, occurs in the run with a larger eddy (Figure 4.5.9). In both runs,  $S$  is roughly proportional to the average of  $v$  over the onshore and offshore sides of the cell. The constant of proportionality was calculated using a least squares fit to the data from the high Rossby number run displayed in Figure 4.5.9. This constant was found to be  $.48 \pm .09$ , with the linear fit apparently a good model based on its reduced chi-square of .6 (see Bevington, 1969).

The transport was calculated assuming that the velocity was independent of depth, and that this homogeneous layer of uniform velocity increased in depth to continue reaching to the bottom as the water flowed offshore. If the column of the flowing water separated from the sloping floor as the column flowed offshore, however, it would appear to be transporting more water as the bottom depth increased, even though the actual transport could not change. When the column travelled back towards the coast, its apparent transport would decrease. This is what was observed in the experiment. Since the vertical profile of velocity was not measured in the experiment, we can not tell if this is the actual explanation for the observations. However, separation of the current from the bottom would be a simple explanation for the observed changes in the quantity  $uH$ .

The hypothesis that the current separates from the bottom is supported by the fact reported above that, within experimental error, the divergence of  $\mathbf{u}H$  is equal to  $sv$ , where  $s = .5$  is the bottom slope. A simple application of the product rule shows that  $\nabla \cdot (\mathbf{u}H) = \mathbf{u} \cdot \nabla H + H \nabla \cdot \mathbf{u}$ . Since  $H = sy$ , we have  $\nabla \cdot (\mathbf{u}H) = sv + H \nabla \cdot \mathbf{u}$ , which together with our experimental result  $\nabla \cdot (\mathbf{u}H) = sv$  implies that  $\nabla \cdot \mathbf{u} = 0$ : the surface flow is nondivergent. If we hypothesize that the horizontal velocity is vertically uniform down to a depth  $h$  which may be less than or equal to the fluid depth  $H$ , then continuity tells us that  $\nabla \cdot (\mathbf{u}h) = 0$ . Applying the product rule to this equation and using the nondivergence of  $\mathbf{u}$ , we find that  $\mathbf{u} \cdot \nabla h = 0$ . This means that the hypothesis that the current is confined to a layer of uniform flow extending down from the surface is consistent with the depth of this layer being uniform along each streamline, just as we might expect if the current were to separate from the bottom as it flows offshore.

These experiments were conducted with the theory of rotating, homogeneous, depth-independent flow in mind, but the most interesting phenomena occur in the limit where the Taylor-Proudman theorem and the hydrostatic approximation break down. Since these are the constraints which allow us to eliminate vertical shear in our fluid layers, let us examine these relations to see what bearing they have on the laboratory experiments. The Taylor-Proudman theorem is associated with low Rossby number flow, while the hydrostatic approximation is associated with flows of low aspect ratio. If the corner gyres produced in the laboratory experiments are a product of the moderately high Rossby number of the experiments, then it is plausible that they may exist in nature, where boundary currents sometimes have a fairly high Rossby number. However, oceanic currents typically have an aspect ratio much smaller than that produced in these experiments, so it is especially important to isolate the role of each of these parameters.

The hydrostatic approximation states that the pressure at any point is dependent only on the weight of the fluid above. Following Pedlosky (1982), we can derive it from the equations of motion, which for a homogeneous, steady-state fluid are

$$uu_x + vv_y + ww_z - fv = -p_x + \nu \nabla^2 u \quad (4.5.4a)$$

$$uv_x + vv_y + ww_z + fu = -p_y + \nu \nabla^2 v \quad (4.5.4b)$$

$$uw_x + vw_y + ww_z = -p_z + \nu \nabla^2 w \quad (4.5.4c)$$

$$u_x + v_y + w_z = 0, \quad (4.5.4d)$$

where  $(u, v, w)$  are the velocity components in  $(x, y, z)$  coordinates,  $f$  is the Coriolis parameter,  $\nu$  is the viscosity, and  $p$  is the dynamic pressure ( $=0$  at all depths for a motionless fluid), divided by the density. The criterion for the hydrostatic approximation to apply appears when we non-dimensionalize the equations. The horizontal length and speed scales are  $L$  and  $U$  and the vertical length and speed length scales are  $H$  and  $W$ . The continuity equation implies  $W/H = U/L$ . There are two scales for pressure,  $P_H$  and  $P_V$ , which represent the size of pressure variations over the horizontal and vertical length scale, respectively. Useful non-dimensional parameters are the aspect ratio  $\delta = H/L$ , the Rossby number  $\epsilon = U/fL$ , and the vertical Ekman number  $E = \nu/fH^2$ . Now the non-dimensionalized momentum equations can be written

$$\epsilon(uu_x + vv_y + ww_z) - v = -(P_H/fUL)p_x + E(\delta^2 \nabla_H^2 + \partial^2/\partial z^2)u \quad (4.5.5a)$$

$$\epsilon(uv_x + vv_y + ww_z) + u = -(P_H/fUL)p_y + E(\delta^2 \nabla_H^2 + \partial^2/\partial z^2)v \quad (4.5.5b)$$

$$uw_x + vw_y + ww_z = \frac{P_V}{(UH/L)^2}p_z + (E/\epsilon)(\delta^2 \nabla_H^2 + \partial^2/\partial z^2)w, \quad (4.5.5c)$$

where  $\nabla_H^2$  is the horizontal component of the Laplacian operator. We use these equations to determine the relative sizes of vertical and horizontal variations in  $p$ . Assuming that the pressure terms are  $O(1)$  in both the horizontal and vertical momentum equations, we obtain  $P_V/P_H = \epsilon\delta^2$ . Therefore the horizontal pressure gradients can



be assumed to be approximately constant with depth when  $\epsilon\delta^2$ , which we can call the "hydrostatic parameter," is very small. When the hydrostatic parameter is small, it is traditional to assume that in addition to the dynamic pressure gradient being depth-independent, the horizontal velocity is also depth independent. For a flow in which viscous effects are confined to thin boundary layers at the upper and lower and side edges of the fluid, this is a reasonable assumption because there is nothing to force the existence of a vertical shear. However, it is important to note that the hydrostatic approximation does not force the velocity to be depth-independent. It does force the sum of the advection terms and Coriolis term to be depth-independent. The only explicit constraints come from the vorticity equation, from which the Taylor-Proudman theorem is derived.

Shallow water dynamics is completely determined by the evolution of the vertical component of the vorticity, but now we need to examine the full vorticity vector, which in dimensional terms is

$$\omega \equiv \nabla \times \mathbf{u} = (w_y - v_z)\hat{\mathbf{x}} + (u_z - w_x)\hat{\mathbf{y}} + (v_x - u_y)\hat{\mathbf{z}}. \quad (4.5.6)$$

We obtain the non-dimensional vorticity equation by taking the curl of the non-dimensional momentum equations. The  $x$ -component of the vorticity equation can then be written

$$\begin{aligned} \epsilon \mathbf{u} \cdot \nabla (\delta^2 w_y - v_z) + \epsilon (\delta^2 w_y - v_z)(v_y + w_z) + \epsilon (\delta^2 u_y w_x - u_z v_x) - u_z = \\ E(\delta^2 \nabla_H^2 + \partial^2 / \partial z^2)(\delta^2 w_y - v_z), \end{aligned} \quad (4.5.7)$$

with a similar term for the  $y$ -component.

When  $\epsilon$  and  $E$  are much smaller than  $O(1)$  and  $\delta$  is not much greater than  $O(1)$ , the horizontal vorticity equations reduce to  $\mathbf{u}_z = 0$ : the Taylor-Proudman theorem. Notice that the constraints on the aspect ratio necessary to make the theorem valid are rather weak ( $\delta$  must not be much greater than one). If we look at the equation above in the limit in which  $\delta$  is small but  $\epsilon$  may not be small, all the

terms which do not have a factor of vertical shear become negligible. In this limit the equation states that the change in the vertical shear as we follow a water parcel is proportional to the vertical shear. Physically, this means that in low aspect ratio flow, a water parcel can not increase its vertical shear unless it already has some vertical shear to begin with. This is in contrast to flow with  $\delta$  of order unity, in which case tilting of vorticity tubes can generate vertical shear.

In the laboratory experiments, the depth of the fluid varied from zero at the coast to  $sL$  at the edge of the current ( $y = L$ ). A reasonable scale for  $\delta$  is  $\delta = s$ . For water flowing around the gyre in the laboratory, both mechanisms of changing vertical shear are present: the failure of the Taylor-Proudman theorem permits the existence of vertical shear at the current source which can be amplified as the current flows around the corner, and the relatively large aspect ratio ( $s = .5$ ) permits twisting of vortex tubes to generate shear. In oceanic flows, where  $\delta$  is presumably small, the second mechanism is not available. However, all real flows possess a source of  $u_z$ , namely the shear layer at the bottom of the current. Just as separation from a side wall may be caused by a flow reversal in the lateral viscous boundary layer, so separation from the bottom may occur due to processes in the bottom viscous boundary layer. In nonrotating two-dimensional theory the ease with which the boundary layer could separate depends on the slope of the bottom and hence the aspect ratio, but as mentioned in Chapter 1, even a quite mild adverse pressure gradient, corresponding to a small aspect ratio, typically induces separation. It is not clear how such two dimensional results carry over to three-dimensional rotating flows, in which the Ekman spiral is bound to play some role in the boundary layer. Even a relatively simple example of separation from a sloped bottom, such as flow in a straight rotating channel that deepens in the alongstream direction, must be solved in three dimensions, because the Coriolis force induces cross-stream velocities and pressure gradients which vary in the along-stream direction.

## 4.6. Discussion and Conclusions

A barotropic coastal current flowing over topography that slopes upward to the coast can generate a single, steady state anticyclonic gyre just downstream of a corner. The current flows around the gyre and re-attaches itself to the coast downstream of the gyre. This basic picture is true for a wide range of topographies, including those with zero coastal depth, finite coastal depth, a sharp corner, a rounded corner, a sink downstream of the corner or no sink downstream.

The behavior of the sloping bottom current is different from the unstable flow patterns of a jet over a flat bottom (Stern and Whitehead, 1990), which generates eddies of both signs that allow the current to globally separate from the coast at the corner, never to return. In my experiments, as the change in depth of the topography across the current decreased relative to the depth of the current at the coast, eddies appeared at the outer edge of the current, but global separation was not observed in the parameter range I studied, probably because a mass sink downstream of the corner imposed an additional constraint on the flow. The sloping bottom gyre looks similar to anticyclones produced downstream of a corner by a baroclinic current (Whitehead and Miller, 1979; Kawasaki and Sugimoto, 1984; Boyer and Tao, 1987; Bormans and Garrett, 1989; and Chapter 3 of this thesis), but in the baroclinic case (except for the case of Boyer and Tao) the gyres grew for as long as they were observed or until they separated from the current or ran up against walls, while in the barotropic flow the eddy attained a constant size within a few rotation periods. Stern and Whitehead's experiments probably give such a different result from all the other experiments because of instability in their upstream current.

I varied both Rossby and Ekman numbers of the flow upstream of the corner, but the Ekman number had an ambiguous influence on gyre parameters, with no clear trend except for the  $H_w = 0$ , sharp corner topography, which produced a larger

eddy for a given Rossby number when the Ekman number was smaller (less friction). It would not be surprising if Ekman number had its most pronounced effect when  $H_w = 0$ , but it is hard to see why this effect would not be seen in the rounded corner experiments. As expected, larger eddies were produced for the same Rossby number when the relative change in depth across a current width was decreased, and smaller eddies were produced as the radius of curvature of the coastline increased. However, the comparison of sharp corner and rounded corner did not reveal any clear influence of the corner sharpness on the gyre size.

For Rossby number on the order of .1, the gyre was either not present or too thin to detect. For larger Rossby numbers, the half width of the gyre (as measured by the distance from the coast to the center of the gyre) was approximately proportional to Rossby number, while the half length of the gyre (alongshore distance from the corner to the center of the gyre) was about as great as the current width for the thinnest gyres and increased linearly with Rossby number. The relation between Rossby number and gyre half width can be restated as  $u/fx_c = B$ , where  $u$  is the maximum current speed (measured just upstream of the corner),  $f$  is the Coriolis parameter,  $x_c$  is the gyre half width, and  $B$  is a constant which depends on the relative change in depth of the fluid across the width of the current. This simple relation is similar to the criterion for gyre formation by a baroclinic current flowing around a wall with a radius of curvature  $x_c$ .

The existence of such a simple scale relation for gyre size is quite evocative, because it directs our attention away from the critical condition for gyre formation and to the properties of currents which have actually formed a gyre. In other chapters, we have tended to look at the generation of an eddy as a consequence of the failure of the current to be able to go around a corner without leaving the coast. The behavior of the barotropic gyres over a sloping bottom invites us to view the lack of an eddy as the limit of a small gyre. The general increase in gyre size with Rossby number

should be caused by the relaxation of the inhibition on cross-isobath flow for high Rossby number. However, the fact that the current flows in essentially an inertial circle downstream of the corner is puzzling. A particle travelling on a rotating plane would be pushed by the Coriolis force into an inertial circle, but fluid parcels do not generally act like independent parcels. The inertial radius is the length scale over which nonlinear terms in the momentum equation act, as described in Chapter 2, but for currents in a barotropic flow should be completely described by the vorticity and continuity equations, making the momentum equation irrelevant to predicting the flow pattern.

In the laboratory, the production of a gyre was accompanied by alongstream variations in the vertical profile of the horizontal velocity. Applying the continuity equation to the surface velocity field gave results that were consistent with the depth of the current remaining constant in places where the current flowed into deeper water or returned to shallower water. Since I only measured the flow velocity at the surface of the water, the actual vertical variations in velocity remain unknown. Gyres were produced when the Rossby number was no longer small, so that the Taylor-Proudman theorem no longer held and the vertical shear could not be assumed to be confined to a thin bottom Ekman layer. Therefore models which do not include vertical shear, such as the hydraulic models of Chapter 2, leave out a degree of freedom which is important in the dynamics of the barotropic current separation observed in the laboratory. Analysis of the vorticity evolution equations shows that vertical shear must come from vertical shear in the current as it originates from the source, from the bottom boundary layer, or, for flows of moderate aspect ratio as in these experiments, from the tilting of vorticity filaments.

The separated currents were roughly steady and took a form which did not seem to depend on the past history of the flow. For instance, raising or lowering the flow rate to a certain value yielded the same result. Therefore steady state theory

should account for the form of the flow and the  $u/fx_c$  relation for the size of the gyre. As in the baroclinic flows, the question of whether friction is responsible for the current separation is left open by the experiments. Friction or mixing must be important in maintaining the anticyclone, because the streamlines in the anticyclone are closed and friction with the sloping bottom and wall would spin down the gyre unless vorticity is transported across streamlines from the current originating upstream of the corner. The gyre does not seem to be necessary for the separation of streamlines at the corner, because in some flows (see Figure 4.3.3a) the current separated even though no gyre formed. If the trend in Ekman number for gyre size in the case of one topography is real, it points to a frictional influence, but the absence of the trend with the other topographies makes the relation suspect. A frictional separation mechanism must involve separation of the flow both from the coast and from the floor. Since the size of the gyre is affected by the relative depth change  $H_w/(H_e - H_w)$ , such a mechanism must explain how such a separated current would feel the bottom.

## Appendix to Chapter 4

### 4.A. Jitter Removal

In the wide current runs, which had a higher spatial resolution than previous runs, there were clear signs of camera jitter with amplitudes as high as  $O(1 \text{ cm})$  in "motionless" pellets that were fixed to the walls as reference marks. The reference pellet at the corner (near the center of the tank) appeared to move in a circle, while each of the pellets on the first and second walls far from the corner moved in an ellipse with its major axis perpendicular to a radial line from the center of the tank to pellet. This apparent motion could be decomposed into two elementary solid body motions. In one, the whole field of view orbits in a small circle, with the orientation of the field of view remaining fixed; in the other, the orientation of the field oscillates around the center like a small amplitude torsion pendulum. Both motions had the same period as the rotation of the tank. The orbital motion is caused by a small dis-alignment between the tank's rotation axis and the camera's rotation axis. The angular oscillation is more mysterious, but must be caused by either the camera or the tank slowing down and speeding up by about 1% in the course of one rotation period.

Denoting the actual position of a point in the tank by  $(x, y)$ , its apparent position due to orbital motion by  $(x_*(t), y_*(t))$ , and its apparent position due to both orbital and twisting motions by  $(x'(t), y'(t))$ , we model the motion artifacts as

$$x_* = x + d_x \quad (4.A.1a)$$

$$y_* = y + d_y \quad (4.A.1b)$$

with  $d_x = r \cos(-\omega t + \phi)$  and  $d_y = r \sin(-\omega t + \phi)$ , where  $\omega$  is the tank rotation period and  $r$  is the centering discrepancy, and

$$x' = x_* \cos \theta - y_* \sin \theta \quad (4.A.2a)$$

$$y' = x_* \sin \theta + y_* \cos \theta, \quad (4.A.2b)$$

where  $\theta(t)$  is the angular displacement due to twisting motion. Since the angular motion is of small amplitude (only about one degree), we can approximate the second set of relations by

$$x' = x_* - y_* \theta \quad (4.A.3a)$$

$$y' = y_* + x_* \theta. \quad (4.A.3b)$$

We assume that  $\theta$  varies sinusoidally in time, so that

$$\theta = a \cos \omega t + b \sin \omega t. \quad (4.A.4)$$

Letting  $c = r \cos \phi$  and  $d = r \sin \phi$ , combining the expressions for  $(x_*, y_*)$  and  $(x', y')$ , and neglecting terms which are products of the two kinds of motion, we get

$$x' = x + p_1 \cos \omega t + p_2 \sin \omega t \quad (4.A.5a)$$

$$y' = y + p_3 \cos \omega t + p_4 \sin \omega t, \quad (4.A.5b)$$

where  $p_1 = c - ay$ ,  $p_2 = d - by$ ,  $p_3 = d + ax$ ,  $p_4 = -c + bx$ . Thus given a time series of apparent positions of a point, least squares fits to the  $x$  and  $y$  coordinates yield  $(x, y, p_1, p_2, p_3, p_4)$ , from which we can find the motion parameters  $(a, b, c, d)$ . Once these parameters are found for a particular point, they can be used to find the actual position of other points (such as pellets moving with the flow) from the apparent positions. We invert equations (A.5a,b) to get

$$x = \frac{x' - d_x + \theta(y' - d_y)}{1 + \theta^2} \quad (4.A.6a)$$

$$y = \frac{y' - d_y - \theta(x' - d_x)}{1 + \theta^2}. \quad (4.A.6b)$$



This model accounted for much of the motion of the ostensibly fixed pellets at the ends of the first and second walls. Typically, the standard deviation of the position of such a point was reduced from around .2 cm and .5 cm in the radial and tangential directions to .1 cm or less in both directions. The path of each "motionless" point generally looked well-fit by a sinusoid, with no obvious patterns in the residuals. Given the .15 cm radius of the tracer pellets and the .4 cm pixel width, the residuals can be plausibly attributed to noise. For each run, the motion parameters were estimated from either one or two fixed pellets, depending on how good the data from each pellet was. In cases for which two pellets were used, the parameters obtained from the two were within ten percent of each other, and the two sets of parameters were averaged before inverting the positions of the floating pellets. Once the motion artifacts were removed from the path data in this way, the velocity fields looked noticeably cleaner. In particular, waves in the paths of slow-moving pellets offshore of the coastal current disappeared after correction.

## Chapter 5.

# Summary and Conclusions

Laboratory experiments showed that an anticyclonic gyre can be produced at a corner by a current which flows along the coast both upstream and downstream of the gyre. A surface density current will produce a growing anticyclonic gyre similar to that observed by Whitehead and Miller (1979), Bormans and Garrett (1989) and Kawasaki and Sugimoto (1984) for flow emerging from a channel. A barotropic current over a sloping bottom generates a gyre which quickly attains a steady state. This behavior is qualitatively different from the flow separation that a boundary current undergoes at a sharp corner in a barotropic system with a flat bottom.

Since two-layer coastal currents and two-layer strait-basin flows produce similar eddies, the dynamics governing the eddy generation is probably similar, so that studies of either system extend our knowledge of the behavior of both kinds. To the criteria for gyre production by Bormans and Garrett (1989) and Kawasaki and Sugimoto (1984), we added another, that the corner angle must attain a minimum value in order to form a gyre. Angles which did not produce an eddy nevertheless displayed an asymmetry between the flow upstream and downstream of the corner; as the critical angle was approached from below, the flow near the wall downstream of the corner decreased, displaying a trend which culminates in reversed flow and gyre formation at the critical angle. The experiments also showed that the characteristics of the eddies are the same for very different initial conditions, indicating that it is not necessary to understand the details of the initial interaction of the nose of the current with the corner in order to explain gyre formation. The relative depths of the upper and lower layer did not affect the qualitative eddy features or the approximate critical angle for gyre formation, but a shallower lower layer produced a faster growth rate when an eddy was generated at the corner and a solitary wave propagating away

from the corner when no corner eddy was generated. This indicates that baroclinicity affects the production of a gyre, but it does not prove that baroclinicity is essential for gyre formation, especially in light of Werner *et al.*'s (1988) reduced gravity model simulation of the Alboran Sea gyre. When the surface current was accompanied by a countercurrent in the lower layer, a cyclonic eddy formed at the corner in the lower layer. At a right angle corner, the two vortices propagated away from the coast, probably due to heton-like coupling between them. When the corner angle was  $45^\circ$ , the gyres did not drift away. This indicates that there are two critical angles or radii of curvature for the curved or sharp corner systems: one for eddy generation and one for eddy shedding.

The angle criterion described above is of oceanographic interest because it limits the coastal locations where we might expect corner eddies to appear. The unimportance of the initial condition details shows that an oceanic coastal current need not be impulsively started in order to have the potential to generate an eddy. While the anticyclones generated in the laboratory experiments needed to couple with cyclones caused by flow in the other layer in order to propagate away from the coast, this very mechanism is not ruled out for the Mediterranean Outflow, which has oppositely directed currents both above and below.

A barotropic pumped current flowing over a sloping bottom behaved very differently than a similar current flowing over a flat bottom. The flat bottom current was turbulent and for a sufficiently large corner angle globally separated from the corner in a series of cyclones and anticyclones (Stern and Whitehead, 1990). The sloping bottom current was relatively laminar and formed a single anticyclonic gyre immediately downstream of the corner. In all runs, the corner was a right angle, but various topographies were used, including a sharp corner, a rounded corner for two radii of curvature, and various water depths at the coast. For each topography, the width of the gyre was proportional to the Rossby number of the upstream flow for

Rossby numbers of approximately .2 to 2. In other words, for a given topography the radius of the gyre was proportional to the inertial radius  $u/f$ , with the proportionality constant between .5 and 1 for different topographies. Analysis of the volume flux based on the measured surface velocity showed that the assumption of depth-independent horizontal velocity was not consistent with the continuity equation in the gyre in places where the flow was directed across isobaths. This indication of vertical shear became more pronounced as the Rossby number increased, relaxing the constraint of the Taylor-Proudman theorem. The observations were consistent with a current that did not change its depth as it flowed across isobaths. Thus the fluid flowing around the gyre may have separated from and then re-attached to the bottom.

An analysis of the horizontal component of the vorticity equation shows that possible sources for the vertical shear include the twisting of vorticity filaments and the shear that is initially confined to the bottom Ekman layer. In the limit of low aspect ratio, the twisting mechanism no longer becomes a major source term. In the laboratory, the aspect ratio was not very small (only about .5), and the vertical shear of the fluid leaving the current source was not well known. It would be fruitful to conduct a numerical experiment in which the aspect ratio was kept low and the current contained no vertical shear at the source. If an eddy is produced in this limit, it would be a sign that the bottom shear layer is indeed the source of vorticity which allows the current to separate from the coast.

The barotropic experiments show that the shoaling towards the coast of a sloping bottom will inhibit barotropic coastal flows in the ocean from completely separating from a corner (in contrast to Stern and Whitehead's (1990) barotropic currents), but that for such flows local separation and gyre formation are still possible, as in the baroclinic case.

The hydraulic model, which is only applicable to flow structures which have an alongstream length scale that is greater than the cross stream length scale, was used to test whether the experimental results of Bormans and Garrett (1989) are consistent with the separation mechanism of Røed (1980), in which a coastal current separates from a curved coast because the layer depth at the coast goes to zero. In much of the parameter space which governs the flow, separation only occurred for radii of curvature which were small compared to the local width of the current, thus violating the condition of applicability of the approximation. Nevertheless, in the valid range, for a density front the critical radius of curvature  $\rho_c$  was approximately equal to the inertial radius  $u/f$ , as observed by Bormans and Garrett, if we base the inertial radius on the cross stream average of the upstream flow speed  $\bar{u}$ . For the free streamline case,  $\rho_c$  is roughly proportional to  $(W/R)\bar{u}/f$  (where  $W$  is the upstream current width and  $R$  is the Rossby radius), rather than  $\bar{u}/f$ . Bormans and Garrett's experiments were based on a collection of flows which looked similar to both the free streamline case and the front case, so there is only partial agreement between theory and experiment.

Hydraulic theory was also applied to barotropic flows. Hughes (1989) showed that for a certain relation between streamfunction and potential vorticity and a given bottom slope, a current must separate from the coast if the radius of curvature of the coast becomes small enough, because otherwise reverse flow develops near the wall. This occurred for the wider of two modes with the same potential vorticity and volume flux; the wider mode was subcritical with respect to potential vorticity waves on the jet. I demonstrated that flows with uniform potential vorticity, which are mathematically simpler than Hughes' case, could never separate from the coast for either a flat bottom or a linear bottom slope, implying that a cross-stream potential vorticity gradient is necessary for separation. However, flows with two regions of uniform potential vorticity, which are also mathematically more tractable than Hughes' currents, also do not separate. This result is probably linked to the fact that only the

narrower of the two conjugate solutions for a given volume flux and potential vorticity is unidirectional for no wall curvature, so that the wide solution is automatically discarded. It was found that a barotropic current of piecewise uniform potential vorticity flowing with the wall on the left could display unidirectional conjugate solutions if the depth had a linear slope but did not go to zero at the coast. These results show that the details of the potential vorticity distribution and cross-shore topography can make a qualitative difference in the separation characteristics of a current. Moreover, the barotropic experiments described above cast doubt on the applicability of the shallow water equations to flow separation, since substantial cross-isobath flow was accompanied by vertical shear.

With the exception of the barotropic, flat-bottom flows of Stern and Whitehead (1991), all the flows that separated from coastal topography that have been reported in the literature (see Chapter 1) or in this thesis have been marked by a single gyre that is steady or slowly evolving in time. Similar eddies are seen for barotropic and baroclinic flow sweeping past obstacles, two-layer flow at the mouth of a channel, and one- and two-layer coastal flows past corners. The difference in behavior of the Stern and Whitehead case is probably due to the instability of the barotropic coastal current they studied. In all the other cases, the similarity in behavior of currents with such different flow profiles is a hint that a common dynamical factor is operating to produce the gyre in each case. The obvious factor that all the cases have in common is the existence of an adverse pressure gradient in the viscous boundary layer along the wall, and nothing in my experiments has disproven the possibility that viscous boundary layer separation is the source of eddy generation by a coastal current at a corner. The fact that the inertial radius is a relevant quantity both for baroclinic flow around a curved coast and for sloping bottom barotropic flow around a corner indicates that rotation is of first order importance in the eddy generation process. I attempted to produce a purely rotational, inviscid explanation for separation of an upper-layer flow from a curved corner using hydraulic theory.

While this theory did reproduce the importance of the inertial radius, the results overall were mixed, as described in the discussions in Chapter 2 and Chapter 3. An inviscid explanation based on the stability and wave propagation properties of coastal currents may reproduce the behavior of the baroclinic currents. However, the most promising avenues for exploring corner eddy generation in both the baroclinic and barotropic cases studied here are those which look at steady-state flows in which the effects of both friction and rotation are included.

## References

- Ambar, I., Howe, M. R., Abdullah, M. I. (1976). A physical and chemical description of the Mediterranean Outflow in the Gulf of Cadiz. *Deut. Hydr. Z.*, **29**, 58–68.
- Ambar, I., Howe, M. R. (1979). Observations of the Mediterranean Outflow — I. Mixing in the Mediterranean Outflow. *Deep-Sea Research*, **26**, 535–554.
- Ambar, I., Howe, M. R. (1979). Observations of the Mediterranean Outflow — II. The deep circulation in the vicinity of the Gulf of Cadiz. *Deep-Sea Research*, **26**, 555–568.
- Armi, L., Zenk, W. (1984). Large lenses of highly saline Mediterranean water. *Journal of Physical Oceanography*, **14**, 1560–1576.
- Batchelor, G. (1967). *An Introduction to Fluid Dynamics*, Cambridge University Press, New York.
- Bevington, P. (1969). *Data Reduction and Error Analysis for the Physical Sciences*, McGraw-Hill Book Company, New York.
- Bormans, M. (1988). A model of the exchange through the Strait of Gibraltar. Ph.D. Thesis, Dalhousie University.
- Bormans, M., Garrett, C. (1989). A simple criterion for gyre formation by the surface outflow from a strait, with application to the Alboran Sea. *Journal of Geophysical Research*, **94**, 12637–12644.
- Boyer, D. L., Davies, P. A. (1982). Flow past a circular cylinder on a beta-plane. *Philosophical Transactions of the Royal Society, London*, **A306**, 533–556.
- Boyer, D. L., Kmetz, M. L. (1983). Vortex shedding in rotating flows. *Geophysical and Astrophysical Fluid Dynamics*, **26**, 51–83.



- Boyer D. L., Tao, L. (1987) On the motion of linearly stratified rotating fluids past capes. *Journal of Fluid Mechanics*, **180**, 429-440.
- Chao S.-Y., Boicourt, W. (1986). Onset of estuarine plumes. *Journal of Physical Oceanography*, **16**, 2137-2149.
- Cherniawsky, J., LeBlond, P. H. (1986). Rotating flows along indented coastlines. *Journal of Fluid Mechanics*, **169**, 379-407.
- Conlon, D. M. (1982). On the outflow modes of the Tsugaru Warm Current. *La Mer*, **20**, 60-64.
- D'Asaro, E. A. (1988). Generation of submesoscale vortices: a new mechanism. *Journal of Geophysical Research*, **93**, 6685-6693.
- Donde Va Group (1984). Donde Va? An oceanographic experiment in the Alboran Sea. *Eos, Transactions of the American Geophysical Union*, **65**, 682-683.
- Gill, A. E. (1977). The hydraulics of rotating-channel flow. *Journal of Fluid Mechanics*, **80**, 641-671.
- Grundlingh, M. L. (1981). On the observation of a solitary event in the Mediterranean Outflow west of Gibraltar. *Meteor Forsch-Ergebnisse*, 15-46.
- Howe, M. R. (1982). The Mediterranean water outflow in the Gulf of Cadiz. *Annual Reviews of Oceanography and Marine Biology*, **20**, 37-64.
- Howe, M. R. (1984). Current and hydrographical measurements in the Mediterranean undercurrent near Cape St. Vincent. *Oceanologica Acta*, **7**, 163-168.
- Hughes, R. (1989). The hydraulics of local separation in a coastal current with application to the Kuroshio Meander. *Journal of Physical Oceanography*, **19**, 1809-1820.

- Kase, R. H., Zenk, W. (1987). Reconstructed Mediterranean salt lens trajectories. *Journal of Physical Oceanography*, 17, 158-163.
- Kase, R. H., Beckmann, A., Hinricksen, H.-H. (1989). Observational evidence of salt lens formation in the Iberian Basin. *Journal of Geophysical Research*, 94, 4905-4912.
- Kawasaki, Y., Sugimoto, T. (1984). Experimental studies on the formation and degeneration processes of the Tsugaru warm gyre. In: *Ocean Hydrodynamics of the Japan and East China Sea*, T. Ichiye, editor, 225-238.
- Kawasaki, Y., Sugimoto, T. (1988). A laboratory study of the short-term variation of the outflow pattern of the Tsugaru Warm Water with a change in its volume transport. *Bulletin of the Tohoku Regional Fisheries Research Laboratory*, 50, 203-215. Japanese with English abstract and captions.
- Killworth, P., Stern, M. (1982). Instabilities on density-driven boundary currents and fronts. *Geophysical and Astrophysical Fluid Dynamics*, 22, 1-28.
- Killworth, P., Paldor, N., Stern, M. (1984). Wave propagation and growth on a surface front in a two-layer geostrophic current. *Journal of Marine Research*, 42, 761-785.
- Kubokawa, A. (1986). Instability caused by the coalescence of two modes of a one-layer coastal current with a surface front. *Journal of the Oceanographical Society of Japan*, 42, 373-380.
- Kubokawa, A. (1988). Instability and nonlinear evolution of a density-driven coastal current with a surface front in a two-layer ocean. *Geophysical and Astrophysical Fluid Dynamics*, 40, 195-223.
- Kubokawa, A. (1991). On the behavior of outflows with low potential vorticity from a sea strait. *Tellus*, 43A, 168-176.

- Kubokawa, A., Hanawa, K. (1984). A theory of semi-geostrophic gravity waves and its application to the intrusion of a density current along a coast. Part I. Semi-geostrophic gravity waves. *Journal of the Oceanographical Society of Japan*, 40, 247-259.
- Lanoix, F. (1974). Projet Alboran. Etude hydrologique et dynamique de la Mer d'Alboran. *NATO Technical Report 66*, Brussels, 39 pp. plus figures.
- Loth, L., Crepon, M. (1984). A quasi-geostrophic model of the circulation in the Mediterranean. In: *Remote Sensing of Shelf-Sea Hydrodynamics*, J.C.J. Nihoul, editor, Elsevier Oceanography Series, No 38, pp. 277-285.
- Madelain, F. (1970). Influence de la topographie du fond sur l'écoulement Méditerranéen entre le Détroit de Gibraltar et le Cap Saint-Vincent. *Cahiers Ocean.*, 22, 43-61.
- McWilliams, J. C. (1985). Sub-mesoscale coherent vortices in the ocean. *Reviews of Geophysics*, 23, 165-182.
- Merkine L.-O., Solan, A. (1979). The separation of flow past a cylinder in a rotating system. *Journal of Fluid Mechanics*, 92, 1657-1678.
- Ou, H. W., de Ruijter, W.P.M. (1986). Separation of an inertial boundary current from a curved coastline. *Journal of Physical Oceanography*, 16, 280-289.
- Paldor, N. (1983). Stability and stable modes of coastal fronts. *Geophysical and Astrophysical Fluid Dynamics*, 27, 217-228.
- Pedlosky, J. (1982). *Geophysical Fluid Dynamics*. Springer-Verlag, NY.
- Prandtl, L., Tietjens, O. (1957). *Fundamentals of Hydro- and Aeromechanics*, L. Rosehead, translator, Dover, NY.

- Preller R. H. (1986). A numerical study of the Alboran Sea Gyre. *Progress in Oceanography*, **16**, 113-146.
- Press, W. H., B. P. Flannery, S. A. Teukolsky, W. T. Vetterling (1986). *Numerical Recipes*. Cambridge University Press, NY.
- Qiu, B., Imasato, N., Awaji, T. (1988). Baroclinic instability of buoyancy-driven coastal density currents. *Journal of Geophysical Research*, **93**, 5037-5050.
- Richardson P. L., Walsh, D., Armi, L., Schroder, M., and Price, J.F. (1989). Tracking three meddies with SOFAR floats. *Journal of Physical Oceanography*, **19**, 371-383.
- Røed, L. P. (1980). Curvature effects on hydraulically driven inertial boundary currents. *Journal of Fluid Mechanics*, **96**, 395-412.
- Schlichting, H. (1979). *Boundary Layer Theory*, J. Kestin, translator, 7th edition, McGraw-Hill, NY.
- Signell, R. P., W. R. Geyer (1991). Transient eddy formation around headlands. *Journal of Geophysical Research* **96** 2561-2576.
- Speich, S., M. Crepon. (1992) Study of the inflow-outflow in the strait of Gibraltar and in the Alboran Sea by means of a numerical model. Lecture at AGU 1992 Ocean Sciences Meeting; abstract in supplement to *Eos, Transactions, American Geophysical Union* **72** No. 51, December 17, 1991, p. 49.
- Stern, M. E., J. A. Whitehead, (1990). Separation of a boundary jet in a rotating fluid. *Journal of Fluid Mechanics*, **217**, 41-69.
- Thorpe, S. A. (1976). Variability of the Mediterranean undercurrent in the Gulf of Cadiz. *Deep-Sea Research*, **23**, 711-727.

- Wang, D.-P. (1987). The strait surface outflow. *Journal of Geophysical Research*, 92, 10807-10825.
- Werner, F. E., Figuerola, A. C., Parilla, G. (1988). A sensitivity study of reduced-gravity channel flows with application to the Alboran Sea. *Journal of Physical Oceanography*, 18, 373-383.
- Whitehead, J. A. (1985). The deflection of a baroclinic jet by a wall in a rotating fluid. *Journal of Fluid Mechanics*, 157, 79-93.
- Whitehead, J. A., Miller, A. R. (1979). Laboratory simulation of the gyre in the Alboran Sea. *Journal of Geophysical Research*, 84, 3733-3742.
- Zenk, W. (1970). On the temperature and salinity structure of the Mediterranean water in the Northeast Atlantic. *Deep-Sea Research*, 17, 627-631.
- Zenk, W. (1975). On the Mediterranean Outflow west of Gibraltar. *Meteor Forsch-Ergebnisse*, 23-34.
- Zenk, W. (1980). The sub-Mediterranean undercurrent. *Deep-Sea Research*, 27, 97-98.

## DOCUMENT LIBRARY

March 11, 1991

### *Distribution List for Technical Report Exchange*

Attn: Stella Sanchez-Wade  
Documents Section  
Scripps Institution of Oceanography  
Library, Mail Code C-075C  
La Jolla, CA 92093

Hancock Library of Biology &  
Oceanography  
Alan Hancock Laboratory  
University of Southern California  
University Park  
Los Angeles, CA 90089-0371

Gifts & Exchanges  
Library  
Bedford Institute of Oceanography  
P.O. Box 1006  
Dartmouth, NS, B2Y 4A2, CANADA

Office of the International  
Ice Patrol  
c/o Coast Guard R & D Center  
Avery Point  
Groton, CT 06340

NOAA/EDIS Miami Library Center  
4301 Rickenbacker Causeway  
Miami, FL 33149

Library  
Skidaway Institute of Oceanography  
P.O. Box 13687  
Savannah, GA 31416

Institute of Geophysics  
University of Hawaii  
Library Room 252  
2525 Correa Road  
Honolulu, HI 96822

Marine Resources Information Center  
Building E38-320  
MIT  
Cambridge, MA 02139

Library  
Iamont-Doherty Geological  
Observatory  
Columbia University  
Palisades, NY 10964

Library  
Serials Department  
Oregon State University  
Corvallis, OR 97331

Pell Marine Science Library  
University of Rhode Island  
Narragansett Bay Campus  
Narragansett, RI 02882

Working Collection  
Texas A&M University  
Dept. of Oceanography  
College Station, TX 77843

Library  
Virginia Institute of Marine Science  
Gloucester Point, VA 23062

Fisheries-Oceanography Library  
151 Oceanography Teaching Bldg.  
University of Washington  
Seattle, WA 98195

Library  
R.S.M.A.S.  
University of Miami  
4600 Rickenbacker Causeway  
Miami, FL 33149

Maury Oceanographic Library  
Naval Oceanographic Office  
Stennis Space Center  
NSTL, MS 39522-5001

Marine Sciences Collection  
Mayaguez Campus Library  
University of Puerto Rico  
Mayaguez, Puerto Rico 00708

Library  
Institute of Oceanographic Sciences  
Deacon Laboratory  
Wormley, Godalming  
Surrey GU8 5UB  
UNITED KINGDOM

The Librarian  
CSIRO Marine Laboratories  
G.P.O. Box 1538  
Hobart, Tasmania  
AUSTRALIA 7001

Library  
Proudman Oceanographic Laboratory  
Bidston Observatory  
Birkenhead  
Merseyside L43 7 RA  
UNITED KINGDOM

<b>REPORT DOCUMENTATION PAGE</b>	<b>1. REPORT NO.</b> <b>WHOI-92-22</b>	<b>2.</b>	<b>3. Recipient's Accession No.</b>
<b>4. Title and Subtitle</b> Eddy Generation at a Convex Corner by a Coastal Current in a Rotating System		<b>5. Report Date</b> March 1992	
		<b>6.</b>	
<b>7. Author(s)</b> Barry A. Klinger		<b>8. Performing Organization Rept. No.</b>	
<b>9. Performing Organization Name and Address</b>  Woods Hole Oceanographic Institution Woods Hole, Massachusetts 02543		<b>10. Project/Task/Work Unit No.</b> WHOI-92-22	
		<b>11. Contract(C) or Grant(G) No.</b> (C) OCE89-15408  (G)	
<b>12. Sponsoring Organization Name and Address</b>  Funding was provided by the National Science Foundation under Grant OCE89-15408.		<b>13. Type of Report &amp; Period Covered</b> Ph.D. Thesis	
		<b>14.</b>	
<b>15. Supplementary Notes</b> This thesis should be cited as: Barry A. Klinger, 1992. Eddy Generation at a Convex Corner by a Coastal Current in a Rotating System. Ph.D. Thesis. MIT/WHOI, WHOI-92-22.			
<b>16. Abstract (Limit: 200 words)</b>  Rotating baroclinic and barotropic boundary currents flowing around a corner in the laboratory were studied in order to discover the circumstances under which eddies were produced at the corner. Such flows are reminiscent of oceanic coastal flows around capes. When the baroclinic currents, which consisted of surface flows bounded by a density front, encountered a sharp corner, immediately downstream of the corner an anticyclone grew in the surface layer for an angle of greater than 40 degrees. Varying the initial condition of the flow or the depth of the lower layer did not noticeably affect the gyre's properties except for its growth speed, which was greater when the lower layer was shallower. The barotropic currents were pumped along a sloping bottom, and also formed anticyclonic gyres which quickly attained an approximately steady state. For a given topography, the size of the gyre was proportional to the inertial radius $u/f$ . Volume flux calculations based on the surface velocity revealed vertical shear which increased with gyre size. Hydraulic models were also applied to flow around gently curving topography to determine the critical separation curvature as a function of upstream parameters.			
<b>17. Document Analysis a. Descriptors</b>  eddy coast corner  <b>b. Identifiers/Open-Ended Terms</b>     <b>c. COSATI Field/Group</b>			
<b>18. Availability Statement</b>  Approved for publication; distribution unlimited.		<b>19. Security Class (This Report)</b> UNCLASSIFIED	<b>21. No. of Pages</b> 202
		<b>20. Security Class (This Page)</b>	<b>22. Price</b>